THERMAL STRUCTURE OF THE CENTRAL SCOTIAN SLOPE: SEAFLOOR HEAT FLOW AND THERMAL MATURATION MODELS

by

Eric W. Negulic

Submitted in partial fulfillment of the requirements
for the degree of Master of Science

at

Dalhousie University
Halifax, Nova Scotia
November 2010

DALHOUSIE UNIVERSITY

DEPARTMENT OF EARTH SCIENCES

The undersigned hereby certify that they have read and recommend to the Faculty of Graduate Studies for acceptance a thesis entitled "THERMAL STRUCTURE OF THE CENTRAL SCOTIAN SLOPE: SEAFLOOR HEAT FLOW AND THERMAL MATURATION MODELS" by Eric W. Negulic in partial fulfillment of the requirements for the degree of Master of Science.

Dated: November 24th 2010

Supervisor: _____

Readers: _____

_____

_____

DALHOUSIE UNIVERSITY

DATE: November 24th 2010

AUTHOR: Eric W. Negulic

TITLE: THERMAL STRUCTURE OF THE CENTRAL SCOTIAN SLOPE: SEAFLOOR HEAT FLOW AND THERMAL MATURATION MODELS

DEPARTMENT OR SCHOOL: Department of Earth Sciences

DEGREE: M.Sc. CONVOCATION: May YEAR: 2011

_____

Signature of Author

Dedication

This thesis is dedicated to the late Hans Wielens. Over the past three years I have had the pleasure of getting to know Hans as both a colleague and a friend. I spent many early mornings working with Hans on my petroleum systems models in his small office at the GSC Atlantic. Despite Hans keeping strange hours which often found me hard at work by 7 a.m. I always looked forward to getting up and going to see Hans. He would always greet me with a smile as if genuinely happy and excited I was there. His enthusiasm and positive attitude made modelling more fun than work. I learned a lot from Hans over the years in terms of both geology and modelling. However, the thing that Hans affected most strongly in me was his positive outlook and laid back take on life. It was refreshing to see someone so happy and at ease in his work and this will stick with me for life. Hans touched the lives of many geologists over his career, be it through supervision of projects, working relationships, or simply enthusiastic presentations on his work. We are all very fortunate to have met Hans and he will be remembered for the positive impact he had on all of us. I therefore dedicate this thesis to Hans Wielens, not only for being the best role model and mentor a young student could have asked for, but also for being such a good friend.

Table Of Contents

List of Tables

List of Figures

Abstract

Many factors such as rift history, crustal structure and distribution of high thermal conductivity salt bodies throughout the sediment pile affect the present day thermal structure of the deepwater Scotian Slope. Understanding the basin's thermal evolution is crucial in determining the hydrocarbon maturation potential of this deepwater frontier basin. The Late Jurassic Verrill Canyon Formation of the deepwater slope has been inferred as the primary source rock interval for the Scotian Basin. However, to date, only twelve boreholes have sampled the Scotian Slope, and of these, none penetrate beneath the uppermost Jurassic sediments. Therefore, the distribution and maturation of deeper source rock intervals through standard vitrinite reflectance analysis remains unknown. In this study we attempt to better constrain the thermal history and maturation potential of the central Scotian Slope using a combination of recently acquired seafloor heat flow data, 2D seismic reflection data, available well data, simple lithospheric rift models and 3D thermal and petroleum systems modelling. We have derived a method of combining seafloor heat flow data with simple lithospheric rift models to provide first order constraints on the hydrocarbon maturation potential of frontier basins in dynamic 3D thermal models for regions lacking vitrinite reflectance and temperature data from boreholes.

In July 2008, 47 seafloor heat flow measurements were acquired across the central Scotian Slope in an attempt to better constrain the region's thermal structure. Locations seaward of the salt diapiric province, thus unaffected by the high thermal conductivity of salt, recorded seafloor heat flow values of ~41-46 mWm^{-2}. Significant increases in seafloor heat flow were noted for stations overlying salt diapiric structures, reaching values upwards of 72 mWm^{-2}. The seafloor heat flow data have been corrected to remove the conductive effects of salt and the cooling effects of seafloor sedimentation on measured heat flow. The corrected data are compared with basal heat flux predictions from simple lithospheric rift models as constrained using crustal (β) and lithospheric (δ) stretching factors after Wu (2007) to constrain heat flux history through time. Seafloor heat flow and simple modelling results suggest present day basal heat flux does not vary significantly across the slope. Present day basal heat flux across the central Scotian Slope is ~44-46 mWm^{-2}.

Basal heat flux curves from simple lithospheric rift models are used to constrain the heat flux history in 3D thermal and petroleum systems models of the central Scotian Slope. Numerous basal heat flux histories were tested to determine which heat flux history yielded the best match between modelled and measured seafloor heat flow data and to determine how varying basal heat flux affects the modelled hydrocarbon maturation of Verrill Canyon source rocks. The basal heat flux history which yielded the best match to measured seafloor heat flow data suggests that the Late Jurassic source rock interval rests primarily within the late oil window. Variations in radiogenic heat production across the margin associated with thickening continental crust were tested and suggest that significant variations in both maturation and seafloor heat flow may occur if radiogenic heat producing elements occur in high enough concentrations in the crust.

List of Abbreviations Used

AFZ - Azores Fault Zone
BTF - Biscay Triple Junction
BWT - Bottom Water Temperature
CCFZ - Cobequid Chedabucto Fault Zone
CCGS - Canadian Coast Guard Ship
COB - Continent Ocean Boundary
CTD - Conductivity Temperature Depth ES - Echo Sounder
ECMA - East Coast Magnetic Anomaly
FB - Fault Blocks
GFZ - Charlie-Gibbs Fracture Zone
HF - Heat Flow
HI - Hydrogen Index
HSM - Highly Serpentinized Mantle
HVLV - High Velocity Lower crustal layer
NFZ - Newfoundland Fracture Zone
OCT - Ocean Continent Transition zone
PSE - Petroleum Systems Elements
PSM - Partially Serpentinized Mantle
PWD - Paleo Water Depth
SDR - Seaward Dipping Reflectors
SWIT - Sediment Water Interface Temperature
TOC - Total Organic Carbon

Acknowledgements

First and foremost I would like to thank Keith Louden for his continued encouragement and assistance throughout the course of this project. Over that past two years I have learned a lot from Keith; without his expertise, insight and extreme patience my completion of this project would not have been possible. My committee members Mladen Nedimovic and Hans Wielens have not only provided advice and feedback throughout the course of this project, but it was thanks to their wonderful introduction to scientific research during my Honours project that I pursued graduate studies. I would like to thank Pengrowth and OETRA for providing the funding which supported me throughout my studies and made the Hudson heat flow cruise and thus this project possible. I thank ION/GX Technology for providing us with the NovaSPAN 2D seismic reflection survey. I extend a warm thank you to Wolfe Rotke and the rest of the Schlumberger PetroMod team in Aachen Germany for both providing such a thorough training course and for being so accommodating during my stay in Aachen. I thank Prasanta Mukhopadhyay (Dr. Muki) for the many constructive discussions we've had regarding petroleum systems modelling and for sharing with me his previous work on the hydrocarbon systems of the central Scotian Slope. Grant Wach and Marcos Zentilli, although not directly involved with the project itself, were always helpful and crucial in many ways to the positive experience I've had at Dalhousie; I owe them both a big thank you. I would like to thank my lab mates Omid Aghaei, Joanna Gerlings, Matthias Delacluse and Yue Wu for both their technical assistance in such a broad range of disciplines and for making the lab such an enjoyable place to be, day in day out. I thank the Dalhousie Salt Dynamics group for the many discussions we've had regarding salt tectonics and for their insight and assistance during my seismic interpretations of salt structures. Finally, I would like to thank all of the faculty and students at Dalhousie University from whom I have learned so much and who have combined to create a wonderful, fun work environment.

Chapter 1: Introduction

In this study we investigate the thermal structure of the central Scotian Slope and attempt to determine what factors affect present day seafloor heat flow and the thermal maturation of hydrocarbons. We employ a combination of seafloor heat flow data, well data, 2D seismic reflection data, simple lithospheric models and dynamic 3D thermal models in our investigations. The Scotian Slope comprises the deepwater portion of the Scotian Basin, located offshore Nova Scotia (Fig. 1). The Scotian Slope is underlain by transitional continental crust which thins in the seaward direction as a result of the Late Triassic rifting of the North American and African plates (Jansa and Wade 1975). Following rifting, the margin entered a drift phase which has endured from the Early Jurassic to present day, and a thick accumulation of marine sediments has formed across the Scotian Margin. The sediment pile, upwards of 16 km thick in the deep sedimentary subbasins, has been a target for hydrocarbon exploration (Wade 2000).

While exploration on the Scotian Shelf has led to production from the Sable subbasin, which contains an estimated 12.8 Tcf of recoverable gas reserves, exploration on the deepwater Scotian Slope has yet to identify economic hydrocarbon accumulations (CGPC 1997). A recent phase of drilling on the Scotian Slope which began in 2000 has resulted in the completion of seven new wells (Kidston et al. 2007). Despite minor oil and gas shows, no significant hydrocarbon accumulations were identified, largely due to a lack of adequate reservoir sands. The lack of success raises questions as to whether or not economic hydrocarbon accumulations exist on the deepwater slope. In this thesis we attempt to constrain the thermal history of the margin to predict the hydrocarbon maturation potential of the central Scotian Slope. Constraining the thermal maturation of

source rocks will allow future emphasize to be placed on identifying reservoir sands and traps.

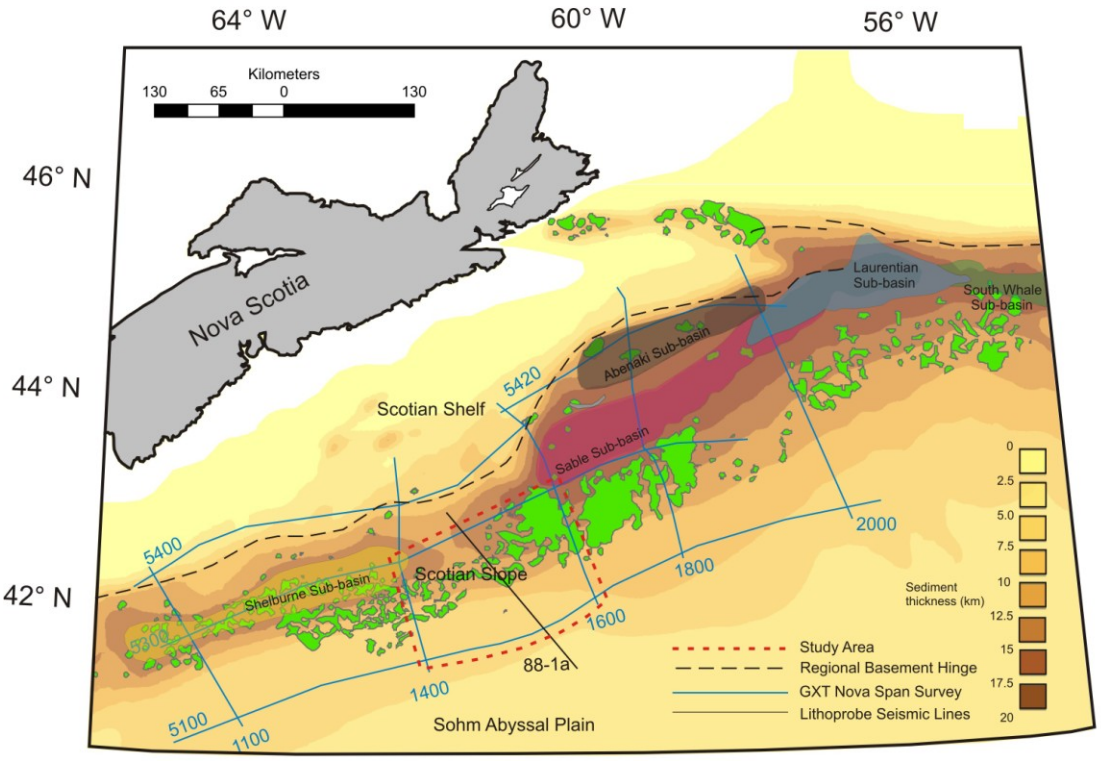

Figure 1. 1: Scotian Basin location map with study area outlined in dashed red. Location of shallow salt bodies after Shimeld (2004) are shown in green.

The thermal history and present day seafloor heat flow of passive rifted continental margins are known to be affected by several factors including:

1) Pre-rift lithospheric thickness, temperature at the base of the lithosphere and the amount of lithospheric thinning during rifting.
2) Presence and distribution of highly thermally conductive salt structures throughout the basin.
3) Radiogenic heat production within the continental crust and sediment pile.

In this thesis we address the effects of the above factors on the thermal structure of the central Scotian Slope.

1.1 Statement of Motivation

Global hydrocarbon exploration has found recent success in deepwater sedimentary basins. This has led to the recent push towards deepwater exploration of the Scotian Slope, offshore eastern Canada. Despite seven wells drilled on the slope since 2000, no economic hydrocarbon deposits have been identified. Thermal and petroleum systems models are useful in predicting the hydrocarbon potential of under explored basins and reducing risk associated with drilling. However, the primary thermal constraints in these models are derived from temperature and vitrinite reflectance data from wells, which are lacking on the central Scotian Slope. Understanding the thermal history of the region is important when predicting the depth to maturation window and maturity of source rock intervals. Determining the maturation of source rock intervals on the Scotian Slope is fundamental to the regions exploration success. We aim to provide thermal constraints for the region by coupling seafloor heat flow data with simple lithospheric rift models in an innovative approach to bridge the information gap associated with the lack of well data on the central Scotian Slope.

1.2 Study Area

The Scotian Basin is located offshore Nova Scotia, eastern Canada. It is subdivided by the 200 m water depth contour into the shallow water Scotian Shelf and deep water Scotian Slope. The basement consists of numerous interconnected subbasins which formed as a result of Late Triassic rifting. Our study is focused on the central Scotian Slope, in particular the region between the eastern Shelburne subbasin and the western Sable subbasin bounded by NovaSPAN 2D seismic lines 1400 and 1600 (Fig.

1.1). The study area crosses the salt diapiric sub-province of the Scotian Slope; thus stratigraphy and thermal structure are affected by salt tectonic deformation.

1.3 Objectives

In this thesis we present recently acquired seafloor heat flow data across the central Scotian Slope to provide further constraints on the region's thermal structure. These data are to be coupled with simple lithospheric rift models in constraining 3D thermal models predicting the maturation potential of the study area. Prior to data synthesis in 3D modelling numerous preliminary goals must be completed.

Seafloor heat flow data are to be acquired across the central Scotian slope both above salt diapirs and in regions unaffected by salt. Seafloor heat flow data are to be corrected for the effects of high thermally conductive salt bodies and cold sedimentation atop the seafloor. Once corrected for effects of the sediment pile the measured heat flow data are representative of the basal heat flux. The corrected data may then be compared with basal heat flux predictions from simple lithospheric models of the central Scotian Slope to provide insight on the regions heat flow history through time and initial lithospheric thicknesses. Simple lithospheric modelling results constrained after corrected seafloor heat flow data will be used to constrain the basal heat flux in dynamic 3D models. 3D models are built to predict the 3D effects of salt on present day seafloor heat flow and determine the maturation potential of source rocks within the basin.

The objectives of this work are to:

- Acquire and process seafloor heat flow data from across the central Scotian Slope both in regions overlying salt bodies and regions unaffected by salt to constrain both regional and local variations in seafloor heat flow;

- Correct for the effects of high thermally conductive salt bodies and cool seafloor sedimentation on seafloor heat flow measurements;
- Compare corrected seafloor heat flow data with predictions from simple lithospheric rift models as constrained using known crustal stretching factors to provide further constraints on lithospheric models and basal heat flux across the central Scotian Slope;
- Run 3D thermal models of the central Scotian Slope with varying basal heat fluxes constrained after our simple lithospheric modelling results to determine if our measured seafloor heat flow data can be replicated using dynamic 3D models and to predict the maturation potential of the study area.

1.4 Hypothesis

Three hypotheses are tested in this work:

1) While present day seafloor heat flow values across the central Scotian Slope are not expected to vary significantly due to variations in lithospheric thinning as a result of the great age of the margin, we expect notable variations in seafloor heat flow may exist due to presence of highly thermally conductive salt structures and/or variations in radiogenic heat production within the thinned continental crust;
2) Seafloor heat flow data coupled with simple lithospheric stretching models and 2D seismic data are useful in constraining basal heat flux histories in dynamic 3D thermal models for first order predictions of the maturation potential of frontier basins with limited well data;

3) Variations in basal heat flux history and/or radiogenic heat production in the basement will have significant implications on hydrocarbon maturation.

1.5 Thesis Organization

The remainder of the thesis is organized as a series of chapters and supporting appendices in order to efficiently present the completed work and the results obtained. The thesis is structured as follows:

- Chapter 2 discusses the geography, tectonic history, stratigraphy and structure of the Scotian Basin.
- Chapter 3 focuses on the recently acquired seafloor heat flow data and simple lithospheric modelling of the study area as constrained by seafloor heat flow data. The chapter includes a summary Scotian Basin heat flow and the results from the 2008 Hudson heat flow cruise. Corrections applied to the seafloor heat flow data are discussed and simple lithospheric models constrained by the corrected heat flow data are investigated in an attempt to better constrain the basal heat flux history of the study area.
- Chapter 4 focuses on 3D thermal modelling of the central Scotian Slope. Models are constrained by available well, seismic, lithospheric modelling and heat flow data in an attempt to both constrain the hydrocarbon maturation potential of the study area and to determine if measured seafloor heat flow data can be replicated using dynamic 3D models.
- Chapter 5 provides the conclusions from our work as well as suggestions for future work.

- Appendices A-H contain additional data and background information supporting to the main body of the thesis.

Chapter 2: Scotian Basin Geology: Geography, Tectonic History, Stratigraphy and Structure

2.1 Scotian Basin Geography

The Nova Scotia rifted continental margin consists of a shallow, stable, basement platform underlying the inner continental shelf, a hinge zone leading to the deep sedimentary subbasins of the outer continental shelf and continental slope and the deepwater Scotian Slope which terminates at the onset of the deep, distal, Sohm oceanic abyssal plain marking the seaward limit of the Scotian Basin (Fig. 2.1). To the northwest the Scotian Basin is bounded by the stable shallow water Lahave Platform and Canso Ridge. Basement depths are generally less than 4 km on these continental platforms (Wade and MacLean 1990) (Fig. 2.1(B)). This landward limit of the margin is underlain by relatively thick unstretched continental crust. An adjacent basement hinge zone marks the transition from the stable continental platforms to the deeper subsiding sedimentary subbasins, which overly thinned continental crust (Wade and MacLean 1990, Wu et al. 2006) (Fig. 2.1(A)).

The northeast trending basement hinge zone persists along the northwest flank of the Scotian Margin (Fig. 2.1(A)). The hinge zone is comprised of many fault bounded half grabens across which the basement depths increase from ~4 km on the continental platforms to more than 10 km in the deep subsiding sedimentary subbasins (Fig. 2.1(B)) (Wade and MacLean 1990). The basement gradient landward of the hinge zone is ~3 degrees, while seaward of the hinge basement drops at a gradient of ~20 degrees (Wade and MacLean 1990). Seaward of the basement hinge zone exist a series of interconnected fault bounded subbasins which combine to form the deep sedimentary depocenters of the Scotian Basin (Fig. 2.1) (Welsink et al. 1989).

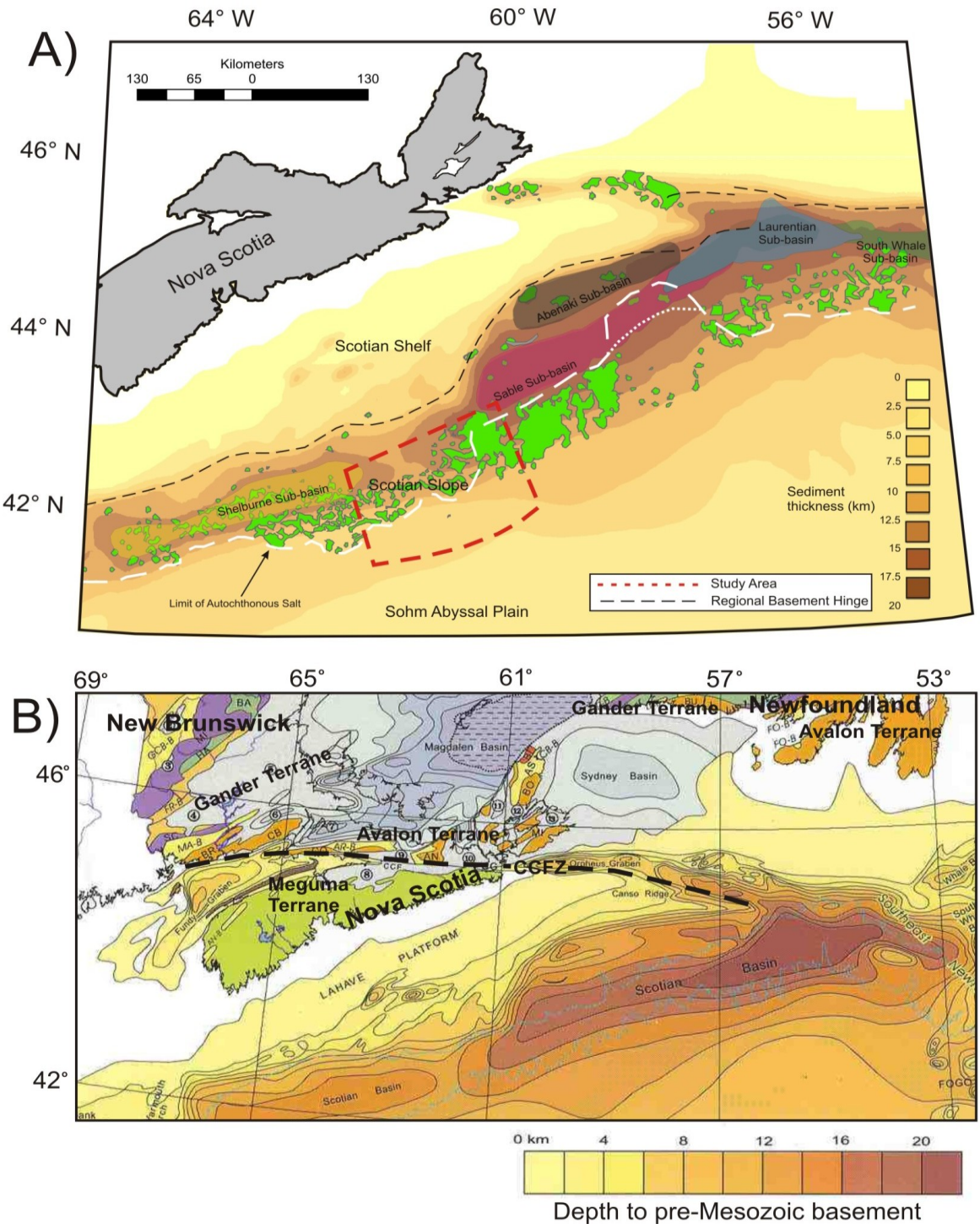

Figure 2. 1: Scotian Basin location maps showing A) major geographical elements including shelf, slope, abyssal plain, major subbasins and trend of the basement hinge line. Background map shows sediment thickness with shallow salt bodies shown in green. Dashed white lines mark the seaward limit of autochtonous salt after Shimeld (2004) (modified after MacDonald 2009) and B) geological map of eastern Canada showing terranes of the Appalachian Orogen. CCFZ, Cobequid Chedabucto Fault Zone. Modified from Williams and Grant (1998).

The numerous deep sedimentary subbasins of the outer Scotian Shelf and Slope began forming at the onset of rifting as heating, stretching and thinning of the continental lithosphere resulted in faulting and subsidence of the brittle upper crust (Louden 2002). Subbasin geometry is controlled by the faulting and rotation of basement blocks during lithospheric extension (Wade and MacLean 1990). These basement lows act as sediment depocenters further subsiding with the loading of Mesozoic-Cenozoic sediments (Jansa and Wade 1975). From east to west, the major sediment depocenters are the Shelburne, Sable, Abenaki, Laurentian, and South Whale subbasins (Fig. 2.1(A)). In addition to these, the Mohican and Orpheus Grabens of the Scotian Shelf contain notably thick deposits of syn-rift sediments (Wade and MacLean 1990).

Underlying the deep water Scotian Slope exists a region dominated by salt deformation structures referred to as the Slope Diapiric Province (Fig. 2.1(A)) (Jansa and Wade 1975). This region is characterized by numerous salt deformation structures including salt diapirs, walls, nappes, canopies, tongues and welds by which the regional stratigraphy has been significantly distorted. Shimeld (2004) has designated five salt tectonic sub-provinces across the slope based on deformation style as discussed in Section 2.4.1. Finally, seaward of the Scotian Slope is deep water Sohm Abyssal Plain marking the seaward limit of the Scotian Basin.

2.2 Rifting and Crustal Structure

The Ordovician Appalachian Orogeny formed during a period of convergent tectonics as the Paleozoic Iapetus Ocean closed and the Pangaean super-continent began to form (Williams 1984). The orogen resulted in the amalgamation of five distinct tectonic zones, of which the easternmost two, the Avalon and Meguma Terranes,

comprise the basement rocks of mainland and offshore Nova Scotia (Williams 1979) (Fig. 2.1(B)). Onshore Nova Scotia we see exposures of the Avalon Terrane to the Northeast and the Meguma Group to the Southwest contrasted along the Cobequid Chedabucto Fault Zone (Fig. 2.1(B)). The Avalon Terrane is composed of Pre-Cambrian volcanic and sedimentary rocks while the adjacent, younger, Early Ordovician Meguma Group is dominantly low grade metamorphosed greywacke and shales intruded by Late Devonian granites (Williams 1984).

Scotian Shelf wells that pierce basement (e.g. Mohawk B-93, Naskapi N-30) report granite and metamorphic rocks of the Meguma Group (Jansa and Wade 1975). These basement rocks record northeast trending structural fabrics remnant of the previous collisional orogen (Welsink et al. 1989). As structural trends recorded by Late Triassic-Early Jurassic rift basins follow a similar northeast orientation, it has been inferred that the current basement configuration of the rifted continental Scotian Margin has been influenced by previous tectonic history of the region (Welsink et al. 1989).

The Mesozoic history of the Scotian Margin has been dominated by extensional tectonics and continental drift. Rifting of Pangaea began in the Mid Triassic with the onset of crustal thinning and extension across what currently form the Nova Scotia/Morocco conjugate margins (Jansa and Wade 1975) (Fig. 2.2). Rifting persisted throughout the Late Triassic and into the Early Jurassic allowing deposition of syn-rift sediments into subsiding, fault controlled, basement lows. Final continental separation and crustal breakup marking a complete rift event occurred ~160 Ma (Louden 2002). Later plate separation between Newfoundland and Iberia (125 Ma), Northern Newfoundland and Europe (120 Ma), Greenland and Labrador (70 Ma) and Greenland

and Europe (55 Ma) persisted following the onset of Pangaean rifting and may have contributed to renewed stages of later subsidence along the Nova Scotia margin through the Jurassic to Tertiary (Louden 2002).

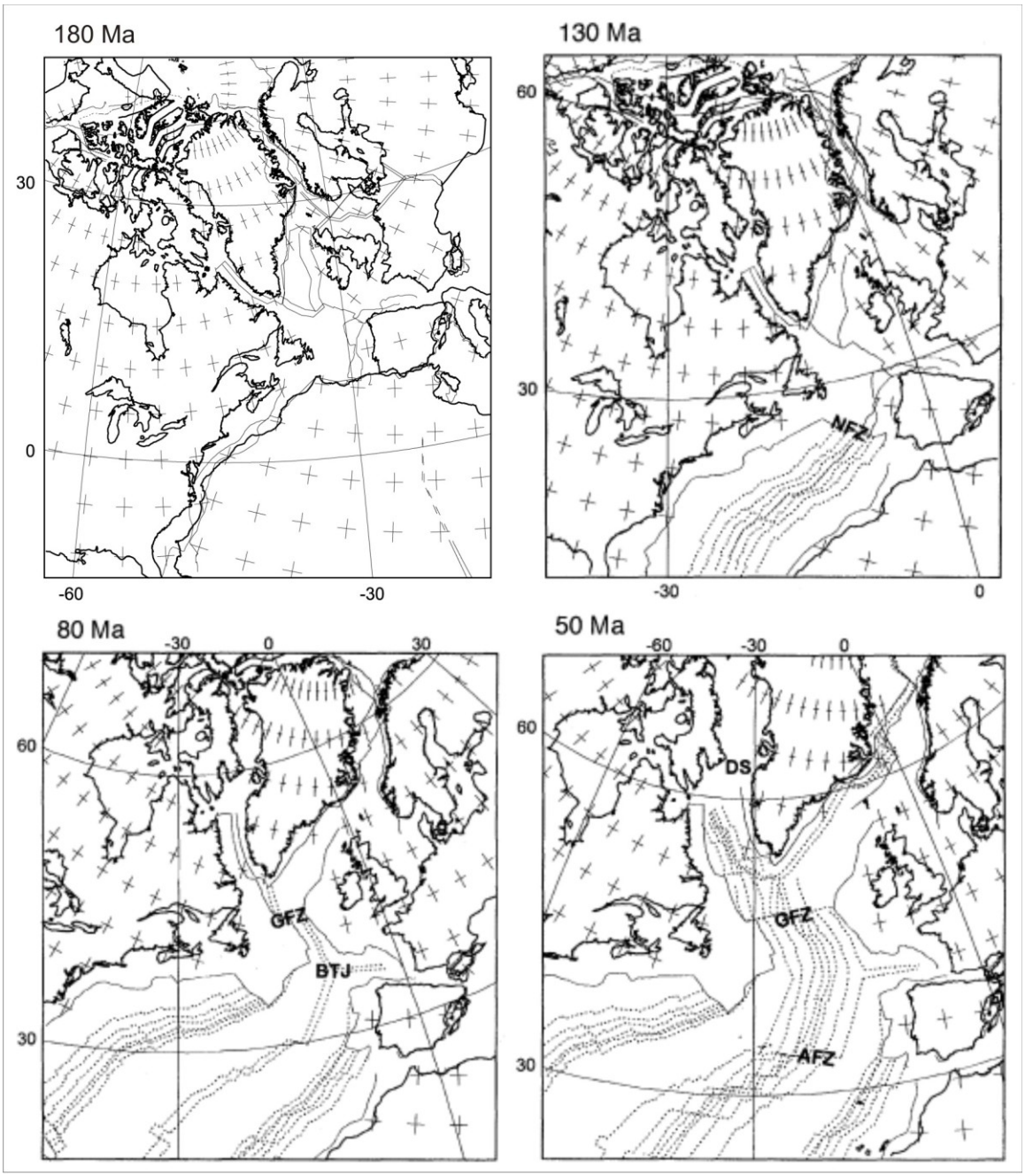

Figure 2. 2: Plate reconstructions for the North Atlantic Ocean showing positions at 180 Ma, 130 Ma, 80 Ma and 50 Ma. Dashed lines represent select magnetic isochrons. NFZ, Newfoundland Fracture Zone; GFZ, Charlie-Gibbs Fracture Zone; BTJ, Biscay Triple Junction; AFZ, Azores Fracture Zone. From Coffin et al. (1992), modified after Louden and Chian (1999).

The crustal structure of the Scotian Margin shows significant variations in both the North/South and East/West directions. The Scotian Margin marks the transition from the southern volcanic rifted margin offshore the United States (e.g. south Baltimore Canyon Trough) to the northern non-volcanic rifted margin offshore Newfoundland (e.g. Grand Banks) (Fig. 2.3). In the northwest/southeast direction the margin records extension and thinning in the seawards direction typical of rifted continental margins. The transition from old unstretched continental crust beneath Nova Scotia, across the thinned transitional crust underlying the Scotian Basin, to the younger oceanic crust of the Atlantic Ocean has been imaged by velocity modelling of deep seismic refraction experiments (Fig. 2.4) (Funck et al. 2004, Wu et al. 2006).

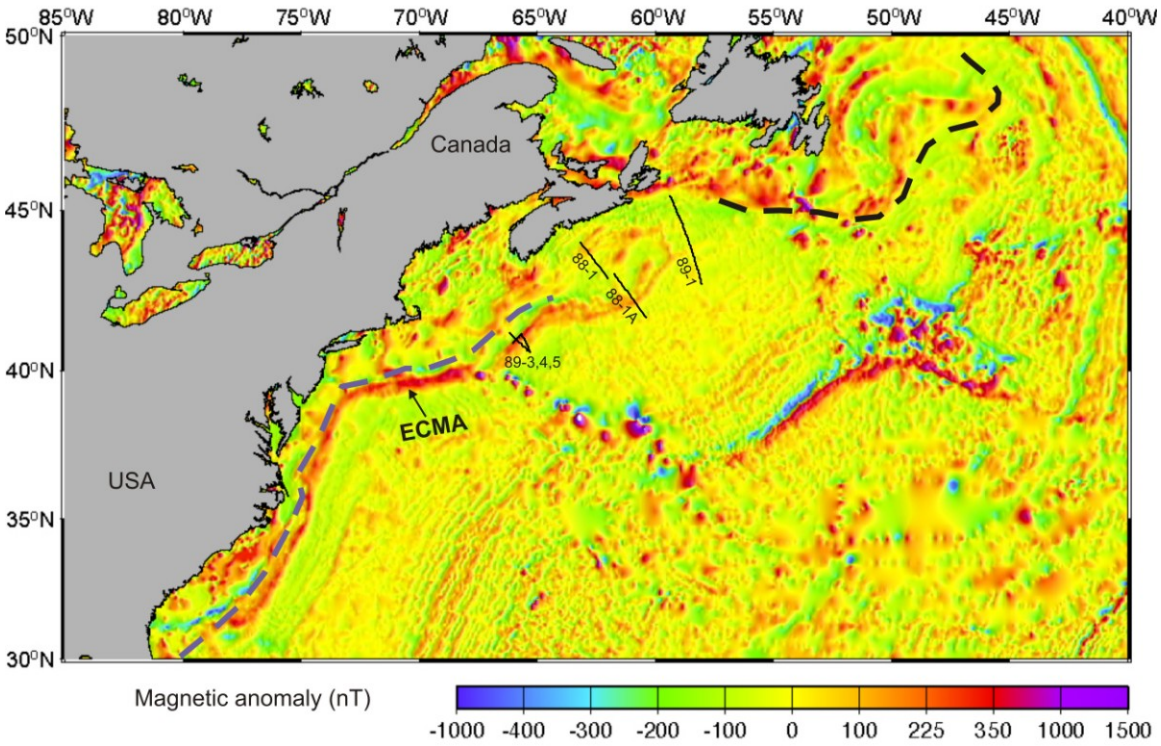

Figure 2. 3: Magnetic anomaly map of the eastern United States and Canadian offshore showing volcanic margins with purple dashed lines and non-volcanic margins with black dashed lines. Select seismic reflection profiles are shown as solid black lines for reference. ECMA, East Coast Magnetic Anomaly. Modified after Wu (2007).

A strong positive magnetic anomaly (~200-300 nT) persists along the East Coast of North America from Georgia to Nova Scotia and is referred to as the East Coast Magnetic Anomaly (ECMA) (Keen 1969, Keen and Potter 1995a) (Fig 2.3). This magnetic anomaly has been inferred by many to mark the boundary between thinned continental and oceanic crust as extrusive basaltic flows commonly occur at volcanic margins with the onset of final continental separation (Keen and Potter 1995a). The magnetic anomaly is recorded at full strength near the southern limit of the Scotian Basin, and diminishes in amplitude to the North before splitting into two anomalies and disappearing completely near Sable Island (Keen and Potter 1995a) (Fig. 2.3).

In the southern Scotian Margin, Seaward Dipping Reflections (SDR) characteristic of volcanic extrusives have been identified in seismic lines 89-3,4, and 5, coinciding with the ECMA providing support that the magnetic anomaly coincides with the continent ocean boundary of a volcanic continental margin (Keen and Potter, 1995a). In the northern Scotian Margin near the northern limit of the ECMA, seismic line 89-1 (Fig. 2.3) demonstrates an absence of SDR (Keen and Potter 1995b). The lack of SDR associated with the diminished to non-existent ECMA suggests that this portion of the margin is non-volcanic. The Scotian Margin is thus a transitional volcanic to non-volcanic margin.

To better constrain the crustal structure across the Scotian Margin the SMART seismic refraction survey was conducted, during which, three long seismic refraction profiles were acquired crossing the margin from the interior continental shelf to the deepwater Sohm Abyssal Plain. These lines were shot across the southern, central and northern portions of the margin in order to constrain variations in crustal structure across

the transitional continental margin. SMART line 1 supports the interpretation of a non-volcanic margin to the north (Funck et al. 2004). Velocity models derived from SMART line 1 show unstretched continental crust underlying the inner Scotian Shelf changing to thinned continental crust across the outer shelf and upper slope (Fig. 2.4). The lower slope is underlain by the Ocean Continent Transition Zone (OCT), a region of partially to highly serpentinized and exhumed mantle overlain by altered continental crust (Fig. 2.4). The seaward limit of SMART Line 1 is composed of young undeformed oceanic crust.

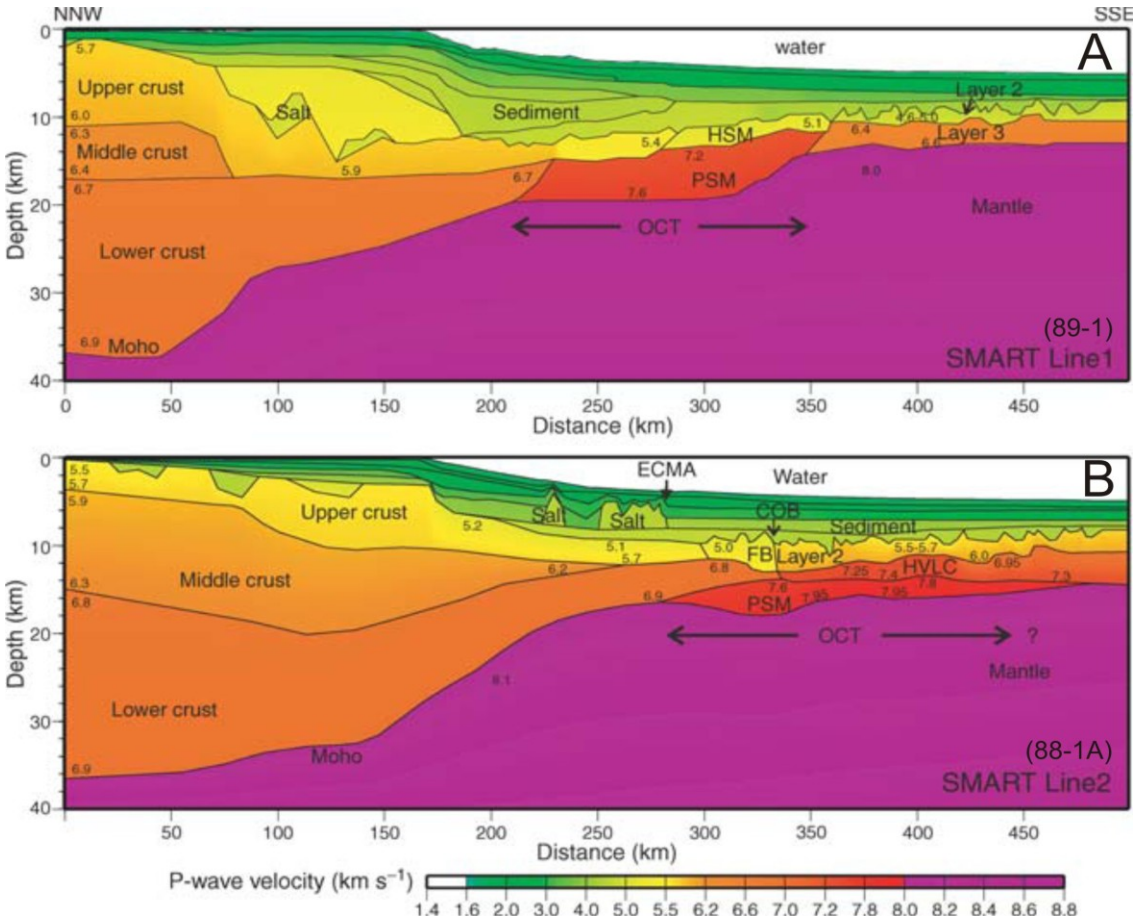

Figure 2. 4: Comparison of crustal structure from velocity models along seismic refraction lines A) SMART Line 1, coincident with reflection profile 89-1, across the northern Scotian Margin (Funck et al. 2004) and B) SMART Line 2, coincident with reflection profile 88-1A, across the central Scotian Margin (Wu et al. 2006). HSM, Highly Serpentinized Mantle; PSM, Partially Serpentinized Mantle; OCT, Ocean Continent Transition zone; ECMA, East Coast Magnetic Anomaly; COB, Continent-Ocean Boundary; FB, Fault Blocks; HVLV, High Velocity Lower Crustal Layer. From Wu et al. (2006).

The ECMA, although decreasing in intensity, persists across the central Scotian Margin. Seismic reflection profiles 88-1 and 88-1A across the central margin in the region of the diminished ECMA do not record SDR (Keen et al. 1991). As SDR were thought to be associated with the ECMA to the south this leaves some ambiguity in the volcanic character, and the cause of the reduced amplitude ECMA across the central portion of the margin. Velocity modelling of SMART line 2 which is coincident with line 88-1A, was used to determine the crustal structure and volcanic character of the central Scotian Margin (Wu et al. 2006). Similar to Line 1, Line 2 contains unstretched continental crust, thinned continental crust, a OCT characterized by partially serpentinized mantle, and undeformed oceanic crust (Wu et al. 2006) (Fig. 2.4).

SDR are absent from both the central and northern portions of the margin and neither velocity models of SMART line 1 or 2 contain evidence of magmatic underplating. The transition from the high amplitude ECMA and extrusive volcanic wedge (SDR) of the southern Scotian Margin to the reduced amplitude ECMA and absent volcanic extrusives of the central and northern Scotian Margin supports the interpretation of a transitional, yet dominantly non-volcanic margin with the exception of its southernmost volcanic limit. The reduced amplitude ECMA may be the result of the transition from thinned continental crust to serpentinized mantle within the OCT. Variations in the amplitude of the weakened magnetic anomaly may result from varying degrees of serpentinization within the OCT (Wu et al. 2006).

Crustal structure and rift history have direct implications for basin subsidence and sedimentation (Keen 1979). Thermo-mechanical models are used to predict the subsidence history of a developing rifted margin. This includes subsidence due to density

variations associated with lithospheric thinning and asthenospheric replacement and subsidence due to thermal expansion and contraction following the onset of crustal thinning. Mechanical loading and associated flexure resulting from sedimentation atop the thinned crust results in further total subsidence (Keen and Beaumont 1990). Models are constrained by Scotian Basin seismic and well data. Thermo-mechanical models allow for variation of crustal (β) and sub-crustal (δ) thinning as proposed by Royden and Keen (1980).

Scotian Margin models show that greater landward sub-crustal thinning (δ) than crustal thinning (β) resulted in buoyancy driven uplift for the interior regions of the margin, the Lahave platform. Initial uplift of up to 2 km followed by limited later thermal contraction resulted in limited sedimentation on the inner shelf and major sediment bypass depositing large amounts of sediment in the deeper water outer shelf and slope basins (Keen and Beaumont 1990). Wu et al. (2006), although to a lesser degree (0.75 km), also predict early uplift of the Lahave Platform from velocity modelling across SMART line 1. Crustal models of the adjacent deeper Scotian Basin with greater crustal thinning (β) values show a subsiding concave-up basement surface allowing for much thicker sediment accumulations than the interior, concave-down Lahave platform (Keen and Beaumont 1990). This explains the development of the much thicker sedimentary subbasins seaward of the hinge zone (e.g. Abenaki and Sable subbasins) as further subsidence results in more accommodation space for sediments which in turn results in further subsidence.

2.3 Lithostratigraphy of the Scotian Basin

The lithostratigraphy of the Scotian Basin has been interpreted by numerous authors (e.g. McIver 1972, Jansa and Wade 1975, Wade and MacLean 1990) and a detailed summary of available literature is presented in Appendix A. The primary constraints on Scotian Basin stratigraphy are well data from the numerous exploration wells drilled on the continental shelf. Lithostratigraphic interpretations of the Scotian Slope are difficult, due to both the lack of well data and the presence of salt deformation structures, which significantly distort stratigraphy and hamper lateral correlations of shelf stratigraphies onto the slope via seismic data. A recent global push towards deeper water exploration has resulted in increasing interests in the hydrocarbon potential of the Scotian Slope, which has in turn resulted in more recent studies of the region (Kidston et al. 2002, Young 2005). A brief overview of the major stratigraphic formations of the shelf and slope are included below. All information is derived from McIver (1972), Jansa and Wade (1975), Hardy (1975), Eliuk (1978), Wade and MacLean (1990) and Kidston et al. (2002). Formations described, unless specified, refer to shelf lithologies, many of which grade laterally into shale rich, age equivalent strata on the deeper water Scotian Slope.

A stratigraphic chart of the Scotian basin shows the relative position and ages of all formations mentioned below (Fig. 2.5). Syn-rift red beds of Late-Triassic to Early Jurassic age overlie the rifted continental basement in fault bounded lows. These are conformably overlain by further red beds of the Early Jurassic Eurydice Formation, and the thick salt deposits of the Argo Formation, which interfinger the Eurydice Formation. The Early Jurassic records a basin scale erosive event associated with final separation of the African and North American plates referred to as the breakup unconformity. This

unconformity separates the Argo Formation from the overlying carbonates and clastics of the overlying Iroquois and Mohican Formations respectively.

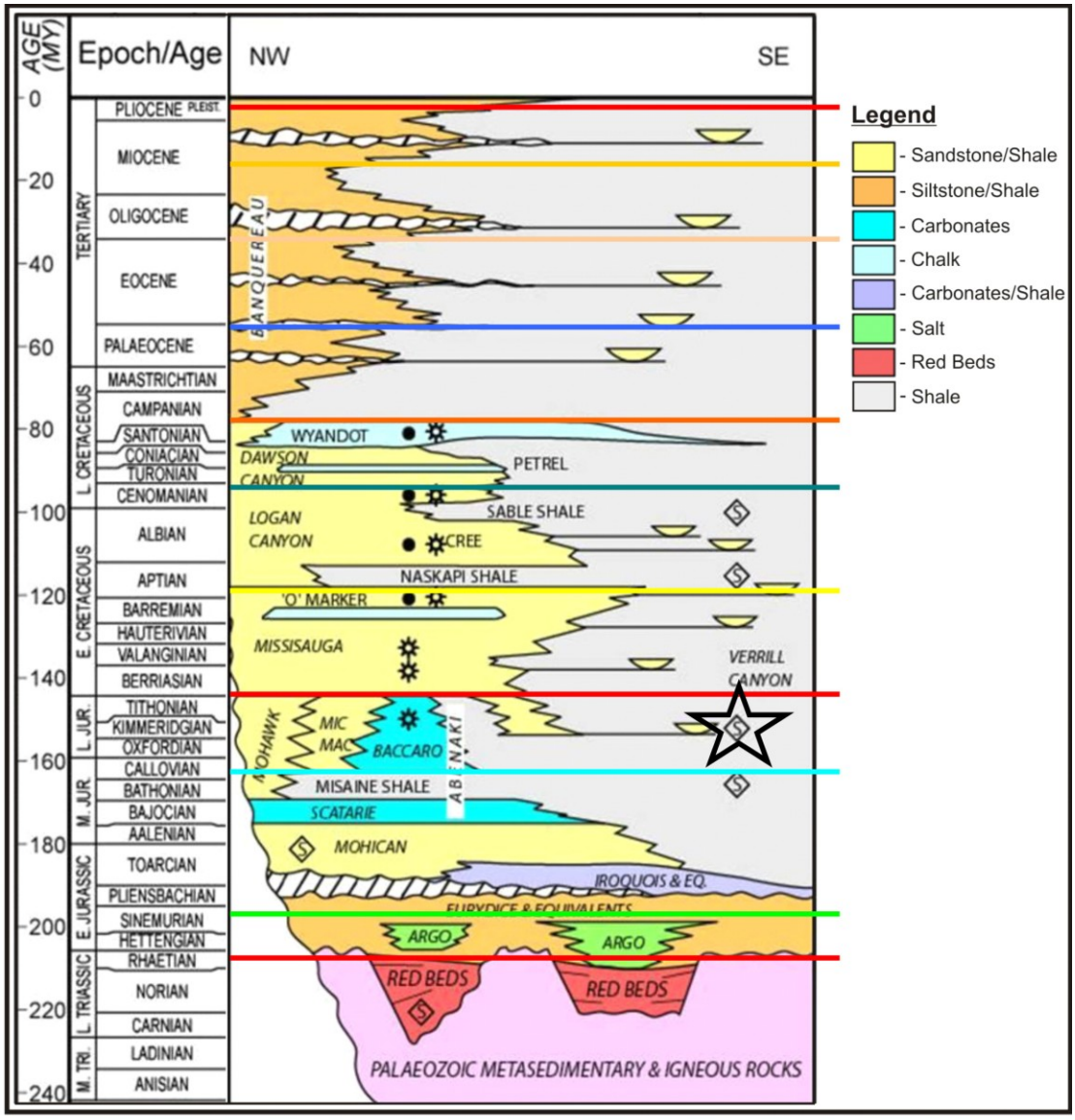

Figure 2. 5: Stratigraphic chart showing major formations of the Scotian Shelf and Slope. "S" represents source rock interval, lens shaped sands represent deepwater turbidites, and black circles represent gas (hollow) and oil (filled) shows. Modified after Kidston et al. (2002) as modified from MacLean et al. (1993) and Wade et al. (1995). Time scale from Palmer and Geismann (1999). Colored horizontal lines correspond to horizons picked in our seismic interpretations (Chapter 4). Black star shows inferred Late Jurassic source rock interval.

The Middle to Late Jurassic contains four approximately coeval formations referred to as the Western Bank Group. These are the Mohawk, the Mic Mac, the Abenaki, and the Verrill Canyon Formation. The coarse grained continental clastics of

the Mohawk Formation interfinger with the slightly finer, deeper water sediments of the Mic Mac Formation. These in turn correspond to the interior and eastern equivalents of the Abenaki Carbonate Bank, which can be subdivided into four prominent members of different, dominantly carbonate, lithologies. These are the Artimon, Baccaro, Misane and Scatarie Members. The seaward equivalents to all Mid Jurassic to Mid Early Cretaceous Scotian Shelf sediments are the predominantly shale deposits of the Scotian Slope's Verrill Canyon Formation. These include all formations of the Western Bank Group, as well as the overlying Missisauga Formation.

The deposition of the Missisauga Formation resulted from increased sediment supply to the Scotian Basin by the Sable Delta. The Missisauga Formation can be separated into three sandstone facies, a lower, middle and upper member, based on sand content and depositional environment. The Early Cretaceous Missisauga Formation is overlain by the slightly finer sands and shales of the upper Aptian to Cenomanian Logan Canyon Formation and its seaward equivalent Sable Shale. Regional transgression resulted in the deposition of the predominantly shale, Late Cretaceous Dawson Canyon Formation atop the Logan Canyon Formation. The Dawson Canyon Formation is capped by the chalk of the Wyandot Formation of Santonian-Campanian age. The remainder of the Late Cretaceous and the entirety of the Tertiary sediments consist of the interbedded shales and sandstones of the Banquereau Formation. Four prominent sets of beds have been identified throughout the Banquereau Formation. They are the Maskonomet, Nashwauk, Manhasset and Esperanto Beds.

2.4 Salt Tectonics

Salt basins occur globally. Many of them have been extensively studied and mapped due to the common occurrence of trapped hydrocarbons within their strata. Salt basins most commonly occur on passive rifted continental margins where deeply subsiding rifted basement, coupled with repeated inundation and evaporation of seawater, result in broad, thick, regional salt deposits. Salt, compared to the brittle sediments which are deposited atop it, behaves as a viscous fluid, and begins to flow under differential loading of sediments, or tectonic tilting of the margin, in an attempt to equilibrate the distribution of stress within the salt. Once set into motion, the salt forms a variety of deformational structures such as diapirs, nappes, tongues, canopies and welds, which significantly distort the stratigraphy of the overlying sediments.

Salt, as originally deposited via evaporation in basement lows, is referred to as autochtonous salt. Salt which has been extruded from its original depositional basin is referred to as allochtonous salt. As the timing and mechanics of salt tectonics have been extensively researched by others (e.g. Vendeville and Jackson 1992; Jackson and Vendeville 1994; Rowan 2005; Vendeville 2005; Adam et al. 2006; Ings et al. 2005; Ings and Shimeld 2006), we provide only a brief summary of this work, with an emphasis on the timing of salt movement, and the formation of structures underlying the present central Scotian Slope (after Cribb 2009; MacDonald 2009).

2.4.1 Scotian Margin Salt Tectonics

The Scotian Slope has been largely effected by salt tectonic deformation since the onset of clastic sedimentation in the Early Jurassic. The Slope Diapiric Province of the Scotian Slope has been subdivided into 5 salt tectonic sub-provinces by Shimeld (2004),

based on the structural style of salt tectonic deformation (Fig. 2.6). As our central Scotian Slope study area lies within sub-provinces II and III we will limit further description to these sub-provinces.

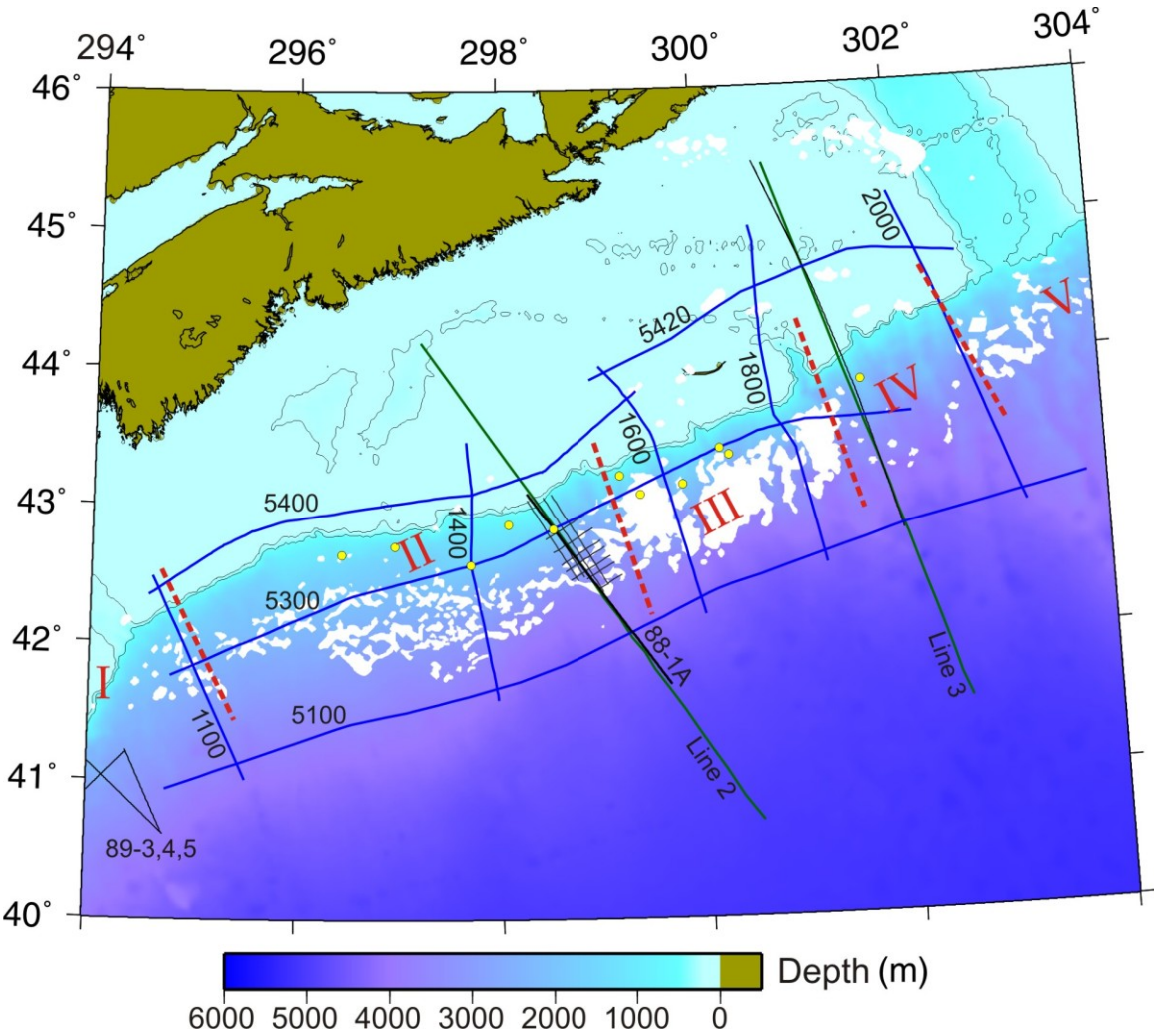

Figure 2. 6: Location map showing NovaSPAN lines in blue, Lithoprobe lines in black, TGS Nopec lines in grey, and SMART lines in green. Background color map shows water depth, shallow salt is shown in white and yellow circles represent Scotian Slope wells. Dashed red lines separate salt tectonic sub-provinces after Shimeld (2004).

Sub-province II consists of a series of linear salt walls which trend roughly parallel to the seaward front of the Abenaki carbonate bank (Shimeld 2004). The upper slope is characterized by vertical isolated diapirs while the salt walls are more prominent towards the seaward limit of the salt province. There exists a transition from vertical

rounded diapirs to increasingly squeezed diapirs capped with stock and tongue canopies in the western direction across sub-province II (Shimeld 2004). Diapirs also become increasingly squeezed to the point of welding to the west. Although the primary phase of diapiric growth and salt deformation of the Scotian Slope is interpreted to have ceased by the end of the Cretaceous (MacDonald 2009), contractional rejuvenation of diapirs has occurred from the Miocene to the present in sub-province II, as evidenced by positive bathymetric relief and faulting of younger sediments above salt diapirs (Shimeld 2004).

The western portions of sub-province III correspond to the eastern limit of our study area (Fig. 2.6). Salt deformation in this region is characterized by coalesced tongue canopy systems fed by multiple diapirs (Shimeld 2004). The canopies rest upon Early to Late Cretaceous strata, and seismic imaging beneath these structures is often poor, hampering the interpretation of the presence and style of feeders. Feeders are inferred to be present at the landward limit of most canopy systems, and suggest that the seaward limit of tongues and canopies may have been expelled upwards of 100 km from the original autochthonous basins (Shimeld 2004).

The Dalhousie Salt Dynamics Group have tested the effects of different basement morphologies and sedimentation patterns on salt tectonic deformation via sandbox analogue modelling experiments. Campbell (2010), Cribb (2009) and MacDonald (2009) have attempted to reproduce basement structure and sedimentation rates using analogue models mimicking NovaSPAN lines 1800, 2000 and 1600 across the northeastern Scotian Basin to better constrain the timing and evolution of salt deformation structures within the Basin. There results have shown that while sedimentation rates and basement

morphology significantly affect the timing and shape of salt structures present, salt movement and diapirism, in general, keep pace with sedimentation.

MacDonald (2009) focused on modelling the Scotian Slope along the trace of NovaSPAN profile 1600, the western most line of the salt dynamics group's studies. MacDonald's analogue modelling experiments suggest that evolution of salt structures began during the early post-rift stage during the Early-Mid Jurassic with the seaward inflation of salt, as basinward loading began to expel salt seawards to regions of lesser overpressure. This formed seaward nappes and landward reactive diapirs. Throughout the Mid-Late Jurassic, sedimentation corresponding to the Mic Mac Formation (Fig 2.5) resulted in active to passive diapirism across the slope, as salt began piercing the overlying sediments in regions where lower overpressure corresponding to extended overburden occurred (MacDonald 2009). High rates of salt expulsion resulted in the initiation of salt tongues and canopies during the Early Cretaceous. Through the Early and Late Cretaceous, salt movement slowed and only minor landward down-building occurred, as much of the salt mass had already been expelled seawards and upwards. Canopies continued to spread through the Early and into the Late Cretaceous. By the end of the Late Cretaceous expulsion of salt essentially stopped as the salt basin became depleted and welds became common (MacDonald 2009). Throughout the experiment, salt diapirism kept pace or outpaced sedimentation from the onset of sediment deposition until salt basins were depleted and no more salt was available to supply further diapiric growth.

Chapter 3: Heat Flow Data and Simple Lithospheric Models

3.1 Introductory Remarks

The focus of this chapter is heat flow through the central Scotian Slope. Heat flow is measured in ocean basins using shallow penetrating seafloor heat flow probes. The methodology of seafloor heat flow data acquisition and processing has been discussed in detail by others (e.g. Lister 1979; Hyndman et al. 1979; Villinger and Davis 1987). The general acquisition and processing methodology is presented in Appendix B. In this chapter we introduce the 2008 Hudson heat flow cruise across the central Scotian Slope and present the 47 new seafloor heat flow measurements acquired on the cruise, as well as 4 previously unpublished measurements acquired in 2004. We will discuss corrections to the data associated with bottom water temperature (BWT) variations, the effects of sedimentation and high thermal conductivity salt bodies on heat flow. Corrected seafloor heat flow data will then be compared with predictions from simple lithospheric rift models to constrain the basal heat flux of the study area.

The rate of heat loss across the Earth's surface is not laterally uniform. Large variations in crustal heat flow occur between continental and oceanic crust as a result of variations in crustal composition and thickness. In summarizing the global heat flow dataset, Pollack et al. (1993) proposed that the global mean crustal heat flow is ~87 mWm^{-2}, where heat flow through the oceans and continents average ~101 mWm^{-2} and ~65 mWm^{-2} respectively. As oceanic crust is composed primarily of basalt with low concentrations of radioactive elements, the major source of oceanic heat is the cooling of young lithosphere generated at ocean spreading centers upon thinning of the lithosphere during extension (Lister 1980). The primary source of heat in the thicker continental crust

is radiogenic heat produced during the radioactive decay of potassium, uranium and thorium which occur in much greater concentrations in continental than oceanic crust.

3.2 Passive Continental Margin Heat Flow

The thermal evolution of rifted passive continental margins results in unique heat flow histories sensitive to the rift style, geometry and amount of initial lithospheric thinning prior to continental breakup. Numerous simple 2D numerical thermal models such as the uniform stretching model (McKenzie 1978), the dual stretching model (Royden and Keen 1980) and the simple shear model (Wernicke 1981; Wernicke 1985) have been proposed to predict the basal heat flux and subsidence histories across rifted continental margins following the onset of rifting. Each model predicts different seafloor heat flux histories based on the amount of initial lithospheric extension associated with rifting. Brief introductions to these models are included in Appendix F.

The pure shear model assumes instantaneous thinning of the entire lithosphere by a factor β at the onset of rifting. This thinning is accompanied by increased crustal heat flux immediately following rifting, followed by a period of conductive cooling returning to original unstretched values as time approaches infinity (McKenzie 1978). Royden and Keen (1980) proposed the addition of a second, lower lithospheric layer, to the pure shear model of McKenzie. This dual stretching model allows for varying components of upper (β) and lower (δ) lithospheric stretching which will in turn affect the subsidence and basal heat flux experienced by the margin. Young margins experience significantly increased present day basal heat fluxes due to varying amounts of upper and/or lower lithospheric stretching. However, old margins, such as the Scotian Margin (~200 Ma), yield similar

present day heat flux values independent of variations in β and δ due to the extensive period of conductive cooling.

These simple crustal rift models have been applied to the margins of the North Atlantic in attempts to better constrain crustal structure, subsidence histories and heat flow. These models, when coupled with present day seafloor heat flow measurements and seismic interpretations, can be used to further constrain lithospheric models and the margin's evolution. Louden et al. (1991; 1997) coupled pure and simple shear rift models with seafloor heat flow data across the Goban Spur, Galicia Bank and Iberian margins to better constrain lithospheric models for the region. Seafloor heat flow data corrected for sedimentation and basement structure were compared with the predicted present day heat flux values from pure and simple shear rift models with stretching factors constrained by available seismic reflection and refraction data. This same workflow will be followed later in this chapter to better constrain lithospheric models across the central Scotian Slope, and to determine the basal heat flux history through time.

3.2.1 Scotian Basin Heat Flow

The Scotian Basin's heat flow is relatively poorly constrained, especially in the deeper water regions of the Scotian Slope (Fig. 3.1). Seafloor heat flow measurements from the deepwater Sohm abyssal plain yield values of ~53 mWm^{-2} (Louden et al. 1987). A recent study by Goutorbe et al. (2007) presented an average heat flow of 47 ± 07 mWm^{-2} for the Scotian Basin. The study used bottom hole temperatures for gradient analysis and a combination of commonly available well logs to determine sediment thermal conductivity. Data from available Scotian Basin wells were used, from which average heat flow was determined. The study did not take into account the effects of salt

bodies on heat flow, and thus the reported value of 47 ± 07 mWm^{-2} may be a slight overestimate of the present day heat flow as many wells target salt flank and salt crest traps, thus, experiencing elevated gradients.

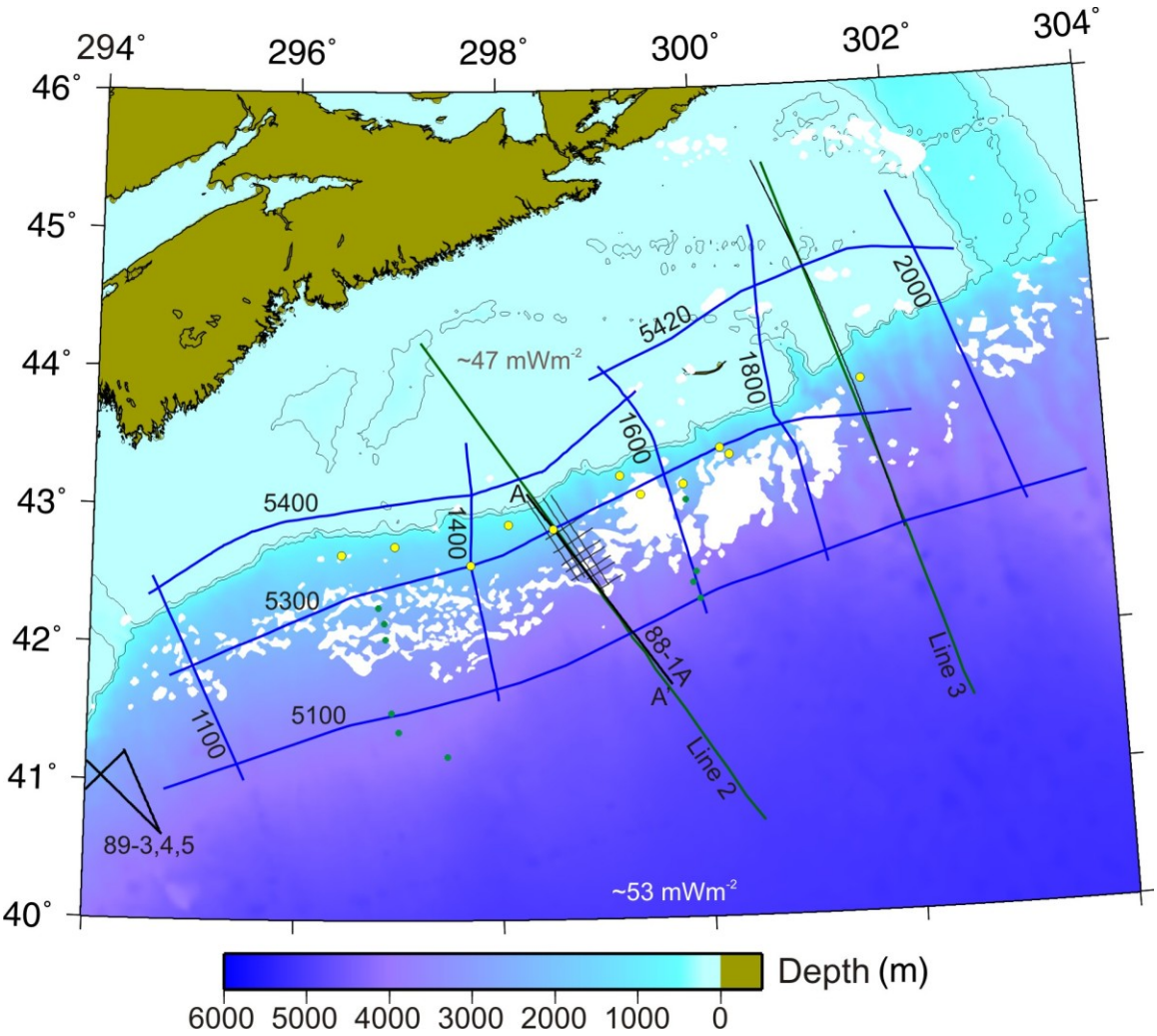

Figure 3. 1: Location map of Scotian Basin showing seismic lines of the NovaSPAN survey (blue), Lithoprobe survey (thick black), SMART refraction lines (green) and TGS-Nopec NS-100 (thin grey). Scotian Slope well locations are represented with yellow circles and Lewis and Hyndman (1976) heat flow station locations are shown with green. Background map shows water depth and white represents location of shallow salt after Shimeld (2004). Measured Sohm abyssal plain heat flow is shown in white after Louden et al. (1989) and Scotian Basin average after Goutorbe et al. (2007) is shown in brown.

The only published seafloor heat flow measurements from the Scotian Basin to date are ten measurements reported by Lewis and Hyndman (1976) from two transects across the Scotian Slope (Fig. 3.1). These measurements record a large variability in

seafloor heat flow from 24-75 mWm^{-2}. A mean value of 52 ± 5 mWm^{-2} was reported. The variation in measured heat flow has been attributed to the presence of salt diapiric structures underlying the Scotian Slope. Large salt diapirs have a focusing effect as they work as low resistance thermal conduits funneling heat to the seafloor above them, thus resulting in the observed variations. The effects of salt on heat flow are discussed in further detail in Section 3.4.3.

3.3 Hudson 2008 Heat Flow Cruise

The 2008 Hudson heat flow cruise was designed to measure seafloor heat flow across the central Scotian Slope. Seven days of ship time aboard the CCGS Hudson were allotted for the measurement of heat flow from the central Scotian Slope using the 32 thermistor Dalhousie heat flow probe (Appendix B-3). The goal of the cruise was two-fold: determine the regional heat flow trends across the central Scotian Slope, including any along strike or down dip variations in heat flow; and measure the local effects of high thermal conductivity salt bodies on seafloor heat flow. In total 47 successful heat flow measurements were acquired from the Torbrook gas hydrates mound and along the traces of three 2D seismic reflection profiles, NovaSPAN lines 1400 (heat flow transect Line 1) and 1600 (heat flow transect Line 3) and Lithoprobe line 88-1A (heat flow transect Line 2) (Fig. 3.2). We were unable to obtain measurements from all sites due to limited ship time and coarse surface sediments preventing penetration of the probe in certain regions. Of the 47 successful measurements, 7 were located at the Torbrook gas hydrates mound, 18 were taken along Line 1, 13 were taken along Line 2, and 9 were taken along Line 3 (Fig. 3.2). The results of the cruise are summarized in Table 3.1, and further data tables for each station are included in Appendix C.

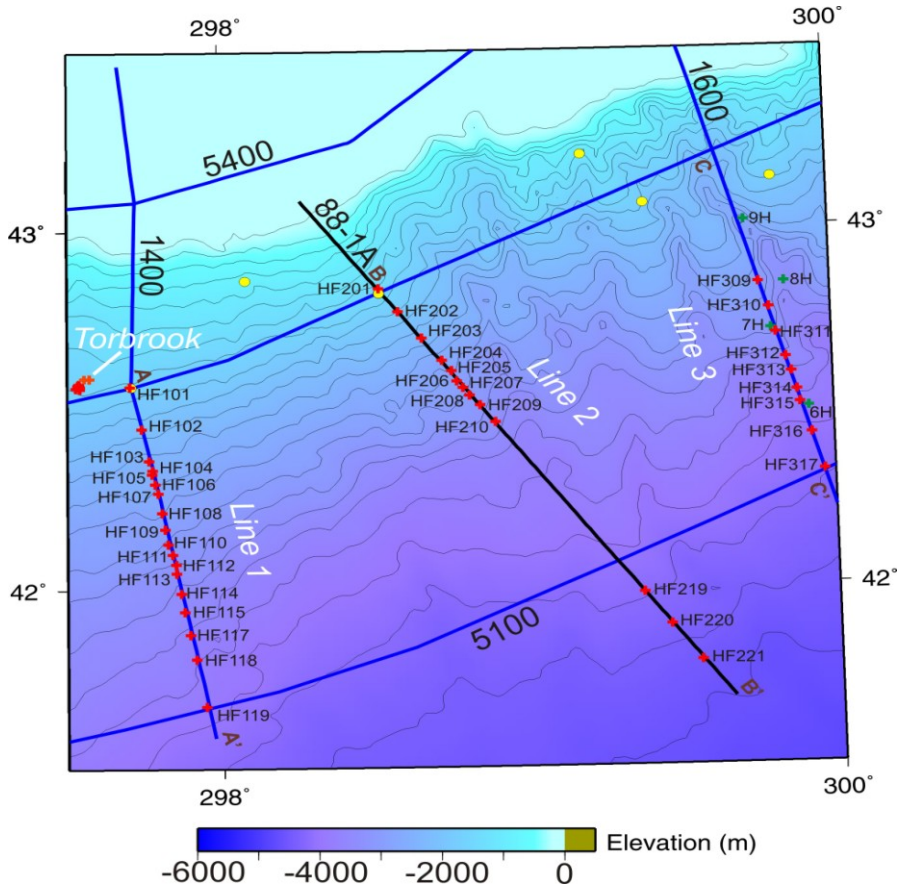

Figure 3. 2: Location map of the central Scotian Slope showing 2D seismic lines of the NovaSPAN survey in blue and the Lithoprobe survey in black. Background map shows seafloor topography. Heat flow transects of the Torbrook mound and Lines 1-3 are shown in white text. 2008 heat flow stations are shown as red crosses, 2004 stations as orange crosses, and Lewis and Hyndman (1976) stations are shown as green crosses. Yellow circles represent Scotian Slope well locations and cross sections locations corresponding to figures 3.4-3.6 are shown by brown letters.

3.3.1 Torbrook Results

Seven new seafloor heat flow measurements were acquired at the Torbrook gas hydrates mound in 2008 (Fig. 3.3). Two additional heat flow measurements were acquired from the Torbrook mound on a previous cruise in 2004 and will be compared with the more recent data recorded on the 2008 cruise in order to determine the precision of conductivity values recorded by the probe between different cruises. Recorded geothermal gradients may vary between cruises if bottom water temperature variations

Station No.	Lat. (N)	Long. (W)	X	Y	Offset (m)	Shot Point	E.S. Depth (m)	CTD Depth (m)	BWT (°C)	No. Temp. Points	Gradient (mK/m)	σ	No. of Cond. Points	Thermal Cond. (W/m*K)	σ	Heat Flow (mW/m²)	σ	Bullard Heat Flow (mW/m²)	σ	Tilt
Line 1 (1400 profile)																				
HF101	42°34.07	62°17.48	557731.47	4713136.40	100700	3177	1700.00	1672.00	3.74	20	20.29	0.86	20	1.191	0.161	24.18	4.3	23.9	0.8	1.5
HF102	42°26.62	62°15.32	560933.71	4700057.71	114200	2908	2180.00	2140.00	3.31	25	34.2	0.55	25	1.065	0.112	36.43	4.41	34.7	0.6	1.5
HF103	42°21.42	62°13.71	562881.08	4690215.09	124300	2708	2467.00	2438.00	3.10	23	37.63	0.3	23	1.013	0.104	38.12	4.23	37.3	0.4	1
HF104	42°20.07	62°13.29	563876.25	4687289.61	127300	2646	2530.00	2503.00	3.06	23	37.76	0.32	23	1.031	0.053	38.94	2.32	38.1	0.5	1
HF105	42°18.89	62°12.98	563678.13	4686122.53	128500	2626	2616.00	2585.00	3.03	23	45.36	0.24	23	0.999	0.084	45.33	4.04	46.9	0.3	2.5
HF106	42°17.50	62°12.60	564565.41	4683077.27	131700	2563	2685.00	2655.00	2.92	24	39.74	0.43	24	0.941	0.088	37.4	3.9	39.3	0.4	0
HF107	42°16.15	62°12.24	565420.07	4680149.96	134800	2500	2750.00	2726.00	2.88	23	40.72	0.25	23	0.959	0.087	39.04	3.77	40.3	0.2	1
HF108	42°13.00	62°11.40	566488.09	4674153.31	140900	2378	2888.00	2864.00	2.74	24	35.99	0.19	24	0.983	0.091	35.39	3.48	37.1	0.2	1.5
HF109	42°10.15	62°10.65	567341.83	4669073.51	146100	2276	3031.00	3009.00	2.61	23	39.32	0.44	23	1.007	0.058	39.61	2.74	39.4	0.3	1.5
HF110	42°07.45	62°09.93	568113.59	4664439.62	150900	2182	3095.00	3075.00	2.55	22	45.02	0.46	22	0.945	0.052	42.53	2.79	43.3	0.4	1.5
HF111	42°05.61	62°09.38	569409.65	4661258.96	154300	2114	3191.00	3167.00	2.40	28	64.05	0.24	28	0.966	0.092	61.88	6.11	65.7	0.5	0
HF112	42°04.19	62°09.03	570250.24	4658122.33	157600	2050	3301.00	3253.00	2.40	22	51.99	0.33	22	1.047	0.129	54.41	7.04	54.9	0.3	2
HF113	42°02.51	62°08.61	570317.60	4655408.38	160300	1995	3370.00	3345.00	2.33	26	42.94	0.38	26	0.93	0.12	39.95	5.5	43.1	0.3	1
HF114	41°58.88	62°07.66	571647.14	4649142.90	166800	1868	3475.00	3459.00	2.31	24	43.71	0.28	24	0.964	0.067	42.13	3.22	43.4	0.3	0
HF115	41°55.85	62°06.87	572606.96	4643508.66	172600	1753	3520.00	3503.00	2.30	23	52.63	1.05	23	1.029	0.163	54.19	9.64	56.6	0.5	1
HF117	41°51.93	62°05.80	574221.49	4636377.85	180000	1606	3778.00	3699.00	2.25	22	47.09	0.56	22	1.079	0.082	50.82	4.47	51.7	0.7	1
HF118	41°47.85	62°04.74	575833.58	4628743.21	187800	1451	3789.00	3783.00	2.22	26	41.31	0.46	26	1.054	0.087	43.54	4.09	43.3	0.4	3.5
HF119	41°40.29	62°02.83	578541.73	4614105.16	201700	1178	3910.00	3906.00	2.19	21	44.34	0.64	22	0.987	0.108	43.75	5.4	46	0.7	0.5
Line 2 (88-1a profile)																				
HF201	42°49.75	61°28.46	624265.79	4743901.45	34300	2492	1482.00	1466.00	3.82	19	22.55	1.56	19	1.243	0.145	28.02	5.2	29.1	1.4	2
HF202	42°46.25	61°24.59	629556.52	4736882.50	43100	2602	1890.00	1871.00	3.43	16	30.49	1.88	17	1.187	0.132	36.2	6.25	31.7	1.7	2
HF203	42°42.55	61°20.22	636002.1336	4728696.165	53500	2731	2341	2359	3.16	20	41.48	1.2	20	1.027	0.132	42.61	6.72	43.9	0.7	1
HF204	42°37.68	61°16.32	641390.7036	4721797.612	62200	2841	2671	2652	2.85	13	53.77	2.28	13	0.991	0.243	53.27	15.34	54.7	2	0.5
HF205	42°35.84	61°14.42	643952.2479	4718624.638	66300	2893	2763	2741	2.79	21	56.2	0.61	22	1.114	0.097	62.59	6.13	65.5	0.8	1
HF206	42°34.40	61°13.00	645449.1237	4715442.52	70000	1605	2920	2899	2.76	22	59.76	1.08	22	0.997	0.113	59.61	7.85	61.3	1.1	0
HF207	42°33.32	61°11.91	647061.2141	4713378.41	72600	2970	3010	2995	2.7	22	67.76	0.38	22	1.055	0.074	71.49	5.38	72.8	0.4	1
HF208	42°32.13	61°10.75	648830.8865	4710985.725	75600	3007	3170	3157	2.59	21	57.08	1.11	21	1.041	0.145	59.41	9.44	60.7	1	0.5
HF209	42°30.36	61°09.11	651737.4651	4708062.383	79500	3057	3249	3229	2.49	22	45.78	0.64	22	0.98	0	44.87	0.63	N/A	N/A	1
HF210	42°27.51	61°06.22	655833.0709	4702850.292	86000	3139	3535	3501	2.33	16	45.14	0.8	16	0.922	0.158	41.62	7.89	47.1	1	4
HF219	41°58.54	60°37.64	695968.9103	4650443.79	152000	3964	4180	4184	2.19	23	41.19	0.39	23	1.072	0.093	44.15	4.27	42.6	0.4	2.5
HF220	41°53.29	60°32.54	703388.3668	4640612.751	164500	4120	4337	4344	2.18	22	43.29	0.42	22	1.039	0.054	44.98	2.78	44.5	0.5	0.5
HF221	41°47.24	60°26.66	711751.4859	4629585.37	178200	4292	4464	4470	2.2	20	40.81	0.76	20	0.986	0.154	40.25	7.03	41.1	0.4	2
Line 3 (1600 profile)																				
HF309	42°49.85	60°13.60	726101.8034	4746783.642	150400	2406	2915	2893	2.65	21	45.8	0.59	21	1.043	0.063	47.76	3.52	47	0.4	2
HF310	42°45.70	60°12.05	728958.3947	4739021.285	158700	2242	3085	3066	2.49	19	45.38	0.72	19	1.063	0.043	48.22	2.73	48.3	0.7	0.5
HF311	42°41.52	60°10.51	730914.9098	4731120.244	166800	2077	3256	3240	2.31	19	48.82	0.71	19	1.058	0.041	51.66	2.77	51.4	0.5	2
HF312	42°37.46	60°09.03	733626.4161	4723602.946	174800	1919	3539	3530	2.23	15	39.04	0.64	16	1.075	0.053	41.96	2.77	41.4	0.4	0
HF313	42°34.77	60°08.05	735106.5278	4719050.445	179500	1824	3650	3640	2.21	19	33.82	0.54	19	1.018	0.039	34.44	1.87	34.4	0.4	0
HF314	42°32.15	60°07.08	736643.6373	4713450.953	185300	1708	3785	3780	2.2	17	42.86	0.66	18	1.04	0	44.57	0.69	44.57	N/A	1
HF315	42°30.07	60°06.32	737558.9535	4709570.841	189300	1626	3890	3883	2.2	13	39.7	0.63	13	1.086	0.038	43.11	2.18	43.1	0.5	0
HF316	42°24.60	60°04.31	740639.5733	4700195.174	199200	1429	4065	4061	2.21	19	40.66	0.3	20	1.064	0.054	43.26	2.53	43.1	0.2	0
HF317	42°18.54	60°02.10	744260.9093	4689008.382	211000	1196	4220	4221	2.18	21	41.18	0.61	21	1.01	0.072	41.57	3.59	41.4	0.5	0.5
Torbrook Site																				
HF001	42°33.95	62°27.49					1563	1541	3.71	22	21.78	0.62	22	1.067	0.159	23.24	4.12	20.6	1.2	3
HF002	42°33.80	62°27.45					1567	1550	3.7	25	21.29	0.47	25	1.098	0.116	23.37	2.99	21.5	0.5	2
HF003	42°33.48	62°27.39					1594	N/A	N/A	24	22.25	0.52	24	1.146	0.078	25.49	2.33	24.9	0.3	2
HF004	42°33.54	62°27.84					1590	1572	3.7	24	19.56	0.59	24	1.192	0.15	23.32	3.64	21.9	0.9	3
HF005	42°33.78	62°27.65					1592	1563	3.69	24	22.02	0.31	24	1.132	0.141	24.92	3.45	23.7	0.4	2
HF006	42°33.88	62°27.56					1564	N/A	N/A	25	22.34	0.32	25	1.154	0.118	25.77	2.99	24.2	0.4	2
HF007	42°34.11	62°27.34					1572	1549	3.7	23	22.49	0.46	23	1.093	0.101	24.57	2.77	24.4	0.4	3
2004_Data																				
HYD401	44°34.10	54°51.79					1703	N/A	N/A	8	26.7	0.4	10	1.186	0.054	31.6	1.9	28.9	0.6	4
HYD402	44°33.45	54°52.63					1730	N/A	N/A	10	26.0	0.5	12	1.171	0.070	30.4	2.4	28.2	0.6	6.5
HYD503	42°34.92	62°25.46					1526	1535	3.73	24	31.5	0.4	23	1.143	0.114	36.0	4.1	36.8	0.3	0
HYD504	42°35.30	62°26.44					1545	1544	3.73	22	37.6	0.3	19	1.146	0.100	43.1	4.2	42.3	0.4	1

Table 3. 1: Summary table of heat flow data acquired during the July 2008 Hudson heat flow cruise as well as unpublished data from 2004. E.S. = echo sounder., BWT = Bottom Water Temperature.

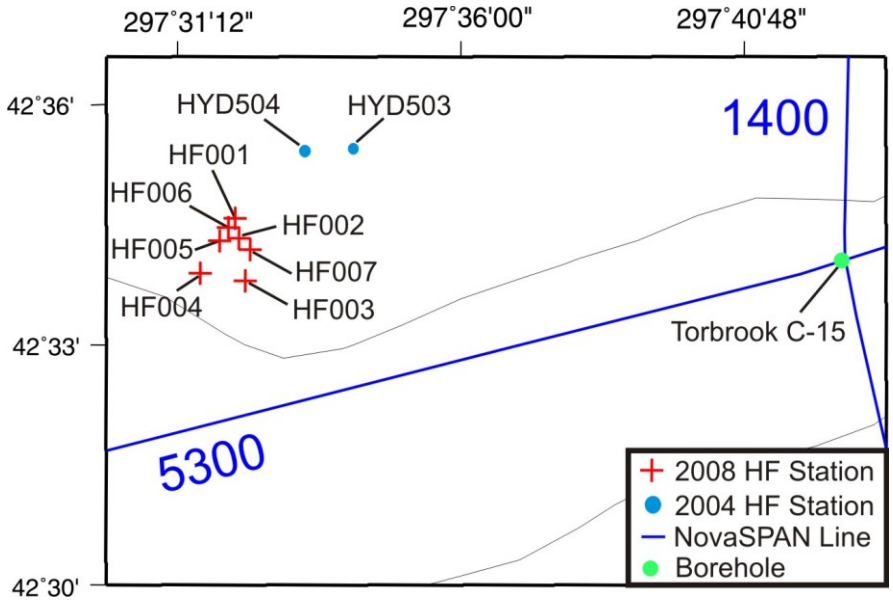

Figure 3. 3: Location map showing seafloor heat flow stations recorded in 2008 (red crosses) and 2004 (blue circles).

exist; however, sediment thermal conductivity values should remain constant, providing a good test for the consistency of the probe.

For all stations, recorded gradients are roughly linear over the length of the probes penetration, with the exception of some disturbances of thermistors in the uppermost 2 m of the probe (Fig. 3.4). The uppermost 2 m of temperature data are likely affected by penetration of water from above upon penetration of the probe into the seafloor and thus are not included in our gradient calculation. Gradient measurements showed little variation between stations with the exception of a low gradient of 19.6 ± 0.6 mKm^{-1} recorded at site HF004. Geothermal gradients varied from 19.6 ± 0.6 to 22.5 ± 0.5 mKm^{-1} with a mean gradient of 21.7 ± 0.5 mKm^{-1}. Thermal conductivity values ranged from 1.07 ± 0.16 to 1.19 ± 0.15 $Wm^{-1}K^{-1}$, with a mean conductivity of 1.13 ± 0.12 $Wm^{-1}K^{-1}$. Heat flow values for the Torbrook sites ranged from 20.6 ± 1.2 to 24.4 ± 0.4 mWm^{-2} with a mean heat flow of 23.0 ± 0.6 mWm^{-2} for the Torbrook gas hydrates mound. The maximum distance between heat flow sites at the Torbrook mound was ~1000 m, and

with little assumed lateral variation in lithology between sites and consistent measured conductivity and gradient values we can assume that the probe is functioning well.

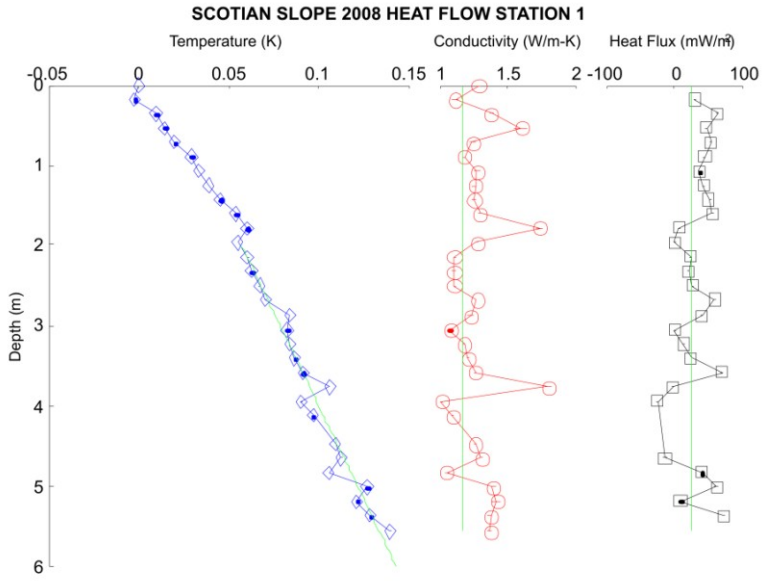

Figure 3. 4: Example plot of 2008 Hudson heat flow station showing temperature, conductivity, and heat flux vs. depth plots.

We will also take this opportunity to report the results of two unpublished heat flow measurements acquired from the Torbrook gas hydrates mound in 2004. Measurements were acquired using the Dalhousie heat flow probe following the same method as described in Appendix B. The data have not previously been publicly released and are presented in Table 3.1. Gradients measured for stations HYD503 and HYD504 were 31.5 ± 0.4 mKm^{-1} and 37.6 ± 0.3 mKm^{-1} respectively, with thermal conductivity values of 1.14 ± 0.11 $Wm^{-1}K^{-1}$ and 1.15 ± 0.10 $Wm^{-1}K^{-1}$. Heat flow values of 36.8 ± 0.3 mWm^{-2} and 42.4 ± 0.4 mWm^{-2} for stations HYD503 and HYD504 are significantly higher than those recorded at the Torbrook mound on the 2008 cruise due to the notably higher gradients. This suggests that in addition to purely conductive vertical heat transfer a second mechanism such as convective heat transfer through the upper sediments or

varying bottom water temperatures may have effected the measured gradient. Variations in BWT's are investigated in Section 3.4.1.

3.3.2 Line 1 Results

Line 1 resulted in the successful acquisition of 18 of the 19 heat flow measurements planned along the trace of GXT NovaSPAN 2D seismic reflection profile 1400. Station HF116 was skipped to save time. From this line 13 measurements were taken in regions unaffected by salt structures to determine the regional trends across the slope and 5 measurements were taken above salt bodies to quantify the effects of salt on heat flow (Fig. 3.5).

Measurements in regions unaffected by salt showed a general increase in the seaward direction. Ignoring the abnormally low value of 23.9 ± 4.3 mWm^{-2} at station HF101, the background heat flow values in the landward regions of the survey range from ~35-40 mWm^{-2}, while the more seaward stations show values of ~43-46 mWm^{-2}. Increased heat flow above salt bodies is evident in the data. The increase in measured heat flow above salt varies from one diapir to another. Values above the most landward diapir (D1) increase by ~8 mWm^{-2} from the surrounding background values of ~39 mWm^{-2} to 46.9 ± 4.0 mWm^{-2} above the salt body at heat flow station HF105. The small salt body which underlies HF107 does not have a significant effect on seafloor heat flow likely because its increased distance from the seafloor and welded, non-rooted, feeder. Stations HF109 and HF110 are both located above what is interpreted as a deeply buried salt canopy, and similar to station HF107 do not record significantly elevated heat flow values, likely as a result of the depth of salt. Values above the central salt diapir D2 show the largest increase in heat flow, reaching upwards of 65.7 ±0.5 mWm^{-2} at station HF111,

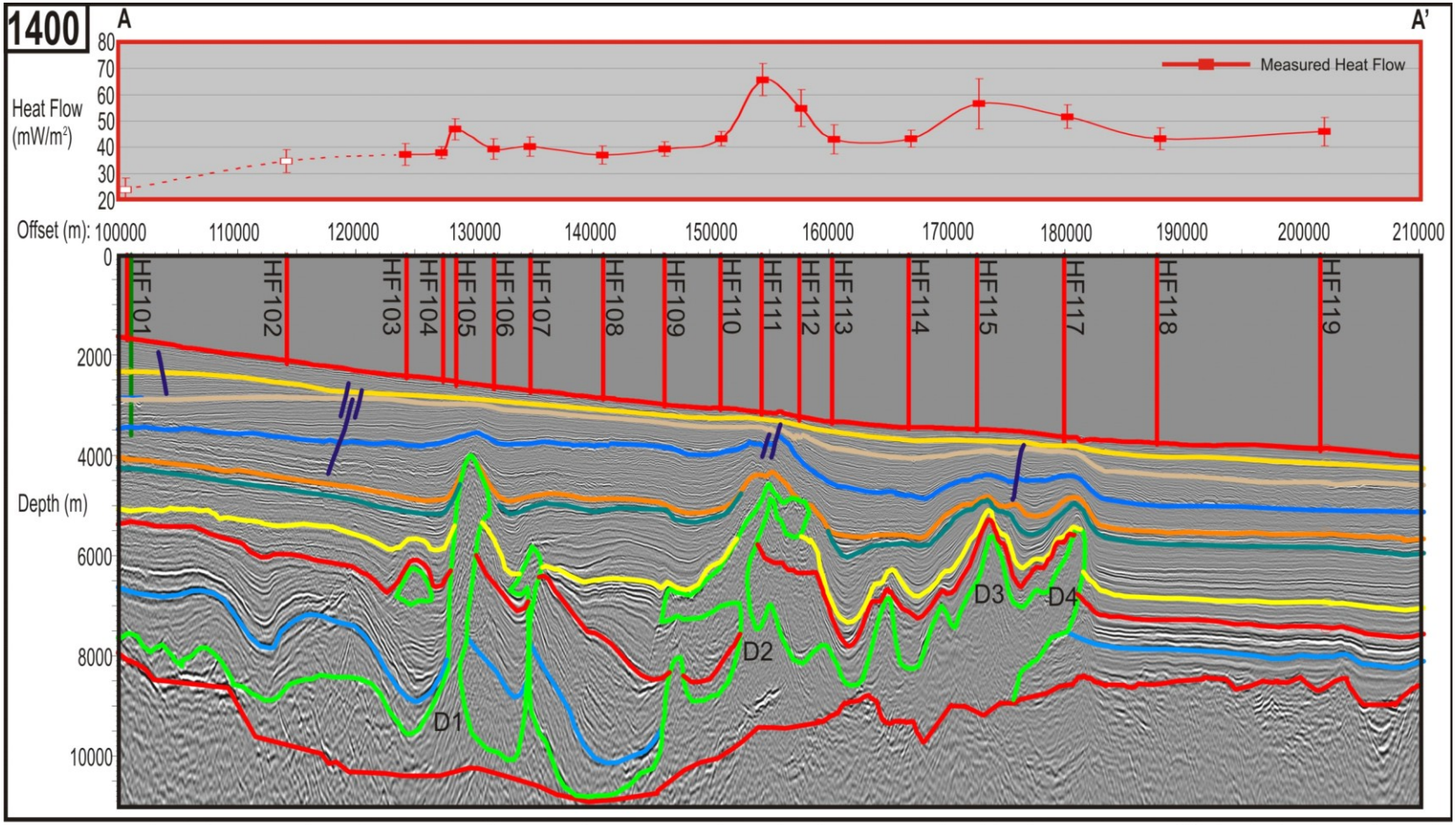

Figure 3. 5: Seismic interpretation of NovaSPAN line 1400 from A-A' as shown in Figure 3.3. Colored horizons represent lithological units as shown in Figure 2.5. Vertical red lines show locations of seafloor heat flow measurements, steep blue lines represent faults and the vertical green line represents the Torbrook C-15 well. Above the seismic interpretation is a plot of measured seafloor heat flow in red; hollow boxes are likely erroneous and may be disregarded.

~23 mWm^{-2} above the surrounding background values of ~43 mWm^{-2}. This station is located directly above the squeezed feeder and is the second shallowest salt body identified on Line 1400. Station HF112 is located above a shallow salt canopy fed by the attached diapir underlying HF111, thus, recording a high heat flow value of 54.9 ± 0.3 mWm^{-2}. The most seaward salt bodies show increases of ~8-13 mWm^{-2} above the background values of ~43 mWm^{-2}, reaching values of 51.7 ± 0.7 mWm^{-2} and 56.6 ± 0.5 mWm^{-2} at stations HF115 and HF117 above diapirs D3 and D4 respectively.

It is noted that the largest increase in measured seafloor heat flow does not correspond to the tallest, shallowest diapir (D1). However, as neither station HF105 or HF106 is located directly above the crest of this diapir, they may not have recorded the maximum associated heat flow. Station HF111, located directly above the crest of the second tallest and shallowest salt body (D2), records the highest seafloor heat flow value of heat flow transect Line 1.

3.3.3 Line 2 Results

In total, 13 of the 21 proposed measurements were successfully acquired along heat flow transect Line 2. Successful stations include HF201-210 and HF219-221 (Fig. 3.6); however, station 209 recorded only a measure of gradient, and thus conductivity values were averaged from stations HF210 and HF208 yielding a conductivity value of 0.98 $Wm^{-1}K^{-1}$. This value is a low value for conductivity and reflects the anomalously low value of 0.92 ± 0.16 $Wm^{-1}K^{-1}$ recorded at station HF210. Stations HF217 and HF218 were attempted, however problems were encountered in penetrating the seafloor due to the presence of coarse sediments. Stations HF216-211 were skipped as they appeared to be located in a large channel where accumulations of coarser sediments would make

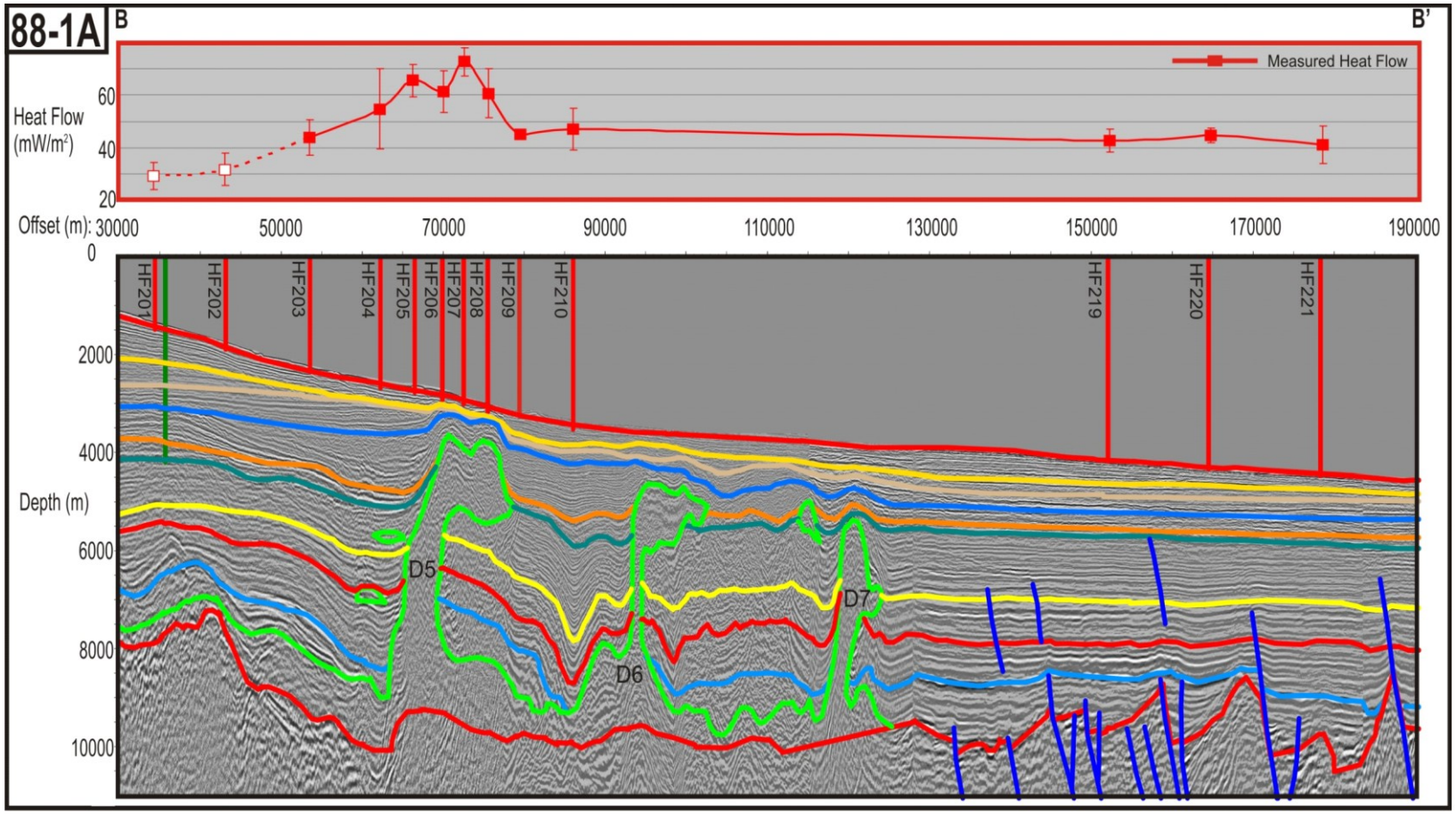

Figure 3. 6: Seismic interpretation of Lithoprobe line 88-1a from B-B' as shown in Figure 2.1. Colored horizons represent different lithological units. Vertical red lines show locations of seafloor heat flow measurements, steep blue lines represent faults and the vertical green line represents the Shubenacadie H-100 well. Above the seismic interpretation is a graph showing plots of measured heat flow values in red; hollow boxes are likely erroneous and may be disregarded.

successful penetration of the probe unlikely. Of the 13 measurements acquired across Line 2, four measurements were taken above a salt structure D5, while the rest were taken in regions unaffected by salt.

Similar to Line 1, we see a general increase in heat flow in the seaward direction. In line 2 we record low heat flow values of ~30 mWm^{-2} at the landward limit of the line increasing to ~43 mWm^{-2} at the seaward limit similar to Line 1. The low heat flow values at stations HF201 and HF202 are associated with the anomalously low geothermal gradients of 22.6 ± 1.6 mKm^{-1} and 30.5 ± 1.2 mKm^{-1} respectively as the corresponding thermal conductivities of 1.24 ± 0.14 $Wm^{-1}K^{-1}$ and 1.19 ± 0.13 $Wm^{-1}K^{-1}$ are actually higher then the mean value of 1.05 ± 0.13 $Wm^{-1}K^{-1}$ for the line. Salt structure D5 has been interpreted as a large, thick, salt canopy fed by a broad vertical feeder. The heat flow spike above D5 is not uniform across the structure. A range of heat flow values from 60.7 ± 1.0 to 72.8 ± 0.4 mWm^{-2} are identified above the salt structure. Little variation in depth to salt in the seismic images coupled with large variations in measured heat flow above the salt diapir suggests that the variations in heat flow above this diapir are not the result of purely conductive heat transfer and that there is likely a second mechanism affecting the measured temperature gradients.

3.3.4 Line 3 Results

Line 3 resulted in the successful acquisition of data from 9 of the 17 planned heat flow stations (Fig. 3.7). Measurements were made at stations HF317-309. Many stations required two penetrations as the jog sensor was not triggered on the first attempt, thus no heat pulse was released from the central heater wire (Appendix B-3). This gave us the

opportunity to check gradient values between penetrations. No significant variations in gradient were recorded between penetrations at the same site (Table 3.2). Little variation in conductivity with depth occurred for any station in this line. Therefore the results of the Bullard heat flow calculations were very similar to the uniform conductivity heat flow calculations (Table 3.1).

	First Penetration *(No Heat Pulse)*			Second Penetration *(Heat Pulse)*		
Station No.	**No. Temp. Points**	**Gradient (mK/m)**	**σ**	**No. Temp. Points**	**Gradient (mK/m)**	**σ**
HF317	22	42.35	0.86	21	41.18	0.61
HF316	19	42.16	0.76	19	40.66	0.3
HF313	19	35.14	0.45	19	33.82	0.54
HF312	21	40.34	0.64	15	39.04	0.64
HF311	20	48.88	0.81	19	48.82	0.71
HF310	20	45.81	0.53	19	45.38	0.72
HF309	18	45.06	0.92	21	45.8	0.59

Table 3. 2: Comparison between gradients recorded for stations which required multiple penetrations.

Station HF314 had no heat pulse on either attempt, and thus conductivity values for heat flow analysis at this station were taken from surrounding stations HF316 and HF313. Time did not permit completion of the Line 3 heat flow survey; however, multi-beam imaging beneath the more landward portions of this line provided confidentially to Keith Louden suggest that the region is cut by a large submarine canyon and thus penetration of the associated coarser seafloor sediments may not have been possible even had time permitted. It is unfortunate we were unable to take measurements from this region as the most landward diapir (D6) penetrates within ~200 m of the seafloor, and is the shallowest diapir interpreted in the available seismic images. Of the nine measurements acquired, one station is located above a large salt diapir stalk (D7), four are located over a shallow salt canopy, while only three are located in regions unaffected by salt (Fig. 3.7).

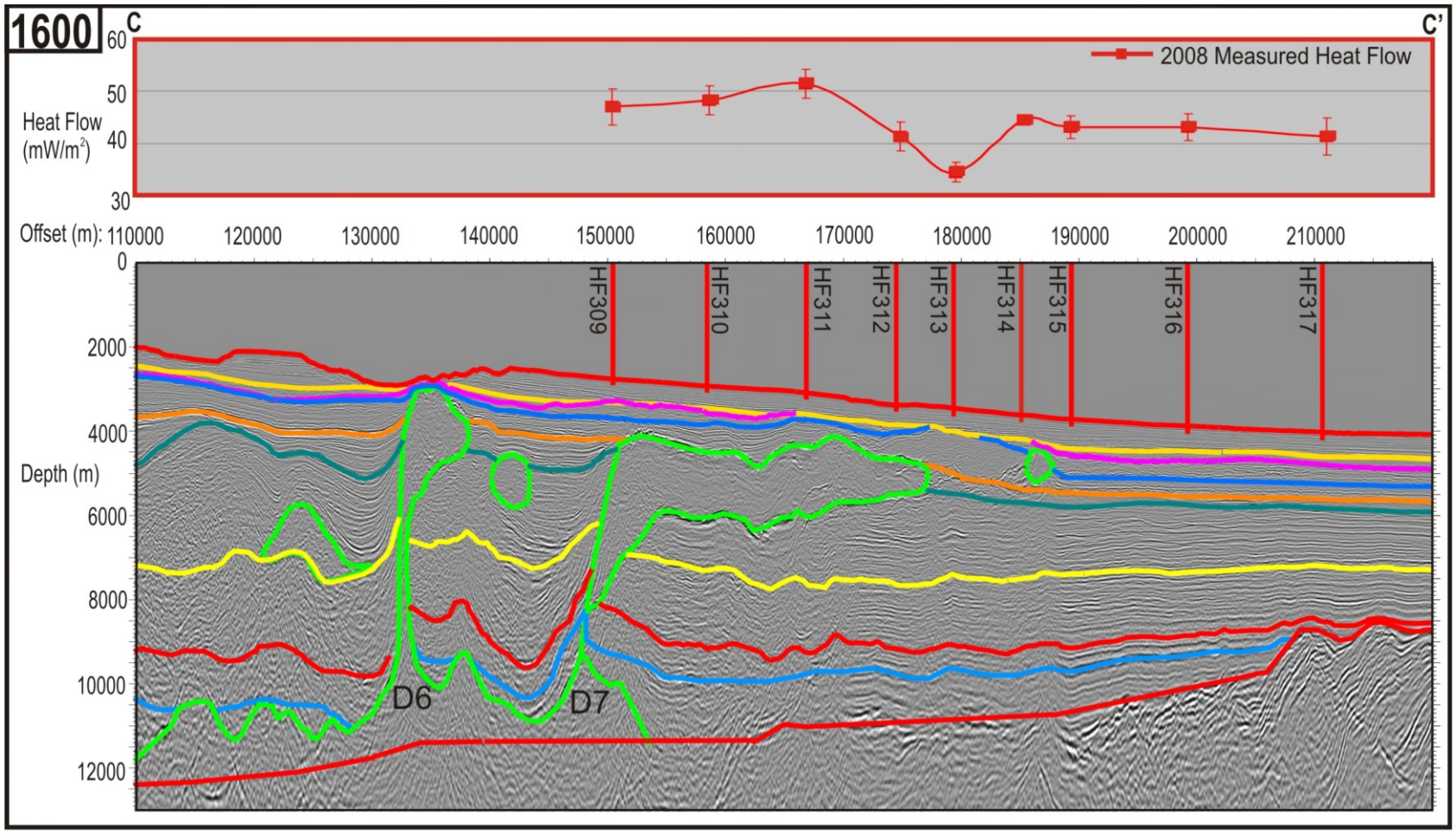

Figure 3. 7: Seismic interpretation of NovaSPAN line 1600 from C-C' as shown in Figure 2.1. Colored horizons represent different lithological units. Vertical red lines show locations of seafloor heat flow measurements. Above the seismic interpretation is a graph showing plots of measured heat flow values in red.

Heat flow measurements recorded seaward of salt ranged from 41.4 ± 0.5 to 43.1 ± 0.5 mWm^{-2} and were in good agreement with measurements from the seaward limits of Lines 1 and 2. Heat flow stations HF309-312 were located above a large diapir/canopy. Stations HF309-311 yielded heat flow values from 47.0 ± 0.4 to 51.4 ± 0.5mWm^{-2}, notably higher than those in regions unaffected by salt. Station HF312, located at the seaward tip of the canopy, recorded a low heat flow value of only 41.4 ± 0.4 mWm^{-2}. Station HF314 recorded a final measurement above salt. It was located above a detached salt canopy. The measured value of 44.6 ± 0.7 mWm^{-2} is higher than both the adjacent values at stations HF313 and HF315 which do not overly salt bodies.

The lack of heat flow measurements from the landward regions of Line 3 is problematic in our analysis of regional heat flow trends across the central Scotian Slope as we have no constraints on the landward heat flow for Line 3. According to the trends measured at Lines 1 and 2 we expect that measured seafloor heat flow values will decrease in the landward direction, however, further measurements are required to verify these assumptions. Further landward measurements in regions unaffected by salt would also be useful in assessing the effects of the salt canopies on heat flow. For now we assume that the higher heat flow above the canopies is due to the high thermal conductivity of the salt; however, verifying this requires lower heat flow values be found in the adjacent regions unaffected by salt diapirism/canopies.

3.4 Heat Flow Data Analysis

To analyze our seafloor heat flow data in terms of basal heat flux we must account for the effects of the sediment column on seafloor heat flow. This includes the effects of sedimentation, salt, and Bottom Water Temperatures (BWT) variations. We

examine BWT variations using a combination of water column temperature data recorded by a CTD probe contained within the Dalhousie heat flow probe, the 6 m of sediment temperature data recorded by the heat flow probe, and temperature gradients determined by Leblanc et al. (2007) from the Torbrook gas hydrates mound (Section 3.4.1). We correct for the effects of sedimentation on seafloor heat flow using the equations of Louden and Wright (1989) (Section 3.4.2) and the effects of salt on heat flow using simple 2D conductivity based numerical models (Section 3.4.3).

3.4.1 Bottom Water Temperature Variations

To address the possible effects of BWT variations on seafloor heat flow measurements we have compared bottom water temperatures and water column temperature gradient profiles recorded at the Torbrook mound from both the 2004 and 2008 cruises. Water column data were recorded with a Conductivity (salinity)-Temperature-Depth (CTD) probe located within the instrument housing of the Dalhousie heat flow probe. Plots of water column temperature gradients are included in Appendix D. Temperature data recorded through the water column are used to determine the stability of bottom water gradients and if significant variations exist in BWT between stations and cruises. If bottom water currents exist they may explain the variations in measured near surface geothermal gradients noted between 2004 and 2008 as associated varying BWT can penetrate downward into the near surface sediments. Finally, in addition to the CTD temperature data we will also investigate heat flow at the Torbrook gas hydrates mound using a geothermal gradient sourced from measured seafloor temperatures and depth to a Bottom Simulating Reflector (BSR) associated with the methane gas hydrates phase boundary after Leblanc et al. (2007).

The CTD probe was employed to record changes in the structure of the water column. The temperature trend recorded through the water column is particularly useful as in it we may identifying anomalous temperature variations associated with bottom water currents. As expected, the general trend recorded by the CTD probe shows increasingly stable temperatures and smaller variations in temperature with increasing depth (Fig. 3.8). At shallow depths up to ~700 m water temperatures vary at a daily to seasonal time period induced by surface temperature variations and shallow penetrating

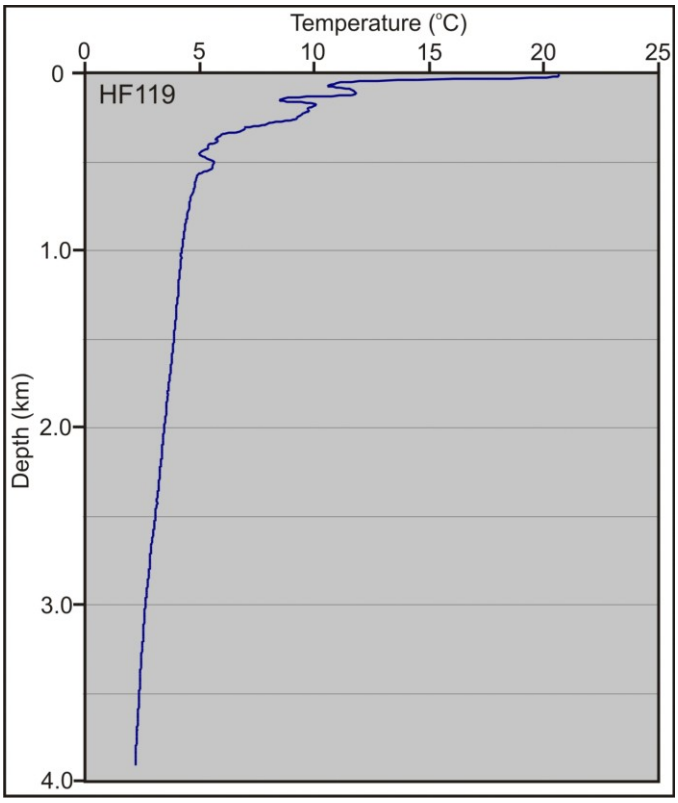

Figure 3. 8: Temperature vs. Depth plot showing temperatures recorded by the CTD probe as it descended through the water column.

currents. Smaller temperature variations can persist to depths greater that 700 m and may effect near surface sediment temperatures. Appendix D contains temperature vs. depth profiles for the bottom 600 m of the water column for all heat flow stations with CTD data. Deeper stations show more stable BWT (Fig. 3.9). Water column temperature

gradients become increasingly stable with increasing water depth, notably so below ~2000 m. Very little variation in bottom water temperature gradients occurred at depths greater than ~3300 m (Appendix D).

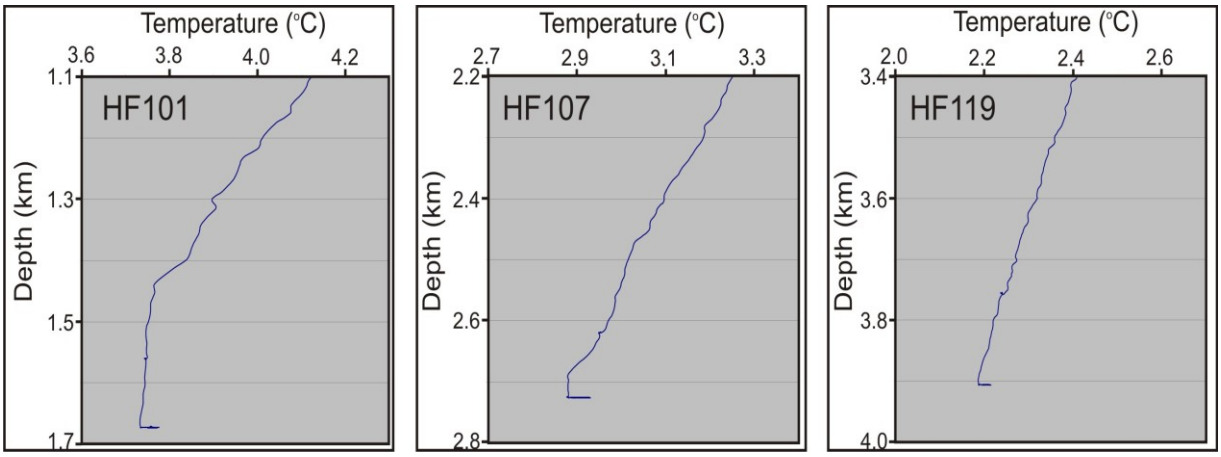

Figure 3. 9: Comparison of bottom water temperatures for different heat flow stations along line 1.

As described in Section 3.4.1 and shown in Table 3.1 the mean seafloor heat flow of 23.0 ± 0.6 mWm^{-2} from the 2008 Torbrook data is significantly lower than the mean value of 39.6 ± 0.4 mWm^{-2} from the 2004 Torbrook data. The mean gradient of 34.5 ± 0.4 mKm^{-1} recorded during the 2004 cruise was much higher than the mean gradient of 21.7 ± 0.5 mKm^{-1} in 2008. However, this relatively high value is still notably lower than all other gradients (>37 mWm^{-2}) recorded across the margin with the exception of station HF313 on heat flow transect Line 3 and of four other measurements made in shallow water regions near the Torbrook gas hydrates mound. The mean sediment thermal conductivity values at the hydrates mound of 1.13 ± 0.12 $Wm^{-1}K^{-1}$ in 2008 and 1.14 ± 0.11 $Wm^{-1}K^{-1}$ in 2004 were similar. As thermal conductivity values remained essentially constant it is the change in temperature gradient that was responsible for the significantly lower estimates of seafloor heat flow in 2008. To determine if these changes in gradient

were the result of variations in BWT penetrating the shallow sediments we have compared the BWT data from the two cruises.

The CTD data from the 2008 cruise showed greater changes in temperature with depth than the more stable bottom water column temperatures recorded in 2004 (Fig. 3.10). The mean BWT of 3.70 °C recorded in 2008 is only 0.03 °C lower than that of 3.73 °C recorded in 2004. The absolute BWT's are similar between the two cruises; however, non-linearity's observed in the water column temperature gradient for the few hundred meters of seawater above the seafloor suggests bottom water currents may exist (Fig. 3.10).

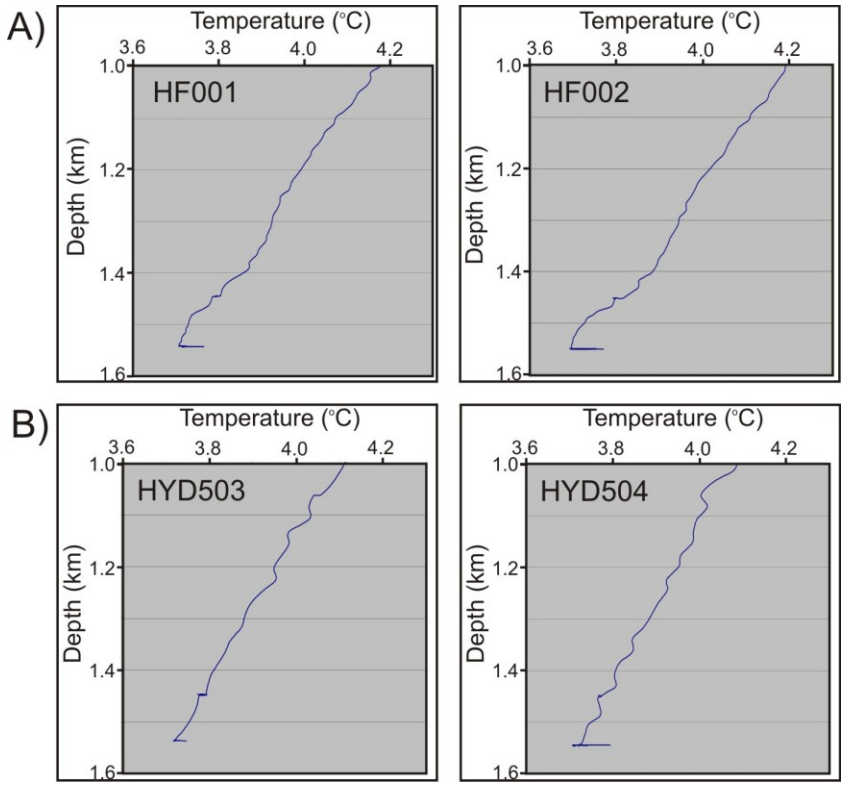

Figure 3. 10: Comparison of BWT data from Torbrook mound in A) 2008 and B) 2004.

The effects of seasonal variations in BWT's penetrating downward into the seafloor sediments should be greatest at the surface, decreasing towards the undisturbed sediment temperatures sourced from Earth's interior with depth. Therefore, all

temperature vs. depth plots for the 6 m of temperature data recorded by the seafloor heat flow probe should converge with depth when plotted from the associated BWT recorded by the CTD probe. Similar geothermal gradients should be experienced at depths beneath the penetration of environmental perturbations (Louden and Wright 1989). The expected convergence is not observed, rather, we see a divergence in our data when comparing the temperature vs. depth plots from the 2008 and 2004 cruises (Fig. 3.11).

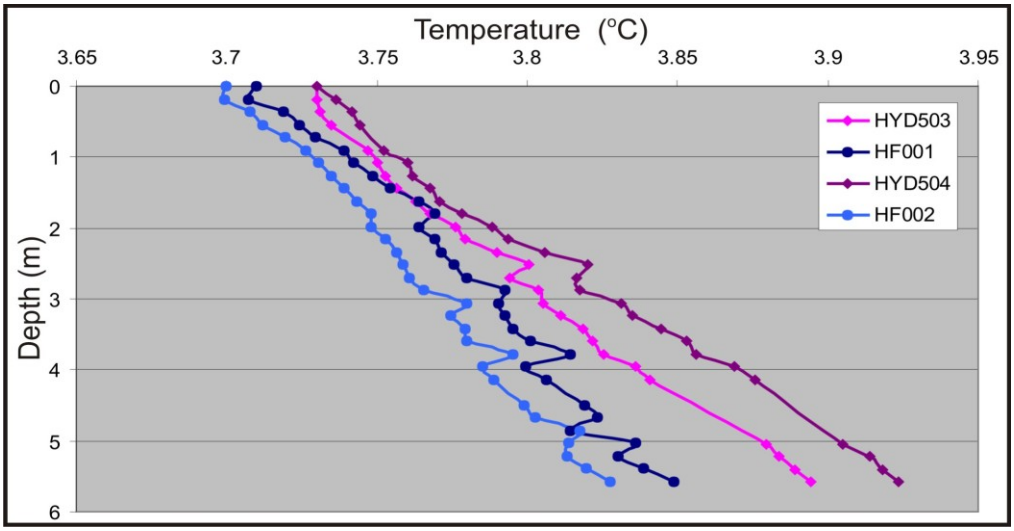

Figure 3. 11: Plots of Temperature vs. Depth recorded by the 32 thermistor Dalhousie heat flow probe in 2004 (reds) and 2008 (blues) showing temperature gradient in the upper 6 m of sediments. Gradient is plotted from the bottom water temperature recorded by the CTD probe at the seafloor (0 m).

This divergence of curves suggests that the near surface sediment temperatures for both datasets have been effected by near surface temperature variations extending to depths greater than 6 m. These may be the result of longer wavelength bottom water temperature variations operating at a period longer than the four years we recorded, or possibly an effect of convective fluid flow within the sediments. More data over a longer sample period are required to determine the true cause of the variations in sediment temperatures recorded between the two cruises. From our early analysis we are unable to conclude if BWT are affecting the recorded gradients.

In addition to BWT analysis a second method of seafloor heat flow calculation for the Torbrook gas hydrate mound has been applied to help us interpret the anomalously low geothermal gradients recorded at the Torbrook mound during the 2004 and 2008 heat flow cruises. The method involves calculation of gradient using measured seafloor temperatures and temperatures associated with the methane gas hydrates phase boundary (Fig. 3.12). Leblanc et al. (2007) have identified a Bottom Simulating Reflector (BSR)

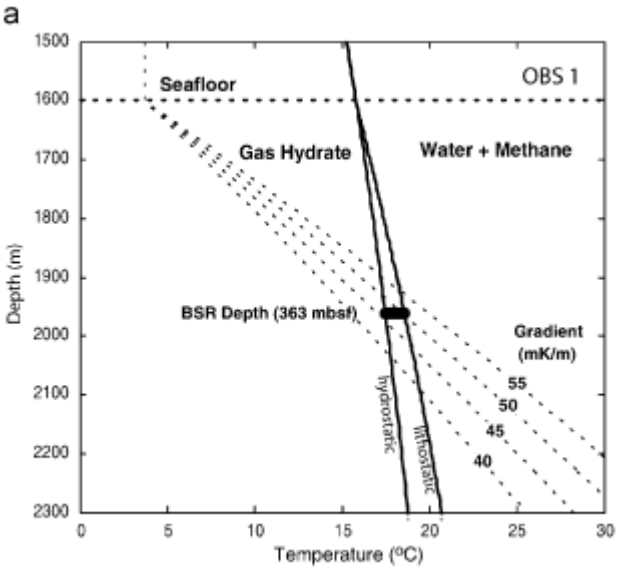

Figure 3. 12: BSR depth at the Torbrook gas hydrates mound. Horizontal dashed black line represents seafloor depth and diagonal dashed black lines represent sediment temperatures based on varying geothermal gradients from 40-55 mKm-1. Solid black lines represent solid to gas phase change boundary for methane gas hydrates under both lithostatic and hydrostatic pressures (From Leblanc et al. 2007).

associated with the methane gas hydrates phase boundary at a depth of 363 m below seafloor. Using a measured seafloor temperature of 3.7 °C and the depth to phase boundary under hydrostatic and lithostatic pressure, geothermal gradients of 45 to 50 mKm^{-1} were determined. Leblanc et al. (2007) report a sediment thermal conductivity of 1.1 $Wm^{-1}K^{-1}$ at the seafloor which is in good agreement with our measured values. As vertical heat flow is simply the product of geothermal gradient and sediment thermal conductivity, a seafloor heat flow value of 49.5 mWm^{-2} has been calculated at the

Torbrook gas hydrates mound using the low (hydrostatic) end member geothermal gradient of 45 mKm^{-1}. The gradient of 45 mKm^{-1} is slightly higher than most gradients recorded in regions unaffected by salt (40 to 44 mKm^{-1}), however, the Leblanc et al. (2007) gradient is in much better agreement with these stations than with the low gradients (<35mKm^{-1}) recorded with our probe for the shallow water stations.

Despite minor fluctuations recorded in the water column temperatures we have no definitive evidence suggesting bottom water temperature variations have effected our seafloor heat flow data in the shallower water regions. However, we do observe large variations in geothermal gradients recorded in 2004 and 2008 suggesting that something is affecting the near surface sediment temperatures. BWT recorded in 2004 and 2008 (3.73 °C and 3.70 °C) were very close, and should not significantly affect shallow sediment temperatures. Furthermore, had near surface sediment temperatures been affected by BWT variations the temperature vs. depth curves recorded by the shallow penetrating probe should converge with depth as BWT variations have a greater effect on shallower sediment temperatures. Finally, the agreement between the heat flow calculated using the gradient derived from the depth to gas hydrates phase boundary with our deeper water heat flow values in regions unaffected by salt suggests that the higher gradient is likely representative of the true gradient for the region. To determine what is causing the anomalously low temperatures recorded at the landward limits of heat flow transects Line 1 and 2, as well as the Torbrook gas hydrates mound, requires further investigation. Shallow temperature variations may be associated with convective heat transfer, possibly a result of the presence of gas hydrates in the area.

3.4.2 Correction for Sedimentation

Sedimentation atop crystalline basement following rifting often results in a temporary decrease in observed heat flow at the seafloor. The influx of new sediments are deposited at the bottom water temperature which is commonly assumed to be 0 °C, although may be higher in shallow water regions (Louden and Wright 1989). Time is required to warm the cool sediments and reestablish the geothermal gradient at the seafloor, prior to which, anomalously low geothermal gradients may be recorded in the seafloor sediments if conduction of heat from below cannot keep pace with sedimentation (Louden and Wright 1989). The seafloor heat flow data are therefore not expected to match the predicted modelled present day heat fluxes after McKenzie (1978) and Royden and Keen (1980) without applying a correction for the effects of sedimentation. A study by Nagihara and Opre Jones (2005) in the Gulf of Mexico showed notably decreased seafloor heat flow values with increasing sedimentation rates associated with the Mississippi Fan suggesting that depressed seafloor heat flow values are not unlikely in regions of continued sedimentation.

In order to correct for the effects of sedimentation on seafloor heat flow, Louden and Wright (1989) have proposed correction factor (C_s) (Eq. 1 and 2).

$$C_s = 1 - (1 - 2X^2)\mathrm{erfc}(X) - (2/\pi)X\exp(-X^2) \quad (1)$$

$$X = v_s*(\mathrm{sqrt}(t)/\mathrm{sqrt}(\kappa)) \quad (2)$$

Here v_s refers to a constant sedimentation rate derived from the compacted sediment thickness and the period of deposition (t) in Ma. κ is thermal diffusivity and radiogenic heat production is ignored. This method allows for the quick, simple, calculation of C_s using compacted sediment thickness' in order to remove the effects of sedimentation from

seafloor heat flow measurements to predict a more realistic present day basement heat flux. Louden and Wright (1989) suggest that calculating a sediment correction factor using this simplified method yields results in relative agreement with the results calculated by Hutchinson (1985) using a more complete method involving decompacted sediment thicknesses. For all sedimentation models an inverse relationship between rate of sedimentation and seafloor heat flux has been predicted (e.g. Hutchinson 1985, Wang and Davis 1992)

We have calculated a correction for sedimentation for all seafloor heat flow measurements acquired along heat flow transects Line 1 and 2 during the 2008 Hudson heat flow cruise (Tab. 3.3). Calculations were made using sediment thicknesses derived from seismic interpretations and depositional velocities calculated using compacted sediment thicknesses. A depositional period of 200 Ma was used for all stations not overlying salt bodies (Tab. 3.3). The sediment thickness for stations overlying salt diapirs refers to sediment above salt. Salt diapirs migrate upwards through the sediment column from depth rather than being deposited at the seafloor, therefore, salt emplacement will not have a cooling effect as surface sedimentation does and should not be included in our correction for cooling due to sedimentation. The age associated with the sediments overlying salt, as required for depositional velocity calculation, are inferred from stratigraphic boundaries as picked in our seismic interpretations.

Corrections for sedimentation were applied to determine the basal heat flux rather than the present day seafloor heat flow for later comparisons with predictions from crustal rift models. As measurements above salt diapirs recorded anomalously high geothermal gradients due to the focusing effects of salt on heat flow, these measurements

Heat Flow Station	Offset (m)	Bullard Heat Flow (mW/m^2)	Sediment Thickness (m)	Depositional Period (Ma)	Depositional Velocity (m/Ma)	Stretching Factor (β)	Cs	Diapir	Salt Increase	Sed. Cor. Basal Heat Flux (mW/m^2)	Salt Corrected Basal Heat Flux (mW/m^2)	Model 1 HF (mW/m^2)	Model 2 HF (mW/m^2)
Line 1													
HF101	100700	23.9	6400	200	32.0	2.01	0.123			26.83731	26.83731	35.85	44.81
HF102	114200	34.7	7700	200	38.5	2.42	0.156			40.11667	40.11667	36.1428	45.17
HF103	124300	37.3	8000	200	40.0	2.84	0.164			43.4172	43.4172	36.33	45.42
HF104	127300	38.1	7900	200	39.5	3.05	0.161			44.24934	44.24934	36.4	45.5
HF105	128500	46.9	2600	90	28.9	3.12	0.065	D1	1.08	49.95788	46.05423529	36.42	45.53
HF106	131700	39.3	7700	200	38.5	3.28	0.156			45.43473	45.43473	36.46	45.58
HF107	134800	40.3	7900	200	39.5	3.4	0.161			46.80442	46.80442	36.49	45.61
HF108	140900	37.1	8100	200	40.5	3.7	0.167			43.28457	43.28457	36.55	45.69
HF109	146100	39.4	3700	120	30.8	3.9	0.085	D2	0.94	42.7293	45.37624779	36.58	45.73
HF110	150900	43.3	3100	120	25.8	4.1	0.068	D2	1.05	46.23141	43.96013629	36.61	45.76
HF111	154300	65.7	1800	90	20.0	4.3	0.042	D2	1.23	68.43969	55.72832454	36.63	45.79
HF112	157600	54.9	1700	70	24.3	4.43	0.045	D2	1.16	57.38697	49.66521203	36.65	45.81
HF113	160300	43.1	5900	200	29.5	4.46	0.111			47.87117	47.87117	36.65	45.81
HF114	166800	43.4	5900	200	29.5	4.6	0.111			48.20438	48.20438	36.66	45.83
HF115	172600	56.6	3000	145	20.7	4.81	0.058	D3	1.11	59.8828	53.96032527	36.68	45.85
HF117	180000	51.7	2500	145	17.2	5	0.046	D4	1.11	54.09371	48.74378264	36.7	45.87
HF118	187800	43.3	4800	200	24.0	5.06	0.070			46.31368	46.31368	36.7	45.88
HF119	201700	46	4800	200	24.0	5.2	0.070			49.2016	49.2016	36.71	45.89
Line 2													
HF201	34300	29.1	6500	200	32.5	2.01	0.125			32.7	32.7	35.82	44.7772
HF202	43100	31.7	5900	200	29.5	2.24	0.111			35.2	35.2	36	44.9995
HF203	53500	43.9	7000	200	35.0	2.59	0.138			50	50	36.2	45.2434
HF204	62200	54.7	6000	200	30.0	3.12	0.161			63.5	47.8	36.38	45.4799
HF205	66300	65.5	3000	80	37.5	3.35	0.084	D5	1.330	71	53.4	36.44	45.5516
HF206	70000	61.3	1000	40	25.0	3.51	0.034	D5	1.330	63.4	47.6	36.51	45.5938
HF207	72600	72.8	1000	40	25.0	3.63	0.034	D5	1.330	75.3	56.6	36.54	45.6221
HF208	75600	60.7	800	40	20.0	3.75	0.026	D5	1.330	62.3	46.8	36.56	45.6478
HF209	79500	N/A	6300	200	31.5	3.9	0.120			50.3	50.3	36.58	45.6768
HF210	86000	47.1	6500	200	32.5	4.22	0.125			53	53	36.62	45.7291
HF219	152000	42.6	5500	200	27.5	4.46	0.101			46.9	46.9	36.65	45.7614
HF220	164500	44.5	5200	200	26.0	4.04	0.094			48.7	48.7	36.6	45.7012
HF221	178200	41.1	5300	200	26.5	4.45	0.097			45.1	45.1	36.65	45.7602

Table 3. 3: Corrections table showing correction for sedimentation and correction for both salt and sedimentation. In addition, modelled basal heat flux after McKenzie (1978) using a lithospheric thickness of 100 km (Model 1) and 125 km (Model 2) are shown. Cs = Correction for sedimentation, stretching factor after Wu (2006).

are not representative of the true underlying basal heat flux and require an additional correction for the conductive effects of salt, as described in Section 3.4.3. It should also be noted that the predicted values after McKenzie (1978) and Royden and Keen (1980) do not account for any additional heat generation due to radioactive decay of uranium, potassium and thorium which likely occur in the sediment pile overlying the basement.

3.4.3 Effects of Salt on Heat Flow

The thermal conductivity of salt is approximately 6 $Wm^{-1}K^{-1}$ at room temperature, decreasing as temperature increases to a value of ~4.5 $Wm^{-1}K^{-1}$at temperatures of 50 to 100 °C (Birch and Clark 1940). This conductivity value is significantly higher than the values for most clastic and carbonate sediments which range from 1.5 to 2.5 $Wm^{-1}K^{-1}$ dependant on lithology, burial depth, compaction and water content (Clark 1966). As salt has a significantly higher thermal conductivity than most sediments, heat preferentially flows through salt, resulting in thermal anomalies above, beside, and beneath salt structures. Salt bodies are overlain by positive and underlain by negative thermal anomalies (Fig. 3.13) (O'Brien and Lerche 1987, Yu et al. 1992). Assuming a static salt body and purely conductive heat transfer the thermal anomaly predicted is directly proportionate to the shape, height and volume of the salt body, as well as the contrast in thermal conductivities between the salt and surrounding sediments (Jensen 1983).

To determine the effects of salt diapirs on seafloor heat flow, a series of static, purely conductive, 2D numerical models were run (Appendix E). The models were designed to replicate the effects of salt bodies present in lines 1400 and 88-1A on seafloor heat flow. The relative increase in seafloor heat flow above salt observed in the models is used remove the effects of salt on measured seafloor heat flow in an attempt to

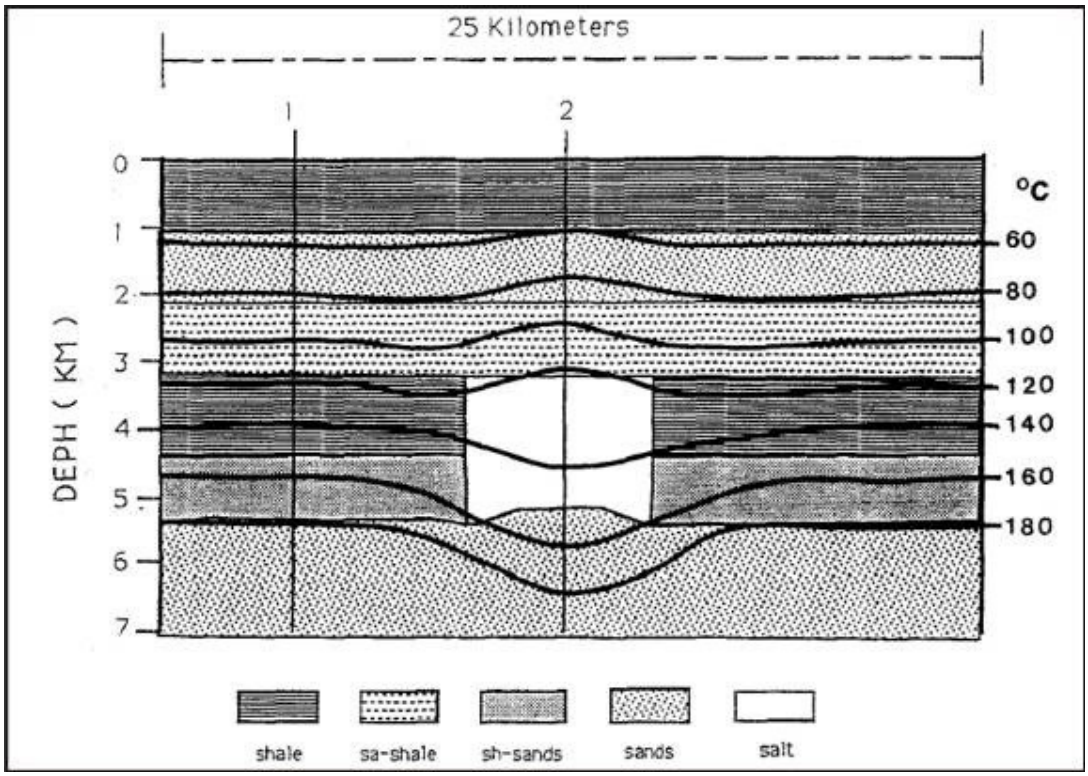

Figure 3. 13: Simple 2D conductivity based numerical model showing the effects of a square shaped salt body on temperature distribution in the case of constant uniform basal heat flux (from Yu et al. 1992).

determine the basal heat flux across the central Scotian Slope. Models were run replicating diapirs D1-D4 on line 1400, and D5 on line 88-1A. Our modelling script does not allow for the presence of salt overhangs/canopies only allowing us to model vertical salt diapirs (Appendix E). As a result, the slight overhangs observed in our seismic interpretations of the salt diapirs had to be removed.

Our model is a simple two layer model consisting of a basal salt layer with a thermal conductivity of 5.9 $Wm^{-1}K^{-1}$ overlain by sediments with increasing conductivity with depth from 2.2 $Wm^{-1}K^{-1}$ at the seafloor to 3.1 $Wm^{-1}K^{-1}$ at the salt/sediment boundary. The increase in thermal conductivity with depth in the sediment pile is included to account for increasing conductivity due to compaction. A constant basal heat flux of 50 mWm^{-2} was assigned in the models. This value is slightly higher than the

measured sediment corrected seafloor heat flow values of ~47 mWm^{-2} at the seaward limit of lines 1400 and 88-1A. The basal heat flux of 50 mWm^{-2} was used as a high end member in an attempt to match the measured values above salt diapirs.

It was noted by Yu et al. (1992) that in order to allow the basement heat flux to flow preferentially through the less resistant, higher thermal conductivity, material that the model must be wide enough for the heat pathways to be affected only by the conductivity of the materials and not by the edges of the models. Thus, varying distances between the salt body and the edges of the models were tested to determine how edge effects affected the model output and how far laterally the models needed to be extended to escape these effects. To escape significant seafloor heat flow variations due to edge effects a distance equivalent to twice the width of the salt body on either side of the diapir was required in the models.

As with all salt bodies, multiple interpretations of diapir size, shape and distribution are possible. Two possible interpretations of diapir D5 are shown in Figure 3.14 showing the salt body as a large salt canopy with a thick vertical feeder (A), and as a thick vertical diapir (B). The heat flow measurements recorded above this salt body are anomalously high, reaching values upwards of 72 mW/m^2, and thus in the simple models the salt was interpreted as a thick vertical diapir as a high heat flow end member. In total, eight simple salt models were run. Of these five were modelled after diapir D5 in line 88-1A, and one was run for each diapir D1, D2 and D3/D4 in line 1400. The numerous runs for diapir D5 were undertaken to test the effects of variations in diapir height/proximity to the seafloor, as well the effects of variations in basal heat flux on modelled seafloor

heat flow (Appendix E). Of the models run after diapir D5 it was determined that Salt Model 2 was in best agreement with the observed seafloor heat flow data (Fig. 3.15).

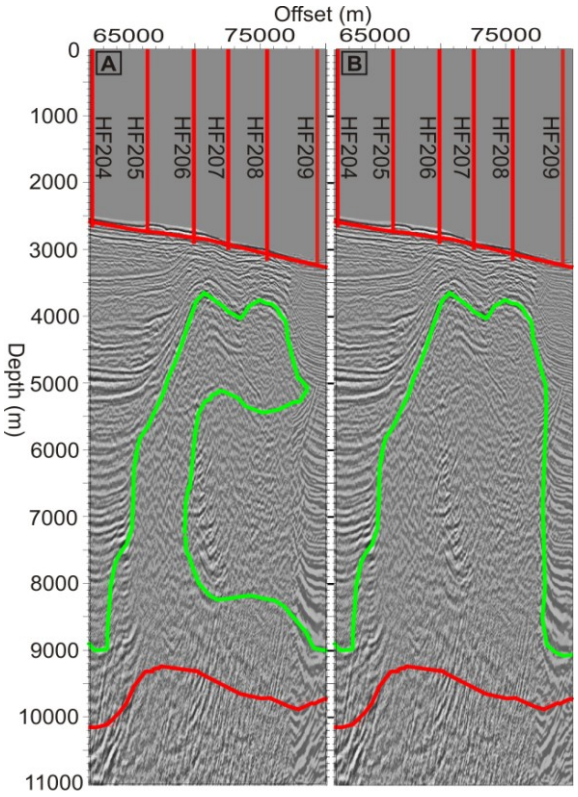

Figure 3. 14: Two possible interpretations of salt diapir D5 on Lithoprobe Line 88-1A (Fig. 3.5) showing A) large tongue canopy with thick, squeezed, feeder and B) large vertical salt diapir.

In an attempt to better constrain the basal heat flux across the central Scotian Slope, sediment corrected heat flow values were further corrected for the conductive effects of salt on heat flow for heat flow stations overlying salt bodies. To do this we use the relative increase in modelled heat flow above diapirs D1-D5 to remove the associated increase in heat flow associated with the purely conductive effects of salt from our measured, sediment corrected, heat flow measurements. The sediment corrected measured heat flow values were simply divided by the ratio modelled heat flow above salt over modelled heat flow unaffected by salt to remove the conductive effects of salt as

measured at the seafloor from true basal heat flux. Salt and sediment corrected heat flow data are included in Table 3.3.

Salt Model 2 mimics diapir D5 in height and shape. With lateral distances of 40 km between the diapir and edges of the models the model is wide enough to escape any edge effects as noted by Yu et al. (1992). Measured seafloor heat flow above this diapir could not be matched perfectly using a simple 2D conductivity based numerical model with a constant basal heat flux as large variations in measured seafloor heat flow occurred across the diapir despite little variation in diapir height or proximity to the seafloor. The model predicts a maximum heat flux of ~56 mWm^{-2} above the salt diapir, 1.33 times the predicted heat flow of ~42 mWm^{-2} predicted in regions unaffected by salt (Fig. 3.15). We applied a uniform correction factor of 1.33 (decrease measured heat flow by a factor of 1.33) to all seafloor heat flow measurements acquired above this diapir to remove the increase in seafloor heat flow associated with the conductive effects of salt from the measured values.

Salt Model 6, representative of diapir D1 in line 1400, is overlain by heat flow station HF105. The modelled seafloor heat flow of 45.6 mWm^{-2} is 1.08 times higher than the modelled background values of ~42 mWm^{-2} in regions unaffected by salt (Fig. 3.16). Salt Model 8 is modelled after both diapirs D3 and D4 and is overlain by heat flow stations HF115 and HF116. A modelled increase from ~41 mWm^{-2} in regions unaffected by salt to 45.5 mWm^{-2} above salt was observed for both diapir D3 and D4. Both heat flow stations are located just off the crest of diapirs the salt diapirs, and experience a relative increase in modelled heat flow of 1.11 mWm^{-2} (Fig. 3.17).

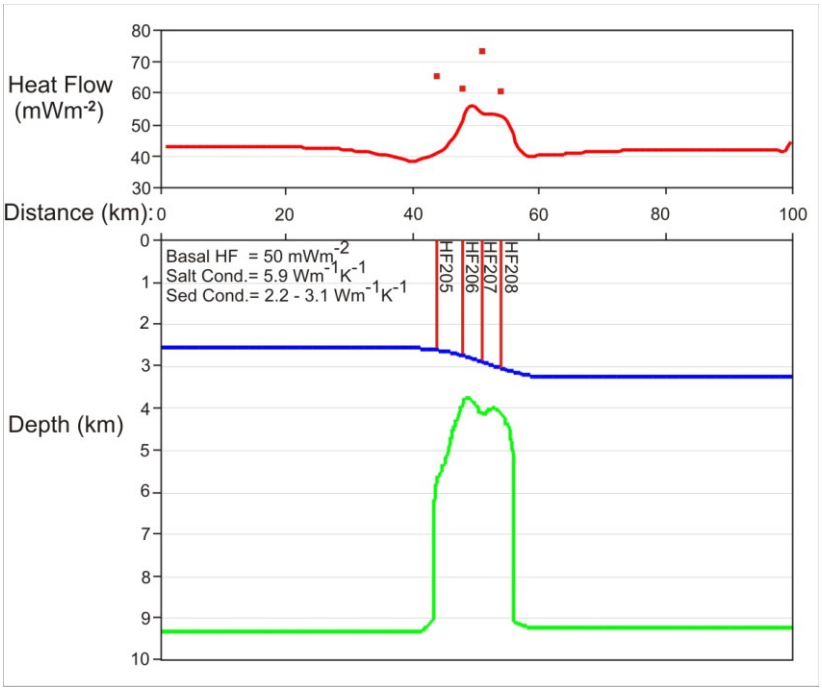

Figure 3. 15: Simple 2D conductivity based thermal model of diapir D5 showing effects of salt on seafloor heat flow. Salt is outlined in green, and the seafloor in blue. The modelled seafloor heat flow is plotted above as a red line and measured values are plotted as red squares.

Salt diapir D2 is overlain by heat flow stations HF209-HF212. Salt Model 7 is representative of this diapir, however, as canopies are not possible in our models, the diapir has been inferred as a thick, vertical, basement rooted salt body (Fig. 3.18). Modelled heat flow in regions unaffected by salt yielded a value of ~42 mWm^{-2}. Modelled seafloor heat flow values above salt varied from one station to the next, thus different correction factors were applied for the different stations located across the diapir. Station HF209, located at the very edge of diapir D2, recorded a modelled value of 39.5 mWm^{-2}, only 0.94 times the background value of ~42 mWm^{-2}. This low heat flow value associated with the stations location at the edge of the diapir will actually require an increase in heat flow to correct for the conductive effects of salt. Stations HF110, HF111 and HF112 recorded modelled seafloor heat flow values of 44.2 mWm^{-2}, 51.8 mWm^{-2} and 48.5 mWm^{-2}, yielding respective correction factors of 1.05, 1.23 and 1.16.

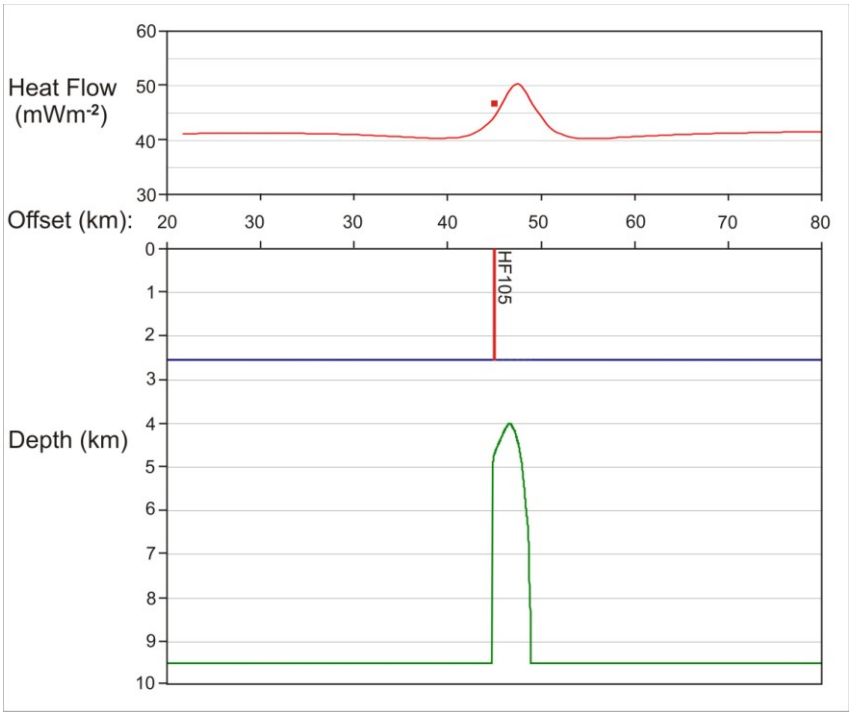

Figure 3. 16: Simple 2D conductivity based thermal model of diapir D1 showing effects of salt on seafloor heat flow. Salt is outlined in green, and the seafloor in blue. The modelled seafloor heat flow is plotted above as a red line and measured values are plotted as red squares.

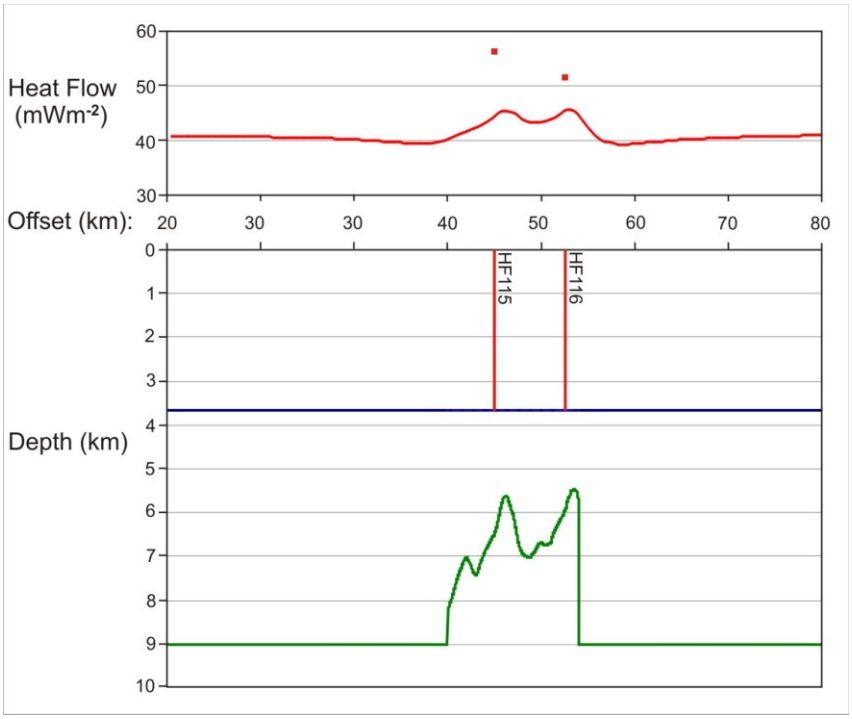

Figure 3. 17: Simple 2D conductivity based thermal model of diapir D3/D4 showing effects of salt on seafloor heat flow. Salt is outlined in green, and the seafloor in blue. The modelled seafloor heat flow is plotted above as a red line and measured values are plotted as red squares.

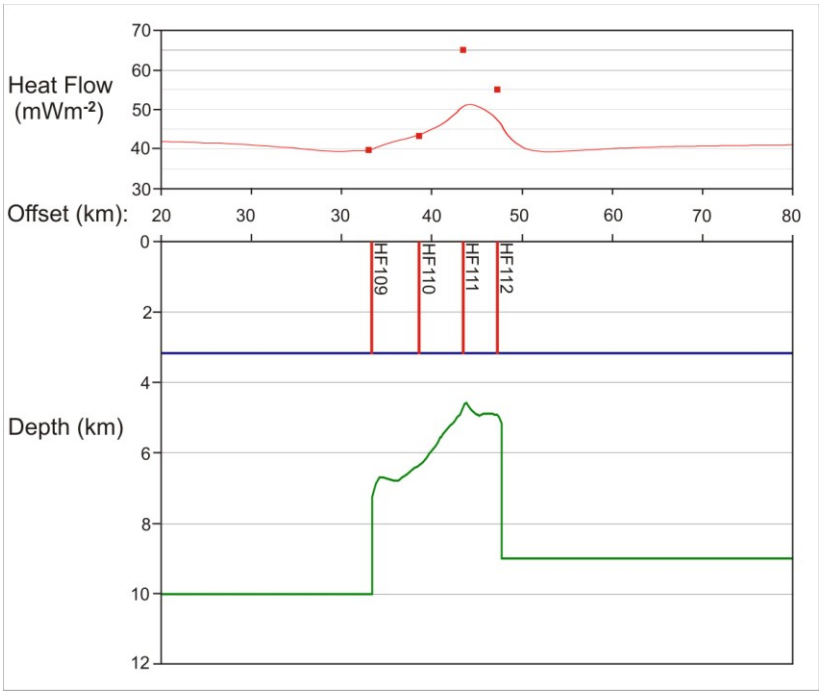

Figure 3. 18: Simple 2D conductivity based thermal model of diapir D2 showing effects of salt on seafloor heat flow. Salt is outlined in green, and the seafloor in blue. The modelled seafloor heat flow is plotted above as a red line and measured values are plotted as red squares.

Our simple modelling suggests that the increase observed above salt bodies in our measured heat flow data can not be reproduced by the strictly conductive effects of salt alone. In general, the purely conductive 2D models under-predict the heat flow above salt. A second mechanism such as convection of fluids is likely affecting the temperatures observed above the salt bodies. Keen (1983) ran a series of similar conductivity based 2D models in an attempt to determine if the conductive effects of salt could sufficiently increase temperatures above the Primrose diapir on the Scotian Shelf to account for an observed maturation anomaly (Rashid and MacAlary 1977). While the temperature increase due to the conductive effects of salt were calculated to be 10-20 °C, this alone was not enough to result in the observed maturation anomaly.

Keen (1983) hypothesized that upon diapiric intrusion, faulting and fracturing of the sediments adjacent to the diapir could create a migration pathway for hot fluids from

depth to the top of the diapir, which could cause significant increases in temperature and thus maturation above the diapir. Under favourable circumstances, it was found that in addition to the conductive effects of salt, migration of hot fluids from depth could produce the observed maturation anomaly above the Primrose diapir. Keen suggests that much of the rising fluid will likely continue to flow vertically beyond the crest of the diapir towards the surface, which supports the idea that convection of fluids could be affecting our observed variation in seafloor heat flow measurements. However, further modelling is required to test this hypothesis.

3.5 Simple Lithospheric Models

Once measured heat flow data have been corrected for the effects of sedimentation and salt to give approximations of present day basal heat flux are were able to begin analysis and comparisons of our measured data with predictions from simple lithospheric rift models. To theoretically predict the basement heat flux across our study area the uniform stretching model of McKenzie (1978) and the dual stretching model of Royden and Keen (1980) were employed. We attempt to match modelled present day basal heat flux to our sediment and salt corrected measured heat flux data to constrain basal lithospheric temperatures and lithospheric thicknesses while predicting the margins heat flux history. An introduction to simple rift models and our MatLab scripts used in modelling are included in Appendix F.

To determine the basal heat flux across the central Scotian Slope we must first determine the crustal stretching factors across the margin. The pure shear model assumes uniform extension of the crust upon initiation of rifting. The predicted basal heat flux as a function of time is directly related to the initial crustal stretching factor (β),

asthenospheric temperature (T1), and total lithospheric thickness (A). Varying crustal stretching factors (β) were defined by Wu (2007) along the trace of SMART refraction Line 2 based on crustal thicknesses derived from velocity modelling (Fig. 3.19). SMART Line 2 runs coincident with Lithoprobe line 88-1A. An offset of 156 km on SMART Line 2 corresponds with the 0 offset of Lithoprobe Line 88-1A. Using this, we were able to determine crustal stretching factors at known positions (thus at our heat flow stations) on line 88-1A (Fig.3.19).

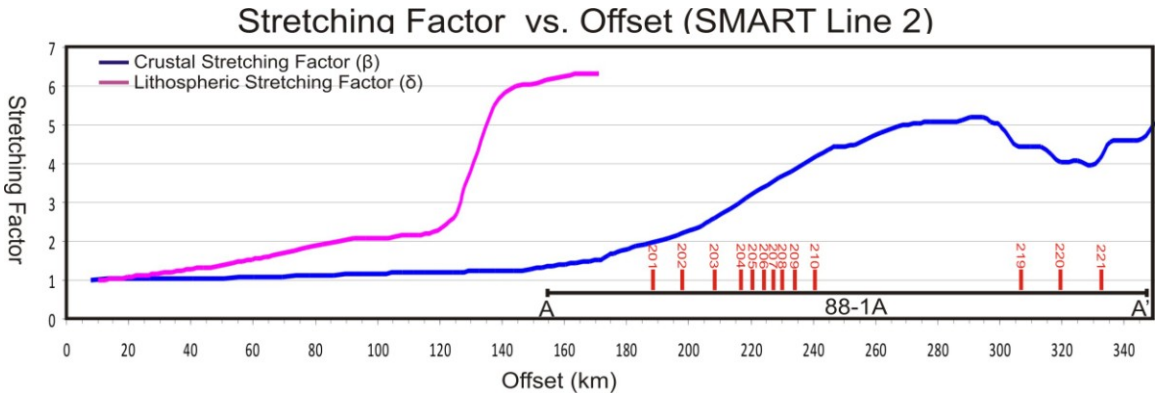

Figure 3. 19: Stretching factor (β and δ) vs. Offset (km) for SMART Line 2 after Wu (2007) and Keen and Beaumont (1990). Black line represents the trace of coincident seismic reflection profile 88-1A. Vertical red lines represent seafloor heat flow locations. Corresponding location of Lithoprobe line 88-1A is shown from A to A' in Figure 3.1.

The predicted values for present day basal heat flux are calculated according to a rift age of 200 Ma with crustal stretching factors derived from Wu (2007). Stretching factors range from 2.01 at station HF201 on the upper continental slope to 4.46 at station HF219 towards the seaward limit of the Scotian Slope (Tab. 3.3). As expected, no significant variations in present day heat flux are predicted by the models associated with variations in β. All modelled present day basal heat flux values are within 1 mWm^{-2}, independent of β values used. However, variations in β across the margin do significantly affect the heat flow history over the past 200 Ma (Fig. 3.20, Fig. 3.21). Therefore, although no significant present day heat flow variations exist associated with varying β,

varying stretching factors across the margin may still have implications for hydrocarbon maturation and the thermal evolution of the margin. Using the pure shear lithospheric rift model present day crustal heat flux was predicted at all heat flow stations as constrained by associated crustal thicknesses after Wu (2007) and lithospheric thicknesses (A) of both 125 km (Lithospheric Model 1) and 100 km (Lithospheric Model 2) (Tab. 3.4). Varying lithospheric thicknesses were tested in an attempt to match modelled basal heat flux to measured data (seafloor heat flow data as corrected to remove the thermal effects of the sediment pile). Varying T1 would have a similar effect on heat flow as varying A and as neither T1 or A are known, we maintained a constant T1 while varying A in an attempt to vary basal heat flux while maintaining known crustal thicknesses.

The dual stretching model predictions for the regions heat flow history vary depending on the amounts of upper lithospheric stretching (β) and lower lithospheric stretching (δ). Keen and Beaumont (1990) used large δ values in comparison with the small β values to explain the observed uplift of the Lahave Platform on the central Scotian Shelf. The proportions of lower lithospheric stretching are uncertain across the central Scotian Slope. We are able to obtain varying crustal heat flux histories while maintaining known crustal thicknesses by varying the amount of sub-crustal thinning. Applying a large sub-crustal stretching factor has a negligibly small effect on present day basal heat flux when compared to the uniform stretching model predictions. However, it should be noted that uniform and dual stretching models, although arriving at similar present day heat flux values, have very different heat flux histories, particularly over the first ~50 Ma (Fig. 3.21, Fig. 3.22). This may significantly effect the hydrocarbon maturation history of the margin and is discussed in further detail in Chapter 4.

Lithospheric Model 3 is run to determine how significantly varying proportions of β and δ stretching factors affect basal heat flux (Fig. 3.23). Lithospheric Model 3 is constrained using a constant δ value of 6 across the study area while constraining β factors after Wu (2007) (Tab. 3.4). Keen and Beaumont (1990) suggest that towards the upper Scotian Slope the lithosphere is stretched by a factor of ~6 and has become relatively stable. Thus, the lithospheric stretching factor in Lithospheric Model 3 was set constant at 6 across the central Scotian Slope.

				Modelled Heat Flow		
HF Stations	881A Offset	Beta	Delta	Model 1	Model 2	Model 3
OBS_5	3800	1.38	6	34.9615	43.7019	36.11
OBS_6	21800	1.76	6	35.5616	44.452	36.31
HF201	34300	2.01	6	35.8217	44.7772	36.4
HF202	43100	2.24	6	35.9996	44.9995	36.45
HF203	53500	2.59	6	36.1947	45.2434	36.51
HF204	62200	3.12	6	36.3839	45.4799	36.57
HF205	66300	3.35	6	36.4413	45.5516	36.59
HF206	70000	3.51	6	36.4751	45.5938	36.6
HF207	72600	3.63	6	36.4977	45.6221	36.61
HF208	75600	3.75	6	36.5183	45.6478	36.62
HF209	79500	3.9	6	36.5415	45.6768	36.62
HF210	86000	4.22	6	36.5833	45.7291	36.64
OBS_10	104900	4.81	6	36.6403	45.8004	36.66
OBS_11	124100	5.06	6	36.6589	45.8236	36.67
OBS_12	143800	5.01	6	36.6554	45.8192	36.67
HF219	152000	4.46	6	36.6091	45.7614	36.65
HF220	164500	4.04	6	36.5609	45.7012	36.63
HF221	178200	4.45	6	36.6082	45.7602	36.65

Table 3. 4: Present day basal heat flux predicted by our three lithospheric models. Lithospheric stretching factor (D) corresponds only to Lithospheric Model 3.

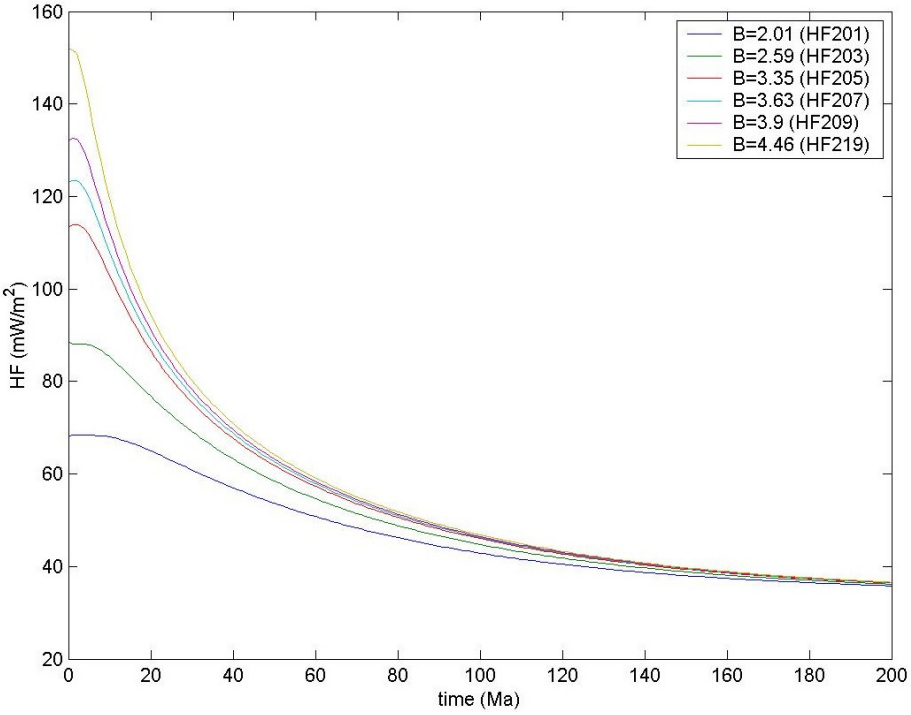

Figure 3. 20: Heat flux vs. Time graph for Lithospheric Model 1 showing change in crustal heat flux with time for select heat flow stations based on associated crustal stretching factors as shown in Fig. 3.14 and A =125 km. Time (in Ma) represents time following rifting.

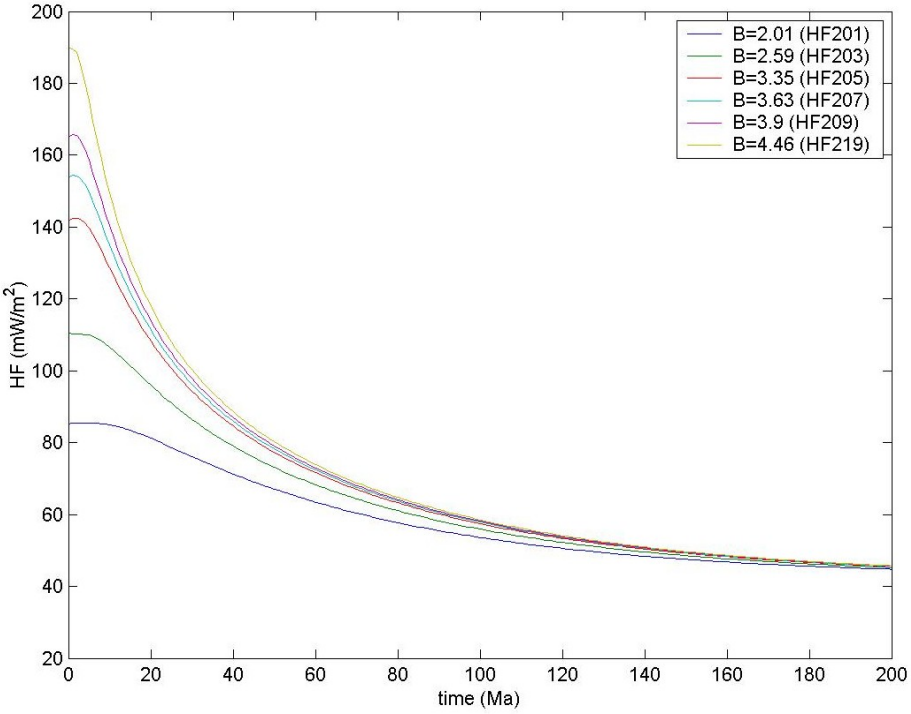

Figure 3. 21: Heat flux vs. Time graph for Lithospheric Model 2 showing change in crustal heat flux with time for select heat flow stations based on associated crustal stretching factors as shown in Fig. 3.14 and A =100 km. Time (in Ma) represents time following rifting.

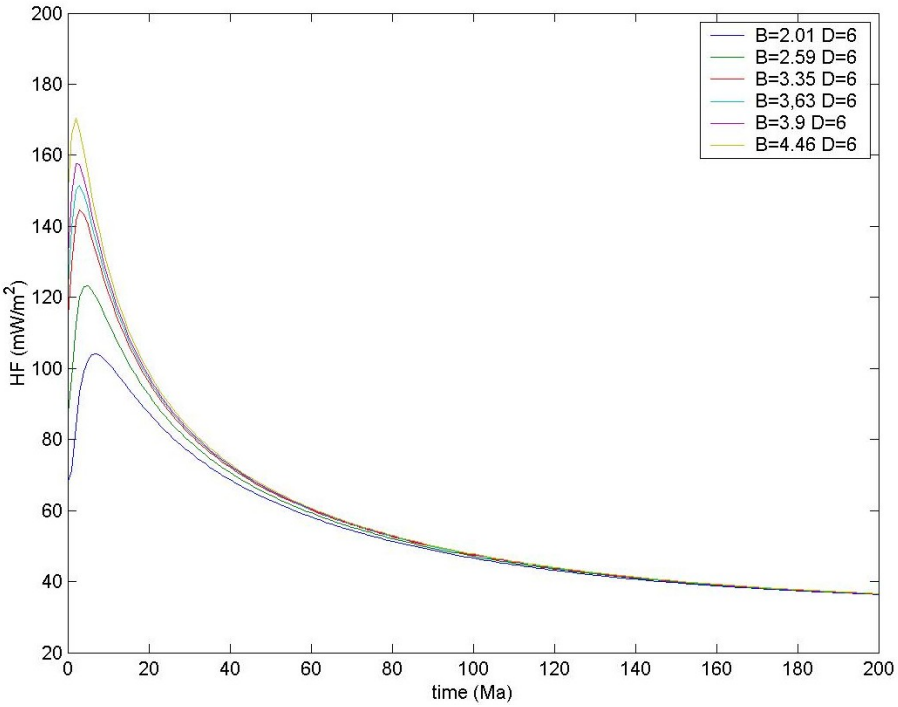

Figure 3. 22: Heat flux vs. Time graph for Lithospheric Model 3 showing change in crustal heat flux with time for select heat flow stations based on associated varying crustal stretching factors (β), constant lithospheric stretching factor (δ=6) and A=125 km. Time (in Ma) represents time following rifting.

Our goal is to use the predicted basement heat flux histories from the uniform and dual stretching models in combination with measured seafloor heat flow data to produce a self-consistent 3D thermal model of the central Scotian Slope. Once the 3D model configuration has been set we will test the effects of varying basement heat flux histories after Lithospheric Models 1-3 (Section 3.5) on seafloor heat flow. By testing various basement heat flux histories and comparing the predicted seafloor heat flow from the 3D models with the measured seafloor heat flow values of the 2008 Hudson cruise we produce a 3D model constrained by both measured seafloor heat flow data and modelled basal heat flux data that remains consistent with observed crustal thicknesses.

3.6 Heat Flow Data Discussion and Interpretations

After analysis of our measured seafloor heat flow data we conclude that all stations from the Torbrook gas hydrates mound and shallow water stations HF101,

HF102, HF201 and HF202 recording gradients <35 mKm^{-1} are not representative of purely conductive heat transfer sourced from Earth's interior. At present we are unable to determine the cause of these anomalously low gradients recorded at these stations, however, after comparison with the deeper sourced temperature data from the gas hydrates phase boundary after Leblanc et al. (2007) we suggest the data should not be included in our overall analysis of the study area's heat flux. Corrections for the effects of sedimentation and salt on measured seafloor heat flow have been applied to approximate the present day basal heat flux from our measured seafloor heat flow data. Plots of corrected seafloor heat flow data are compared with present day basal heat flux predictions from the uniform shear rift model across both seismic lines 1400 and 88-1A in Figure 3.23.

Across Lithoprobe line 88-1A the general basal heat flux trend varies slightly across the margin increasing from ~45-48 mWm^{-2} towards the seaward limit of the line to ~47-53 mWm^{-2} in the central/landward regions of the line. These values exclude the slightly elevated values above stations HF205 and HF207 and the anomalously low values for stations HF201 and HF202. This increase in heat flow in the direction of thickening continental crust is counter to what one would expect for a young margin, however, for an old margin such as ours the majority of increased heat flow associated with thinning has since decayed. The increase in heat flow in the landward direction is possibly due to the increase in radiogenic heat production associated with the thickening continental crust. Our simple 2D models do not account for radiogenic heat production in the crust or sediments and the effects of adding radiogenic heating will be investigated in further detail in Chapter 4.

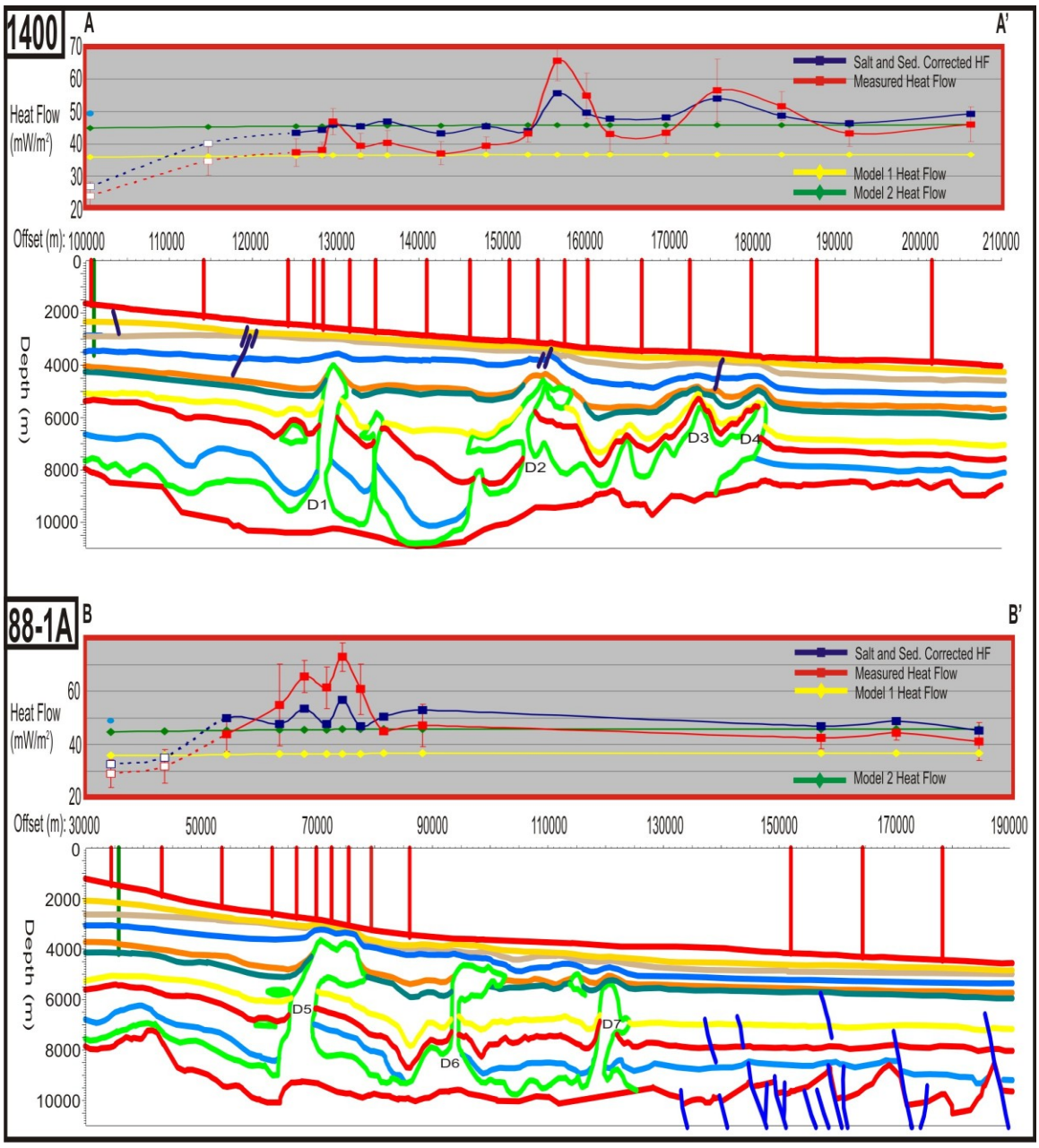

Figure 3. 23: Comparisons between corrected measured seafloor heat flow and modelled basal heat flux data for different lithospheric thicknesses and crustal stretching models after the uniform shear model of McKenzie (1978) for both line 1400 and 88-1A. White squares represent stations with anomalously low gradients and the blue circle represents heat flow value calculated after Leblanc et al. (2007) from the Torbrook gas hydrates mound. Below the heat flow plots are our stratigraphic interpretations from the seismic images as shown in Figures 3.5 and 3.6 for lines 1400 and 88-1A respectively.

The corrected basal heat flux values calculated above salt diapir D5 are in relatively good agreement with the surrounding measurements at stations HF203, HF209 and HF210. We note that the increase in measured heat flow above salt is not uniform

and cannot be entirely removed using a correction factor derived from a simple, static, 2D conductivity based numerical model. Large variations in measured heat flow above salt persist even after correction for the conductive effects of salt. Other factors such as salt movement, out of plane variations in salt geometry or convective fluid flow through sediments overlying the diapir may also be effecting the measured heat flow values (Keen 1983).

In comparing our corrected seafloor heat flow data across line 88-1A with the predictions for present day basal heat flux from the McKenzie (1978) uniform shear rift model we find that the thinner lithospheric thickness of Lithospheric Model 2 (A = 100 km) yields a better fit to the corrected heat flow data than Lithospheric Model 1 (A = 125 km) (Fig.3.24). Lithspheric Model 2 yields a relatively good fit between our measured and modelled data, particularly towards the seaward limits of the line. When the heat flow calculated from the Torbrook gas hydrates phase boundary is extrapolated onto Lithoprobe Line 88-1A and used in place of the anomalously low values calculated from HF201 and HF202 we see fairly constant heat flow across the line. Above the central region of the line the measured data records slightly higher basal heat flux values than those predicted by Lithospheric Model 2 (A = 100 km).

Heat flow data across NovaSPAN line 1400 recorded a corrected basal heat flux of ~42-47 mWm^{-2} in the landward portions of the line and ~46-49 mWm^{-2} towards the seaward end, excluding the anomalously high measurements above salt which persisted even following correction. Here we ignore stations HF101 and HF102 due to their anomalously low measured gradients. The slight increase in basal heat flux in the seaward direction recorded for this transect is opposite to the decrease identified in Line

2. However, as the error in measured heat flow is ~2-7 mWm^{-2} for regions unaffected by salt an interpretation of average basal heat flux between ~44 and 50 mWm^{-2} is not unreasonable.

After the correction for salt was applied, only stations HF111 (55.7 mWm^{-2}) and HF115 (54.0 mWm^{-2}) recorded anomalously high heat flow values. Again, we see the increase in heat flux above salt is not uniform and cannot be corrected using a simple conductivity based 2D model. All other heat flow stations are in relatively good agreement with the predictions from Lithospheric Model 2 (Fig. 3.24). The increase in heat flow in the seaward direction agrees with the model predictions, however, the measured increase is slightly greater than the modelled increase. The heat flow of 49.5 mWm^{-2} calculated from the depth to BSR after Leblanc et al. (2007) at the Torbrook mound is slightly higher than the other recorded landward heat flow at stations HF103-107 (43-47 mWm^{-2}); however, it is still in much better agreement than with the anomalously low measurement of 26.8 mWm^{-2} at HF101.

Our sediment and salt corrected basal heat flux is plotted against crustal stretching factor (β) in Figure 3.25 along with our modelled results from both Lithospheric Models 1 and 2. The general trend shows good agreement between our corrected heat flux data and the predicted values using the high heat flow end member, Lithospheric Model 2. Although there exists notable scatter in our measured corrected data, we see that with the exception of station HF209, which has an extremely small error bar due to the lack of in-situ conductivity analysis for this station, that all modelled data from Lithospheric Model 2 fall within the error of the measured heat flow (Fig. 3.24).

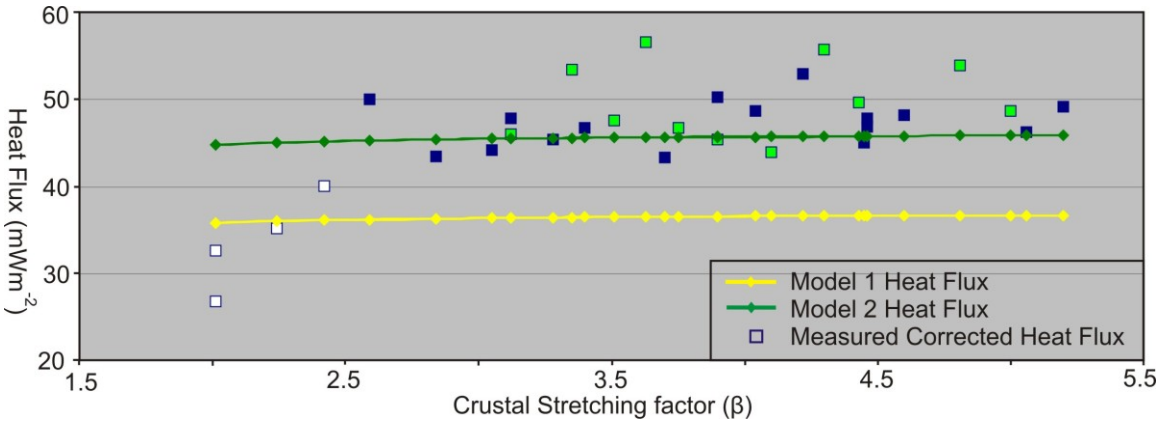

Figure 3. 24: Heat flux vs. Crustal stretching factor (β) plot showing corrected (sediment and salt) measured seafloor heat flow data as blue squares. Green filled squares represent measurements above salt bodies and white filled squares represent stations with anomalously low gradients.

We can conclude that using simple 2D lithospheric rift models without including the effects of radiogenic heating that Lithospheric Model 2, with the thinner initial lithosphere, yields a much better match to our corrected measured data than Lithospheric Model 1. With the addition of radiogenic heating within the sediment pile and underlying crust we may find that the thinner lithospheric model over predicts the present day heat flux when compared with our modelled data and that, in fact, the thicker lithosphere yields a better fit to our measured data. To test this hypothesis and to determine how significantly 3D effects of salt bodies affect seafloor heat flow we will run a series of more complex, dynamic, 3D models in Chapter 4 using PetroMod 11® software.

Chapter 4: Thermal and Petroleum Systems Modelling

In this chapter we attempt to incorporate available well data, seismic interpretations (Section 4.2), heat flow data and simple lithospheric modelling results (Chapter 3) to produce a self consistent 3D thermal model of the central Scotian Slope using PetroMod 11® software. PetroMod ® is a bottom up basin modelling software package designed to model the evolution of a basin through time and provide analysis of its thermal maturation and petroleum systems potential. We will use PetroMod ® to investigate the thermal evolution and maturation potential of the central Scotian Slope from the onset of rifting to present day.

The 3D models also serve to predict the effects of salt diapirs on heat flow. Our 2D, conductivity based, numerical models suggest that to match seafloor heat flow values above salt very high basal heat fluxes are required, which result in over predictions of seafloor heat flow in regions unaffected by salt. It is hypothesized that the 3D effects of salt not included in 2D models may account for some of the variation in measured heat flow above salt bodies. Our goal is to use dynamic 3D models to predict both the maturation potential of central Scotian Slope source rocks, and to determine if measured seafloor heat flow values across the study area can be matched in 3D models as constrained by simple lithospheric rift models and available well and seismic data.

4.1 Seismic Data and Interpretation

To constrain basement topography, stratigraphy and distribution of salt structures in our 3D thermal models we interpret available 2D seismic reflection data from within the study area. Our seismic database includes data from three separate 2D seismic surveys: four lines from the 2003 ION-GXT NovaSPAN survey, line 88-1A from the

1988 Lithoprobe survey, and twelve lines from the first phase of the TGS-Nopec NS-100 survey shot in 1998 (Fig. 4.1). Seismic lines 1400, 88-1A and 1600 were interpreted to constrain stratigraphy and structure underlying heat flow transects 1, 2 and 3 respectively. Initial interpretations of these lines were completed prior to the Hudson heat flow cruise to determine locations for seafloor heat flow stations. The interpretations of twelve 2D seismic reflection profiles of the TGS-Nopec NS-100 survey were added to better constrain the stratigraphy and salt distribution of the region surrounding Lithoprobe line 88-1A. Given the constraints on crustal thickness defined for this line by Wu (2007), line 88-1A was selected as our primary line for 3D thermal modelling.

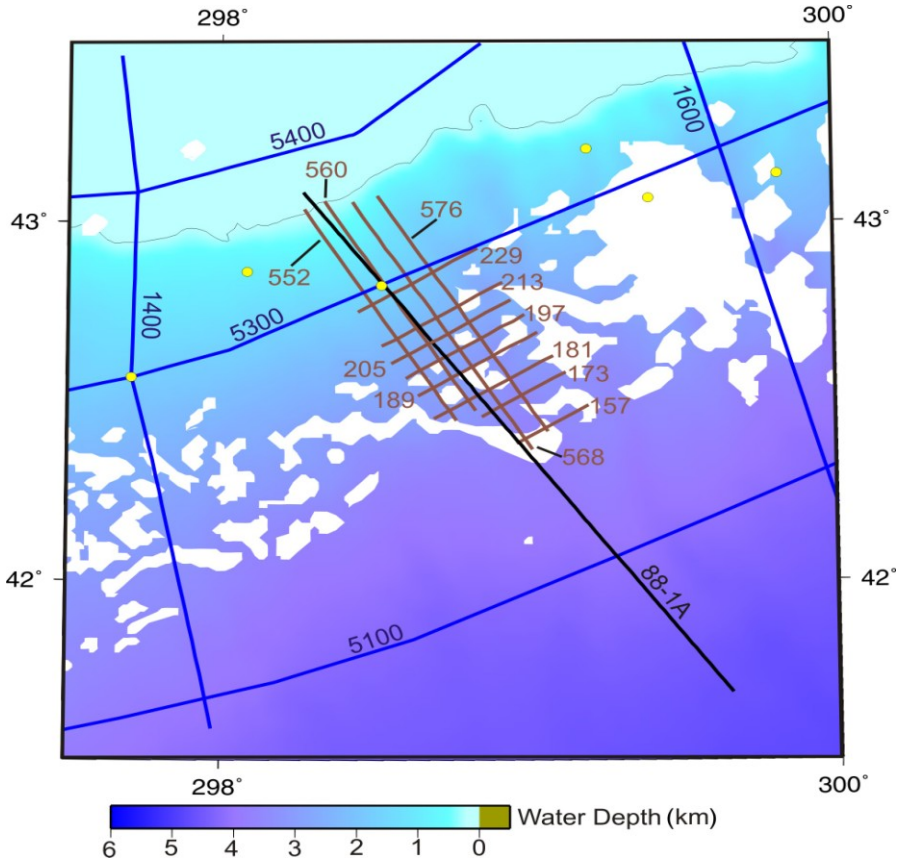

Figure 4. 1: Location map of the Scotian Basin showing select seismic lines of the TGS Nopec NS-100 survey (brown), Lithoprobe survey (black) and ION-GXT NovaSPAN surveys (blue). Salt is shown in white (after Shimeld 2004) and yellow circles represent Scotian Slope well locations.

4.1.1 Seismic Data

Digital data of the TGS-Nopec NS-100 survey were not publicly available. However, paper copies of the data were available through the CNSOPB data repository, referred to as file NS24-G26-1P. The paper profiles were scanned and converted back to digital data through a workflow outlined in Appendix G to allow us to interpret the locations of salt bodies and correlate stratigraphy with picks in surrounding lines of our seismic database. The scanned data were converted to SEG Y format using an existing script written by Andrew McCrae (MacCrae 2001). The SEG Y files were then converted from time to depth to maintain consistency with the other seismic profiles, as required for interpretation and input into PetroMod® for thermal and petroleum systems modelling. The basic velocity model used for depth conversion was that of Wu (2007) for Lithoprobe line 88-1A. This velocity model was modified to account for variations in basement structure and salt distribution from line to line (Appendix G).

As different processing workflows were applied to the seismic data of the three surveys present in our seismic database notable differences in imaging quality exist. The most problematic difference in the processing workflows is the lack of consistent velocity models between the ION-GXT NovaSPAN, the Lithoprobe and TGS Nopec NS-100 surveys. Variations in the velocity model used to depth convert may result in variations in depth to stratigraphic boundaries between lines. However, variations in depths between lines appear to be minimal as loop correlations of seismic stratigraphy show good agreement throughout the study area.

4.1.2 Seismic Interpretation

Interpretations of all primary seismic lines used in constraining 3D models and heat flow transects are included in Appendix H. In total, eleven seismic horizons were picked throughout the study area. These include picks for basement, salt, seafloor and eight other stratigraphic intervals throughout the sediment column. Formation top picks from three Scotian Slope and three Scotian Shelf wells were used to provide depth constraints to important stratigraphic boundaries (Table 4.1). Formation top picks in wells were associated with prominent reflections, which were then correlated across the seismic images. Basement and salt horizons were picked based on their characteristic reflectivity. Loop correlations were used to increase correlation confidence and to insure agreement in interpretations between lines. Picks were tied to the available well data where possible.

Correlation confidence is good landward of the salt diapiric sub-province where the stratigraphy remains relatively undeformed yielding strong, continuous, reflections. Correlation confidence decreases in the seaward direction. Throughout the salt diapiric province salt bodies significantly distort stratigraphy making it difficult to follow reflections seaward of salt. No wells exist seaward of the salt diapiric province making it very difficult to constrain stratigraphy in these regions. To provide further constraints on seaward stratigraphy Ebinger and Tucholke (1988) correlated seismic pinch-outs atop magnetic anomalies in the adjacent Sohm Abyssal Plain with regional seismic stratigraphy in the Scotian Basin. Ings and Shimeld (2006) used two seismic lines across the deep water slope, Lithoprobe line 89-1 and BGR Line 89-12, to tie the picks of Ebinger and Tucholke (1988) to the landward equivalent strata of the Scotian Basin.

Color	Stratigraphic Boundary	Horizon Age	Formation Top Depth (m)					
			Torbrook C-15	Shubenacadie H-100	Annapolis G-24	Moheida P-15	Oneida_ O-25	Panuke F-09
	Seafloor	Recent (0 Ma)	N/A	N/A	N/A	N/A	N/A	N/A
	Top Pliocene (Top Esperanto Beds)	Top Pliocene (1.6 Ma)	N/A	N/A	N/A	N/A	274	N/A
	Mid Miocene (above Top Manhassat Beds)	~Top Langhian (16.6 Ma)	2962	N/A	N/A	N/A	N/A	N/A
	Top Eocene (above Top Naswauk Beds) (M/E)	Top Eocene (36.6 Ma)	3488	3181	2682	N/A	661	N/A
	Top Wyandot (Wy)	Top Maastrichtian (66.4 Ma)	N/A	3701	3457	1103	1219	914
	Top Logan Canyon Eq. (LC)	Top Early Cretaceous (97.5 Ma)	N/A	N/A	3490	1444	1458	1313
	Top Missisauga Eq. (Ms)	Top Barremian (119 Ma)	N/A	N/A	5041	2213	2468	2374
	Top Abenaki Eq. (Ab)	Top Jurassic (144 Ma)	N/A	N/A	N/A	2711	2882	3154
	Top Misane Eq.	Early Oxfordian (~160 Ma)	N/A	N/A	N/A	3365	3667	N/A
	Top Argo Salt	Sinemurian (~198 Ma)	N/A	N/A	N/A	N/A	N/A	N/A
	Top Basement	Late Triassic (208 Ma)	N/A	N/A	N/A	N/A	N/A	N/A

Table 4. 1: Horizons picked and associated colors as shown in seismic interpretations. Horizon age and formation top depths are included after MacLean and Wade (1993), Annapolis G-24 well report (Archibald 2002), Panuke F-09 well report (Pan Canadian 2000), Shubenacadie H-100 well report (Sine et al. 1983), Moheida well report (Thompson 1977), and Oneida 0-25 well report (Shell Canada Ltd. 1970).

The Dalhousie Salt Dynamics Group extrapolated the picks of Ings and Shimeld (2006) onto NovaSPAN line 5100 from which we carried them southwest into our study area. Seismic horizons were carried through the salt diapiric sub-province while maintaining consistency between the well constraints on the Scotian Shelf and Upper Slope with the stratigraphy proposed by Ebinger and Tucholke (1988) in the deeper water basin.

4.2 Building 3D Thermal Models

Model building is an involved process and the success of the model is directly dependant on the input parameters and constraints used during model configuration. When modelling the evolution of a specific region the model geometries, lithologies, stratigraphy, structures, distribution and timing of emplacement of salt structures and thermal properties including the heat flow history, Paleo Water Depth (PWD) and Sediment Water Interface Temperatures (SWIT) through time must be defined. Once all model geometries and parameters have been set a simulation is run to predict the regions thermal evolution and structure through time and the present day hydrocarbon maturation potential.

4.2.1 Defining the Area of Interest

The original goal for modelling was to model a large portion of the central Scotian Slope bounded by 2D seismic lines 1400, 5100, 1600 and 5300 of the ION-GXT NovaSPAN survey (Fig. 4.1). This would have a allowed us to model seafloor heat flow along all three of our primary heat flow transects (1400, 88-1A and 1600) and determine if any lateral variations in maturation potential existed throughout the central Scotian Slope. The TGS Nopec 2D NS-100 seismic survey covers the majority of the central Scotian Slope with an 8 km line spacing, sufficient for our analysis. To date only the first

phase of the NS-100 seismic data was released and only released as paper copies. We therefore did not have the required seismic control to produce a 3D model across the entire region. Available paper copy data spanned from just west of Lithoprobe line 88-1A in the eastward direction beyond NovaSPAN line 1600. The process of converting analogue data to digital SEG Y format was too time consuming for us to convert all the data required to model the whole eastern region of the study area and thus we were forced to choose between modelling line 88-1A or 1600. Seafloor heat flow data coverage was better on line 88-1A and along this line we also have constraints on crustal thicknesses after Wu (2007). Therefore, we decided to model the region surrounding Lithoprobe line 88-1A.

We hoped to model the region defined by 12 2D seismic lines from the TGS-Nopec NS-100 survey surrounding Lithoprobe line 88-1A that we loaded into our seismic database (Fig. 4.2). Unfortunately, due to computational restrictions the modelling area had to be further reduced to the region within ~3 km of Lithoprobe line 88-1A (Fig. 4.2). We still constrain the distribution of salt structures in 3D around line 88-1A using the TGS-Nopec 2D seismic data, however, the model is laterally restricted to a width of ~6 km. The model still accounts for the effects of 3D variations in salt geometry on heat flow despite the significantly smaller modelled area.

4.2.2 Defining Stratigraphy

The first stage of model building involves defining and importing stratigraphic surfaces. These are produced by gridding horizons from our 2D seismic interpretations described in Section 4.1. Once a uniform horizon has been picked throughout the study area, continuous 3D surfaces are created using the "Flex Gridding" algorithm of

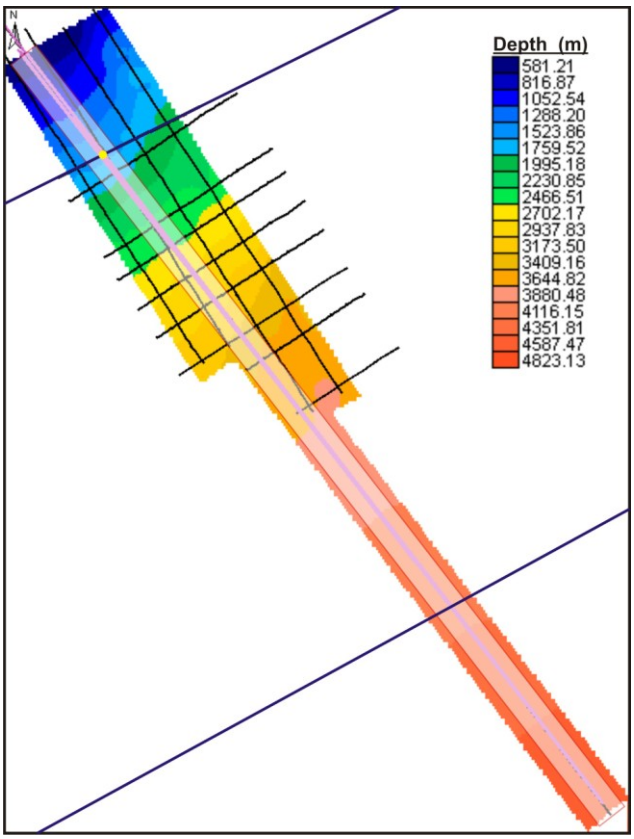

Figure 4. 2: Model study area before resizing (entire colored background) and after refining the area of interest (transparent white rectangle). 2D seismic lines of the NovaSPAN survey are shown in blue, of the TGS-Nopec survey in black, and Lithoprobe line 88-1A is shown in pink. Shubenacadie H-100 well is shown as a yellow circle.

Kingdom Suite 8.3® software. All horizons present in Table 4.1, with the exception of salt, were gridded and imported into PetroMod® to define the basic stratigraphic framework of the 3D model. Accurate gridding of salt bodies was not possible as the gridding algorithm simply smoothes surfaces between horizons defined in 2D seismic interpretations. As salt is distributed in a series of laterally restricted diapirs and canopies which cut across the other more continuous strata, gridding of salt horizons is not possible at the resolution of our 2D seismic data. Salt bodies must later be input manually as described in Section 4.3.4.

When 2D horizons are gridded and interpolated to create 3D surfaces some surfaces cut across others as a result of the gridding algorithm and the 2D horizon

geometries and we must correct for these cross cutting layers. The space between two surfaces is referred to as a layer in PetroMod®. When correcting for cross cutting layers we give precedence to the overlying layer. A layer thickness table governs the thickness of each layer and in this table, cross cutting layers are represented by negative values. To correct for cross cutting geometries we simply assign the negative values a thickness of zero, resulting in thickening of the overlying layer (Fig. 4.3). Although an obvious error in interpolation, this correction is the simplest and most geologically reasonable as in our passive continental margin we are more likely to see erosion from above than intrusion from below, with the exception of salt emplacement.

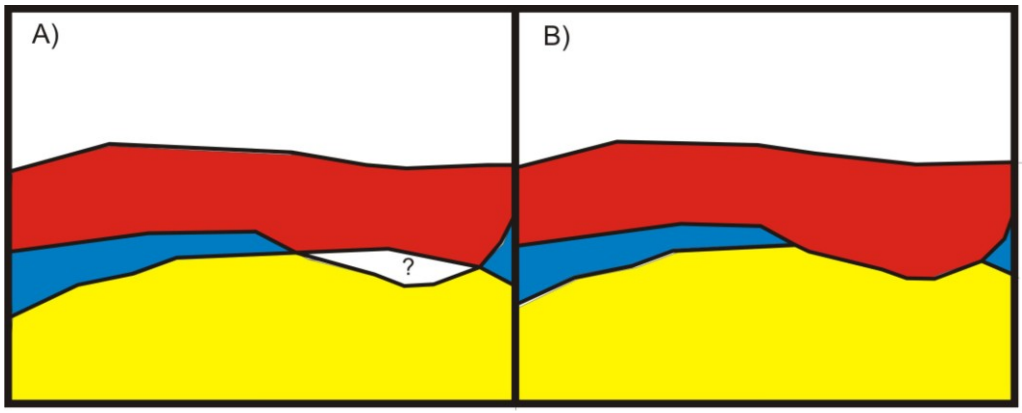

Figure 4. 3: Visual representation of correction for cross cutting layers showing A) layers prior to correction and B) layers post correction.

4.2.3 Assigning Ages and Splitting Layers

Once all layers have been defined in the model, depositional ages must be assigned to the associated layers. This is done by assigning a depositional period to the layer between two surfaces. The surfaces imported into PetroMod® represent the top boundary of geologic units after formation top picks from Scotian Basin wells. Layers are assigned a depositional period corresponding to the time defined by the ages of the two bounding surfaces.

As not all major stratigraphic boundaries were associated with prominent reflectors in the seismic images, some major stratigraphic units are not represented in the 3D model. To add missing geological units to the 3D model some layers were split. Some particularly thick layers were also split to assist in the later addition of salt bodies (Section 4.2.4). Salt bodies are input by assigning a region of a layer an age at which it is pierced and replaced by salt. The more layers present and the thinner the layers the greater the ability for vertical variation in salt geometry and the more accurate and less blocky the appearance of salt diapirs will be. All layers present in the model and their associated depositional periods following layer splitting are included in Table 4.2.

Layers were split giving layer thicknesses proportionate to the thicknesses reported in surrounding wells (e.g. Torbrook C-15, Shubenacadie H-100, Acadia K-62) or literature where well data were not available (Jansa and Wade 1975, Wade and MacLean 1990). In total, six of the initial eleven input layers were split into fifteen new layers, yielding a total of twenty layers in the model. The lowermost Banquereau layer bounded by the Wyandot and Top Eocene surfaces was split into Paleocene (50%) and Eocene (50%) layers of the Banquereau Formation. The Logan Canyon to Wyandot layer was split into the Dawson Canyon (90%) and Wyandot (10%) Formations. The Logan Canyon Formation was subdivided into five layers referred to as Logan Canyon layers 1-5 from bottom up. Layers 1, 2 and 5 were assigned 25% thickness each, while layer 3, representative of a channel, was given a thickness of 2.5%, and layer 4 acquired the remaining 22.5%. The Missisauga Formation was split into an upper and lower member each inheriting 50% of the previous strata. The Top Abenaki to Top Scatarie layer was split into the Baccaro (80%) and Misane (20%) Member equivalents. Finally, the Scatarie

to Basement/Salt layer was split into the Scatarie Member (20%) and Mohican Formation (80%).

Layer Name	Dep. From (Ma)	Dep. To (Ma)
Recent	1.6	0
M_Mio_to_M_Plio	16.6	1.6
T_Eocene_to_M_Mio	36.6	16.6
E_Eocene_T_Eocene	51.5	36.6
Paleocene_E_Eocene	66.4	51.5
Wyandot	84	66.4
Dawson_Canyon	97.5	84
Logan_Canyon_Top_5	102.88	97.5
Logan_Canyon_4	107.71	102.88
Logan_Canyon_3_Channel	108.25	107.71
Logan_Canyon_2	113.62	108.25
Logan_Canyon_Bot_1	119	113.62
Missisauga_Top	131	119
Missisauga_Bot	144	131
Baccaro_Low_VC	160	144
Misane	169	160
Scatarie_Eq	176	169
Mohican	198	176
Salt	208	198
Basement	209	208

Table 4. 1: Stratigraphic layers and their associated depositional ages (age assignment table).

4.2.4 Inputting Salt Bodies

Salt bodies must be defined manually in the models. Due to the anomalous shape and cross cutting relationships between salt and stratigraphy we were unable to produce an accurate gridded salt surface. To determine the locations of salt bodies, all available seismic data from the study area were interpreted for top and bottom salt (Appendix H). The addition of the 12 lines of the TGS Nopec NS-100 survey in the region surrounding Lithoprobe line 88-1A were essential in constraining salt distribution, both in lateral and vertical extent, as they provide further constraints on the 3D salt geometry.

Unfortunately, the 8 km line spacing of the TGS-Nopec NS-100 survey is not dense enough to determine the exact lateral distribution of salt bodies and they must therefore be inferred between lines. When defining location and distribution of salt bodies we looked to identify which salt bodies appeared in consecutive seismic lines and which salt bodies were laterally restricted and isolated. Salt bodies that could be seen in

consecutive lines were interpreted as continuous salt walls, while isolated bodies seen in only one line were inferred as single, laterally restricted, diapirs. Although the exact extent of salt bodies between seismic lines remains unknown, we were able to infer lateral distribution and continuity of salt bodies from our ~8 km line spacing grid of 2D seismic lines. Figure 4.4 shows surface views of our extended study area at four stratigraphic levels showing the distribution of salt bodies after our seismic interpretations.

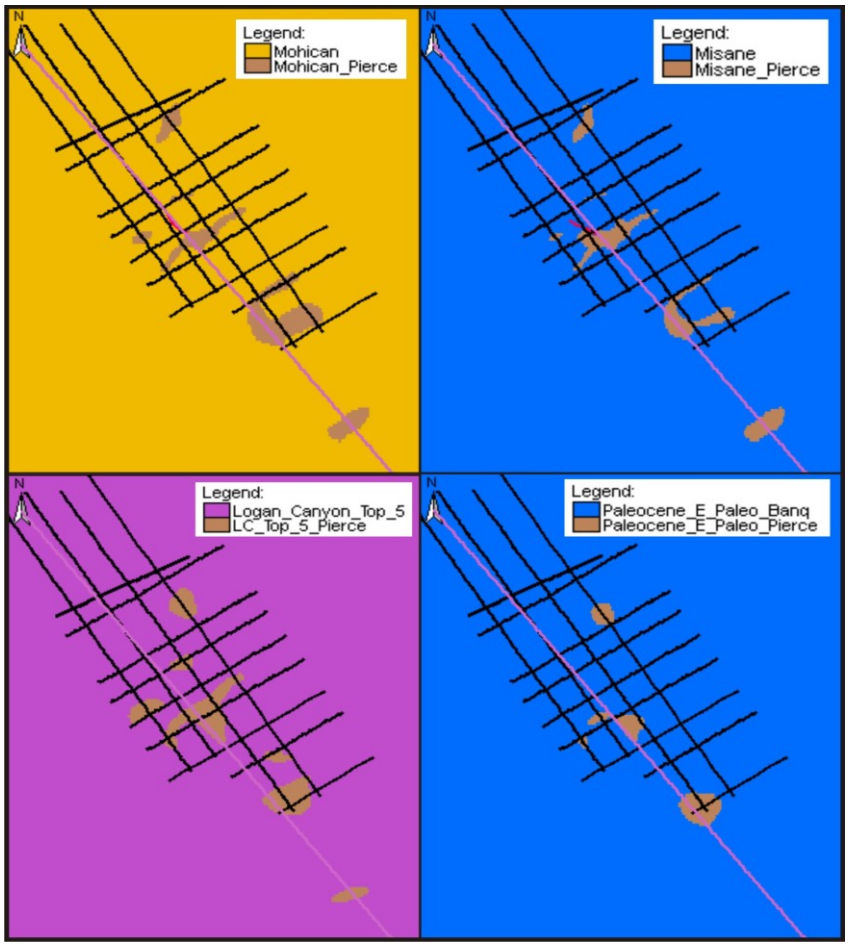

Figure 4. 4: Surface view of different layers in 3D model showing location of salt diapirs (brown) at different stratigraphic levels. Facies colors correspond to Table 4.3, black lines are TGS Nopec Lines and purple line is Lithoprobe line 88-1A.

To input salt diapirs we use a combination of the "facies assignment" and "piercing" tools included in the PetroMod 11® software package. We define both the

lateral and vertical distribution of salt bodies using the "facies assignment" tool and the timing of emplacement using the "piercing" tool. We assume that salt movement keeps pace with sedimentation (Fig. 4.5) (Section 2.4.1). The facies assignment tool allows for lateral variations in facies in a particular layer. In the model structure, each layer consists of a simple grid where each cell is assigned a particular facies and thickness. To define the salt geometry we draw the distribution of salt as interpreted in our 2D seismic images on the surface view of a layer pierced by the salt (Fig. 4.4). We rename all cells that are to be replaced with salt from "Layer_Name" to "Layer_Name_pierced". The "Layer_Name_Pierced" facies is assigned the same lithology as the rest of the layer; however, this lithology will later be replaced with salt using the "piercing" tool. This is done for each layer pierced by salt. Certain layers which are particularly thick such as the Logan Canyon Formation layer have been split into multiple thinner layers as discussed

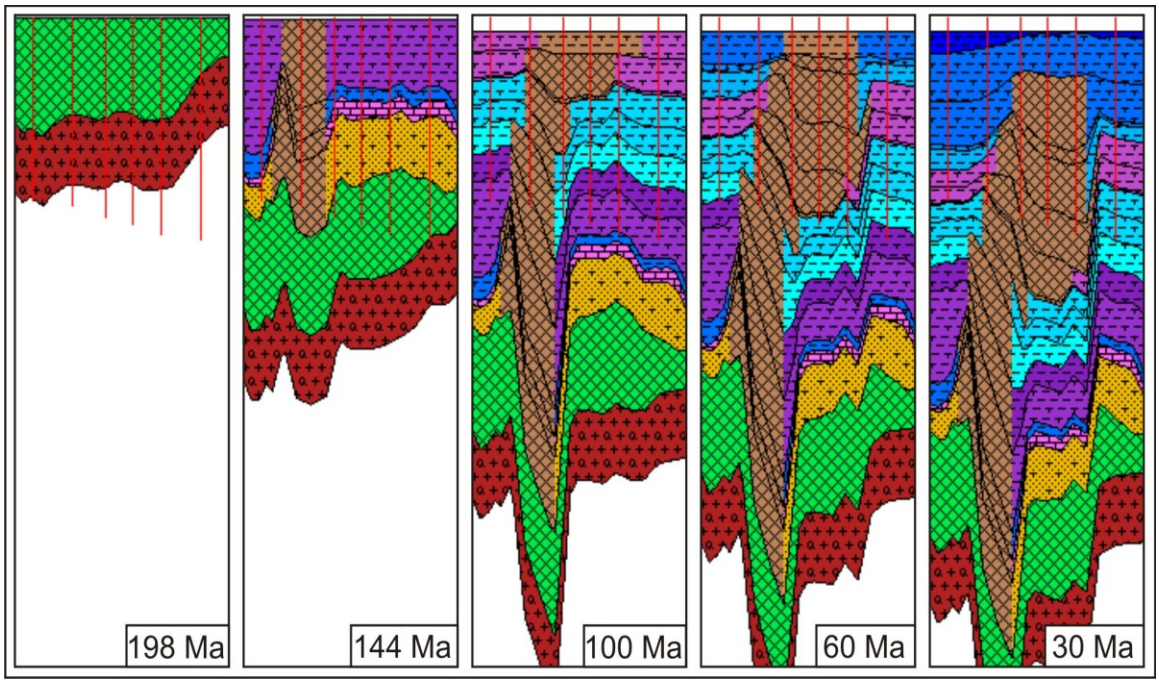

Figure 4. 5: Evolution of salt diapir D5 through time. Green represents salt remaining in the original salt basin and brown represents salt which has pierced overlying strata. All other colors are representative of facies in the model as shown in Table 4.3. Vertical red lines show locations of seafloor heat flow stations HF204-209 from left to right.

previously (Section 4.3.4) to allow for more accurate vertical variations in salt geometries as over large vertical intervals salt distribution can change dramatically.

Once all layers cut by salt have the salt geometry picked as the "Layer_Name_Pierced" facies we must then define the timing that the layers are pierced by salt. As we have accepted that the salt piercing roughly keeps pace with sedimentation, the timing of salt piercing will simply be the timing of deposition of the layers. This is specified in the salt piercing table (Tab. 4.3) and simply tells the model to replace the "Layer_Name_Pierce" facies with salt at the time specified in the table.

Geologic Facies	Piece Time (Ma)	Pierce Lithology
Mohican_Pierce	176	Eric_Salt
Scat_Pierce	169	Eric_Salt
Misane_Pierce	160	Eric_Salt
Baccaro_VC_Pierce	144	Eric_Salt
Low_Miss_Pierce	131	Eric_Salt
Upper_Miss_Pierce	119	Eric_Salt
LC_B_1_Pierce	113.62	Eric_Salt
LC_2_Pierce	108.5	Eric_Salt
LC_3_Pierce	102.88	Eric_Salt
LC_Top_5_Pierce	97.5	Eric_Salt
Dawson_Canyon_Pierce	84	Eric_Salt
Wyandot_Pierce	66.4	Eric_Salt
Paleocene_E_Paleo_Pierce	51.5	Eric_Salt

Table 4. 2: Salt piercing table defining timing of salt emplacement.

4.2.5 Defining Lithologies

Once the general stratigraphy has been defined and the layers have been assigned their proper depositional ages, lithologies must be assigned. PetroMod® has a database of general lithologies which can be assigned to layers. In addition, the "Litho Editor" tool can be used to modify and mix existing lithologies, or to create entirely new ones with the physical properties of the modelled layers. Lithological properties which can be edited include thermal conductivity, radiogenic heat production, heat capacity,

mechanical and chemical compaction, permeability, seal properties and fracturing. In our models we used a combination of original unmodified lithologies from the PetroMod® database and new mixed lithologies created from the existing PetroMod® lithologies in an attempt to better match Scotian Basin lithologies. Lithologies and their associated layers are included in Table 4.4.

Facies	Color	PSE	Lithology	TOC Value (%)	Kinetics	HI Value (mgHC/gTOC)
Recent Seds		none	Eric_Shale_lowRGH	0	none	0
Upper_Banq_M_Plio		none	Eric_Shale_lowRGH	0	none	0
Middle Banq_M_Mio		none	Eric_Shale_lowRGH	0	none	0
Eocene_E_Paleo_Pierce		none	Eric_Shale_lowRGH	0	none	0
Eocene_E_Paleo_Banq		none	Eric_Shale_lowRGH	0	none	0
Paleocene_E_Paleo_Pierce		Source Rock	Eric_Banq_Shale_Chalk	3	none	300
Paleocene_E_Paleo_Banq		Source Rock	Eric_Banq_Shale_Chalk	3	none	300
Wyandot_Pierce		none	Chalk (typical)	0	none	0
Wyandot		none	Chalk (typical)	0	none	0
Dawson_Canyon_Pierce		none	Eric_Shale_lowRGH	0	none	0
Dawson_C		none	Eric_Shale_lowRGH	0	none	0
LC_Top_5_Pierce		none	Eric_Shale_lowRGH	0	none	0
Logan_Canyon_Top_5		none	Eric_Shale_lowRGH	0	none	0
LC_4_Pierce		none	Eric_Shale_lowRGH	0	none	0
Logan_Canyon_4		Seal Rock	Eric_Shale_lowRGH	0	none	0
LC_3_Channel		Reservoir Rock	Sandstone (quartzite, typical)	0	none	0
LC_3_Pierce		Source Rock	Eric_VC_organic	4.5	Weymouth_CVC	500
Logan_Canyon_3		Source Rock	Eric_VC_organic	4.5	Weymouth_CVC	500
LC_2_Pierce		none	Eric_Shale_lowRGH	0	none	0
Logan_Canyon_2		none	Eric_Shale_lowRGH	0	none	0
LC_B_1_Pierce		none	Eric_Shale_lowRGH	0	none	0
Logan_Canyon_B_1		none	Eric_Shale_lowRGH	0	none	0
Upper_Miss_Pierce		none	Eric_Shale_lowRGH	0	none	0
Upper Miss		none	Eric_Shale_lowRGH	0	none	0
Low_Miss_Pierce		Source Rock	Eric_VC_organic	4.5	Weymouth_CVC	500
Lower_Miss		Source Rock	Eric_VC_organic	4.5	Weymouth_CVC	500
Baccaro_VC_Pierce		Source Rock	Eric_VC_organic	6	Alma_JVC	600
Baccaro_VC		Source Rock	Eric_VC_organic	6	Alma_JVC	600
Misane_Pierce		Source Rock	Shale (organic rich, 3% TOC)	2.5	Misaine	250
Misane		Source Rock	Shale (organic rich, 3% TOC)	2.5	Misaine	250
Scat_Pierce		none	Eric_Scatarie	0	none	0
Scat_Eq		none	Eric_Scatarie	0	none	0
Mohican_Pierce		Source Rock	Eric_Mohican	2.5	Mohican	250
Mohican		Source Rock	Eric_Mohican	2.5	Mohican	250
Salt		none	Eric_Salt	0	none	0
Uniform_Basement		none	Eric_Basement	0	none	0

Table 4. 3: Facies definition table. PSE=Petroleum Systems Elements; TOC=Total Organic Carbon; HI=Hydrogen Index.

A small section of reservoir rock was included in the central Logan Canyon Formation in the form of a sandy channel body. The overlying shales of the upper Logan Canyon Formation were included as a seal rock in order to create the required trap for

hydrocarbons. This reservoir/trap configuration is arbitrary and was included only to test if existing traps would become filled with hydrocarbons. As a result of our decreased study area size the channel sand body has been reduced to a negligibly small volume. As few wells penetrate the central Scotian Slope, constraining PSE in the deep water regions is very difficult.

Only three lithologies from the PetroMod® database have been used without modification. These are the "Chalk (typical)", "Sandstone (quartzite, typical)" and the "Shale (organic rich, 3% TOC)" lithologies assigned to the Wyandot Formation, the Logan Canyon channel sands and the Misane Member respectively. Much of the Scotian Slope is inferred to be dominantly shale, with minor siltstone and carbonates.

- The "Eric_Shale_lowRGH" lithology was produced by mixing the "Shale (typical)" (94%), "Siltstone (organic lean)" (5%) and "Marl" (1%) lithologies. This predominantly shale lithology was assigned to much of the Scotian Slope sediment pile as the deep water equivalents to shelf lithologies are inferred to shale out with increasing water depth.
- The "Eric_Banq_Shale_Chalk" lithology was created for the more chalk rich portions of the lower Banquereau Formation, which, in the Acadia K-62 core, showed higher chalk content than the shallower Banquereau layers. This lithology consists of "Shale (organic rich, 3% TOC)" (95%) and "Chalk (Typical)" (5%).
- The "Eric_VC_organic" lithology was assigned to all source rocks of the Verrill Canyon Formation and consists of "Shale (organic rich, 3% TOC)" (87%), "Sandstone (typical)" (5%) and "Siltstone (organic rich, typical)" (8%).

- The Scatarie equivalents were assigned a lithology comprised of "Limestone (ooid grainstone)" (40%), "Limestone (micrite)" (15%), "Sandstone (quartzite, typical)" (10%) and "Shale (typical)" (35%).
- The "Eric_Mohican" lithology was composed of "Dolomite (typical)" (15%), "Sandstone (subarkose, dolomite rich) " (60%), "Shale (organic rich, 3% TOC)" (20%), and "Siltstone (organic rich, typical)" (2%).
- The "Eric_Salt" lithology is representative of the Argo Formation salt. This Lithology consisted of "Salt" (90%), "Anhydrite" (5%) and "Shale (organic lean, typical)" (5%). The thermal conductivity of the salt was assigned a value of 6.07 WmK^{-1} at 20 °C as a high end member to yield the maximum effects of salt on heat flow.
- The "Eric_Basement" lithology was assigned for the Meguma Group basement rocks inferred to underlie the study area and consisted of "Granite (500 Ma old)" (34%), "Slate" (33%) and "Quartzite" (33%). The radiogenic heat production in the basement concentrations of radiogenic heat producing elements of U=2.65 ppm, Th=9.79 ppm, and K=3.21 % were assigned.

4.2.6 Assigning Petroleum System Elements

In addition to ages and lithologies, Petroleum Systems Elements (PSE) had to be assigned to layers in the models. PSE include source rocks, reservoir rocks, and seal rocks, and are included in Table 4.3. As we are concerned primarily with determining the thermal structure and the seafloor heat flow across the central Scotian Slope defining accurately all PSE is not crucial to the success of our models. However, as determining the thermal maturation of source rocks within the study area is one of our goals, source

rock layers must be assigned. As few wells cut deep into the Scotian Slope strata, source rock intervals and properties are poorly defined. It has been inferred that the Late Jurassic, Kimmeridgian shales of the Verrill Canyon Formation are likely important source rocks for the Scotian Basin (Enachescu et al. 2010). Additional source rock intervals were assigned throughout the Early Cretaceous Verrill Canyon Formation and in the lowermost Banquereau Formation following after the work of Mukhopadhyay (2008, 2010).

4.2.7 Assigning Source Rocks and Kinetics

As the type of organic matter and kinetic reactions defined for the source rocks has direct implications on the type and volumes of hydrocarbons produced upon transformation we discuss briefly the source rocks and properties defined in our models. Within the Scotian Basin it is the Late Jurassic and Early Cretaceous portions of the distal Verrill Canyon Formation which have been inferred to contain prolific source rocks of the Scotian Margin. Mukhopadhyay (2006) has analyzed the source rock properties and kinetics of Scotian Basin source rocks from the Alma K-85 (Late Jurassic Verrill Canyon), Annapolis G-24 and Weymouth A-45 (Early Cretaceous Verrill Canyon) wells using a combination of vitrinite reflectance, Rock-Eval pyrolysis, total organic carbon (TOC) and multi-component kinetics analysis. The source rocks are comprised of mixed oil/gas prone type II-III kerogen.

Mukhophadhyay (2008) has defined source rock properties and kinetics for the Late Jurassic and Early Cretaceous Verrill Canyon Formation in PetroMod models after the work of Mukhopadhyay (2006) and these same properties were assigned in our models. The Alma_JVC source rock was defined after analysis of the Jurassic source

rocks from the Alma K-85 well while the Weymouth_CVC was defined after analysis of the Cretaceous interval of the Weymouth A-45 well. Kinetics and source rocks were defined for the Misane equivalents after Mukhopadhyay (1995, 2006) and the Mohican source rock properties were derived from the PetroMod kinetics database for Early Jurassic source rocks as little data was available from the Scotian Basin on this deeply buried interval.

4.3 Defining Thermal Boundary Conditions

Once the geologic framework has been defined in the models, the boundary conditions and thermal parameters must be set. Boundary conditions to be defined in the models include the heat flow history, Paleo Water Depth (PWD), and Sediment Water Interface Temperature (SWIT). These parameters, in particular the heat flow history, are what determine the thermal evolution and structure of the model.

4.3.1 Defining SWIT and PWD

SWIT is calculated using the "AutoSWIT" function of PetroMod 11® after Wrygala (1989). For our study area we assigned the SWIT for North America at Latitude 42°. The given SWIT curve is shown in Figure 4.7. The assigned SWIT was not changed between model runs. PWD was defined after the work of Mukhopadhyay (2008, 2010). Water depths increase from ~0 m at the onset of rifting to ~500 m at present day (Fig. 4.6). We have assigned only one PWD trend for the entire study area which is an oversimplification as we know water depth varies across the slope. The water depth defined corresponds to the uppermost portions of the central Scotian Slope. This will slightly overpredict temperatures at the model surface as with greater water depths come cooler temperatures.

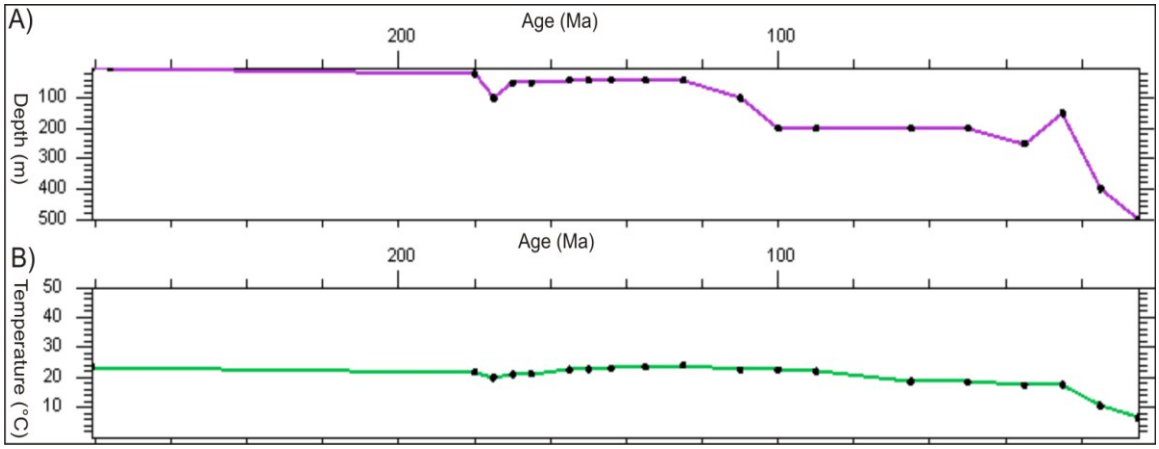

Figure 4. 6: Boundary condition plots showing A) Paleo Water Depth (PWD) showing Depth vs. Age and B) Sediment Water Interface Temperature (SWIT) showing Temperature vs. Age.

4.3.2 Defining Heat Flow History

Defining heat flow history for the study area is very important to our models as the thermal evolution of the region is directly related to the heat flow history. We have tried to model the basal heat flux history across the central Scotian Slope in Section 3.5 using a combination of simple lithospheric rift models constrained by crustal stretching factors and measured, sediment/salt corrected, seafloor heat flow data. These models suggest that the basal heat flux history is largely affected by the initial lithospheric thickness and that the present day basal heat flux is no longer significantly affected by variations in crustal stretching factors. As varying crustal stretching factors will have implications on the heat flow history through time, varying heat flow histories must be defined across the margin associated with variations in crustal stretching factors.

Four separate heat flow histories have been defined to test the effects of varying basal heat flux on the thermal structure of the study area through time and on present day seafloor heat flow. The first heat flow history does not account for variations in basal heat flux across the transitional crust, and has a uniform basal heat flux constrained by temperature and vitrinite reflectance data from the Shubenacadie H-100 well. The second

and third basal heat fluxes defined do account for variations in basal heat flux associated with varying crustal stretching factors (β) across the central Scotian Slope as described in Section 3.5. Basal heat flux in both of these models are calculated from the McKenzie uniform stretching model. The difference between these models is the initial lithospheric thicknesses of A=100 km and A=125 km assumed in the McKenzie heat flow equations after Lithospheric Models 2 and 1 respectively. Finally a fourth heat flux history is defined after the dual stretching model of Royden and Keen (1980). This heat flux history accounts for variations in both β and δ across the margin to determine if adding a component of sub-crustal stretching will have notable effects on hydrocarbon maturation or seafloor heat flow.

All models run contain the same stratigraphy, structure and salt geometries. Layer thicknesses, salt distribution and age of emplacement, depositional ages and PSE do not vary from one model to another. PWD and SWIT also remain identical between models. Changes between models are confined strictly to variations in the basal heat flux history (3D Models 1-3, 5) and the crustal thickness and concentrations of radiogenic heat producing elements within the crust (3D Model 4). The descriptions of the models below describe the basal heat flux tested, the rationale for running the model and the model output.

4.5 3D Thermal Models

As PetroMod 3D models are dynamic, bottom up models, they inherently account for the effects of salt movement, high thermal conductivity salt and influx of cold sediments on seafloor heat flow. Therefore we are able to make direct comparisons between our measured and modelled data. In our earlier lithospheric models corrections

to seafloor heat flow data were required to remove the affects of the sediment pile on seafloor heat flow. In addition to accounting for the thermal affects of the sediment pile on heat flow the 3D models also account for radiogenic heat production in both the sediment pile and basement, which is ignored in our earlier 2D models.

As mentioned previously, the only parameters that change between model runs are basal heat flux, crustal thickness, or radiogenic heat production in the basement and sediment columns. The parameters defined for each model are as follows:

3D Model 1:

- Constant basal heat flux across the entire model (no increase with crustal stretching)
- Heat flux history constrained using A=100 km (Lithospheric Model 2) and β=2.01
- Radiogenic heating throughout the sediment column, uniform radiogenic heat input from the basement across the model

3D Model 2:

- Varying basal heat flux across the model associated with increasing crustal thinning
- Heat flux history constrained using A=100 km (Lithospheric Model 2) and varying β with offset after Wu (2007)
- Radiogenic heating throughout the sediment column, uniform radiogenic heat input from the basement across the model

3D Model 3:

- Identical to Model 2 however basal heat flux is constrained using a thicker lithospheric thickness (A=125 km) after Lithospheric Model 1

3D Model 4 (a and b):

- Identical basal heat flux history as 3D Model 3

- Addition of increasing radiogenic heat production in the basement layer in the landward direction to account for increasing crustal thickness not included in the model setup
- 3D Model 4a maintained original basement thickness of 1 km, 3D Model 4b increased basement thickness to 3 km, thus increased radiogenic heat production

3D Model 5:

- Basal heat flux calculated with varying crustal (β) and lithospheric (δ) stretching factors
- Varying radiogenic heat production in the basement layer as in 3D Model 4a

4.5.1 3D Model 1 Heat Flux

The first basal heat flux history, constraining 3D Model 1, was defined using limited vitrinite reflectance (%Ro) and temperature data from the Shubenacadie H-100 well. This is the only well located within the modelled area and with the exception of our recent seafloor heat flow data, provides the only available thermal data in the study area. In this model we applied thermal constraints exclusively from the Shubenacadie H-100 well to determine what thermal structure, present day seafloor heat flow and maturation potential our 3D models would predict in the absence of constraints from our seafloor heat flow data.

Vitrinite reflectance analysis was conducted by Avery (1999). In total, ten vitrinite samples were analyzed for reflectance from depths between 2130 m to 4050 m

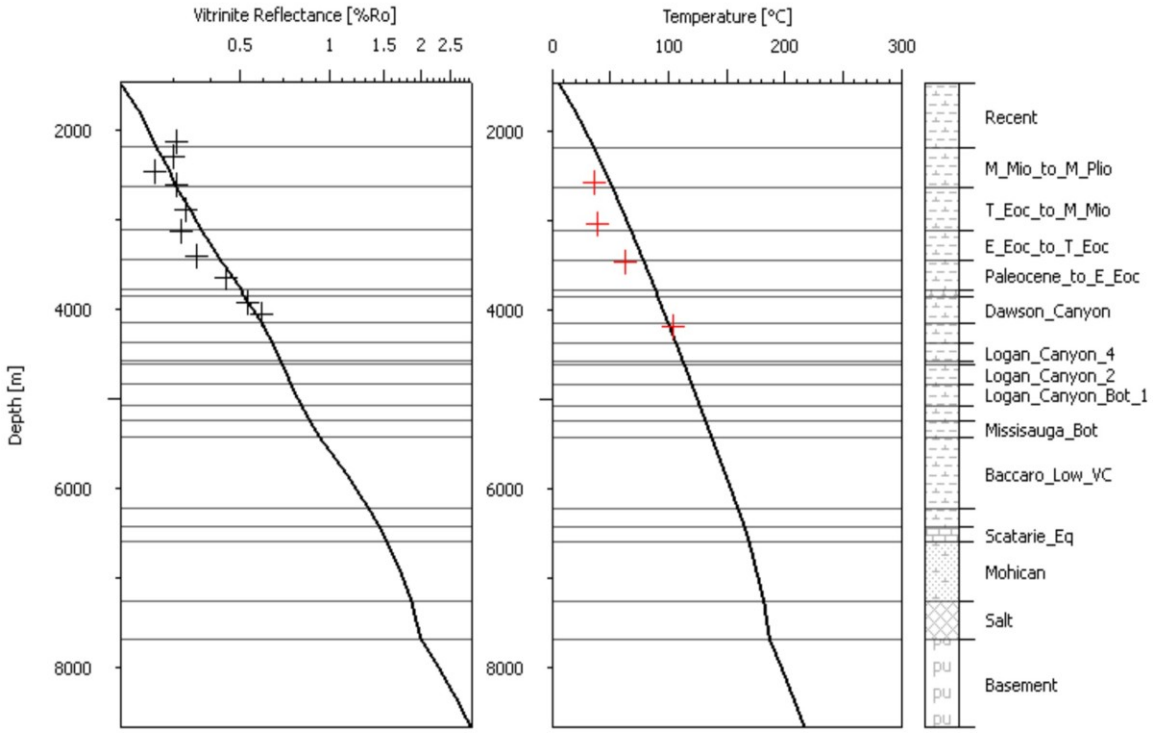

Figure 4. 7: %Ro (black) and Temperature (red) vs. Depth plots showing fit of modelled values (black lines) to measured well data (black and red crosses respectively) with heat flow history constrained after Lithospheric Model 2 (A=100 km) and β=2.01.

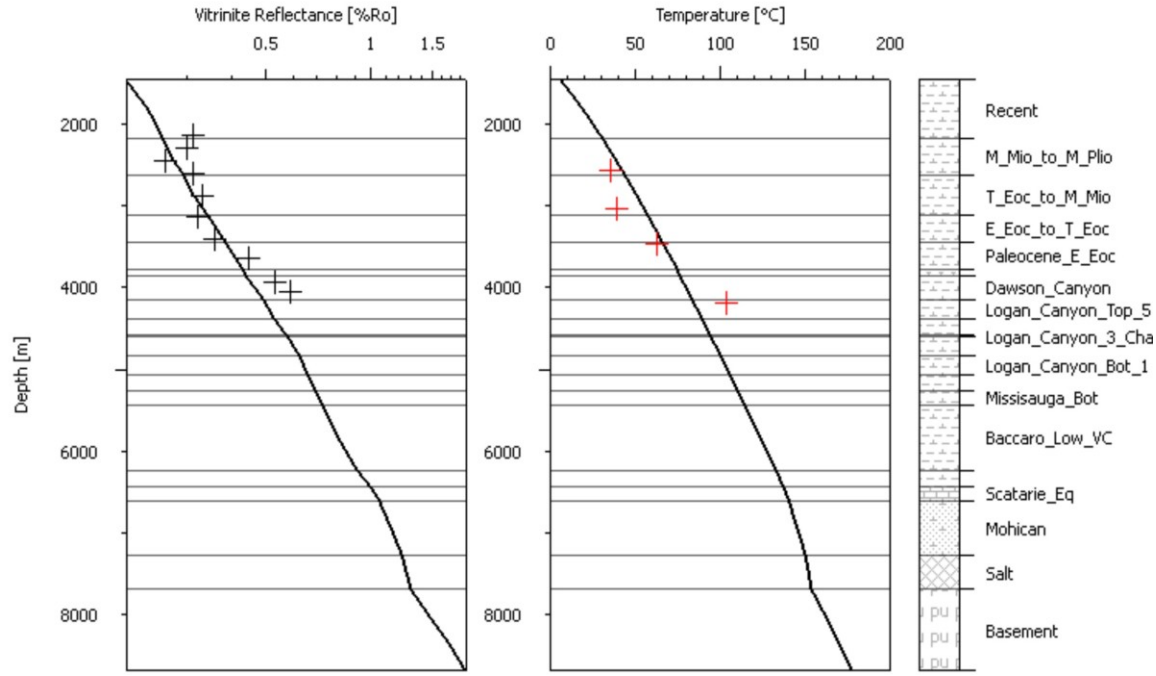

Figure 4. 8: %Ro (black) and Temperature (red) vs. Depth plots showing fit of modelled values (black lines) to measured well data (black and red crosses respectively) with heat flow history constrained after Lithospheric Model 1 (A=125 km) and β=2.01.

(Fig. 4.7, Fig. 4.8). The uppermost eight vitrinite samples suggest the shallow organic material is under mature, while the deepest two samples suggest maturation within the oil producing zone. In addition to the vitrinite reflectance data, four temperature data points were also acquired from the Shubenacadie H-100 well (Fig. 4.7, Fig. 4.8). Horner corrections (Zetaware 2003) were applied to the temperature data using circulation times acquired from the Shubenacadie H-100 well report (Sine et al. 1983). The goal was to determine if the measured well data (both temperature and %Ro) could be matched using the uniform stretching pure shear heat flow model with the stretching factor of β=2.01 (Wu 2007) corresponding to crustal thickness at the Shubenacadie H-100 well.

To define a basal heat flux history in our 3D models that would match temperatures and maturation data from the Shubenacadie H-100 well a simple 1D model was run. The 1D model was defined by extracting layer thicknesses and lithologies from the 3D model at the location of the Shubenacadie H-100 well. The 1D model was run two times with heat flow histories constrained by Lithospheric Model 2 (A=100 km) (Fig. 4.7) and Lithospheric Model 1 (A=125 km) (Fig. 4.8). Neither of the 1D models matched the well data perfectly. The 1D models suggest that the basal heat flux history constrained after Lithospheric Model 2 yields a smaller RMS deviation between modelled and measured maturation data (0.10 and 0.16 for Lithoshperic Model 2 and 1 respectively) (Fig. 4.7). The temperature data predicted from Lithospheric Model 2 yielded slightly higher temperatures than the measured well data for all data points except the deepest. The basal heat flux constrained after Lithospheric Model 1 yielded slightly low values for maturation when compared with the well data, particularly for deeper data points (Fig. 4.8). When running our first 3D model we constrained the basal heat flux

history after our uniform shear Lithospheric Model 2 as this basal heat flux yielded a better fit to the measured maturation data while maintaining a good fit to the temperature data.

4.5.2 3D Model 1 Output

3D Model 1 has a basal heat flux history constrained after Lithospheric Model 2, which in our simple models excluded radiogenic heat production in the basement and sediment pile. However, Lithospheric Model 2 predicted a good fit to measured seafloor heat flow data despite the lack of heat input due to radiogenic heating. We expect that 3D Model 1, using a basal heat flux after Lithospheric Model 2, however including the effects of radiogenic heating on heat flux, should over-predict seafloor heat flow when compared to our measured data.

The output from 3D Model 1, as expected following our lithospheric modelling results, generally over-predicted the present day seafloor heat flow when compared to our measured data (Fig. 4.9). The model predicts basal heat fluxes of 50-55 mWm^{-2} at both the seaward and landward limits of the model with a slight increase in the seaward direction (Tab. 4.5). The modelled seafloor heat flow is ~10 mWm^{-2} higher than the measured data towards the seaward limit of the line (stations HF219-221), and ~7 mWm^{-2} higher than our measured data at station HF203 (Fig. 4.9). Modelled seafloor heat flow values are significantly higher than our measured heat flow at stations HF201-202, however, as discussed in Section 3.4.1 these data points record anomalously low gradients and are likely not representative of purely conductive heat transfer sourced from Earth's interior, and thus should be disregarded. We see very good agreement across the central regions of the model at stations HF209-210. There is a slight decrease in

seafloor heat flow towards the centre of the model between salt diapirs D5 and D6 where the predicted seafloor heat flow drops to ~47 mWm^{-2}. This decrease may be due to the conductive effects of the surrounding salt bodies, which preferentially transfer heat at a higher rate than the surrounding sediments, resulting in the observed depressed heat flow values adjacent to salt.

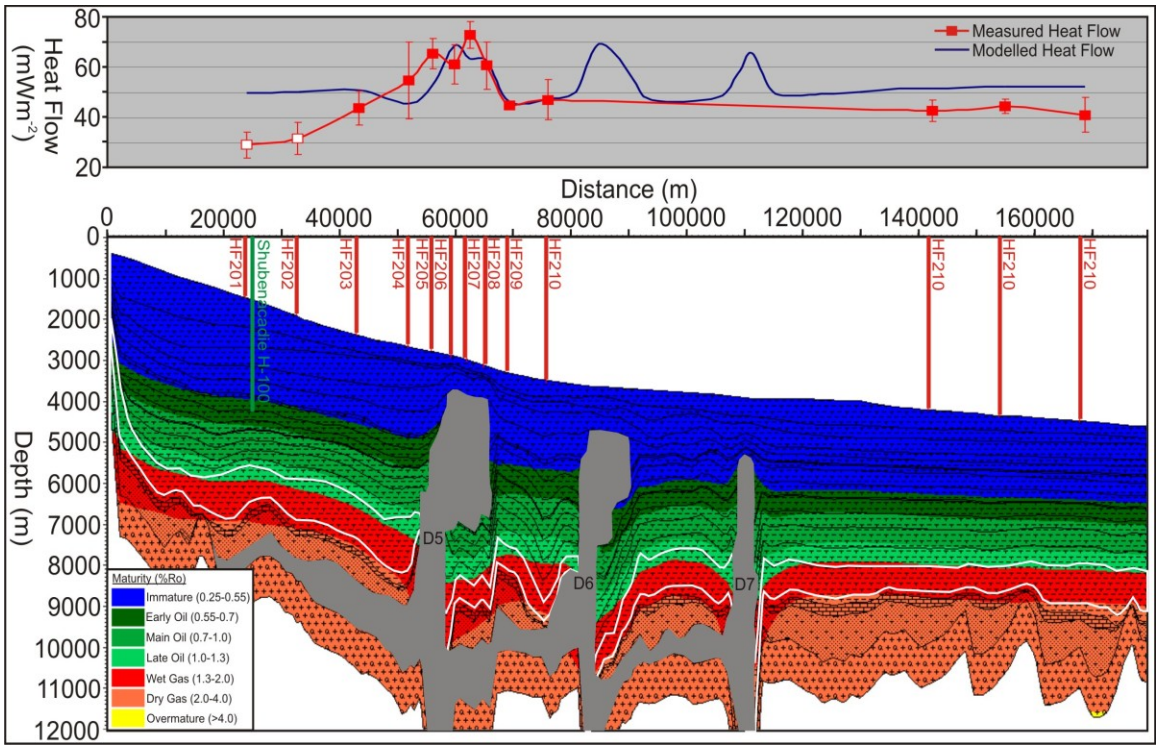

Figure 4. 9: Model output from 3D Model 1 showing depth to modelled maturation windows. Grey represents salt with diapirs labeled D5-D7. White line outlines the Baccaro equivalent Late Jurassic source rock interval. Shubenacadie H-100 well is shown in green and vertical red lines represent heat flow station locations. Plotted above the maturation window are the modelled (blue) and measured (red) seafloor heat flow curves across the study area. White filled squares represent stations which record anomalously low gradients.

The erratic increases in seafloor heat flow across the top of the most landward salt diapir (D5) observed in the measured data is not seen in the modelled data. The models suggest that the 3D conductive effects of salt alone cannot account for the drastic lateral variations in measured seafloor heat flow above the salt diapir. This suggests that as discussed in Section 3.4.1 there must be factors in addition to purely conductive heat transfer affecting the measured seafloor heat flow above the salt bodies. The modelled

increase in seafloor heat flow above salt diapirs D6 and D7 compared to surrounding background heat flow values are ~22 mWm^{-2} and ~18 mWm^{-2} respectively (Fig. 4.10). Unfortunately we have no measured data to compare with these predictions.

Heat Flow Station	Offset (m)		Seafloor Heat Flow (mWm^{-2})						
	88-1A	3D Model	Measured	Model 1	Model 2	Model 3	Model 4a	Model 4b	Model 5
HF201	34300	23901	29.1	49.7	49.73	41.81	43.55	49.38	44.08
HF202	43100	32701	31.7	50.34	50.56	42.37	43.85	49.34	44.29
HF203	53500	43101	43.9	50.86	51.34	42.93	43.99	48.68	44.32
HF204	62200	51801	54.7	45.56	46.17	38.56	39.73	43.3	39.39
HF205	66300	55901	65.5	53.09	53.87	44.98	45.58	50.89	45.77
HF206	70000	59601	61.3	68.73	69.77	58.27	58.99	65.92	59.22
HF207	72600	62201	72.8	63.26	64.23	53.58	54.15	60.01	54.34
HF208	75600	65201	60.7	62.52	63.54	53.02	53.48	58.57	53.65
HF209	79500	69101	44.9	46.16	46.79	39.16	39.24	42.07	39.5
HF210	86000	75601	47.1	47.49	48.38	40.32	40.43	43.19	40.5
	89493	79094		48.36	52.75	41.13	40.76	44.26	41.25
	91236	80837		51.77	61.88	46.68	44.08	47.55	44.14
	94499	84100		68.59	69.9	58.36	58.37	63.28	58.45
	97617	87218		64.99	66.26	54.91	55.22	59.6	55.29
	100399	90000		55.95	57.05	47.58	47.53	50.84	47.58
	103852	93453		47.05	47.95	40.08	40	42.07	39.73
	115103	104704		48.05	49.03	41.01	40.87	43.56	40.9
	118628	108229		57.68	58.85	49.14	48.95	53	48.98
	120932	110533		65.9	67.11	56.16	55.93	60.75	55.97
	124050	113651		51.81	52.88	44.09	43.92	47.11	43.95
	126399	116000		48.92	49.92	41.68	41.51	44.07	41.54
	130936	120537		48.99	49.95	41.97	41.61	43.63	41.63
	139638	129239		50.28	51.29	42.83	42.69	44.87	42.71
	146280	135881		51.75	52.85	44.11	43.99	46.56	44.02
HF219	152000	141601	42.6	51.71	52.68	43.97	43.94	46.79	43.98
HF220	164500	154101	44.5	52.38	53.3	44.43	44.51	47.78	44.58
HF221	178200	167801	41.1	52.24	53.28	44.34	44.38	47.29	44.41

Table 4. 4: Comparison between measured and modelled seafloor heat flow showing predicted present day seafloor heat flow as predicted from each 3D model run.

The 160-144 Ma Baccaro equivalent layer contains the Kimmeridgian source rock interval, which has been inferred as a prominent source rock for the Scotian Slope (Enachescu et al. 2010). The inferred Late Jurassic source rock interval lays mainly within the wet gas window (Fig. 4.9). Seaward of the salt diapiric sub-province, the source rocks lay almost entirely within the wet gas window. Across the salt diapiric province and landward of salt the source rocks are slightly less mature while remaining predominantly in the wet gas window. Here, roughly the upper quarter of the source rock interval is located in the late oil producing zone. As the modelled seafloor heat flow is significantly higher than the measured data in both the landward and seaward portions of

the line, it is likely that the basal heat flux defined is too high and that the model over predicting the hydrocarbon maturation. This suggests that future models using lower basal heat fluxes may be more oil than gas prone.

4.6.1 3D Model 2 Heat Flux

The basal heat flux history defined in 3D Model 2 was constrained by basal heat flux predictions after Lithospheric Model 2 (after the unifrom shear model of McKenzie 1978) with β factors constrained after Wu (2007). Well data were not factored into these basal heat flux calculations as we are attempting to deduce a method combining sea floor heat flow data with simple lithospheric models to constrain basal heat flux histories in regions lacking well data. While in 3D Model 1 a constant basal heat flux history was defined for the entire study area, 3D Model 2 accounts for lateral variations in basal heat flux associated with variations in crustal stretching factors (β) across the margin.

To account for variations in basal heat flux associated with variations in β across the margin 9 basal heat flux maps were created. Each map shows lateral variations in basal heat flux at a particular time step before present (Fig. 4.10). In the case of 3D Model 2 maps are constrained after Lithospheric Model 2 (A=100 km). A heat flow map for each of the following ages has been defined: 200 Ma, 190 Ma, 180 Ma, 165 Ma, 150 Ma, 125 Ma, 100 Ma, 50 Ma and 0 Ma. The maps show variations in basal heat flux at the corresponding age across the study area. Variations in basal heat flux with time are largest at small times following the onset of rifting, decreasing with time as the increased basal heat flux associated with the thinning of the lithosphere decays. Therefore, we have assigned a higher concentration map spacing at times closer to the rift event than at great times following rifting.

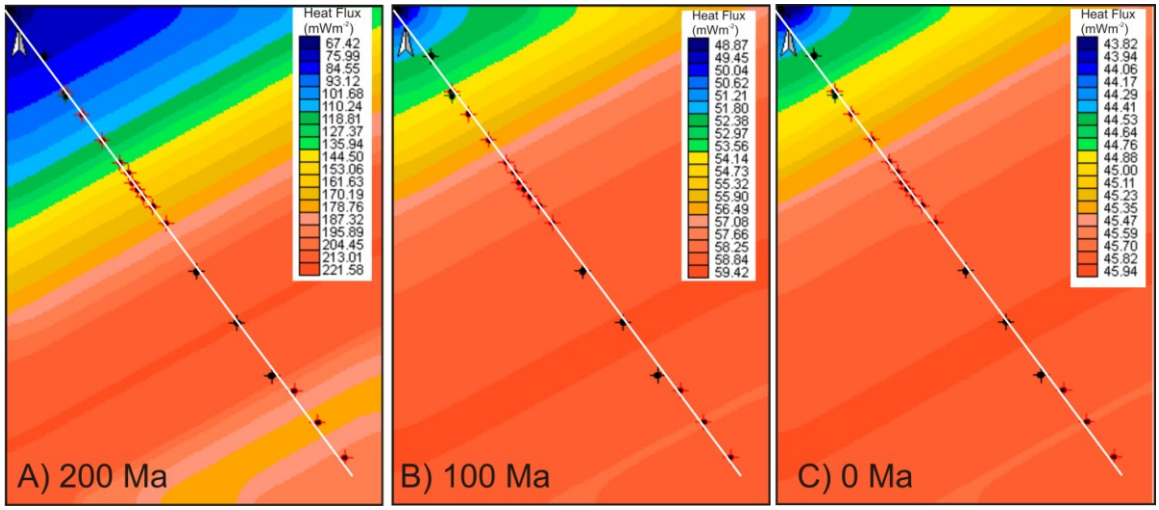

Figure 4. 10: Basal heat flux maps after Lithospheric Model 2 (A=100 km) for A) 200 Ma, B) 100 Ma and C) 0 Ma. Black circles overprinted with crosses represent heat flux control points. Red crosses mark seafloor heat flow station locations and black crosses mark additional control points added to better constrain basal heat flux across the margin. White line represents the trace of Lithoprobe line 88-1A.

For each map basal heat flux was defined at 18 points across the margin (one at the location of each of the 13 heat flow stations, 3 points between stations HF210 and HF219, and 2 points landward of station HF 201) (Fig. 4.10). Each point was given the basal heat flux value calculated after the McKenzie uniform stretching model (1978) for the corresponding age of the map and crustal thickness associated with the location of the control point after Wu (2007). Heat flow values were then interpolated between control points to produce a continuous heat flux gradient across the map (Fig. 4.10). This was done for each map using the maps respective age to define the basal heat flux history across the margin. Once all maps have been defined, PetroMod® then interpolates heat flux continuously between our defined time steps to give a continuous basal heat flux history which accounts for both lateral variations across the margin and the decaying heat flux following rifting.

4.6.2 3D Model 2 Output

3D Model 2, similar to 3D Model 1, generally over-predicted the seafloor heat flow when compared with our measured data. In 3D Model 2 the predicted seafloor heat flow above the most landward heat flow station, HF201, is 49.73 mWm^{-2} (Tab. 4.5). This is nearly identical to the model predictions from 3D Model 1 as expected, as at this location the basal heat flux histories are identical. In regions unaffected by salt seafloor heat flow increases landward to seaward from ~50-53 mWm^{-2}. This increase in the seaward direction is a result of the increasing basal heat flux associated with increasing crustal thinning. However, as much of the basal heat flux has decayed over the past 200 Ma, the difference in present day heat flux along the line is very small.

The modelled seafloor heat flow from 3D Model 2 significantly over-predicts seafloor heat flow in both the landward and seaward portions of the study area when compared with our measured data (Fig. 4.11). The modelled values are ~7-12 mWm^{-2} higher than our measured values in regions unaffected by salt. The fit between measured and modelled seafloor heat flow in the central regions of the study area is relatively good. Heat flow stations HF209 and HF210 are within 2 mWm^{-2} of the modelled values. While the scattered measured values at stations HF204-207 are not matched by the model, their is good agreement in the peak heat flow above salt as the model records a value of 69.8 mWm^{-2} compared to the measured value of 72.8 mWm^{-2}.

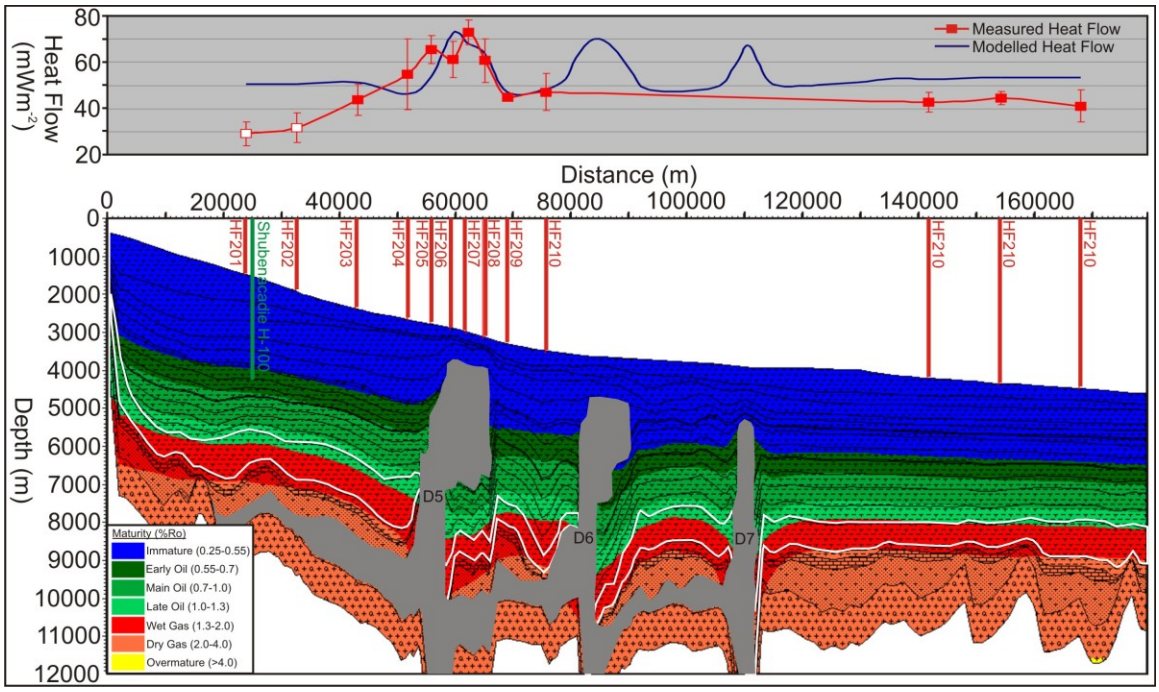

Figure 4. 11: Model output from 3D Model 2 showing depth to modelled maturation windows. Grey represents salt with diapirs labeled D5-D7. White line outlines the Baccaro equivalent Late Jurassic source rock interval. Shubenacadie H-100 well is shown in green and vertical red lines represent heat flow station locations. Plotted above the maturation window are the modelled (blue) and measured (red) seafloor heat flow curves across the study area. White filled squares represent stations which record anomalously low gradients.

The hydrocarbon maturation predicted by the 3D Model 2, similar to 3D Model 1, suggests that the Late Jurassic source rock interval rests almost entirely in the wet gas window. Seaward of salt the source rock interval is predicted to be primarily gas producing with only minor oil produced from the uppermost portions of the source rock interval. Landward of salt the maturation window deepens slightly, resulting in slightly more of the upper most Late Jurassic sediments resting in the late oil producing zone while the underlying sediments, the bulk of the source rock interval, remain within the wet gas zone.

4.7.1 3D Model 3 Heat Flux

3D Models 1 and 2 demonstrated that constraining the basal heat flux across the margin after Lithospheric Model 2 (A = 100 km) generally over predicted the present day

seafloor heat flow as compared to our measured seafloor data. This is an effect of the addition of radiogenic heating in the basement and sediment pile in the 3D models which were not accounted for in the simpler lithospheric models. A third model was run, 3D Model 3, with basal heat flux constrained after Lithospheric Model 1 (A=125 km) in an attempt to lower the modelled present day heat flow to better match our measured seafloor data while maintaining radiogenic heating within the crust and sediment pile. We produced basal heat flux maps as described in Section 4.6, however, the heat flux values were specified using Lithospheric Model 1 (A=125 km), rather than Lithospheric Model 2 (A=100 km). While radiogenic heat production throughout the sediment pile has been shown to significantly increase seafloor heat flow it is hypothesized that the effects of decreasing the basal heat flux will balance the net heat flow such that the modelled present day heat flow will better match our measured data.

4.7.2 3D Model 3 Output

3D Model 3, as constrained using a lower basal heat flux, yielded a very good fit between our modelled and measured data. Good agreement between measured and modelled seafloor heat flow was seen at both seaward and landward ends of the line (Fig. 4.12). Our reliable landward data point, station HF203, and our three seaward most stations, HF219-221, were all within 3 mWm^{-2} of our modelled data which ranged from ~43-45 mWm^{-2} (Tab. 4.5). In the central portions of the line we found that the model under-predicted seafloor heat flow above stations HF209-210 by 7-10 mWm^{-2}. Seafloor heat flow was also under-predicted for all stations above salt diapir D5. The predicted seafloor heat flow values from this model were notably lower than those from either 3D Model 1 or 2.

3D Model 3 predicted the greatest depth to for maturation of the models run so far. This is a result of the lower basal heat flux defined using an original lithospheric thickness of A=125 km. The deeper maturation window is encouraging in regards to oil exploration on the deep water Scotian Slope. The Late Jurassic source rock interval rests almost entirely within the late oil window, suggesting that little to no gas will be produced from this source assuming this basal heat flux is correct.

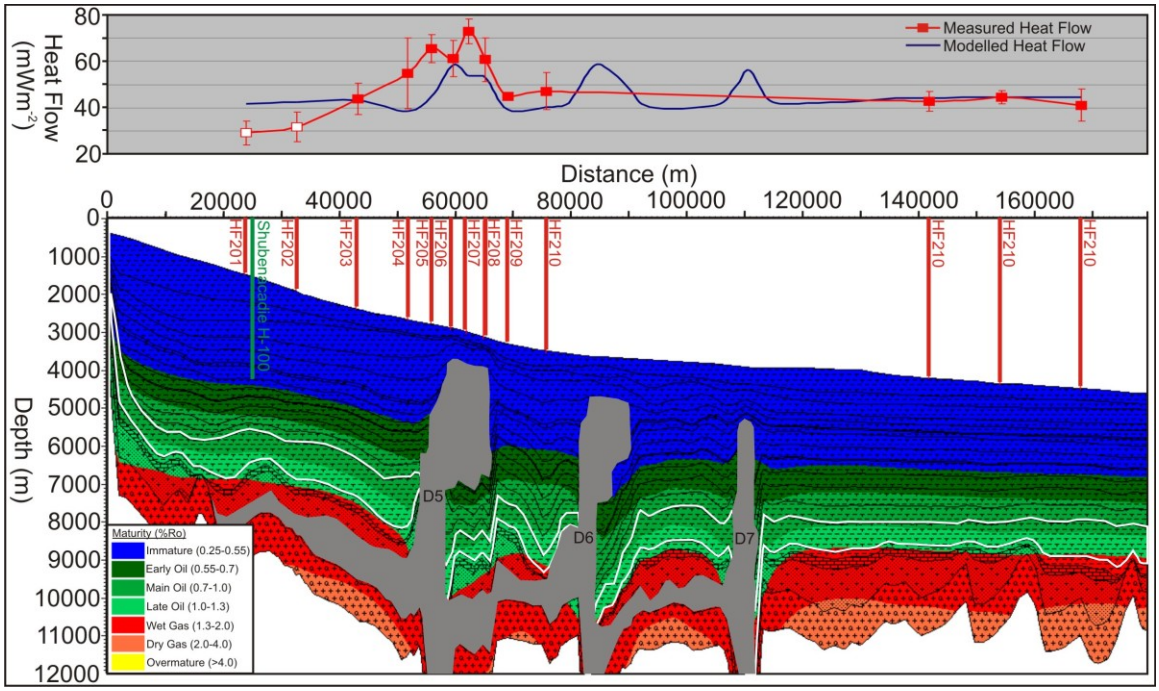

Figure 4. 12: Model output from 3D Model 3 showing depth to modelled maturation windows. Grey represents salt with diapirs labeled D5-D7. White line outlines the Baccaro equivalent Late Jurassic source rock interval. Shubenacadie H-100 well is shown in green and vertical red lines represent heat flow station locations. Plotted above the maturation window are the modelled (blue) and measured (red) seafloor heat flow curves across the study area. White filled squares represent stations which record anomalously low gradients.

The 3D models tested to this point did not include true total crustal thicknesses and instead contained a uniform thickness basement layer of 1000 m underlying the entire modelled region. This is an oversimplification as we know that in nature, as we are modelling a transitional region from continental to oceanic crust, that the crustal thicknesses will decrease with stretching in the seaward direction. Continental crust is

high in radiogenic heat producing elements and thus if heat input from the crust is significant we expect seafloor heat flow may increase in the landward direction associated with increased radiogenic heating from the underlying basement rocks. We theorized that increased radiogenic heat production in the crust might result in increased seafloor heat flow sufficient in matching the elevated values measured in the central regions of the line, while maintaining a basal heat flux constrained using a uniform initial lithospheric thickness. It should be noted that increasing radiogenic heat production in the basement in the landward direction, in an attempt to match the higher measured seafloor heat flow in the central regions of the study area, will likely result in the over prediction of seafloor heat flow at station HF203 towards the landward limit of the line.

4.8.1 3D Model 4 Heat Flux

The heat flux history defined in 3D Model 4 was identical to that in 3D Model 3. The difference between the two models was that 3D Model 4 had varying concentrations of radiogenic heat producing elements across the basement layer. Radiogenic heat production increased in the landwards direction to account for the thickening continental crust and thus increasing volume of radiogenic heat producing elements. It was found to be easier to laterally divide the crust into multiple "facies", increasing the concentration of radiogenic heat producing elements for each "facies" proportionately to the changes in crustal thickness, than to increase the actual crustal thickness across the margin. We maintained the original concentrations of radiogenic heat producing elements specified in 3D Models 1-3 at the seaward limit of the model and increased them proportionately to the increase in crustal thickness across the margin in the landwards direction using crustal thicknesses after Wu (2007). The concentrations increased in ppm from U=2.65 ppm,

Th=9.79 ppm and K=3.21 % at the seaward limit of our model to a maximum of U=8.55 ppm, Th=31.57 ppm and K=10.35 % at the landward limit where the crust was 3.22 times as thick. The original concentrations of radiogenic heat producing elements were taken from the PetroMod® lithologies database for the "Eric_Basement" mixed lithology (Section 4.3.5).

Two models were run using this increasing distribution of radiogenic heat producing elements in the landward direction. We have assigned an arbitrary basement thickness value of 1 km in the earlier models as we were not attempting to consider the effects of increased basal heat flux across the margin associated with radiogenic heat production within the basement layer. 3D Model 4a maintained the thin 1 km thick basement layer applied in the previous three models, however, included laterally varying concentrations of radiogenic heat producing elements to coincide with increasing crustal thickness as described above.

3D Model 4b included a thicker, 3 km thick, basement layer in an attempt to determine how significantly increasing radiogenic heat production in the basement layer would effect maturation potential and seafloor heat flow. A thicker basement layer would result in an increased volume of radiogenic heat producing elements, thus higher basal heat flux. To accurately represent crustal thickness the basement layer should be ~10 km thick to correspond with the interpreted crustal thicknesses towards the seaward limit of the transitional continental crust (Wu 2007). We used a thinner value as we are attempting to model the effects of increased radiogenic heat production in the basement on maturation and heat flow, and it is likely that radiogenic heat producing elements are more concentrated in the upper basement layers.

4.8.2 3D Model 4 Output

We will first discuss the 3D Model 4a, then discuss 3D Model 4b. The present day seafloor heat flow predicted by 3D Model 4a was very similar to that predicted by 3D Model 3. 3D Model 4a predicted identical seafloor heat flow values to 3D Model 3 at station HF221 in the seaward-most region of the model as nothing changed between the two models (Fig. 4.13). As we progressed landwards from this station we began to see slight increases in predicted seafloor heat flow above the predictions from 3D Model 3. Increases in seafloor heat flow were associated with increased radiogenic heat production with increased crustal thickness as defined in this model (in our case increasing concentration of radiogenic heat producing elements). Very little variation (<0.5 mWm^{-2}) between the two model outputs is observed between HF221 and HF209 as variation in crustal thickness between these stations were not particularly large (Fig. 3.20). Landwards of station HF208 we began to see larger variations between the two model seafloor heat flow predictions (Tab. 4.5). At station HF208 the predicted seafloor heat flow of 53.48 mWm^{-2} from 3D Model 4a was almost 0.5 mWm^{-2} higher than the value of 53.02 mWm^{-2} from 3D Model 3. The difference in predicted heat flow between 3D Models 3 and 4a increased gradually in the landward direction reaching a maximum separation of 1.74 mWm^{-2} at station HF201.

The match between our modelled and measured seafloor heat flow from 3D Model 4a was similar to that from 3D Model 3, however, there was a slight improvement in the match above salt diapir D5 and station HF203 in 3D Model 4a. The model predicted similar present day seafloor heat flow values between 43.5-44.5 mWm^{-2} in the landward and seaward limits of the lines suggesting that when accounting for both

variations in radiogenic heating in the crust and basal heat flux following crustal thinning that seafloor heat flux in regions unaffected by salt is likely nearly constant across the central Scotian Slope.

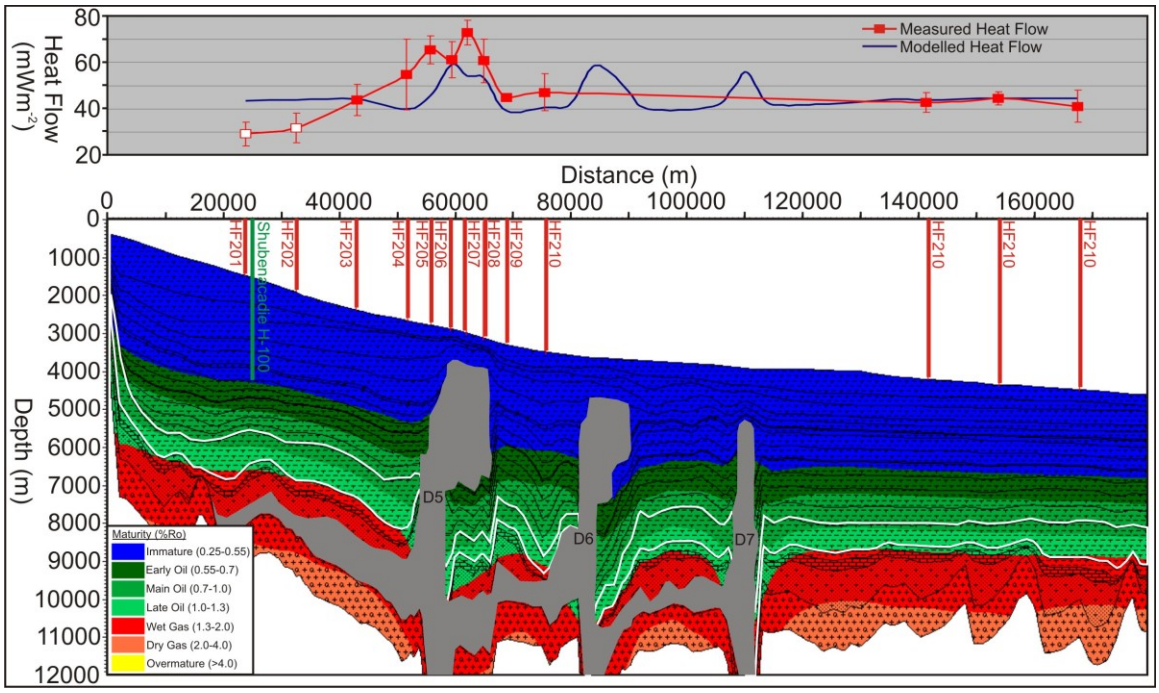

Figure 4. 13: Model output from 3D Model 4a showing depth to modelled maturation windows. Grey represents salt with diapirs labeled D5-D7. White line outlines the Baccaro equivalent Late Jurassic source rock interval. Shubenacadie H-100 well is shown in green and vertical red lines represent heat flow station locations. Plotted above the maturation window are the modelled (blue) and measured (red) seafloor heat flow curves across the study area. White filled squares represent stations which record anomalously low gradients.

The hydrocarbon maturation window predicted by 3D Model 4a was also almost identical to that predicted by 3D Model 3. From the salt diapiric province seaward the Late Jurassic source rock interval remained almost entirely within the late oil window. We note that while also remaining primarily within the late oil window landward of the salt diapiric province, the Late Jurassic source rock interval was slightly deeper than predicted in 3D Model 3.

3D Model 4b predicted slightly higher seafloor heat flow values than 3D Model 4a across the modelled area (Fig. 4.14, Tab. 4.5). When compared to measured seafloor

heat flow, the model over predicted heat flow at both the landward and seaward limits of the model by ~ 5 mWm^{-2} (Tab. 4.5). While seafloor heat flow was over predicted at both ends of the model, the model still under predicted seafloor heat flow at stations HF204-210. The match above salt was slightly better in 3D Model 4b than in 4a, as was the match at stations HF209 and HF210. These models suggest that increasing radiogenic heat production in the basement layer associated with crustal thickening in the landward direction can account for some increase in seafloor heat flow. However, further investigation is required to constrain the concentration and distribution of heat producing elements within the basement layer.

The maturation predicted by the 3D Model 4b is notably different than that predicted by any other model suggesting variations in radiogenic heat production in the basal layer can significantly effect maturation. Due to the increased basal heat flux in the landward direction associated with the increased volume of radiogenic heat producing elements, the maturation window predicts notable increases in maturation in the Late Jurassic source rocks in the landward direction. While seaward of the salt diapiric province the source rock interval lays primarily in the oil producing zone, landward of salt more than half the source rock interval rests within the wet gas producing zone (Fig. 4.14). This suggests that even in the case of significantly increased radiogenic heating within the basement layer, that further seaward in deep water regions the Late Jurassic source rock interval will remain within the late oil producing zone, assuming an initial lithospheric thickness of 125 km after Lithospheric Model 1.

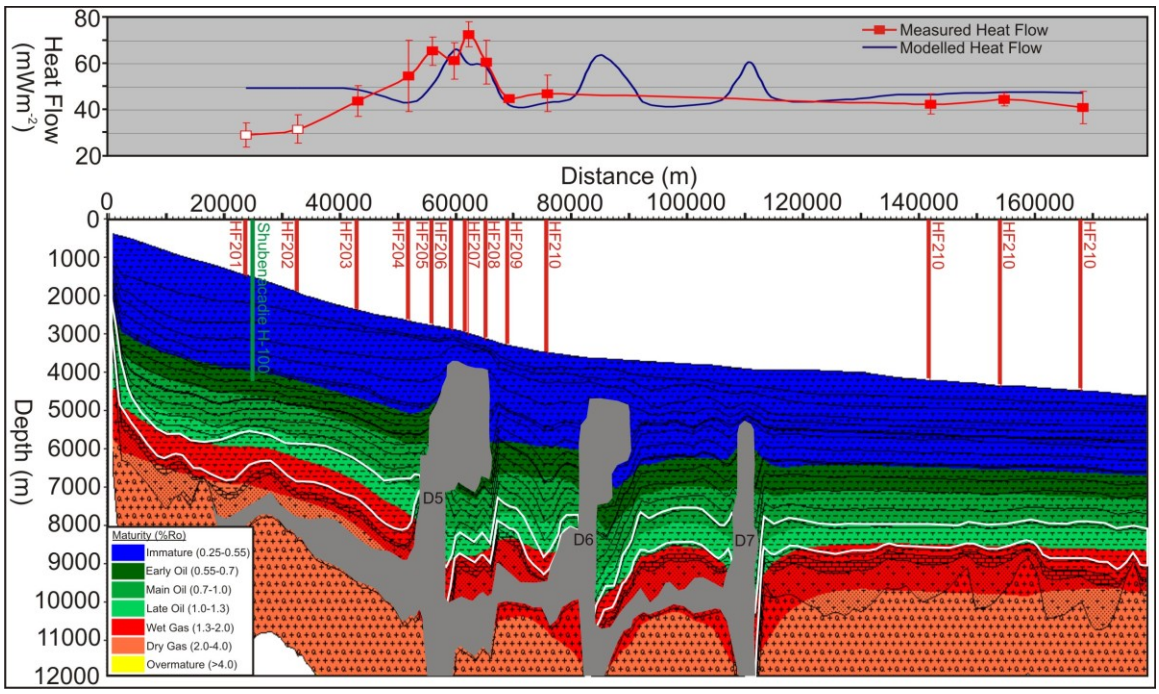

Figure 4. 14: Model output from 3D Model 4b showing depth to modelled maturation windows. Grey represents salt with diapirs labeled D5-D7. White line outlines the Baccaro equivalent Late Jurassic source rock interval. Shubenacadie H-100 well is shown in green and vertical red lines represent heat flow station locations. Plotted above the maturation window are the modelled (blue) and measured (red) seafloor heat flow curves across the study area. White filled squares represent stations which record anomalously low gradients.

4.9.1 3D Model 5 Heat Flux

While in 3D Models 2-4 we determined basal heat flux curves assuming uniform stretching (β only), in 3D Model 5 we include a component of lower lithospheric stretching (δ), which differs from the crustal stretching factor (δ) as proposed by Royden and Keen (1980). While varying amounts of β and δ should have little effect on present day heat flow for this old margin, it is hypothesized that effects of varying β and δ on heat flow through time may affect the maturation potential of the study area. 3D Model 5's basal heat flux is constrained after Lithospheric Model 3. Heat flow maps were produced across the margin to allow for variations in basal heat flux across the study area as was done for 3D Models 2-4. As in 3D Model 4a, variations in concentrations of radiogenic heat producing elements were varied across the basement layer to account for

variations in crustal thickness across the study area, however, the basal layer was not thickened as in 3D Model 4b.

In Lithospheric Model 3 δ was assigned a constant value of 6 across the entire margin. Figure 3.20 shows δ values across the Lahave Platform and onto the landward limit of the Scotian Slope. Unfortunately the study does not constrain δ values across the slope, only to the most landward portions of Lithoprobe Line 88-1A where δ begins to stabilize at a value of ~6. We have taken this landward value as a constant and continued it across line 88-1A to constrain δ in 3D Model 5. Crustal stretching factors (β) are unchanged from previous models (after Wu 2007). Maintaining a constant δ values across the model is an oversimplification, however, in an attempt to determine if variations between β and δ will significantly effect the maturation potential of the study area this simplified lithospheric stretching value should suffice.

4.9.2 3D Model 5 Output

The seafloor heat flow predictions from 3D Model 5 are slightly higher than those predicted by 3D Model 4a. The increase in modelled seafloor heat flow associated with the addition of sub-crustal stretching (δ) ranges from 0.53-0.03 mWm^{-2} in the seaward direction from stations HF201-HF221 respectively (Table 4.5). As our simple lithospheric stretching models (Lithospheric Model 2 and 3) showed little variation between one another in their predictions of present day basal heat flux we did not expect much variation to be calculated in the seafloor heat flow between 3D Models 4a and 5. Modelled seafloor heat flow values at stations HF203 and HF219-221, are in very good agreement with our measured data, all of which agree to within 1.5 mWm^{-2} (Fig. 4.15).

As in 3D Model 4a, the central regions of the model under predict seafloor heat flow when compared with our measured data.

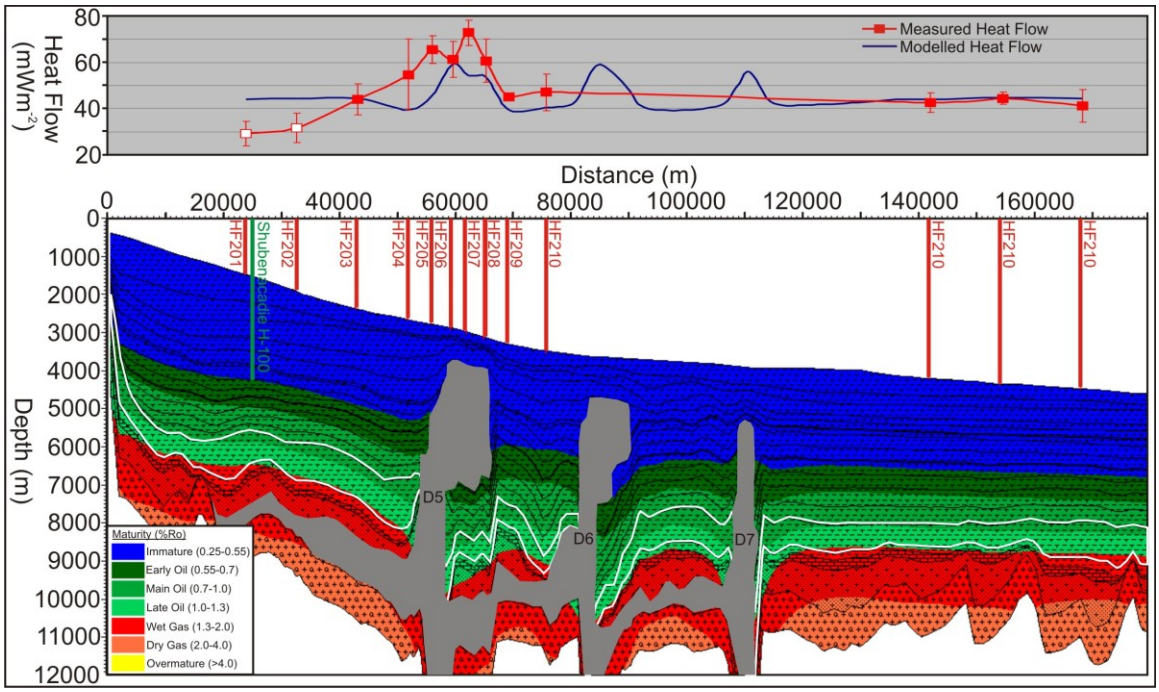

Figure 4. 15: Model output from 3D Model 6 showing depth to modelled maturation windows. Grey represents salt with diapirs labeled D5-D7. White line outlines the Baccaro equivalent Late Jurassic source rock interval. Shubenacadie H-100 well is shown in green and vertical red lines represent heat flow station locations. Plotted above the maturation window are the modelled (blue) and measured (red) seafloor heat flow curves across the study area. White filled squares represent stations which record anomalously low gradients.

Maintaining the fit between the measured and modelled data towards the ends of the transect while improving the fit in the central modelled regions would require significant variations in either basal heat flux or radiogenic heat production in the central regions of the model. Geologically this required lateral variation is impractical while maintaining parameters defined by simple rift models and common rates of radiogenic heat production in the crust and sediment pile. To match the modelled data to the measured data while maintaining basal heat fluxes constrained using a single simple rift model there must be additional factors to conductive heat transfer affecting the measured seafloor heat flow. The addition of fluid flow surrounding and above the diapir as

discussed by Keen (1983) may result in increased heat flow surrounding the diapir, however, this theory requires further investigation.

3D Model 5, with an increased basal heat flux history associated with the addition of sub-crustal stretching in Lithospheric Model 3, has resulted in slight increase in maturation as compared with 3D Model 4a. The Late Jurassic source rock interval remains almost entirely within the late oil window, however, the lowermost regions of the Late Jurassic interval now hovers along the wet gas/late oil boundary. The increase in basal heat flux history associated with addition of a high end member lithospheric stretching factor across the margin (δ=6), has a nearly negligible effect on hydrocarbon maturation.

4.10 3D Model Discussion and Interpretations

The 3D models run can be broken down into three classes of models: models constrained using a basal heat flux after Lithospheric Model 2 (3D Models 1 and 2), models constrained using a basal heat flux after Lithospheric Model 1 (3D Models 3 and 4) and models constrained using a basal heat flux after Lithospheric Model 3 (3D Model 5). As our 3D models are dynamic models that take into account salt movement, the effects of salts high conductivity on heat flow, and the effects of deposition of cool sediments at the seafloor on heat flow we were able to make direct comparisons between modelled and measured seafloor heat flow data.

We found that in our simple lithospheric models (Chapter 3), in the absence of radiogenic heat production, that Lithospheric Model 2 (A = 100 km) yielded the best match to our sediment and salt corrected seafloor heat flow data. As our 3D models account for the effects of radiogenic heat production in the sediment and basement layers,

the seafloor heat flow predicted by 3D Models 1 and 2 generally over predicted seafloor heat flow as compared with our measured data. 3D model 1 was run with a heat flux history constrained after maturation and temperature data from the Shubenacadie H-100 well, yet over predicted seafloor heat flow as compared with our measured data. Similarly, our modelling results from 3D Model 2 also predicted high seafloor heat flow values when compared with our modelled data. The maturation predicted by these models placed the Late Jurassic source rocks in the wet gas zone, however, as the models over predict seafloor heat flow, they may also over-predict the maturation potential.

The second group of 3D models were constrained using the heat flow history after Lithospheric Model 1 (A = 125 km). The 3D models constrained with this lower basal heat flux history yielded a much better fit to our measured seafloor heat flow data (Tab. 4.5). 3D Models 3 and 4a yielded very good fits to the measured data across the study area with the exception of a general slight under predictions in the central regions of the model (heat flow stations 204-210). 3D Model 4b was run with a significant increase in radiogenic heat production through the basement layer in an attempt to match the measured data in the central portions of the margin. The model did result in a notable increase in seafloor heat flow in the landward direction, however, in addition, the model also significantly increased heat flow in seaward regions beyond the measured values. It is possible that towards the seaward limit of the margin where the continental crust has been extremely thinned, that concentrations of radiogenic heat producing elements should be comparatively lower than in the less stretched landward regions of the model. This may account for the extra increase in heat flow observed towards the seaward limit of 3D Model 4b.

3D Model 5, which included both β and δ stretching factors, did not significantly change the predicted seafloor heat flow from 3D Model 4a. We found that of the various basal heat flux histories tested, those constraining 3D Model 4a and 5 yielded the best fits to our measured present day seafloor heat flow data. We were unable to constrain a 3D model using a basal heat flux constrained by a single lithospheric model that would accurately predict seafloor heat flow across the entire study area. However, we were able to obtain good agreement with all data points with the exception of those central values in 3D Models 4a and 5.

Both 3D models 1 and 2 constrained after lithospheric model 2 placed the inferred Late Jurassic source rock interval primarily within the wet gas window. 3D Models 3 and 4a placed the source rocks almost entirely within the late oil window. Due to the significant increase in heat flux from the basement layer upon thickening in the landward direction due to increasing volumes of radiogenic heat producing elements 3D model 4b predicted the source rock interval to be primarily oil producing seaward of salt, and roughly half oil and half wet gas producing landwards of salt. The addition of varying amounts of lower lithospheric and crustal stretching had a very small effect on hydrocarbon maturation potential. Therefore, as all other model parameters were identical, similar to 3D Model 4a, 3D model 5 predicted primarily late oil production from the Late Jurassic source rocks, although slightly deeper than in 3D Model 4a as a result of the slight increase in basal heat flux.

In summary, models constrained after Lithospheric model 2 generally predict Late Jurassic source rocks lay within the wet gas producing zone, while models constrained after Lithospheric Model 1 predict they lay within the late oil producing zone. Maturation

can be increased by increasing the amount of radiogenic heat production in the underlying basement layer of the model. As the distribution of igneous intrusives and concentrations of radiogenic heat producing elements are not well known within the basement rocks, there remains some ambiguity in our model predictions.

Chapter 5: Conclusions

The goal of this project was to provide further insight on the thermal structure, history, and maturation potential of the deepwater central Scotian Slope, offshore Nova Scotia. The project involved three primary sections, each of which focused on constraining the thermal structure of the central Scotian Slope; these are heat flow data acquisition and processing, heat flow data analysis and simple lithospheric modelling, and dynamic 3D thermal and petroleum systems modelling. In this chapter we will briefly review the results of our work and synthesize the heat flow, lithospheric modelling and 3D thermal modelling results previously discussed separately in Chapters 3 and 4. We also suggest future work to provide further constraints and insight on the thermal structure and maturation potential of the central Scotian Slope.

5.1 Discussion of Results

The 2008 Hudson heat flow cruise was successful in the acquisition of 47 seafloor heat flow measurements. Measurements were acquired from the Torbrook gas hydrates mound and three transects along the traces of seismic lines 1400, 1600 and 88-1A. Our successful measurements yield very consistent values of 41-46 mWm^{-2} seaward of the salt diapiric province on all three transects. As expected, we noted significant increases in seafloor heat flow above all salt diapirs identified in our seismic interpretations. Once corrected for the thermal effects of salt and sedimentation on seafloor heat flow our measured data suggested relatively stable basal heat flux values across the margin. Basal heat flux across the margin was most consistent when the anomalously low measured landward heat flux values were replaced with heat flow values calculated from the Torbrook gas hydrates phase boundary after Leblanc et al. (2007). This yielded a general

heat flux across the Scotian Slope from ~43-50 mWm^{-2} with the exception of some scatter above salt bodies which persisted even after corrections for the conductive effects of salt.

Despite the general success of the cruise some problems were encountered. We have gaps in our data coverage across the central/seaward portions of heat flow transect Line 2 (Lithoprobe Line 88-1A) and towards the landward limit of heat flow transect Line 3 (NovaSPAN Line 1600). We were unable to acquire all of the desired measurements due to time constraints and problems penetrating the seafloor with the probe in regions of coarser seafloor sediments. Furthermore, all landward seafloor heat flow measurements in water depths less than ~2000 m recorded anomalously low geothermal gradients, depressing the measured heat flow values. When compared with heat flow calculated in shallow water depths from the depth to gas hydrates phase boundary we saw these values appeared to be erroneously low. It was initially thought to be the result of BWT variations with time affecting shallow sediment temperatures, however, after examining BWT from 2004 and 2008 cruises we were unable to conclude whether or not the sediment temperatures were significantly effected. We hypothesize that convection of fluids may be affecting the shallow sediment temperatures, however, further investigation is required to verify this hypothesis.

In regions above salt bodies we recorded elevated gradients associated with the high thermal conductivity of salt, however, measurements above salt showed large scatter and were not strictly related to the diapir's size, shape and proximity to seafloor as expected. A series of simple conductivity based 2D models with geometries representative of diapirs were run to both remove anomalies associated with the

conductive effects of salt on heat flow from our measured data and to determine if the increase in heat flow measured above salt could be replicated using a purely conductive 2D heat transfer model. The models suggested that heat flow recorded above diapirs could not be replicated using simple 2D models, and thus the measured data, even after correction, still demonstrated some scatter above salt diapirs. Data were further corrected for the effects of cool seafloor sedimentation using the methodology of Louden and Wright (1989). Correction was applied to allow us to examine our data in terms of basal heat flux rather than seafloor heat flow.

The corrected seafloor heat flow values were useful in constraining lithospheric models after McKenzie (1978). Models were run assuming a lithospheric thickness of 100 km (Lithospheric Model 2) and 125 km (Lithospheric Model 1) with crustal stretching factors constrained after Wu (2007) to determine, for our margin, what basal heat flux history would yield present day heat fluxes in agreement with our measured data. It was found, that in the absence of radiogenic heating from the basement and sediment pile, that Lithospheric Model 2 constrained using the thinner, 100 km, lithospheric thickness yielded the best match to our measured, corrected, data. Neither model predicted any significant variation in seafloor heat flux across the margin due to the age of the margin.

The basal heat flux history constrained by the simple lithospheric models to match the sediment and salt corrected heat flow data was found very useful in constraining basal heat flux in our 3D thermal and petroleum systems models. As a result of the dynamic 3D models inclusion of radiogenic heating within the sediment pile, models with heat flow histories constrained using a lithospheric thickness of 100 km (after Lithospheric Model

2), which yielded the best fit to our corrected heat flow data in the simple lithospheric models, over-predicted seafloor heat flow in our 3D models (3D Models 1 and 2). As a result, a decrease in basal heat flux in the presence of radiogenic heating was required to match 3D modelled to measured seafloor heat flow. We simply constrained 3D Models 3-4 using a basal heat flux after Lithospheric Model 1 (A=125 km).

While models constrained using a lower basal heat flux after Lithospheric Model 1 yielded a good fit to measured seafloor heat flow both landward and seaward of salt, this simple basal heat flux was unable to match all measured seafloor heat flow data and under-predicted heat flow above and slightly seaward of salt diapir D5. The scatter in measured heat flow above salt bodies was not mimicked in the modelled data which suggests that these variations are not a 3D effect of the salt. 3D Model 4b (basal heat flux after Lithospheric Model 1) was run with significant increases in radiogenic heat production from the basement in the landward direction. While this model over predicted seafloor heat flow in both landward and seaward regions by ~5 mWm^{-2}, it improved the fit in the central regions of the model, suggesting, that variations in radiogenic heating within the basement can account for some lateral variation in measured seafloor heat flow. We deduce that while simple lithospheric models constrained by seafloor heat flow data are useful in constraining basal heat flux in dynamic 3D models, that other factors such as variations in radiogenic heat production in the basal layer and convection of fluids are also likely affecting heat transfer and thermal structure within the modelled system.

Varying basal heat flux and radiogenic heat production across the study area significantly affects hydrocarbon maturation potential. The original 3D Models (1 and 2)

constrained using a higher basal heat flux predict that potential Late Jurassic source rocks lay within the wet gas window. 3D Models 3 and 4a constrained using a lower basal heat flux predict that the source rock interval lays within the late oil window. Models run using the lower basal heat flux show much better agreement with the measured seafloor heat flow data suggesting that the deepwater Scotian Slope is more likely currently located in the oil producing than gas producing zone. Varying concentrations of radiogenic heat producing elements in the basement can also have a large impact on maturation potential, as the higher concentrations defined in 3D Model 4b push source rocks located landward of salt to lay half in the wet gas and half in the late oil window. Finally, 3D Model 5 constrained using a low basal heat flux assuming a lithospheric thickness of 125 km but with the inclusion of both β and δ stretching factors predicted little variation in seafloor heat flow or maturation potential from 3D Model 4a.

5.2 Future Directions

Here we present some future recommendations to help better constrain the thermal structure and maturation potential of the central Scotian Slope. Following the success of the 2008 Hudson heat flow cruise additional seafloor heat flow measurements would be useful in further constraining the regional heat flux, the effects of salt diapirs on heat flow, and determining the cause/extent of the anomalously low gradients measured in the shallow water regions. A third set of measurements from the Torbrook gas hydrates mound would be useful in supplying yet another measure of gradient and bottom water temperatures for comparison with our previous measurements to try and determine what is responsible for the anomalously low measured gradients in these shallow water regions and if variations occur from year to year. We presume that the anomalously low

geothermal gradients continue to water depths of ~2000 m as at this depth the measured gradients become more stable and similar to the deeper water stations. Denser heat flow data coverage at shallow water depths would be useful in determining if this hypothesis is correct, and if so, at exactly what depth gradients begin to stabilize.

Additional measurements in regions landward of salt on heat flow transect Line 3 (Line 1600) would also be useful for comparison with measurements in landward regions of transects Lines 1 and 2 and stations from the Torbrook mound. If measurements at shallow water depths along Line 3 also record anomalously low gradients we can conclude that the low gradient is likely not the result of convection associated with the gas hydrates as this station would be to far removed to be affected by the hydrates. Additional measurements above the shallowest, most landward, salt diapir in line 1600 would be useful to test how significantly this tall, shallow diapir effected seafloor heat flow. Finally, a densely spaced grid of seafloor heat flow measurements above a large diapir, perhaps D5 in heat flow transect Line 2, would be useful to help us better characterize the effects of 3D variations in salt geometry on seafloor heat flow. If measurement density is high enough we could also determine how laterally restricted these measured variations are and perhaps identify if faults or fractures in the sediment column may be contributing to convection of fluids.

Further improvements could be made to the 3D thermal models. Models are not intended to predict the exact thermal structure or hydrocarbon maturation of the study area, but rather provide insight on the range of possible maturation and to help determine what further work could be done to improve our model predictions. Some simple improvements we could make to the models would include examining gamma ray logs

from Scotian Slope wells to better constrain the radiogenic heat production in the Scotian Slope sediments. Likewise, improvements could be made to our estimates of radiogenic heat production in the basement by analyzing basement rocks of the Meguma group onshore Nova Scotia for their radioactivity, or analyzing wells penetrating basement on the shallower Scotian Shelf. Finally, conductivity analysis of sediments from Scotian Slope wells could allow for improvements in our model results as we could link thermal conductivities to measured values rather than simply using inferred values from the PetroMod® lithology database.

We have attempted to deduce a method constraining the maturation potential of frontier basins with limited well data using a combination of simple lithospheric models, marine seafloor heat flow data and dynamic 3D thermal modelling software. While our models are successful in predicting the maturation of the inferred source rock interval and our predictions are economically favorable as they point to oil rather than gas, to truly determine the maturation of the deepwater Scotian Slope direct sampling by drilling is required. We suggest that maturation is likely not an issue as the majority of Scotian Slope sediments lay within the oil to gas window and that future work should be focused on determining the location and distribution of source rock intervals, as well as the locations of potential reservoir rocks within the deep water Scotian Slope.

References

Adam, J., Shimeld, J., Krezsek, C., and Grujic, D. 2006. How sedimentation controls structural evolution and reservoir distribution in salt basins. Nova Scotia's Energy Research and Development Forum, May 24-25, 2006, Antigonish, Canada (on CD).

Archibald, M., 2002. Geological report for Marathon Canada Limited Annapolis G-24 exploration well. Well history report. Available online through www.cnsopbdmc.ca

Avery, M. P. 1999. Vitrinite reflectance (Ro) of dispersed organics from Shell et al. Shubenacadie H-100. Geological Survey of Canada, Open File 3855, 4 p.

Beardsmore, G.R., and Cull, J.P. 2001. Crustal heat flow: a guide to measurement and modelling. Cambridge University Press, New York, N.Y.

Birch, F. and Clarke, H. 1940. The thermal conductivity of rocks and its dependence on temperature and composition. American Journal of Science, **238:** 133-144.

Bullard, E. 1954. The flow of heat through the floor of the Atlantic Ocean. Proceedings of the Royal Society of London, **A**(222): 408-429.

CGPC, 1997. Natural Gas Potential in Canada Report: Canadian Gas Potential Committee affiliated with the Department of Geology and Geophysics - University of Calgary, 113 p.

Clark, S.P. 1966. Thermal Conductivity. *In* Handbook of Physical Constants. *Edited By* S.P. Clark. Geological Society of America, Memoir 97, p. 459-482.

Coffin, M.F., Gahagan, L.M., Lawver, L.A., Lee, T.Y. and Rosencrantz, E. 1992. Atlas of Mesozoic/Cenozoic reconstructions (200 Ma to Present Day). PLATES Progress Report no. 1-0192, Tech. Rep. no. 122, Austin, TX: University of Texas Institute for Geophysics, 49 p.

Cribb, J.W.A. 2009. Analogue modelling of the salt tectonic processes beneath the shelf and deepwater slope of the eastern Nova Scotian Margin. M.Sc. thesis, Department of Earth Science, Dalhousie University, Halifax, N.S., Canada.

Davis, E.E., and Lister, C.R.B., 1974. Fundamentals in ridge crest topography. Earth and Planetary Science Letters, **21:** 405-413.

Ebinger, C.J., and Tucholke, B.E. 1988. Marine geology of the Sohm Basin, Canadian Atlantic Margin. The American Association of Petroleum Geologists Bulletin, **72:** 1450-1468.

Enachescu, M.W., Atkinson, I., Hogg, J., McCallum, D. and Rowe, C. 2010. Kimmeridgian source rock super-highway in the North Atlantic. Abstract: American Society of Petroleum Geology Annual Convention, New Orleans.

Eliuk, L.S. 1978. The Abenaki Formation, Nova Scotia Shelf, Canada - A depositional and diagenetic model for the Mesozoic carbonate platform. Bulletin of Canadian Petroleum Geology, **26**: 424-514.

Funck, T., Jackson, H.R., Louden, K.E., Dehler, S.A., and Wu, Y. 2004. Crustal structure of the northern Nova Scotia rifted continental margin (eastern Canada). Journal of Geophysical Research, **109:** B09102; doi:10.1029/2004JB003008.

Given, M.M. 1977. Mesozoic and Cenozoic geology of offshore Nova Scotia. Bulletin of Canadian Petroleum Geology, **25:** 63-91.

Goutorbe, B., Loubet, N., Drab, L., and Lucazeau, F. 2007. Heat flow revisited on the eastern Canadian Shield shelf. Terra Nova, **19:** 381-386.

Hardy, I.A. 1975. Lithostratigraphy of the Banquereau Formation of the Scotian Shelf: offshore geology of Eastern Canada, paper 74-30, **2:** 163-174.

Hutchinson, I. 1985. The effects of sedimentation and compaction on oceanic heat flow. Geophysical Journal of the Royal Astronomical Society, **82:** 439-459.

Hutchinson, I., and Owen, T. 1989. A microprocessor heat flow probe. *In* Handbook of seafloor heat flow. *Edited by* K.E. Louden and J.A. Wright. CRC Press, Boca Raton, Fla. Pp.71-90.

Hyndman, R.D., Davis, E.E., Wright, J.A. 1979. The measurement of marine geothermal heat flow by a multipenetration probe with digital acoustic telemetry and insitu thermal conductivity. Marine Geophysical Researches, **4**: 181-205.

Ings, S.J., Beaumont, C., and Shimeld, S. 2005. Salt tectonics at passive continental margins: Resultsfrom numerical models and case study application, offshore Nova Scotia. Geological Association of Canada (GAC) – Mineralogical Association of Canada (MAC). Abstracts vol. 30.

Ings, S.J., and Shimeld, J.W. 2006. A new conceptual model for the structural evolution of a regional salt detachment on the northeast Scotian margin, offshore eastern Canada. American Association of Petroleum Geology Bulletin, **90:** 1407-1423.

Jackson, M.P.A., and Vendeville, B.C. 1994. Regional extension as a geologic trigger for diapirism. Geological Society of America Bulletin, **106**: 57-73

Jansa, L.F., and Wade, J.A. 1975. Geology of the continental margin off Nova Scotia and Newfoundland. In: W.J.M. van der Linden, J.A. Wade (eds.): *Offshore geology of*

Eastern Canada, Vol. 2, Regional geology: Geological Survey of Canada, Paper 74-30, p. 51-106.

Jensen, P.K. 1983. Calculations on the thermal conditions around a salt diapir. Geophysical Prospecting**, 31:** 481-489.

Keen, C.E. 1979. Thermal history of rifted continental margins - evidence from wells on the Nova Scotian and Labrador Shelves. Canadian Journal of Earth Science, **16:** 505-522.

Keen, C.E. 1983. Salt diapirs and thermal maturity; Scotian Basin. Bulletin of Canadian Petroleum Geology, **31:** 101-108.

Keen, C.E., and Beaumont, C. 1990. Geodynamics of rifted continental margins. *In* Volume I-1 of Decade of North America Geology. *Edited by* M.J. Keen and G.L. Williams. Publication of Geological Survey of Canada and Geological Society of America: 393-472.

Keen, C.E., MacLean, B.C., and Kay, W.A., 1991. A deep seismic reflection profile across the Nova Scotia continental margin, offshore Nova Scotia. Canadian Journal of Earth Sciences, **28:** 1112-1120.

Keen, C.E., and Potter, D.P. 1995 (a). The transition from a volcanic to a nonvolcanic rifted margin off eastern Canada. Tectonics, **14:** 359-271.

Keen, C.E., and Potter, D.P. 1995 (b). Formation and evolution of the Nova Scotian rifted margin: Evidence from deep seismic reflection data. Tectonics, **14:** 918-932.

Keen, M.J. 1969. Possible edge effect to explain magnetic anomalies off the eastern seaboard of the U.S. Nature, **222:** 72-74.

Kidston, A.G., Brown, D. E., Altheim, B., and Smith, B.M. 2002. Hydrocarbon potential of the deep-water Scotian Slope. Canada-Nova Scotia Offshore Petroleum Board, Open Report, 111 pp.

Kidston, A.G., Smith, B., Brown, D.E., Makrides, C. and Altheim, B., 2007. Nova Scotia Deep Water Offshore Post-Drill Analysis – 1982-2004. Canada-Nova Scotia Offshore Petroleum Board, Open Report, 181 p.

Leblanc, C., Louden, K., and Mosher, D. 2007. Gas hydrates off Eastern Canada: Velocity models from wide angle seismic profiles on the Scotian Slope. Marine and Petroleum Geology, **24:** 321-355.

Lewis, J.F., and Hyndman, R.D. 1976. Oceanic heat flow measurements over the continental margins of eastern Canada. Canadian Journal of Earth Science, **13:** 1031-1038.

Lister, C.R.B. 1979. The pulse-probe method of conductivity measurement. Geophysical Journal of the Royal Astronomical Society of London, **57:** 451-461.

Lister, C.R.B., 1980. Heat flow and thermal circulation. Annual Review of Earth and Planetary Sciences. **8:** 95-117.

Louden, K.E., Wallace, D.O., and Courtney, R.C., 1987. Heat flow and depth versus age for the Mesozoic northwest Atlantic Ocean: results from the Sohm abyssal plain and implications for the Bermuda Rise. Earth and Planetary Science Letters, **83:** 109-122.

Louden, K. 2002. Tectonic evolution of the east coast of Canada. CSEG Recorder, **27:** 37-49.

Louden, K.E., Sibuet, J.-C., and Foucher, J.-P. 1991. Variations in heat flow across the Goban Spur and Galicia Bank continental margins. Journal of Geophysical Research, **96:** 16131-16150.

Louden, K.E., Sibuet, J.-C., and Harmegnies, F. 1997. Variations in heat flow across the ocean-continent transition in the Iberia abyssal plain. Earth and Planetary Science Letters, **151:** 233-254.

Louden, K.E., and Chian D. 1999. The deep structure of non-volcanic rifted continental margins. Philosophical Transactions: Mathematical, Physical and Engineering Sciences, **357:** 767-804.

Louden, K.E., and Wright, J.A., 1989. Marine heat flow data: A new compilation of observations and brief review of its analysis. *In* Handbook of seafloor heat flow. *Edited by* J.A. Wright, and K.E. Louden. CRC Press, Boca Raton, Fla. pp. 3-67.

MacDonald, C. 2009. Salt Tectonics of the Western Sable sub-basin: insights from regional seismic interpretation and 4D scaled physical experiments. M.Sc. thesis, Department of Earth Sciences, Dalhousie University, Halifax, N.S. Canada.

MacLean, B.C., and Wade, J.A. 1993. Seismic markers and stratigraphic picks in the Scotian Basin wells. *In* East coast basin atlas series. Atlantic Geoscience Centre, Geological Survey of Canada, Dartmouth, N.S., 276 p.

MacCrae, A., 2001. Tif2segy [online]. Available from http://seismic.ocean.dal.ca/pwp_wiki/static/Tif2segy.html [cited December 2009].

McKenzie, D., 1978. Some remarks on the development of sedimentary basins. Earth and Planetary Science Letters, **40:** 25-32.

McIver, N.L., 1972. Mesozoic and Cenozoic stratigraphy of the Nova Scotia Shelf. Canadian Journal of Earth Sciences, **9:** 54-70.

Mukhopadhyay, P.K. 2006. Evaluation of the petroleum systems by 1D and 2D numerical modeling and geochemical analysis in the area of most recent exploration wells on the deepwater Scotian Slope, offshore Nova Scotia. Nova Scotia Department of Energy Report,. 485 p.

Mukhopadhyay, P.K. 2008. Thermal and petroleum systems modelling of two composite seismic lines FGP 88-1A and NovaSPAN 1400, Scotian Basin, offshore Nova Scotia. Final report of phase I study of the proposed work for OETR contract. Submitted to Keith Louden, Dalhousie University.

Mukhopadhyay, P.K. 2010. Thermal and petroleum system modelling (Phase II) of seismic line NovaSPAN 1600 and the revision of 2D PS modelling of seismic lines NovaSPAN 1400 and FGP 88-1A, Scotian Basin, Offshore Nova Scotia based on new heat flow data of 2008. Final report submitted to OETR-Dalhousie Contract 2007-2009. Submitted to Keith Louden.

Mukhopadhyay, P.K., Wade, J.A., and Kruge, M.A., 1995. Organic facies and maturation of Jurassic/Cretaceous rocks, and possible oil-source rock correlation based on pyrolysis of asphaltenes, Scotian Basin, Canada. Organic Geochemistry, **22:** 85-104.

Nagihara, S., and Opre Jones, K., 2005. Geothermal heat flow in the northeast margin of the Gulf of Mexico. American Association of Petroleum Geologists Bulletin, **89:** 821-831.

O'Brien, J.J. and Lerche, I., 1984. The influence of salt domes on paleotemperature distributions. Geophysics, **49:** 2032-2043.

Palmer, A.R., and Geissman, J., 1999. Geologic time scale. Geological Society of America Website: http://www.geosociety.org/science/timescale/timescl.htm

Pan Canadian, 2000. Panuke F-09 well history. Available online through www.cnsopbdmc.ca

Pollack, H.N., Hurter S.J., and Johnson, J.R. 1993. Heat flow from the Earth's interior: Analysis of the global data set. Reviews of Geophysics, **31**: 267-280.

Rashid, M.A. and McAlary J.D. 1977. Early maturation of organic matter and genesis of hydrocarbons as a result of heat from a piercement salt dome. Journal of Geochemical Exploration, **8**: 549-569.

Ratcliffe, E. H. 1960. The thermal conductivities of ocean sediments. Journal of Geophysical Research, **65:** 1535-1541.

Rowan, M.G., 2005. Salt tectonics and sedimentation: A structural and sedimentary framework for petroleum systems in salt basins.

Royden, L, and Keen, C.E., 1980. Rifting process and the thermal evolution of the continental margin of eastern Canada determined from subsidence curves. Earth and Planetary Science Letters, **51:** 343-361.

Shell Canada Ltd., 1970. Well history report Shell Oneida 0-25. Available online through www.cnsopbdmc.ca

Shimeld, J., 2004. A comparison of salt tectonic sub-provinces beneath the Scotian Slope and Laurentian Fan. In: P.J. Post, D.L. Olson, K.T. Lyons, S.L. Palmes, P.F. Harrison, N.C. Rosen (eds): *Salt Sediment interactions and hydrocarbon prospectivity: Concepts, applications and case studies for the 21st century*, 24th Annual GCSSEPM Foundation Bob F. Perkins Research Conference proceedings, p. 291-306.

Sine, G., MacInnis, S., and McKellar, R., 1983. Well history report Shell et al. Shubenacadie H-100. Available online through www.cnsopbdmc.ca

Thompson, W. B., 1977. Offshore well history report Petro-Can/Shell Moheida P-15. Available online through www.cnsopbdmc.ca

Vendeville, B.C., Jackson, M.P.A., 1992. The fall of diapirs during thin-skinned extension. Marine and Petroleum Geology, **9**(4): 354-371.

Vendeville, B.C., 2005. Salt tectonics driven by sediment progradation: Part I — Mechanics and kinematics. American Association of Petroleum Geologists, **89**: 1071–1079.

Villinger, H. and Davis, E.E. 1987. A new reduction algorithm for marine heat flow measurements. Journal of Geophysical Research, **92:** 12846-12856.

Von Herzen, R.P., and Maxwell, A.E., 1954. The measurement of thermal conductivity of deep-sea sediments by needle-probe technique.

Wade, J.A. 2000. Depth to pre-Mesozoic and pre-Carboniferous basements: Geological Survey of Canada Open File 3842.

Wade, J.A. and B.C. MacLean. 1990. The geology of the southeastern margin of Canada. In: *Geology of the Continental Margin of Eastern Canada*. M. J. Keen and G. L. Williams, **2:** 167-238.

Wade, J.A., MacLean, B.C., and Williams, G.L., 1995. Mesozoic and Cenozoic stratigraphy, eastern Scotian Shelf: new interpretations. Canadian Journal of Earth Sciences, **32**: 1462-1473.

Welsink, H.J., Dwyer, J.D., and Knight, R.J., 1989. Tectono-stratigraphy of the passive margin of Nova Scotia, AAPG Memoir, **46:** 215-231.

Wernicke, B., 1981. Low angle normal faults in the Basin and Range Province: nappe tectonics in an extending orogen. Nature, **291:** 645-648.

Wernicke, B., 1985. Uniform-sense simple shear of the continental Lithosphere. Canadian Journal of Earth Science, **22:** 108-125.

Williams, H., 1979. Appalachian Orogen in Canada. Canadian Journal of Earth Sciences, **16:** 792-807.

Williams, H.,1984. Miogeoclines and suspect terranes of the Caledonian-Appalachian orogen: tectonic patterns in the North Atlantic region. Canadian Journal of Earth Sciences, **21:** 887-901

Williams, H., and Grant, A.C., 1998. Tectonic assemblages map, Atlantic region, Canada. Geological Survey of Canada Open File 3657, 1:3,000,000 scale.

Wrygala, B.P., 1989. Integrated study of an oil field in the southern Po basin, northern Italy. PhD dissertation, University of Koln. Ber. Kernforschungsanlage Juelich 2313.

Wu, Y., 2007. Crustal structure of the central Nova Scotia margin and the transition from volcanic to non-volcanic rifting off eastern Canada. PhD dissertation, Dalhousie University, 341 p.

Wu, Y., Louden, K.E., Funck, T., Jackson, H.R., and Dehler, S.A., 2006. Crustal structure of the central Nova Scotia margin off eastern Canada. Geophysical Journal International, **166:** 878-905.

Young, J.L. 2005. The stratigraphy and structural history of the Mesozoic and Cenozoic of the central Nova Scotian Slope, eastern Canada. M.Sc. thesis, Memorial University of Newfoundland, 229 pp.

Yu, Z., Lerche, I., and Lowrie, A., 1992. Thermal impact of salt: Simulation of thermal anomalies in the Gulf of Mexico. Pure and Applied Geophysics, **138:** 181-192.

ZetaWare.Inc, 2003. Bottom hole temperature Horner correction. ZetaWare Utilities [Online]. Available from http://zetaware.com/utilities/bht/horner.html [cited June 2010].

Appendix A: Lithostratigraphy of the Scotian Basin

Syn-Rift Sediments

Syn-rift sediments of Middle to Late Triassic age are found across the Scotian Margin confined to fault bounded basement lows (Jansa and Wade 1975). Seasonally arid conditions across the developing rift valley allowed for fluvial to lacustrine red beds to be deposited in limited topographic lows associated with initial syn-rift subsidence (Wade and MacLean 1990). The sediments are primarily red silts and sands sourced from the surrounding continental platforms. These syn-rift sediments are directly overlain by the Late Triassic to Early Jurassic deposits of the Eurydice and Argo Formations which mark the inundation of the low lying rift valley upon continued subsidence during continental extension.

Argo and Eurydice Formations

Prior to continental breakup and the onset of continental drift came periods of inundation and evaporation of the early rift grabens by seawater from the paleo Tethys Ocean (Kidston et al. 2002). Inundation of topographic lows resulted in periods of restricted marine conditions during which the predominately shale with minor silt and sand red beds of the Eurydice Formation were deposited (Jansa and Wade 1975). The sub-equatorial semi-arid climate during inundation resulted in many periods of evaporation during which the deposition of the extremely thick salt beds of the Argo Formation occurred. The Eurydice and Argo Formations are found to thicken in basement lows forming accumulations greater than 3 km thick in many basement grabens and half-grabens (Jansa and Wade 1975). Either one or both of the Argo and Eurydice Formations are present in all Scotian Basin syn-rift basement lows.

The Argo Formation is particularly important as the Argo salt significantly distorts both stratigraphy and geothermal gradient throughout the Scotian Slope. The Argo salt is deposited in basement lows upon evaporation of seawater, however with time and differential sedimentary loading the salt begins to flow forming various salt tectonic structures as described in Section 2.4. The Argo salt consists of layered, thick, coarsely crystalline colorless to pale orange salt interbedded with thin red shales (Wade and MacLean 1990). Shale content increase upwards in the Argo Formation, however forms a relatively small portion of the composition of the Argo Formation. The Argo salt is deficient in anhydrite indicating the salt must have been precipitated from brines lacking carbonate and sulphate minerals (Wade and MacLean 1990). As the Argo Formation is deposited in basement lows on a rifting, subsiding, continental margin salt thickness vary across the margin based on basement topography and inundation from the paleo Tethys Sea. However, an average original thickness of ~2 km has been predicted for the Argo Formation prior to salt movement by restoring observed volumes of salt to original basement lows (MacDonald 2009).

The top of the Argo and Eurydice Formations are marked by a large scale erosive event associated with the final continental separation of the North American from Africa referred to as the breakup unconformity (Wade and MacLean 1990). This erosive event is prominent across the stable continental platforms, however it can not be clearly identified across the outer shelf and adjacent continental slope. It is inferred to exist at the top of the Argo Formation.

Iroquois and Mohican Formations

Following the break up unconformity came the deposition of the first wave of drift phase sediments on the Scotian Margin in the Early to Middle Jurassic. The Eurydice and Argo Formations are uncomfortably overlain by the carbonates of the Iroquois Formation and the coeval and overlying clastics of the Mohican Formation (Jansa and Wade 1975). The seaward limit of the thinned continental crust saw the deposition of tidally influenced Iroquois dolomites under restricted shallow marine conditions during the onset of drifting. The Late Sinemurian to Early Pliensbachian Iroquois Formation has been interpreted to reach thicknesses greater than 1500 m under the southwestern Scotian Shelf and is best developed along the outer edge of the stable Lahave platform where shallow water and limited clastic influx allowed for the development of thick carbonates (MacLean and Wade 1990).

The lower portion of the Mohican Formation is age equivalent with the Iroquois Formation as evidenced by the biostratigraphic and lithologic correlations of MacLean and Wade (1990). The Pliensbachian to Bajocian Mohican Formation is composed of fine grained sandstones, red to green shales and dolomitic siltstones and is found to interfinger and overlie the Iroquois dolomites. The Mohican Formation fills the remaining accommodation space in tilted basement blocks, allowing all subsequent strata to be deposited uniformly without drastic local thickness variations associated with pre-existing basement lows (Jansa and Wade 1975). The Mohican Formation is conformably overlain by the Scatarie limestone, the lowermost unit of the Abenaki Formation.

The Western Bank Group

The Western Bank group refers to four approximately age equivalent formations of the Scotian Shelf and Slope deposited from the Middle to Late Jurassic (McIver 1972). The Middle to Late Jurassic epochs were dominated by marine transgression and relative sea level rise resulting in more stable marine conditions across the Scotian Margin allowing for the deposition of a wide variety of lithologies on the Scotian Margin (Jansa and Wade 1975). The Western Bank Group consist of the Mohawk, Mic Mac, and Abenaki Formations of the continental shelf deposited on the shallow, stable Lahave Platform, and the distal, fine grained, seaward equivalents of the shelf strata, the lower Verrill Canyon Formations (Wade and MacLean 1990). These Formations represent the transition from continental clastics to deep water shales across the Scotian Shelf and Slope.

Abenaki Formation

The Abenaki Formation is a predominately limestone carbonate formation of Middle to Late Jurassic age. The Abenaki Formation comprises a laterally restricted carbonate bank which formed on the outer continental shelf, extending seaward to the hinge zone, deposited under shallow marine conditions (Wade and MacLean 1990). The southern limit of the carbonate bank runs from the Sable Subbasin in the east to the western limit of the Scotian Basin along the hinge zone. The Abenaki Formation interfingers with the Mic Mac Formation to both the north and east where it pinches out completely west of the Sable subbasin (Jansa and Wade 1975).

Within the Abenaki Formation there exist four prominent stratigraphic members, the Artimon, the Baccaro, the Misane and the Scatarie Members (Eliuk 1978). The

lowermost facies, the Scatarie Member, is dominantly limestone ranging from oolitic to grainstone in composition. The Scatarie member is composed of four cycles, each of which is greater than 10 m thick. Each cycle is in turn composed of four internal units. Each cycle consists of a basal oolitic layer overlain by a oncoilitic layer, a fossiliferous layer and a wackestone layer respectively. Minor interbeds of sand and silts are present throughout. The Scatarie Member has been interpreted to have formed in warm agitated waters ranging from lagoonal to shallow near shore to deep water environments (Eliuk 1978).

Overlying the Scatarie Member is the only clastic sequence of the Abenaki Formation, the Misane Member. The Misane Member is dominantly dark grey to brown shale unit which separates the limestones of the Scatarie and overlying Baccaro Members (Eliuk 1978). This unit is replaced in the Sable Subbasin by the equivalent Mic Mac Formation sandstones and shales, however within the Abenaki carbonate bank, it ranges from 75-170 m in thickness. Foraminifera suggest this shale formed in an inner to outer neritic environment.

The Misane Member is overlain by the dominantly limestone and minor sandstones, shale and siltstones of the Baccaro Member. This is the thickest member of the Abenaki Formation reaching thicknesses in excess of 1100 m. The interior of the Baccaro Member is more clastic rich, and interfingers with the Mohawk and Mic Mac Formations. It has a gradational upper contact with the overlying Missisauga delta sands, and a fairly abrupt seaward transition to the shales of the Verrill Canyon Formation.

The final Member of the Abenaki Formation is the laterally restricted Artimon

Member. This is the least extensive member of the Abenaki Formation, and is composed of shales interbedded with limestones.

Mic Mac and Mohawk Formations

The Callovian to Tithonian Mic Mac Formation is the up-dip equivalent to the Abenaki Formation's Baccaro Member and is primarily composed of shale/siltstone and sandstone with minor limestone (McIver 1972, Wade and MacLean 1990). The Formation is interpreted to have developed on the interior back-bank of the Abenaki carbonate bank as the result of an influx of clastic sediments from the north and northwest preventing further carbonate development in the region (Jansa and Wade 1975, McIver 1992). The Mic Mac Formation has been correlated east of the Abenaki carbonate bank into the Sable subbasin where it was deposited in a shallow marine to near-shore environment (Wade and MacLean 1990, Jansa and Wade 1975).

The Mohawk Formation of Nova Scotia's inner western continental shelf represents the landward equivalents of the Mic Mac Formation (Wade and MacLean 1990). This continental clastic facies is predominantly sandstone with lesser siltstone and minor shale. At approximately the end Jurassic, final separation of the Iberian and North American plates resulted in the Formation of the Grand Banks of Newfoundland (Louden 2002). Plate separation was accompanied uplift of the easternmost portions of the Scotian Margin resulting in removal of Late Jurassic sediments in the Eastern Scotian Basin (Wade and MacLean 1990). This breakup unconformity, referred to as the Avalon unconformity, has been identified as far west as the western flank of the Laurentian Subbasin (Wade and MacLean 1990, Jansa and Wade 1975).

Verrill Canyon Formation

The Verrill Canyon Formation refers to the shaley seaward equivalents to all Middle Callovian to Barremian sediments of the Scotian Shelf and Scotian Slope. This includes the age equivalent Abenaki, Mic Mac and Mohawk Formations as well as the overlying younger Missisauga Formation (McIver 1972, Jansa and Wade 1975). Defining the exact lateral extent and upper boundaries of the Verrill Canyon Formation is difficult. No prominent seismic reflector is associated with the top Verrill Canyon Formation, and the unit grades laterally into the coarser grained fluvial-deltaic Missisauga Formation (Wade and MacLean 1990).

The Verrill Canyon Formation is dominantly grey to olive grey with the presence of fine coalified plant material (Jansa and Wade 1975). The shales contain minor interbeds of siltstone, sandstone and limestone. The depositional environment of the Verrill Canyon Formation has been interpreted as shallow to moderately deep "shelf" by Jansa and Wade (1975), and as neritic, prodelta, and basinal depending on the location and interval sampled by Wade and MacLean (1990). This unit has been inferred to contain prolific source rocks and is a likely source for much of the Scotian Basin oil and gas (Mukhopadhyay 2008).

Missisauga Formation

At the onset of the Early Cretaceous came increased sedimentation to the Scotian Basin associated with tectonic uplift in the east and the development of large drainage systems from the continents. This resulted in thick sediment accumulations in the subsiding offshore basins (Jansa and Wade 1975). The Early Cretaceous clastic Missisauga Formation formed as a result of this massive influx of sandy sediments and

extended southwest with the development of the advancing Sable Delta (Kidston et al. 2002).

The Missisauga Formation has been subdivided into an "up-dip" facies consisting of massive, thick, alluvial plain sandstone deposits and a "down-dip" facies consisting of less massive, finer, lower delta plain to neritic sandstone facies by McIver (1972). Defining the boundary between these units is difficult as it represents a gradational transition from shallower to deeper water depositional environments. Jansa and Wade (1975) report the presence of a prominent Hauterivian to Berremian transgressive limestone unit referred to as the "O" marker across much of the Scotian Shelf. This unit divides the sandy sediments of the Missisauga Formation into upper and lower sequences described by Given (1977). More recent drilling has resulted in the further subdivision of the lower member into a lower and middle member, thus the final subdivision of the Missisauga Formation includes a lower and middle member underlying the "O" marker, and the overlying upper member (Wade and MacLean 1990).

The Lower member of the Missisauga Formation is Kimmeridgian to Valanginian age corresponding to sedimentation from the early Sable Delta (Wade and MacLean 1990). It is interpreted as a delta front to beach environment deposited by distributary channels and alluvial fans. The lower member is dominantly fine to coarse grained sandstone with poor to moderate sorting and shows multiple coarsening upwards sequences (Jansa and Wade 1975, Wade and MacLean 1990). Minor limestone, siltstone and shale beds are present within the lower Missisauga, composing less than 20 % of the strata (Jansa and Wade 1975). The entire lower unit is faulted associated with salt

movement and subsidence in the deep depositional basins (Wade and MacLean 1990). The lower member is capped by an evident shale rich unit.

The middle and upper members of the Missisauga Formation are of similar lithology and are Valanginian to Berremian in age (Wade and MacLean 1990). The two units are separated by the distinctive limestone "O" marker. The middle and upper units combined correspond to the "up-dip facies" of McIver (1972) described as interbedded quartzose sandstone and shale sequences with sands comprising ~35 % of the lithology. Sand units are fine to very fine grained, and thicker shale sequences occur in the lower portions of the sequence (McIver 1972).

Logan Canyon Formation

The onset of the Aptian Epoch was associated with a slow regional transgressive event resulting in the transition from coarser sandy sedimentation of the Aptian to Albian Logan Canyon Formation to the deposition of the more shale rich Cenomanian to Santonian Dawson Canyon Formation (Jansa and Wade 1975). The base of the Logan Canyon Formation is defined by a prominent shale unit referred to as the Naskapi Member (Jansa and Wade 1975). A second major shale interval, the Sable Member, occurs higher up within the Logan Canyon Formation and was first described by McIver (1972) as a fissile shale. The Logan Canyon Formation is composed of thick interbedded sandstone and shale units with sands comprising less than 25 % of the strata. Coarser sands are located near the base of the formation (McIver 1972).

The seaward equivalents to the Logan Canyon Formation are referred to as the Shortland Shale and are defined by the major basinward transition of sandstone beds to

shales (Jansa and Wade 1975). A basinward increase in shale abundance is noted across the Scotian Margin for the Logan Canyon Formation (Wade and MacLean 1990).

Dawson Canyon Formation

The Cenomanian to Santonian Dawson Canyon Formation consists of marine shales with minor siltstone and sandstones. A major Turonian limestone unit referred to as the Petrel Member forms a continuous regional marker within the Dawson Canyon Formation (Wade and MacLean 1990). The Dawson Canyon Formation is fairly uniform throughout the Scotian Basin, with a tendency towards silty layers in its basal regions. The Dawson Canyon Formation is capped by laterally continuous chalks of the Wyandot Formation (McIver 1972).

Wyandot Formation

The Wyandot Formation is relatively thin yet prominent chalky carbonate unit present across most of the Scotian Shelf (McIver 1972). It is Santonian to Maastrichtian age and was deposited in a relatively deep water, outer neritic to marine environment (Wade and MacLean 1990). The top Wyandot has been interpreted as a period of non-deposition leading into the Tertiary deposits of the upper most formation of the Scotian Basin, the Banquereau Formation.

Banquereau Formation

The Banquereau Formation refers to the uppermost package of sediments deposited on the Scotian Margin from Maastrichtian to present (Wade and MacLean 1990). The sediments of the Banquereau Formation are primarily mudstone with more abundant sandstones and conglomerates in the upper portions (McIver 1972). Significant lateral and vertical facies variation within the Banquereau Formation has resulted in the

division of the formation into four informal groups by Hardy (1975). These are the Maskonomet Beds, the Nashwauk Beds, the Manhassat Beds, and the Esperanto Beds.

The Campanian to Maastrichtian Maskonomet Beds consist of mudstones, shales, siltstones and minor sands (Hardy 1975). This unit directly overlies the Wyandot Formation, and is capped by a laterally restricted sandstone unit. The upper unit of the Maskonomet beds marks the Cretaceous-Tertiary boundary. The overlying Nashwauk beds of Paleocene to Eocene age are coarser than the Manhasset beds, comprised of loosely consolidated fine grained sandstones and finer grained mudstones (Hardy 1975). The boundary between the Nashwauk and overlying Manhasset Beds has been interpreted as the Eocence-Oligocene boundary (Hardy 1975).

The Manhassat beds are comprised of Oligocene aged fine to coarse grained sandstones with minor interbeds of siltstone, shale and mudstone (Hardy 1975). The thickest deposits of the Manhassat beds occur within the Sable and Abenaki subbasins reaching thicknesses upwards of 200 m. The transition to the overlying Esperanto beds marks the Oligoncene-Miocene boundary (Hardy 1975). The Miocene to Pliocene Esperanto beds consist of loosely consolidated sandstone with lesser amounts of interbeded siltstone and shale. The Esperanto beds are overlain by young Pleistocene to recent sediments and the upper bound represents a Pliocene-Pleistocene erosional event (Hardy 1975). The Banquereau Formation is characterized by numerous erosive events due to incision of channels and glaciations of the Scotian Shelf, and as with all other formations of the Scotian Shelf, grades into finer, more shale rich slope equivalents.

Appendix B - Heat Flow Data Acquisition and Processing

B.1 Heat Flow Measurement

Heat flow can be measured either on land or at sea; however, the measurement technique varies greatly from one to the other. Terrestrial heat flow measurements are generally taken from deep boreholes, while most marine heat flow measurements are taken using shallow penetrating heat flow probes (Fig. B1). To accurately measure heat flow it is required that the temperature gradient measured accurately reflects the gradient sourced from Earth's interior alone and that the near surface temperatures are not effected by any environmental variations propagating downwards from Earth's surface. We can assume that at great water depths bottom water temperatures are stable year round; however, on land and at shallow water depths significant temperature variations associated with daily and seasonal temperature fluctuations can occur. Therefore, to escape the zone of environmental perturbations we measure marine heat flow using shallow penetrating probes, and terrestrial heat flow with deep penetrating boreholes. As we are dealing with marine heat flow in this project we will focus on the procedure of marine heat flow data acquisition. A series of gravity driven heat flow probes, including the "Bullard", "Ewing", and "Lister" type

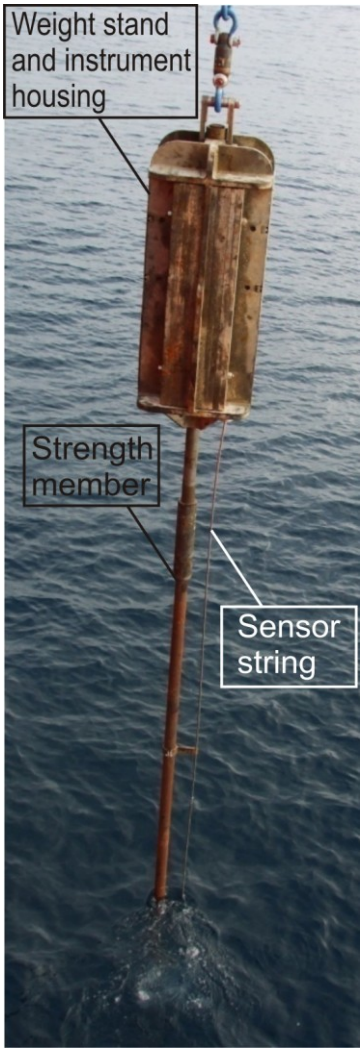

Figure B 1: Dalhousie 32 thermistor heat flow probe showing three major components; weight stand and instrument housing, strength member, and sensor string.

probes, have been developed since the late 1940's to facilitate the acquisition of reliable seafloor heat flow measurements.

The most modern version of marine heat flow probes, "Lister" type probes, contain three primary components: the instrument housing and weight stand, a solid steal strength member, and an outrigger sensor string housing a series of thermistors in as thin a casing as possible in order to precisely and accurately record temperature variations with depth in a short recording period (Fig. B1). The method of recording and processing seafloor heat flow data using "Lister" type heat flow probes has been described in detail by many other authors (e.g. Lister 1979, Hyndman et al. 1979, Villinger and Davis 1987) and therefore is not discussed in detail here. A more complete description of marine heat flow probes including the Dalhousie heat flow probe used on the 2004 and 2008 Scotian Slope heat flow cruises, as well as the acquisition and processing methodology applied in this thesis is included in Appendix B.2.

B.2 Marine Heat Flow Probes

The study of marine heat flow began in the late 1940's with the development of the first seafloor heat flow probe for measurement of geothermal gradient by Bullard and Maxwell (Bullard 1954). Many probes have been modelled after Bullard's first probe and are referred to as Bullard type heat flow probes. These probes are designed to penetrate the seafloor sediments under their own weight. They contain two key components, a long thin bar with two or more temperature sensors located at known distances to measure gradient, and the instrument housing and recorder electronics box, which also serves to provide the weight to ensure penetration.

Upon penetration the temperature sensors record a sudden increase in temperature associated with frictional heating, followed by a transient thermal decay as the heat dissipates through the surrounding sediments by conductive heat transfer (Fig. B2). The function of temperature vs. time is recorded at each temperature sensor in the probe for a substantial period of time following penetration. This record is used to determine the temperature as time approaches infinity (the function will approach the original undisturbed sediment temperature once all the frictional heating has decayed). As the method is rather involved and is described in great detail by others (e.g. Bullard 1954; Lister 1979) it will not be discussed here. It was noted by Bullard (1954) that the frictional decay curve could potentially be used to determine the thermal conductivity in-situ, which led to the later innovation of the Lister type in-situ heat flow probe.

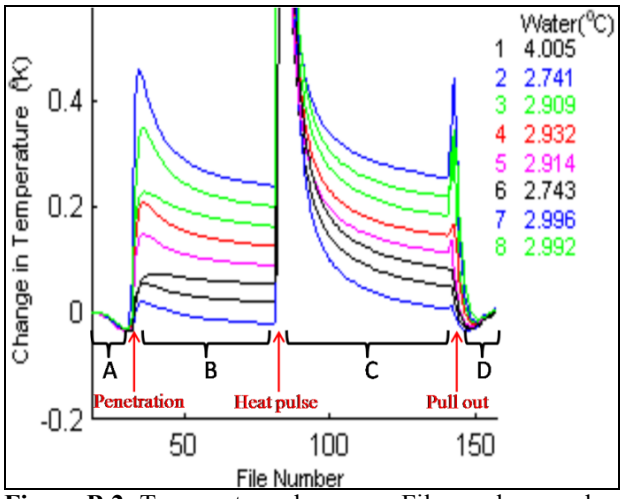

Figure B 2: Temperature change vs. File number graph showing 8 thermistors. Penetration, heat pulse, and pull out heating are shown in red. Cooling associated with probe descending to bottom (A), penetration decay (B), heat pulse decay (C) and probe after pull out (D) are shown in black.

As Bullard type probes did not allow for in situ conductivity analysis, sediment thermal conductivity measurements were taken separately from the gradient measurements. Conductivity analysis was done on core samples from nearby wells or on samples collected from the heat flow site. Conductivity of core samples was determined in the lab using either the steady-state hot-plate heating method, or the needle-probe method (Von Herzen and Maxwell 1959).

The first major advancement in heat flow probes came with the development of the Ewing type probe (Beardsmore and Cull 2001). The Ewing probe saw the addition of small outrigger temperature sensors attached as fins to gravity driven or piston corers at measured distances along the core barrel. The radius of the outrigger temperature sensors was greatly reduced in this design as the core barrel now works as a strength member allowing for temperature sensors to be contained in the thin outrigger fins. The smaller radius of the sensors resulted in a much smaller thermal time constant (τ) which significantly decreased the time required in-situ for each measurement. Although separate conductivity analysis was still required, core samples were collected at the same time and site as the gradient measurement with the Ewing probe as the strength member doubled as a core barrel.

The outrigger needle-probe design of Ewing led to the final major innovation in heat flow probe design, the Lister type violin bow probe with in-situ conductivity analysis (Lister 1979). Lister developed a probe with an outrigger sensor string (Fig. B1). Similar to Ewing's outrigger devices, Lister's sensor string was held away from the strength member (a thick steal bar), allowing for a much smaller radius (thus τ) in the sensor string. With multiple thermistors at fixed distances along the sensor string, geothermal gradient is calculated using the method of Bullard (1954).

Unlike the Ewing probe, the strength member was not a corer, and thus no core sample is collected in-situ. However, the Lister probe incorporated an innovative method for in-situ conductivity analysis by incorporating a central heating wire to release a calibrated heat pulse of a known magnitude at a known time following penetration. The thermal decay following the heat pulse is recorded by the thermistors, similar to the

decay following penetration (Fig. B2). When used in combination the frictional and heat pulse decay curves can be used to determine the thermal conductivity of the sediments surrounding the probe, thus no core need be acquired for conductivity analysis. This method is outlined in detail in many papers, and thus will not be discussed here (e.g. Lister 1979; Hyndman et al. 1979).

B.3 Dalhousie Heat Flow Probe

The seafloor heat flow measurements were acquired using the 32 thermistor Dalhousie heat flow probe (Fig. B1). The probe is a gravity driven, Lister type, in-situ probe, and resembles the design of the Cambridge heat flow probe of Hutchinson and Owen (1989). The instrument has three key components: the weight stand and instrument housing, the strength member, and the violin bow sensor string (Fig. B1). The instrument housing is located within the weight stand and contains the control and recording electronics, the acoustic transducer responsible for telemetering data to the ship for real time monitoring, and the battery packs. Digital data are recorded internally by the probe, and must later be uploaded to a computer once the probe is removed from the water.

The sensor string contains 32 precision thermistors with an accuracy of ~1 mK for temperature measurement. These thermistors are evenly spaced along the 6 m sensor string and continuously record temperature once the probe is activated. The sensor string also contains a central heater wire responsible for supplying a calibrated heat pulse ~7 minutes following penetration of the seafloor as required for in-situ conductivity analysis. The outrigger sensor string is held ~5 cm from the strength member to ensure that any disturbance associated with the thick, highly conductive strength member during or following penetration does not effect the thermal field recorded by the sensor string.

B.4 Heat Flow Data Acquisition

The procedure of heat flow data acquisition, as outlined below, was followed for each heat flow station. An example of the temperature data recorded by the thermistors at each individual station is shown in Figure B-2. The location of each heat flow station is identified using a shipboard GPS. Once on site, the probe is lowered through the water column by a shipboard winch. The probe contains a jog sensor which is constantly reset by movement of the probe during descent. At a distance of ~100 m above the seafloor the probe is stopped and held in place to record a reference background bottom water temperature. The probe is then lowered to the seafloor until penetration. The jog sensor is triggered upon penetration. The thermistors record a brief period of warming from the frictional heating associated with penetration, followed by a period of thermal decay as the heat dissipates through the surrounding sediments (Fig. B2).

Approximately seven minutes after the final jog (penetration), a calibrated heat pulse is released from the sensor string's central heater wire. At this point, the thermistors record a second period of warming followed by a second period of thermal decay associated with the dissipation of the heat pulse through the surrounding sediments (Fig. B2). Approximately ten minutes are allowed for the thermistors to record the thermal decay of the heat pulse before the probe is removed from the seafloor. Upon removal of the probe the thermistors record a final frictional heating which quickly dissipates as the thermistors equilibrate with the bottom water temperature (Fig. B2). The probe is then returned to the surface.

B.5 Heat Flow Data Processing

The processing of the marine heat flow data from Lister type heat flow probes involves determination of the undisturbed background sediment temperature at known depths for calculation of the temperature gradient, and the determination of the surrounding sediment thermal conductivity. Heat flow may then be calculated as it is simply the product of geothermal gradient and sediment thermal conductivity. Heat flow data was processed using a MatLab workflow designed by Keith Louden after the reduction algorithm of Villinger and Davis (1987) for multiple penetration heat flow surveys using violin bow (Lister type) heat flow probes.

B.5.1 Data Reduction

The heat flow probe records temperature data successively producing 32 separate measurements, one for each of the 32 thermistors, in nine seconds including four additional measurements for tilt (2) and reference calibration resistors (2). This yields one temperature measurement per thermistor every nine seconds. Data is recorded from the moment the probe is switched on until it is turned off, and is not automatically sorted into separate files for separate heat flow stations. The data is recorded sequentially following a pre-set sequence of thermistors, calibrations, and tilts. The first step in data reduction involves sorting the continuous stream of temperature data into the individual heat flow stations, and discarding the data recorded between individual heat flow sites. Each station represents a similar sequence from penetration to pullout as shown in Figure B2.

Processing requires that all data from the bottom water temperature measurement prior to penetration to the removal of the probe from the seafloor are present. Every time a heat pulse is released it is recorded in the data stream and the time of the heat pulse is

marked both in the digital data log recorded internally by the probe, and manually by the shipboard data logger monitoring the acoustically telemetered real time analogue data. The time of each heat pulse is used as a starting point in locating the individual heat flow stations in the continuous stream of data. The data sequence recorded by the thermistors is used to select and isolate only the data associated with that particular heat flow station. The data is copied to a new file specific to the individual station.

The second stage of data reduction involves determining the geothermal gradient and the sediment thermal conductivity from the measured resistances at different depths along the probe. Conductive heat flow (Q) is the product of geothermal gradient (dT/dz) and the sediment thermal conductivity (k_s) (Eq. B1). The thermal decay curves recorded following frictional and pulse heating are used to determine the original undisturbed background temperature of the sediment and the thermal conductivity of the sediment respectively.

$$Q = -k_s * dT/dz \qquad \text{(B1)}$$

B.5.2 Determining Sediment Temperature

As there are significant temperature variations in the sediments due to frictional heating upon penetration, the temperatures measured by the probe do not truly reflect the original undisturbed sediment temperatures. To acquire accurate measures of gradient the effects of frictional heating must be removed to determine the true background sediment temperatures. The theory and methodology behind these temperature corrections have been discussed in detail by others (e.g. Bullard 1954, Lister 1979, Hyndman et al. 1979).

Bullard (1954) proposed that the temperature field (T(t)) surrounding a probe, which has been raised an initial temperature (T_o) above the background sediment

temperature (T_s), will decay with respect to time as the excess heat dissipates through the surrounding sediments. The thermal decay curve following frictional heating can be linearized by transforming the x-axis of the temperature vs. time graph to the cylindrical decay function $F(\alpha,\tau)$.

$$T(t) = T_s + T_o F(\alpha,\tau) \tag{B2}$$

The $F(\alpha,\tau)$ function is dependant on α and τ, and changes with respect to time (t). Here α is twice the ratio of sediment heat capacity to that of the probe

$$\alpha = 2\pi a^2 \rho c S^{-1} \tag{B3}$$

which depends on the radius of the probe (a), sediment density (ρ), sediment specific heat (c) and the heat capacity of the probe (S). τ is a the dimensionless thermal time constant

$$\tau = \kappa_s t a^{-2} \tag{B4}$$

where κ_s is the sediment diffusivity. When solving for $F(\alpha,\tau)$, there are three unknown variables, ρ, c and κ_s. We use the conductivity-water content relation of Ratcliffe (1960) to determine ρc values for general ocean sediments (red clay and calcium carbonate),

$$\rho c = 5.79 - 3.67 k_s + 1.016 k_s^2 \tag{B5}$$

We are left with the unknown sediment thermal conductivity (k_s) in Eq. B5 and unknown sediment diffusivity (κ_s) in Eq. B4. We must now make an estimation of k_s, which in turn allows us to solve for κ_s,

$$\kappa_s = k_s (\rho c)^{-2} \tag{B6}$$

Once we have determined κ_s and ρc we can then solve for $F(\alpha,\tau)$, which is in turn plotted against temperature. As time approaches infinity (or $F(\alpha,\tau)$ approaches zero), the sediment temperature recorded by the probe approaches the original undisturbed background temperature (T_s). A best fit line through the Temperature vs. $F(\alpha,\tau)$ plot is

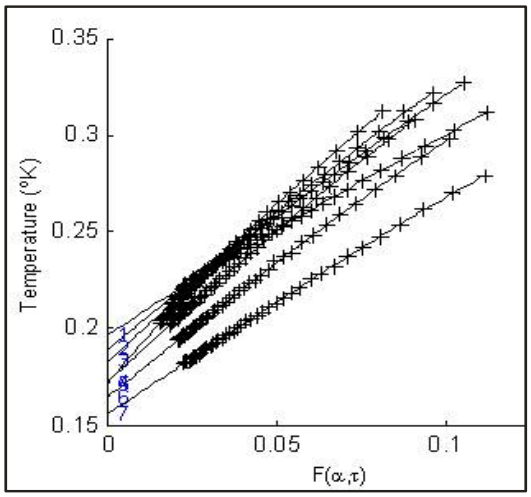

Figure B 4: Temperature vs. F(α,τ) showing thermal decay following frictional heating upon penetration for 7 thermistors. Best-fit lines through the intercept give T_s values (where F(α,τ) = 0).

used to determine this temperature as the y-intersect (where F(α,τ) equals zero and time equals infinity) gives the original background sediment temperature (T_s) (Fig. B3). In reality the plots in Figure B3 are not linear. This is most likely due to poor contact and the presence of water between the probe and the surrounding sediment. Once sediment temperatures at different depths are known geothermal gradient is easily calculated as it is simply the change in temperature with depth.

B.5.3 Determining Sediment Thermal Conductivity

The thermal decay curve following pulse heating can be used to determine the thermal conductivity once T_s has been determined as above. Plots of Temperature vs. F(α,τ) are also made for the thermal decay following pulse heating, and these plots generally record a more linear fit (Fig. B3). The plots in Figure B3 each start at zero (are shifted by 0.1 K for viewing ease) as the T_s calculated above is subtracted from the recorded T. It is important to note that now the source of the heat increase is derived from the central heater wire within the probe rather than

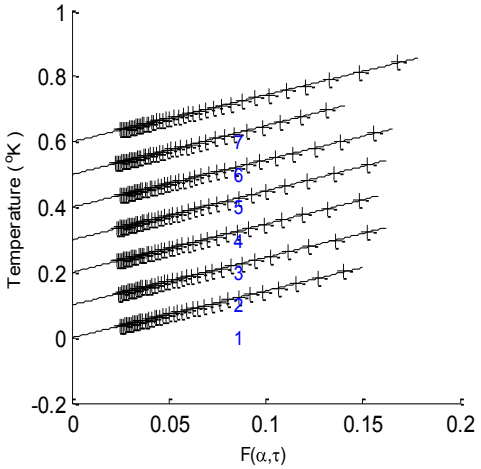

Figure B 3: Temperature vs. F(α,τ) showing thermal decay following pulse heating for 7 thermistors. Each plot is arbitrarily shifted by 0.1 °K so all plots can be seen.

externally at the boundary between the probe and the surrounding sediment. As the sensor string is filled with a poorly conducting mineral oil fluid there is a time delay of ~20-30 s between the time the temperature sensors located adjacent to the heater wire record the increase in temperature, and when the temperature increase reaches the probe sediment boundary. This time delay is varied such that background temperature in the plot of Figure B4 is the same as that in Figure B3.

The temperature increase following pulse heating ($\Delta T=T'(t')-T_s$) can be calculated at time t' following pulse heating. ΔT is calculated taking into account the continued decay of heat associated with the initial frictional heating. Variables T_s, α, τ and $F(\alpha,\tau)$ are the same as those described above and the values calculated in Eq. B2 are now used in Eq. B7.

$$\Delta T = [Q_p'(2\pi k_s t)^{-1}]\alpha\tau F(\alpha,\tau) \quad \text{(B7)}$$

The quantity of energy released by the heat pulse (Q_p) is known as this is a calibrated amount of heat applied from the probe's central heater wire. The only remaining variable in Eq. B7 is the sediment thermal conductivity (k_s). Rather than estimate this value as done initially when solving for $F(\alpha,\tau)$ in Eq. B2 we will now solve for k_s from Eq. B7. We solve for k_s multiple times using different τ values taking the average k_s as the accepted final value.

This new k_s value is placed back in Eq. B6 which is solved to determine a new value for κ_s. The new κ_s value can then be used in Eq. B4 and Eq. B2 to solve for τ and $F(\alpha,\tau)$ respectively, and the whole process is repeated iteratively (generally requires 2-3 iterations) until we have agreement between the k_s used to determine T_s from the frictional heating curve, and the k_s value determined using the pulse heating decay curve.

B.5.4 Calculating Heat Flow

Heat Flow (Q) may now be calculated as sediment temperature and thermal conductivity are known at different depths. Average geothermal gradient between consecutive depth points and average thermal conductivity (weighted average towards the lower conductivity values) are used to calculate heat flow (Eq. B1). This is the simplest method for determining heat flow. However, as conductivity may vary with depth there may be errors associated with using one average conductivity value for all depths. The Bullard depth plot was developed to account for vertical variations in conductivity (Bullard, 1939).

As sediment thermal conductivity is dependant on porosity (water content) and sediment type, any change over depth will result in a change in thermal conductivity. Temperature gradient varies inversely with thermal conductivity for constant heat flow, and thus a change in conductivity with depth results in a change in the calculated gradient. In order to remove this possible error, Bullard (1939) proposed plotting T as a function of R_s rather than z,

$$R_s = \Sigma_i \, (\Delta z_i / k_i) \qquad \text{(B8)}$$

where R_s, the thermal resistance depth referred to as the Bullard depth, takes into account variations in conductivity with depth. The assumption in the Bullard depth plot is that there is no longer any error in the conductivity values used, and that assuming constant vertical heat flow in a state of purely conductive heat transfer, the Bullard depth plot will produce a linear plot assuming these assumptions are correct. The final heat flow values reported are Bullard depth plot values, and represent a minimum associated error value due to the assumption of zero error in the conductivity values (Table 3.1). In order to err

on the side of caution, all data presented in this thesis report the error calculated from the simple uniform conductivity heat flow as the error calculated using the Bullard depth plots may underestimate the true error.

Appendix C: Heat Flow Data Tables

C.1 Torbrook Mound Heat Flow Stations

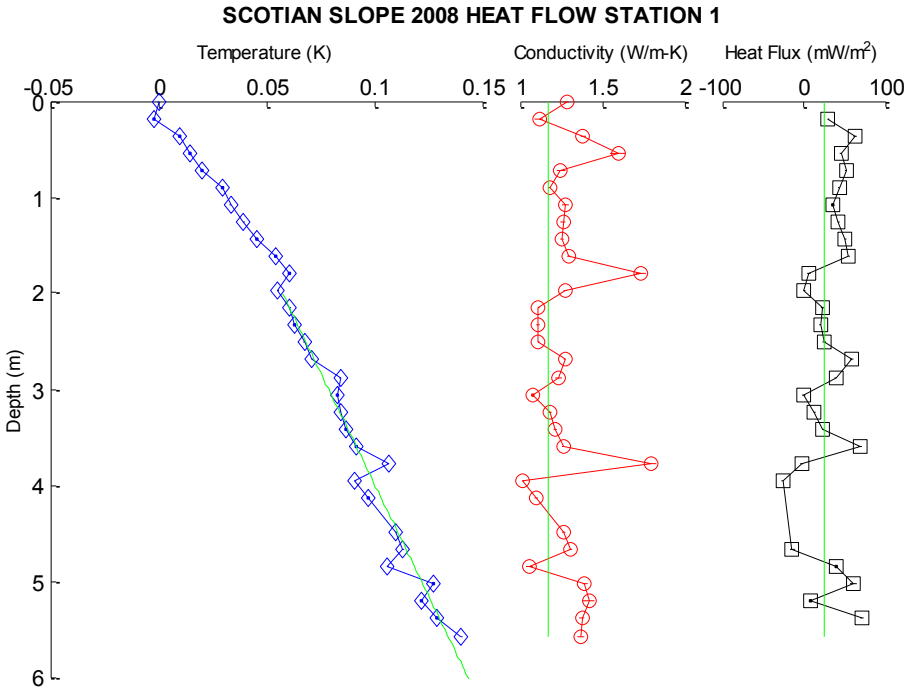

SCOTIAN SLOPE 2008 HEAT FLOW STATION 001
Tilt (deg)= 3.0

Therm #:	1	2	3	4	5	6	7	8
Depth (m):	5.572	5.393	5.213	5.033	4.853	4.674	4.494	4.314
Temp (mK):	128.9	118.5	110.3	116.2	94.3	103.3	99.1	----
Cond (W/m-K):	1.196	1.263	1.287	1.276	0.946	1.200	1.139	----

Therm #:	9	10	11	12	13	14	15	16
Depth (m):	4.134	3.955	3.775	3.595	3.415	3.236	3.056	2.876
Temp (mK):	86.0	79.6	----	80.9	75.1	72.7	70.2	72.5
Cond (W/m-K):	0.993	0.929	----	1.160	1.105	1.073	0.962	1.125

Therm #:	17	18	19	20	21	22	23	24
Depth (m):	2.696	2.517	2.337	2.157	1.977	1.798	1.618	1.438
Temp (mK):	60.0	55.4	51.2	49.3	44.1	49.4	44.0	34.5
Cond (W/m-K):	1.163	0.994	1.007	1.023	1.193	1.581	1.190	1.137

Therm #:	25	26	27	28	29	30	31	32
Depth (m):	1.258	1.079	0.899	0.719	0.539	0.360	0.180	0.000
Temp (mK):	----	----	----	----	----	----	----	----
Cond (W/m-K):	----	----	----	----	----	----	----	----

Gradient (mK/m)= 21.78 ± 0.62
Conductivity (W/m-K)= 1.067 ± 0.159
Heat Flow (mW/m^2)= 23.24 ± 4.12

SCOTIAN SLOPE 2008 HEAT FLOW STATION 2

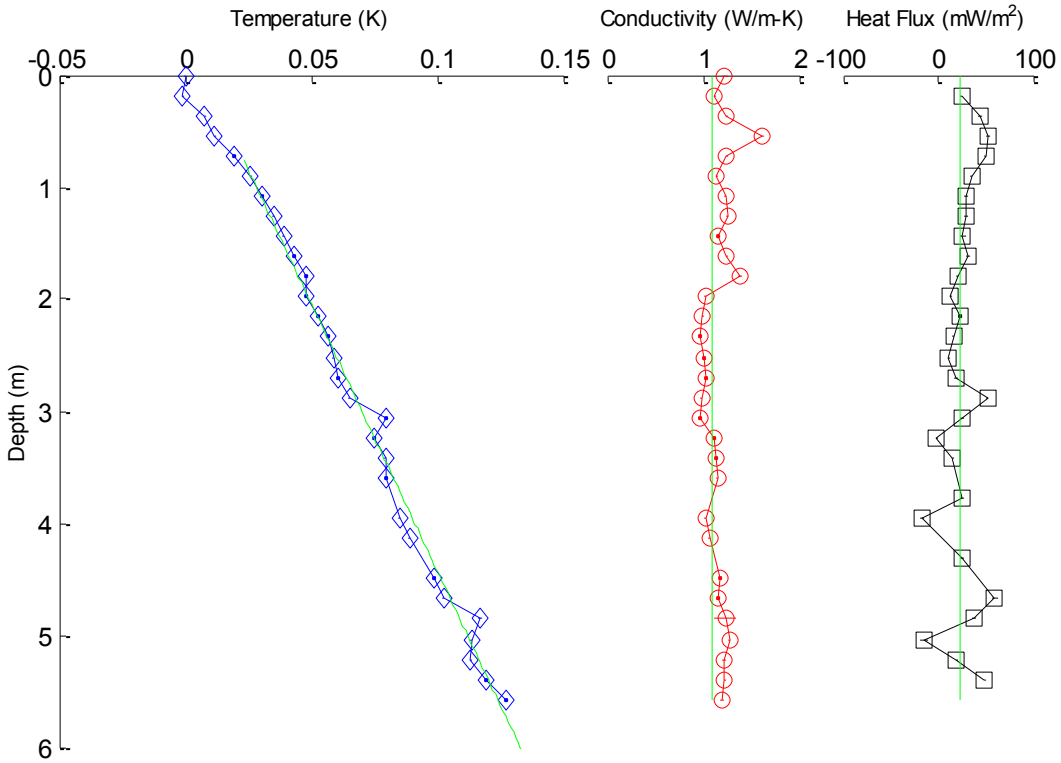

SCOTIAN SLOPE 2008 HEAT FLOW STATION 002
Tilt (deg)= 2.0

Therm #:	1	2	3	4	5	6	7	8
Depth (m):	5.577	5.397	5.217	5.037	4.857	4.677	4.497	4.317
Temp (mK):	122.5	114.2	108.0	108.4	112.1	97.4	93.6	----
Cond (W/m-K):	1.203	1.222	1.219	1.274	1.232	1.155	1.178	----

Therm #:	9	10	11	12	13	14	15	16
Depth (m):	4.137	3.958	3.778	3.598	3.418	3.238	3.058	2.878
Temp (mK):	83.7	79.9	----	74.5	74.2	69.6	74.6	60.2
Cond (W/m-K):	1.069	1.029	----	1.148	1.139	1.117	0.975	0.984

Therm #:	17	18	19	20	21	22	23	24
Depth (m):	2.698	2.518	2.339	2.159	1.979	1.799	1.619	1.439
Temp (mK):	55.4	53.5	51.6	47.5	43.1	42.8	37.9	33.7
Cond (W/m-K):	1.032	1.016	0.967	0.992	1.026	1.386	1.248	1.151

Therm #:	25	26	27	28	29	30	31	32
Depth (m):	1.259	1.079	0.899	0.720	0.540	0.360	0.180	0.000
Temp (mK):	29.7	25.3	21.0	----	----	----	----	----
Cond (W/m-K):	1.253	1.236	1.146	----	----	----	----	----

Gradient (mK/m)= 21.29 ± 0.47
Conductivity (W/m-K)= 1.098 ± 0.116
Heat Flow (mW/m^2)= 23.37 ± 2.99

SCOTIAN SLOPE 2008 HEAT FLOW STATION 3

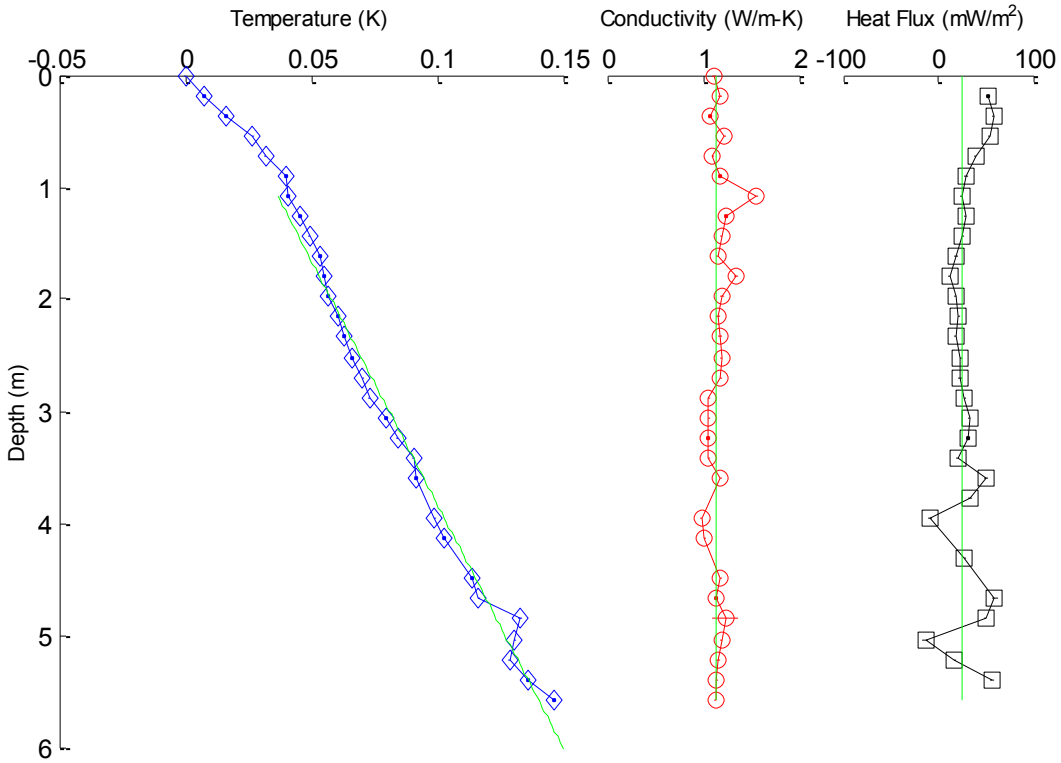

SCOTIAN SLOPE 2008 HEAT FLOW STATION 003
Tilt (deg)= 2.0

Therm #:	1	2	3	4	5	6	7	8
Depth (m):	5.577	5.397	5.217	5.037	4.857	4.677	4.497	4.317
Temp (mK):	123.8	113.7	106.0	108.3	110.1	93.8	91.2	----
Cond (W/m-K):	1.130	1.143	1.155	1.190	1.239	1.138	1.178	----

Therm #:	9	10	11	12	13	14	15	16
Depth (m):	4.137	3.958	3.778	3.598	3.418	3.238	3.058	2.878
Temp (mK):	80.2	76.4	----	68.8	68.0	61.7	57.2	50.6
Cond (W/m-K):	1.014	0.980	----	1.185	1.060	1.054	1.061	1.060

Therm #:	17	18	19	20	21	22	23	24
Depth (m):	2.698	2.518	2.339	2.159	1.979	1.799	1.619	1.439
Temp (mK):	47.8	43.5	40.6	38.0	33.8	32.5	30.7	26.6
Cond (W/m-K):	1.180	1.189	1.180	1.155	1.198	1.344	1.148	1.188

Therm #:	25	26	27	28	29	30	31	32
Depth (m):	1.259	1.079	0.899	0.720	0.540	0.360	0.180	0.000
Temp (mK):	22.8	----	17.1	----	----	----	----	----
Cond (W/m-K):	1.238	----	1.181	----	----	----	----	----

Gradient (mK/m)= 22.25 ± 0.52
Conductivity (W/m-K)= 1.146 ± 0.078
Heat Flow (mW/m^2)= 25.49 ± 2.33

SCOTIAN SLOPE 2008 HEAT FLOW STATION 4a

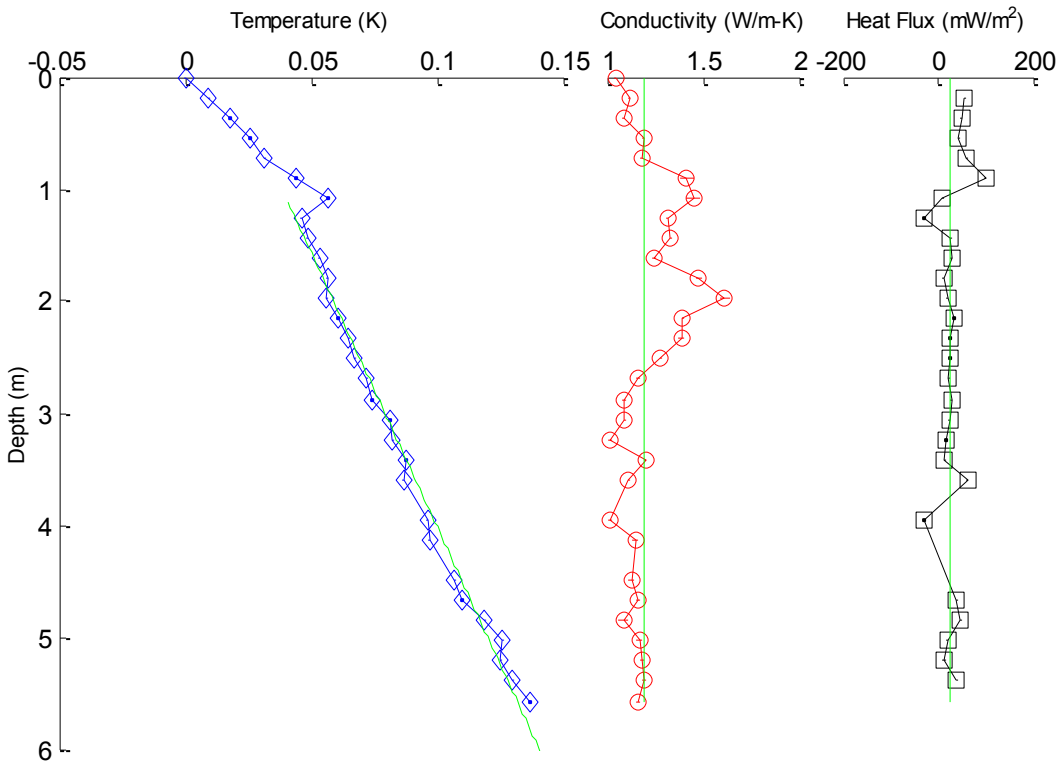

SCOTIAN SLOPE 2008 HEAT FLOW STATION 004
Tilt (deg)= 3.0

Therm #:	1	2	3	4	5	6	7	8
Depth (m):	5.572	5.393	5.213	5.033	4.853	4.674	4.494	4.314
Temp (mK):	182.8	175.7	170.8	171.8	164.7	155.9	152.8	----
Cond (W/m-K):	1.165	1.193	1.183	1.170	1.084	1.166	1.125	----

Therm #:	9	10	11	12	13	14	15	16
Depth (m):	4.134	3.955	3.775	3.595	3.415	3.236	3.056	2.876
Temp (mK):	142.7	142.1	----	132.4	133.3	128.1	127.1	120.0
Cond (W/m-K):	1.148	1.011	----	1.112	1.199	1.018	1.091	1.090

Therm #:	17	18	19	20	21	22	23	24
Depth (m):	2.696	2.517	2.337	2.157	1.977	1.798	1.618	1.438
Temp (mK):	117.9	113.2	110.8	106.8	102.0	102.3	99.2	94.4
Cond (W/m-K):	1.163	1.277	1.386	1.392	1.614	1.478	1.245	1.332

Therm #:	25	26	27	28	29	30	31	32
Depth (m):	1.258	1.079	0.899	0.719	0.539	0.360	0.180	0.000
Temp (mK):	92.2	----	89.8	----	----	----	----	----
Cond (W/m-K):	1.313	----	1.414	----	----	----	----	----

Gradient (mK/m)= 19.56 ± 0.59
Conductivity (W/m-K)= 1.192 ± 0.150
Heat Flow (mW/m^2)= 23.32 ± 3.64

SCOTIAN SLOPE 2008 HEAT FLOW STATION 5

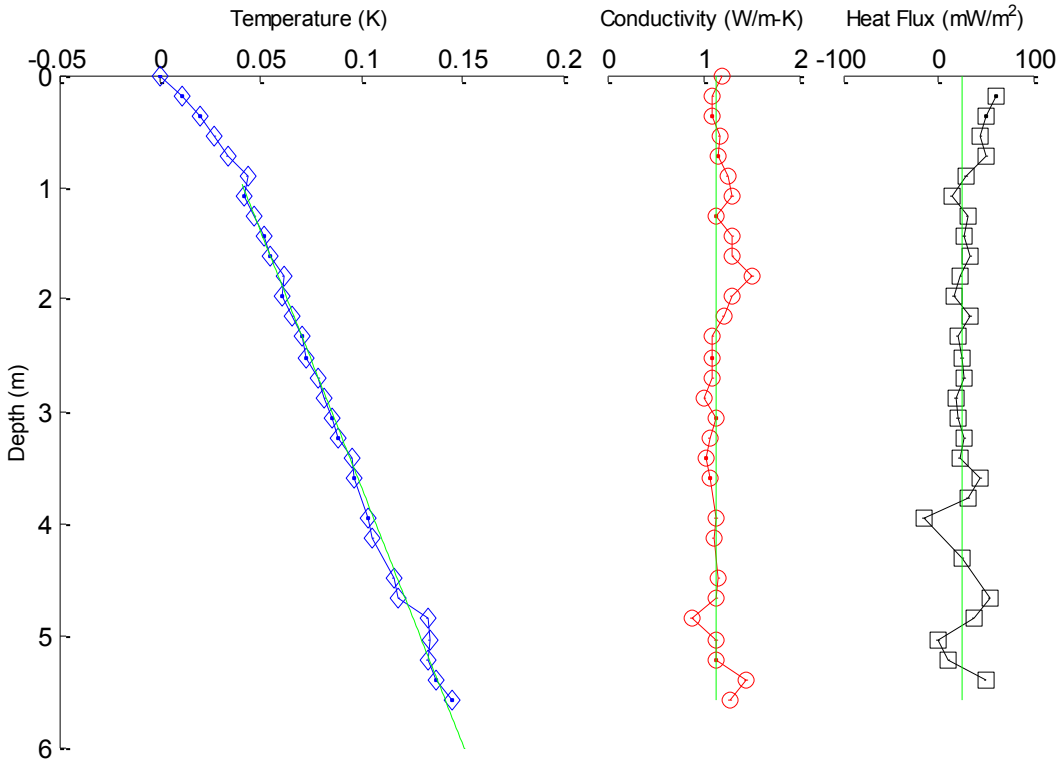

SCOTIAN SLOPE 2008 HEAT FLOW STATION 005
Tilt (deg)= 2.0

Therm #:	1	2	3	4	5	6	7	8
Depth (m):	5.577	5.397	5.217	5.037	4.857	4.677	4.497	4.317
Temp (mK):	127.6	119.7	115.2	116.2	115.3	101.2	98.4	----
Cond (W/m-K):	1.283	1.449	1.136	1.132	0.888	1.141	1.162	----

Therm #:	9	10	11	12	13	14	15	16
Depth (m):	4.137	3.958	3.778	3.598	3.418	3.238	3.058	2.878
Temp (mK):	88.2	85.9	----	79.0	77.6	71.0	68.2	64.2
Cond (W/m-K):	1.106	1.136	----	1.070	1.029	1.067	1.133	1.016

Therm #:	17	18	19	20	21	22	23	24
Depth (m):	2.698	2.518	2.339	2.159	1.979	1.799	1.619	1.439
Temp (mK):	61.4	55.1	53.0	48.5	43.1	43.8	37.4	34.3
Cond (W/m-K):	1.101	1.090	1.101	1.214	1.293	1.514	1.309	1.309

Therm #:	25	26	27	28	29	30	31	32
Depth (m):	1.259	1.079	0.899	0.720	0.540	0.360	0.180	0.000
Temp (mK):	29.7	----	25.9	----	----	----	----	----
Cond (W/m-K):	1.139	----	1.251	----	----	----	----	----

Gradient (mK/m)= 22.02 ± 0.31
Conductivity (W/m-K)= 1.132 ± 0.141
Heat Flow (mW/m^2)= 24.92 ± 3.45

SCOTIAN SLOPE 2008 HEAT FLOW STATION 6

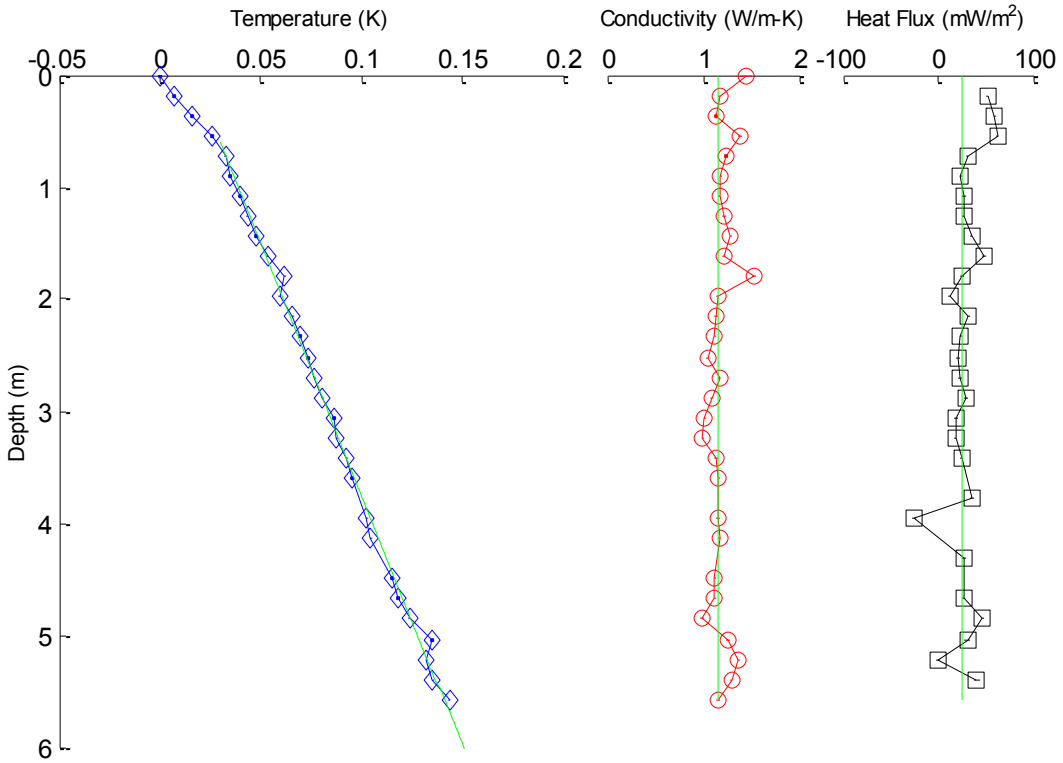

SCOTIAN SLOPE 2008 HEAT FLOW STATION 006
Tilt (deg)= 2.0

Therm #:	1	2	3	4	5	6	7	8
Depth (m):	5.577	5.397	5.217	5.037	4.857	4.677	4.497	4.317
Temp (mK):	125.6	117.4	114.4	117.1	105.7	100.1	97.3	----
Cond (W/m-K):	1.158	1.297	1.373	1.267	0.992	1.124	1.122	----

Therm #:	9	10	11	12	13	14	15	16
Depth (m):	4.137	3.958	3.778	3.598	3.418	3.238	3.058	2.878
Temp (mK):	86.5	84.5	----	77.4	74.9	69.6	68.3	62.8
Cond (W/m-K):	1.172	1.157	----	1.164	1.136	0.998	1.013	1.086

Therm #:	17	18	19	20	21	22	23	24
Depth (m):	2.698	2.518	2.339	2.159	1.979	1.799	1.619	1.439
Temp (mK):	58.6	55.6	51.4	47.9	41.2	44.2	35.3	29.8
Cond (W/m-K):	1.175	1.043	1.116	1.133	1.151	1.526	1.214	1.289

Therm #:	25	26	27	28	29	30	31	32
Depth (m):	1.259	1.079	0.899	0.720	0.540	0.360	0.180	0.000
Temp (mK):	25.6	----	17.1	14.6	----	----	----	----
Cond (W/m-K):	1.217	----	1.186	1.237	----	----	----	----

Gradient (mK/m)= 22.34 ± 0.32
Conductivity (W/m-K)= 1.154 ± 0.118
Heat Flow (mW/m^2)= 25.77 ± 2.99

SCOTIAN SLOPE 2008 HEAT FLOW STATION 7

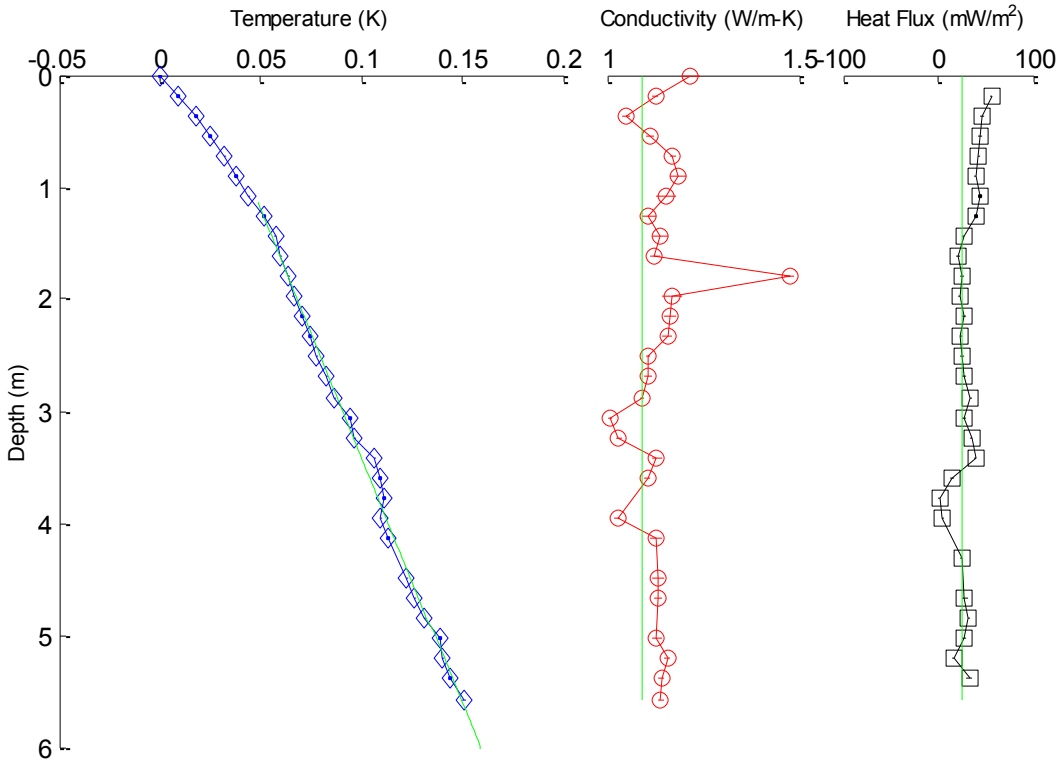

SCOTIAN SLOPE 2008 HEAT FLOW STATION 007
Tilt (deg)= 3.0

Therm #:	1	2	3	4	5	6	7	8
Depth (m):	5.572	5.393	5.213	5.033	4.853	4.674	4.494	4.314
Temp (mK):	122.8	116.4	112.3	111.4	103.6	98.4	94.7	----
Cond (W/m-K):	1.141	1.142	1.157	1.129	0.902	1.134	1.132	----

Therm #:	9	10	11	12	13	14	15	16
Depth (m):	4.134	3.955	3.775	3.595	3.415	3.236	3.056	2.876
Temp (mK):	85.1	81.7	----	81.4	78.7	68.9	66.4	59.0
Cond (W/m-K):	1.128	1.027	----	1.104	1.129	1.030	1.006	1.090

Therm #:	17	18	19	20	21	22	23	24
Depth (m):	2.696	2.517	2.337	2.157	1.977	1.798	1.618	1.438
Temp (mK):	55.0	50.1	46.8	42.9	38.3	36.0	32.0	29.3
Cond (W/m-K):	1.106	1.107	1.158	1.165	1.169	1.475	1.124	1.138

Therm #:	25	26	27	28	29	30	31	32
Depth (m):	1.258	1.079	0.899	0.719	0.539	0.360	0.180	0.000
Temp (mK):	23.7	----	----	----	----	----	----	----
Cond (W/m-K):	1.108	----	----	----	----	----	----	----

Gradient (mK/m)= 22.49 ± 0.46
Conductivity (W/m-K)= 1.093 ± 0.101
Heat Flow (mW/m^2)= 24.57 ± 2.77

C-2: Line 1 Heat Flow Stations

SCOTIAN SLOPE 2008 HEAT FLOW STATION 119
Tilt (deg)= 0.5

Therm #:	1	2	3	4	5	6	7	8
Depth (m):	5.580	5.400	5.220	5.040	4.860	4.680	4.500	4.320
Temp (mK):	----	277.1	266.5	253.8	252.9	244.8	----	----
Cond (W/m-K):	0.921	1.115	1.071	1.128	1.238	1.043	----	----

Therm #:	9	10	11	12	13	14	15	16
Depth (m):	4.140	3.960	3.780	3.600	3.420	3.240	3.060	2.880
Temp (mK):	216.0	207.8	----	192.7	179.6	179.9	177.8	164.9
Cond (W/m-K):	1.057	0.960	----	0.983	0.972	1.044	1.088	1.025

Therm #:	17	18	19	20	21	22	23	24
Depth (m):	2.700	2.520	2.340	2.160	1.980	1.800	1.620	1.440
Temp (mK):	157.7	150.2	138.5	127.8	115.0	118.9	103.7	100.9
Cond (W/m-K):	1.031	1.020	0.997	0.997	0.947	1.301	1.080	1.040

Therm #:	25	26	27	28	29	30	31	32
Depth (m):	1.260	1.080	0.900	0.720	0.540	0.360	0.180	0.000
Temp (mK):	93.8	----	----	----	----	----	----	----
Cond (W/m-K):	1.047	----	----	----	----	----	----	----

Gradient (mK/m)= 44.34 ± 0.64
Conductivity (W/m-K)= 0.987 ± 0.108
Heat Flow (mW/m^2)= 43.75 ± 5.40

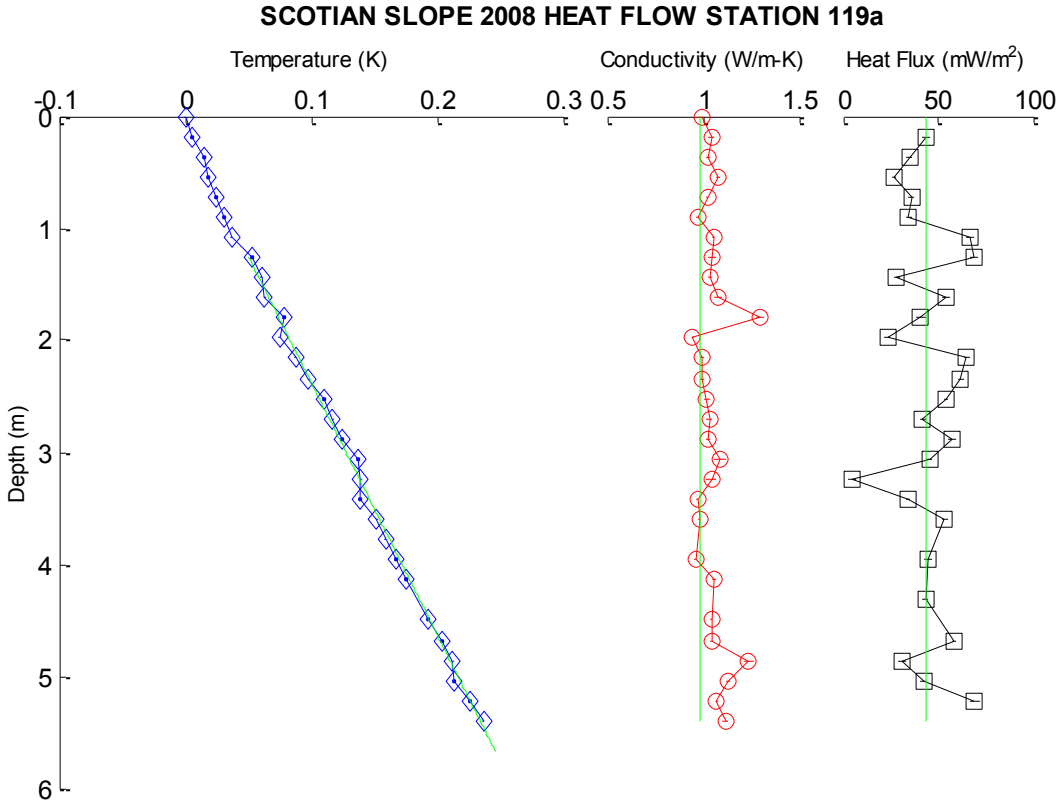

SCOTIAN SLOPE 2008 HEAT FLOW STATION 118
Tilt (deg)= 3.5

Therm #:	1	2	3	4	5	6	7	8
Depth (m):	5.570	5.390	5.210	5.031	4.851	4.671	4.492	4.312
Temp (mK):	138.0	150.6	144.1	131.1	139.5	120.9	114.1	----
Cond (W/m-K):	0.903	1.057	1.059	1.086	1.055	1.036	1.069	----

Therm #:	9	10	11	12	13	14	15	16
Depth (m):	4.132	3.953	3.773	3.593	3.414	3.234	3.054	2.875
Temp (mK):	98.5	90.3	----	77.2	70.7	62.4	55.8	49.2
Cond (W/m-K):	1.348	1.008	----	1.064	1.104	1.148	1.001	0.978

Therm #:	17	18	19	20	21	22	23	24
Depth (m):	2.695	2.515	2.336	2.156	1.976	1.797	1.617	1.437
Temp (mK):	42.0	33.5	26.4	12.6	4.6	-0.6	-8.1	-10.5
Cond (W/m-K):	0.965	0.932	0.979	0.992	1.000	1.202	1.065	1.093

Therm #:	25	26	27	28	29	30	31	32
Depth (m):	1.258	1.078	0.898	0.719	0.539	0.359	0.180	0.000
Temp (mK):	-16.6	-27.5	-33.8	-41.0	----	----	----	----
Cond (W/m-K):	1.089	1.072	1.020	0.997	----	----	----	----

Gradient (mK/m)= 41.31 ± 0.46
Conductivity (W/m-K)= 1.054 ± 0.087
Heat Flow (mW/m^2)= 43.54 ± 4.09

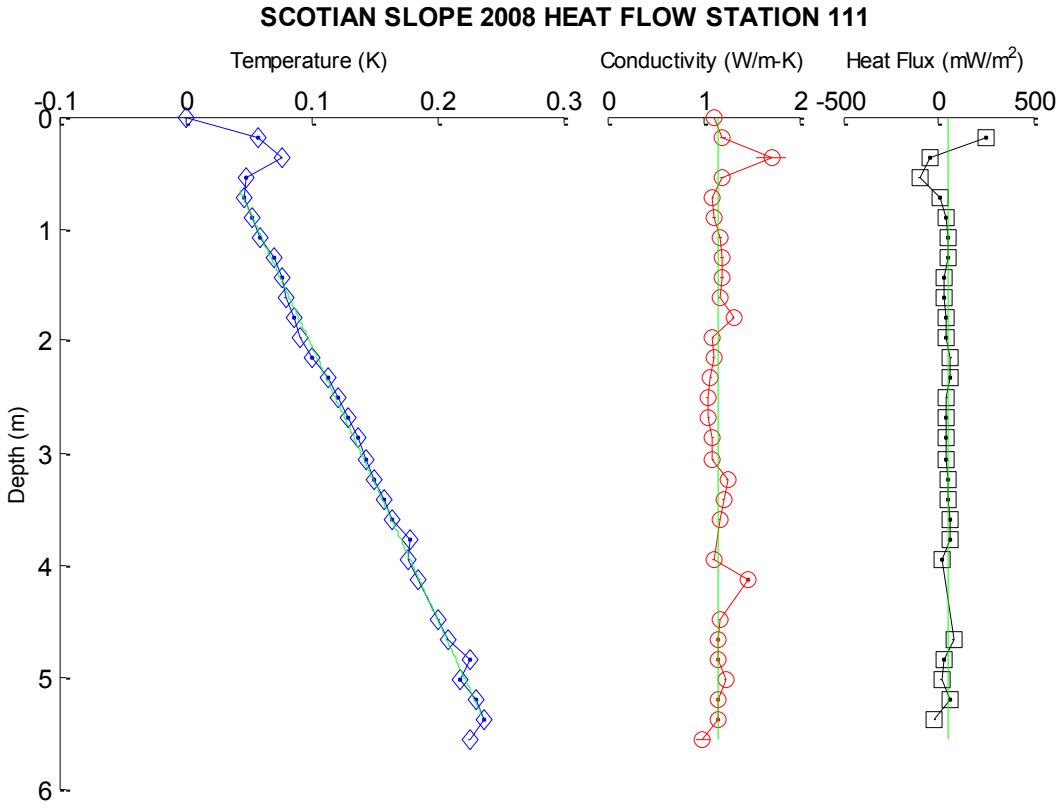

SCOTIAN SLOPE 2008 HEAT FLOW STATION 117
Tilt (deg)= 1.0

Therm #:	1	2	3	4	5	6	7	8
Depth (m):	5.579	5.399	5.219	5.039	4.859	4.679	4.499	4.319
Temp (mK):	215.2	216.6	207.2	190.4	189.4	182.4	169.7	----
Cond (W/m-K):	1.244	1.209	1.189	1.189	1.135	1.190	1.077	----

Therm #:	9	10	11	12	13	14	15	16
Depth (m):	4.139	3.959	3.779	3.599	3.419	3.240	3.060	2.880
Temp (mK):	147.3	142.0	----	129.2	119.2	111.9	----	94.3
Cond (W/m-K):	1.027	1.019	----	1.107	1.071	1.053	----	1.057

Therm #:	17	18	19	20	21	22	23	24
Depth (m):	2.700	2.520	2.340	2.160	1.980	1.800	1.620	1.440
Temp (mK):	84.3	73.6	71.5	56.2	47.0	44.8	33.3	27.5
Cond (W/m-K):	1.069	1.045	1.026	1.012	1.059	1.286	1.107	1.130

Therm #:	25	26	27	28	29	30	31	32
Depth (m):	1.260	1.080	0.900	0.720	0.540	0.360	0.180	0.000
Temp (mK):	22.5	----	----	----	----	----	----	----
Cond (W/m-K):	1.112	----	----	----	----	----	----	----

Gradient (mK/m)= 47.09 ± 0.56
Conductivity (W/m-K)= 1.079 ± 0.082
Heat Flow (mW/m^2)= 50.82 ± 4.47

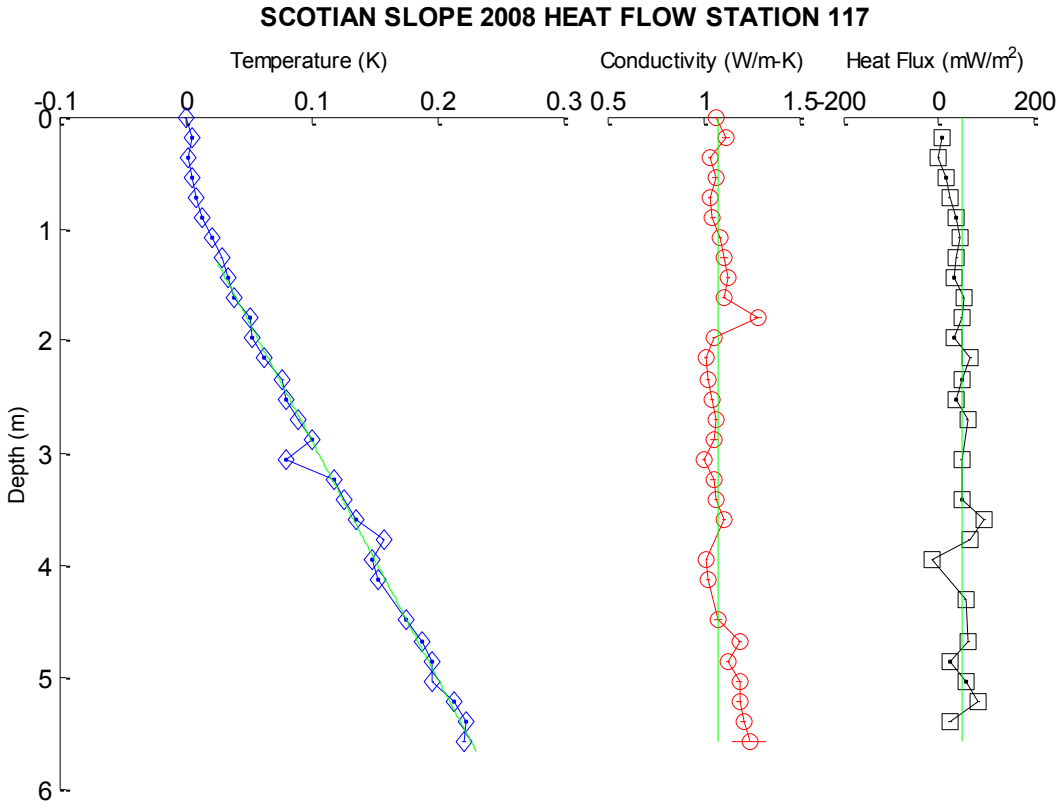

SCOTIAN SLOPE 2008 HEAT FLOW STATION 115
Tilt (deg)= 1.0

Therm #:	1	2	3	4	5	6	7	8
Depth (m):	5.579	5.399	5.219	5.039	4.859	4.679	4.499	4.319
Temp (mK):	207.6	199.5	187.8	173.6	171.1	162.9	153.7	----
Cond (W/m-K):	1.047	1.091	1.066	1.148	1.403	1.045	1.089	----

Therm #:	9	10	11	12	13	14	15	16
Depth (m):	4.139	3.959	3.779	3.599	3.419	3.240	3.060	2.880
Temp (mK):	132.3	159.1	----	113.2	103.5	92.6	81.5	73.7
Cond (W/m-K):	1.081	1.628	----	1.139	0.968	0.957	0.978	0.916

Therm #:	17	18	19	20	21	22	23	24
Depth (m):	2.700	2.520	2.340	2.160	1.980	1.800	1.620	1.440
Temp (mK):	63.9	51.9	40.1	27.2	16.4	10.2	-3.8	-13.2
Cond (W/m-K):	0.993	0.936	1.004	0.986	1.025	1.202	1.049	1.009

Therm #:	25	26	27	28	29	30	31	32
Depth (m):	1.260	1.080	0.900	0.720	0.540	0.360	0.180	0.000
Temp (mK):	-20.7	----	----	----	----	----	----	----
Cond (W/m-K):	0.968	----	----	----	----	----	----	----

Gradient (mK/m)= 52.63 ± 1.05
Conductivity (W/m-K)= 1.029 ± 0.163
Heat Flow (mW/m^2)= 54.19 ± 9.64

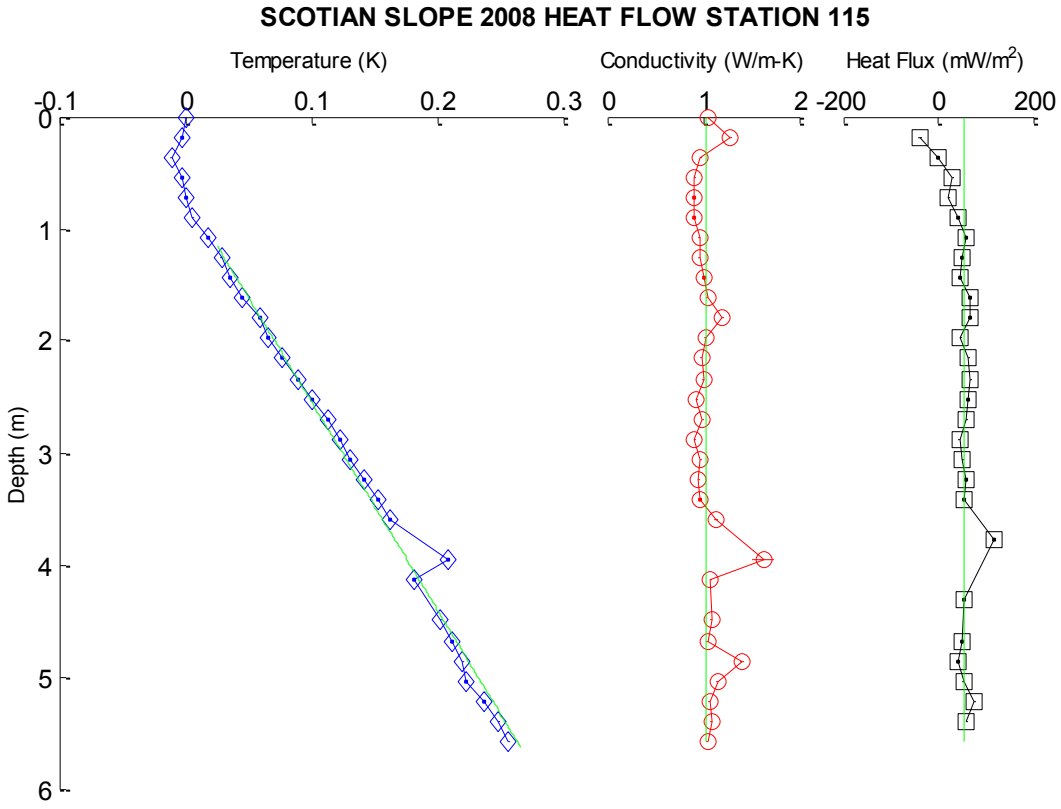

SCOTIAN SLOPE 2008 HEAT FLOW STATION 114
Tilt (deg)= 0.0

Therm #:	1	2	3	4	5	6	7	8
Depth (m):	5.580	5.400	5.220	5.040	4.860	4.680	4.500	4.320
Temp (mK):	184.1	176.2	168.7	153.6	154.2	144.2	137.4	----
Cond (W/m-K):	1.045	1.061	1.075	1.058	1.036	1.026	1.024	----

Therm #:	9	10	11	12	13	14	15	16
Depth (m):	4.140	3.960	3.780	3.600	3.420	3.240	3.060	2.880
Temp (mK):	119.4	113.8	----	96.2	91.9	86.3	76.8	70.7
Cond (W/m-K):	0.920	0.866	----	0.944	0.962	0.958	0.995	0.978

Therm #:	17	18	19	20	21	22	23	24
Depth (m):	2.700	2.520	2.340	2.160	1.980	1.800	1.620	1.440
Temp (mK):	60.7	52.0	40.2	31.4	24.9	18.7	7.8	0.0
Cond (W/m-K):	0.987	1.007	0.950	0.895	0.939	1.112	0.920	0.959

Therm #:	25	26	27	28	29	30	31	32
Depth (m):	1.260	1.080	0.900	0.720	0.540	0.360	0.180	0.000
Temp (mK):	-4.4	----	-17.8	----	----	----	----	----
Cond (W/m-K):	1.009	----	0.854	----	----	----	----	----

Gradient (mK/m)= 43.71 ± 0.28
Conductivity (W/m-K)= 0.964 ± 0.067
Heat Flow (mW/m^2)= 42.13 ± 3.22

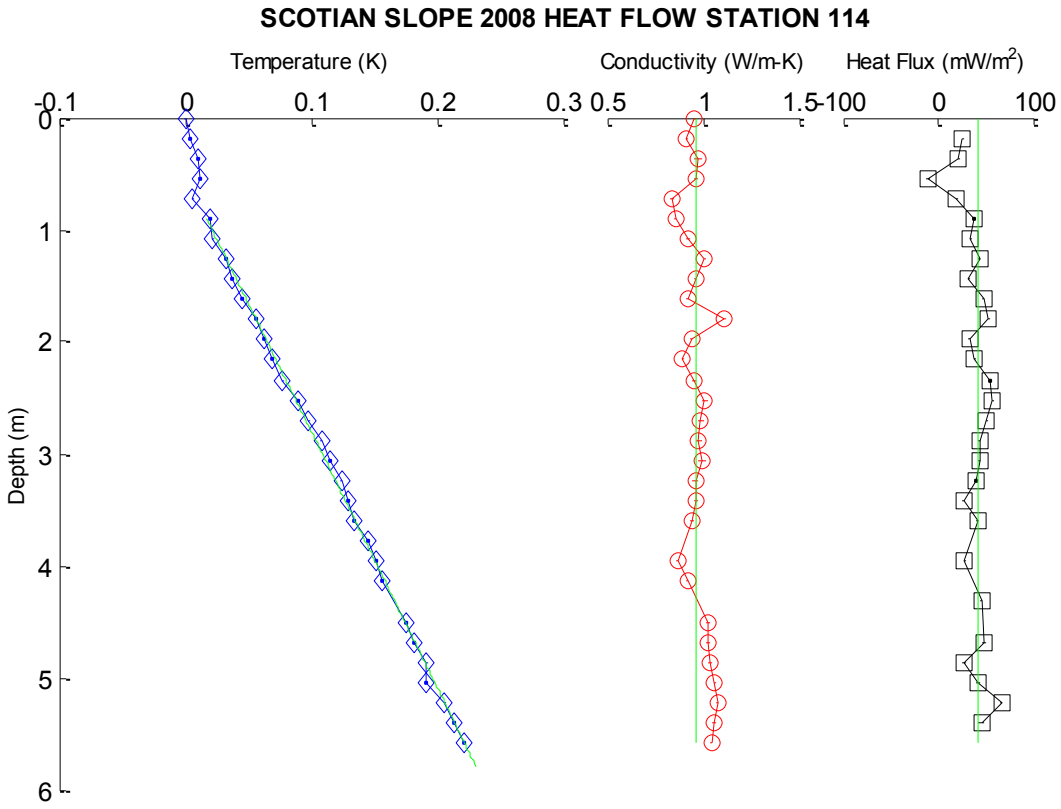

SCOTIAN SLOPE 2008 HEAT FLOW STATION 113
Tilt (deg)= 1.0

Therm #:	1	2	3	4	5	6	7	8
Depth (m):	5.579	5.399	5.219	5.039	4.859	4.679	4.499	4.319
Temp (mK):	160.6	153.6	146.4	133.2	127.5	117.5	110.1	----
Cond (W/m-K):	0.906	0.959	0.966	1.002	1.015	1.031	1.026	----

Therm #:	9	10	11	12	13	14	15	16
Depth (m):	4.139	3.959	3.779	3.599	3.419	3.240	3.060	2.880
Temp (mK):	91.5	85.8	81.0	70.8	68.9	64.8	55.8	46.7
Cond (W/m-K):	0.989	0.969	1.458	0.965	0.997	0.969	0.995	0.950

Therm #:	17	18	19	20	21	22	23	24
Depth (m):	2.700	2.520	2.340	2.160	1.980	1.800	1.620	1.440
Temp (mK):	37.9	25.8	17.8	9.7	2.3	-2.9	-10.6	-18.8
Cond (W/m-K):	0.977	0.924	0.920	0.894	0.905	1.105	0.912	0.905

Therm #:	25	26	27	28	29	30	31	32
Depth (m):	1.260	1.080	0.900	0.720	0.540	0.360	0.180	0.000
Temp (mK):	-21.2	----	-36.1	-42.3	----	----	----	----
Cond (W/m-K):	0.919	----	0.857	0.880	----	----	----	----

Gradient (mK/m)= 42.94 ± 0.38
Conductivity (W/m-K)= 0.930 ± 0.120
Heat Flow (mW/m^2)= 39.95 ± 5.50

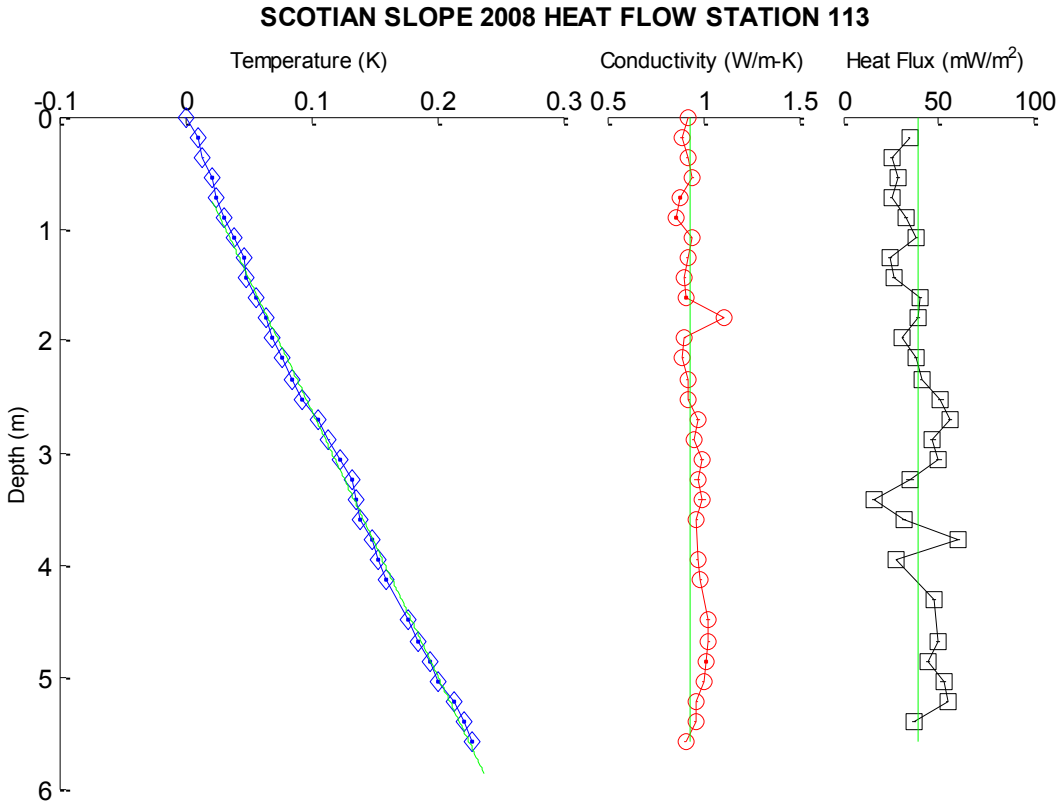

SCOTIAN SLOPE 2008 HEAT FLOW STATION 112
Tilt (deg)= 2.0

Therm #:	1	2	3	4	5	6	7	8
Depth (m):	5.577	5.397	5.217	5.037	4.857	4.677	4.497	4.317
Temp (mK):	210.2	202.0	193.9	178.5	176.2	166.3	158.6	----
Cond (W/m-K):	1.206	1.096	1.063	1.122	1.056	1.037	1.037	----

Therm #:	9	10	11	12	13	14	15	16
Depth (m):	4.137	3.958	3.778	3.598	3.418	3.238	3.058	2.878
Temp (mK):	139.5	129.2	----	107.4	95.7	85.7	76.3	67.5
Cond (W/m-K):	0.964	0.982	----	1.467	1.090	1.050	1.051	1.006

Therm #:	17	18	19	20	21	22	23	24
Depth (m):	2.698	2.518	2.339	2.159	1.979	1.799	1.619	1.439
Temp (mK):	58.7	48.2	38.9	31.9	22.0	12.6	----	-2.8
Cond (W/m-K):	1.093	0.974	0.956	1.032	1.122	1.372	----	1.157

Therm #:	25	26	27	28	29	30	31	32
Depth (m):	1.259	1.079	0.899	0.720	0.540	0.360	0.180	0.000
Temp (mK):	-10.8	----	----	----	----	----	----	----
Cond (W/m-K):	1.016	----	----	----	----	----	----	----

Gradient (mK/m)= 51.99 ± 0.33
Conductivity (W/m-K)= 1.047 ± 0.129
Heat Flow (mW/m^2)= 54.41 ± 7.04

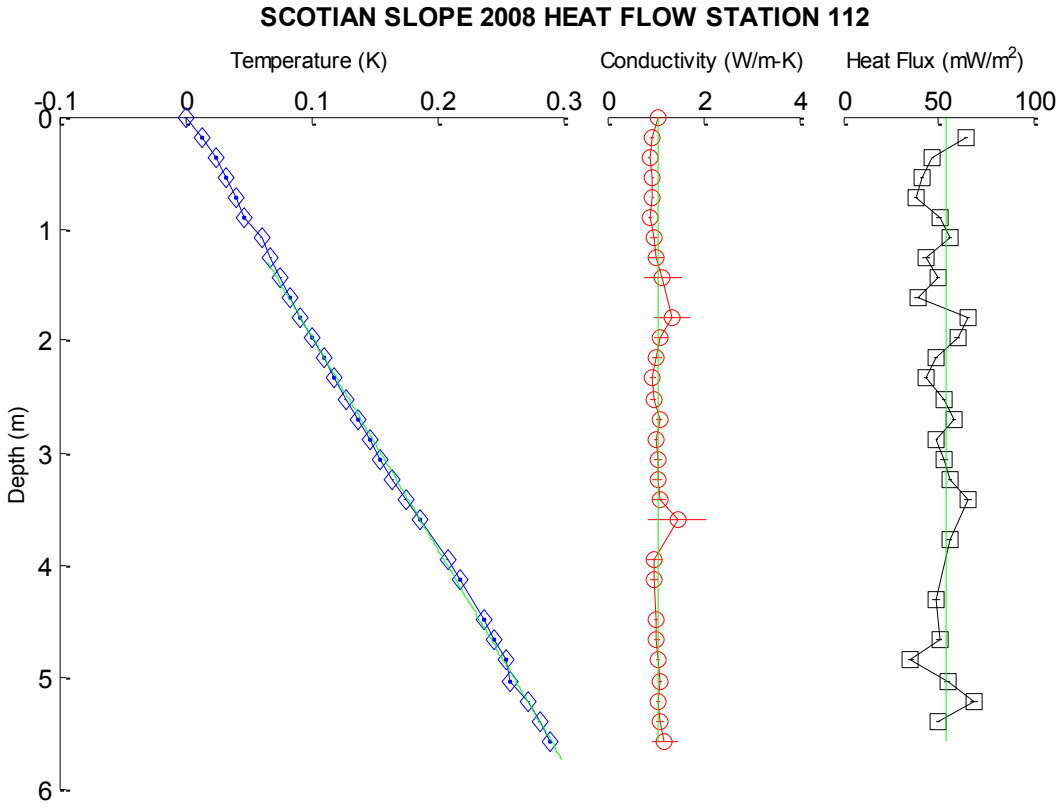

SCOTIAN SLOPE 2008 HEAT FLOW STATION 111
Tilt (deg)= 0.0

Therm #:	1	2	3	4	5	6	7	8
Depth (m):	5.580	5.400	5.220	5.040	4.860	4.680	4.500	4.320
Temp (mK):	278.7	267.0	254.1	236.4	231.5	220.4	209.1	----
Cond (W/m-K):	1.155	1.120	1.115	1.080	1.029	1.038	1.013	----

Therm #:	9	10	11	12	13	14	15	16
Depth (m):	4.140	3.960	3.780	3.600	3.420	3.240	3.060	2.880
Temp (mK):	180.7	170.5	----	147.7	134.8	122.4	111.6	103.5
Cond (W/m-K):	1.082	1.046	----	1.082	1.053	1.035	1.022	1.053

Therm #:	17	18	19	20	21	22	23	24
Depth (m):	2.700	2.520	2.340	2.160	1.980	1.800	1.620	1.440
Temp (mK):	92.0	77.8	69.0	58.4	44.4	29.3	21.8	13.1
Cond (W/m-K):	1.047	0.932	0.920	0.933	0.965	1.168	1.024	0.984

Therm #:	25	26	27	28	29	30	31	32
Depth (m):	1.260	1.080	0.900	0.720	0.540	0.360	0.180	0.000
Temp (mK):	1.0	----	-22.3	-33.9	-45.9	-55.0	-69.6	----
Cond (W/m-K):	0.958	----	0.856	0.912	0.971	0.973	1.025	----

Gradient (mK/m)= 64.05 ± 0.24
Conductivity (W/m-K)= 0.966 ± 0.092
Heat Flow (mW/m^2)= 61.88 ± 6.11

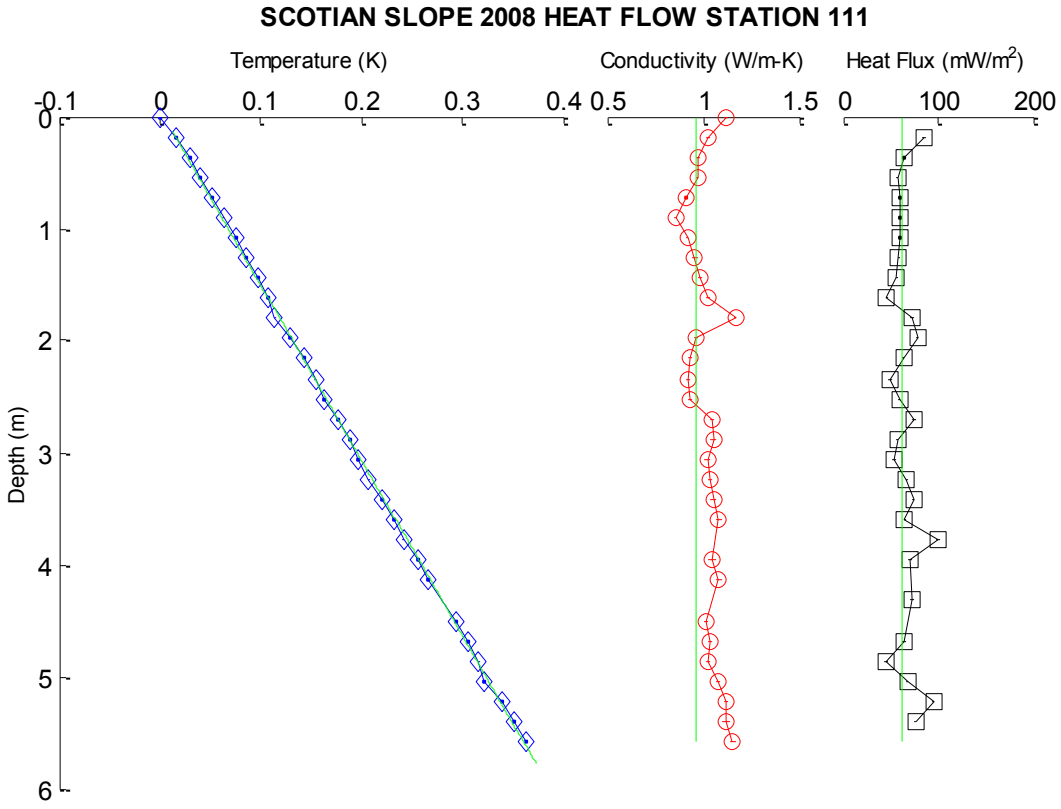

SCOTIAN SLOPE 2008 HEAT FLOW STATION 110
Tilt (deg)= 1.5

Therm #:	1	2	3	4	5	6	7	8
Depth (m):	5.578	5.398	5.218	5.038	4.858	4.678	4.498	4.319
Temp (mK):	99.2	91.2	82.5	70.8	64.9	50.5	46.2	----
Cond (W/m-K):	0.960	1.021	0.973	1.016	0.974	1.017	1.065	----

Therm #:	9	10	11	12	13	14	15	16
Depth (m):	4.139	3.959	3.779	3.599	3.419	3.239	3.059	2.879
Temp (mK):	24.7	17.4	----	2.4	-7.0	-14.1	-22.2	-29.1
Cond (W/m-K):	1.014	0.930	----	1.011	0.946	0.984	0.959	0.928

Therm #:	17	18	19	20	21	22	23	24
Depth (m):	2.699	2.519	2.339	2.159	1.979	1.799	1.619	1.440
Temp (mK):	-35.3	-43.2	-52.4	-61.7	-69.4	----	----	-89.6
Cond (W/m-K):	0.995	1.010	0.953	0.895	0.917	----	----	0.939

Therm #:	25	26	27	28	29	30	31	32
Depth (m):	1.260	1.080	0.900	0.720	0.540	0.360	0.180	0.000
Temp (mK):	-96.6	----	-113.2	----	----	----	----	----
Cond (W/m-K):	0.868	----	0.930	----	----	----	----	----

Gradient (mK/m)= 45.02 ± 0.46
Conductivity (W/m-K)= 0.945 ± 0.052
Heat Flow (mW/m^2)= 42.53 ± 2.79

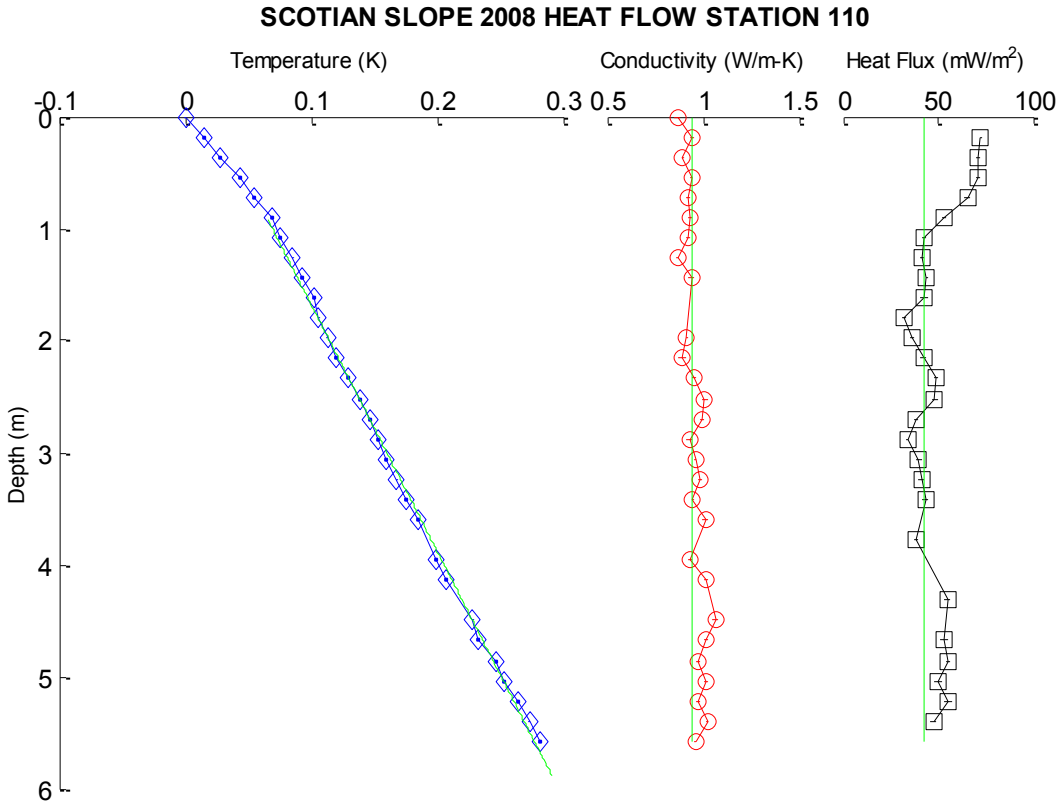

SCOTIAN SLOPE 2008 HEAT FLOW STATION 109
Tilt (deg)= 1.5

Therm #:	1	2	3	4	5	6	7	8
Depth (m):	5.578	5.398	5.218	5.038	4.858	4.678	4.498	4.319
Temp (mK):	117.2	112.4	103.2	93.2	87.8	79.5	75.5	----
Cond (W/m-K):	1.045	1.094	1.087	1.112	1.026	1.036	1.076	----

Therm #:	9	10	11	12	13	14	15	16
Depth (m):	4.139	3.959	3.779	3.599	3.419	3.239	3.059	2.879
Temp (mK):	65.0	52.4	----	40.2	32.8	22.2	16.5	10.0
Cond (W/m-K):	1.116	0.927	----	1.015	0.959	0.950	0.995	0.978

Therm #:	17	18	19	20	21	22	23	24
Depth (m):	2.699	2.519	2.339	2.159	1.979	1.799	1.619	1.440
Temp (mK):	1.7	-5.8	-12.0	-19.4	-26.1	-32.3	-37.7	-43.3
Cond (W/m-K):	1.074	1.042	0.995	0.969	0.934	1.086	0.965	1.009

Therm #:	25	26	27	28	29	30	31	32
Depth (m):	1.260	1.080	0.900	0.720	0.540	0.360	0.180	0.000
Temp (mK):	-51.8	----	----	----	----	----	----	----
Cond (W/m-K):	0.978	----	----	----	----	----	----	----

Gradient (mK/m)= 39.32 ± 0.44
Conductivity (W/m-K)= 1.007 ± 0.058
Heat Flow (mW/m^2)= 39.61 ± 2.74

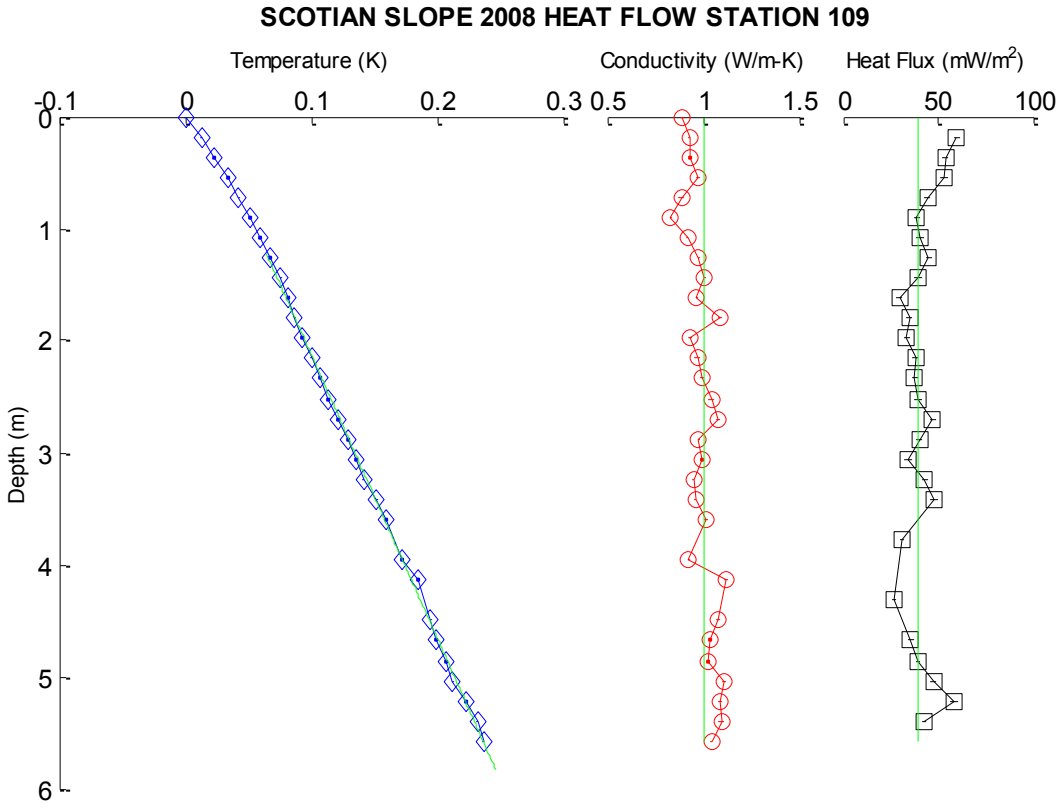

SCOTIAN SLOPE 2008 HEAT FLOW STATION 108
Tilt (deg)= 1.5

Therm #:	1	2	3	4	5	6	7	8
Depth (m):	5.578	5.398	5.218	5.038	4.858	4.678	4.498	4.319
Temp (mK):	59.3	51.4	46.8	39.3	33.4	23.8	19.4	----
Cond (W/m-K):	1.028	1.064	1.221	1.242	1.021	1.053	1.035	----

Therm #:	9	10	11	12	13	14	15	16
Depth (m):	4.139	3.959	3.779	3.599	3.419	3.239	3.059	2.879
Temp (mK):	11.4	5.3	----	-11.7	-17.5	-25.3	-31.6	-37.9
Cond (W/m-K):	1.083	0.970	----	0.964	0.999	0.934	0.956	0.940

Therm #:	17	18	19	20	21	22	23	24
Depth (m):	2.699	2.519	2.339	2.159	1.979	1.799	1.619	1.440
Temp (mK):	-46.9	-52.7	-59.9	-66.8	-73.0	-76.3	-83.9	-89.8
Cond (W/m-K):	1.066	1.032	0.970	0.938	0.930	1.142	0.959	0.966

Therm #:	25	26	27	28	29	30	31	32
Depth (m):	1.260	1.080	0.900	0.720	0.540	0.360	0.180	0.000
Temp (mK):	-94.8	----	-108.7	----	----	----	----	----
Cond (W/m-K):	0.947	----	0.947	----	----	----	----	----

Gradient (mK/m)= 35.99 ± 0.19
Conductivity (W/m-K)= 0.983 ± 0.091
Heat Flow (mW/m^2)= 35.39 ± 3.48

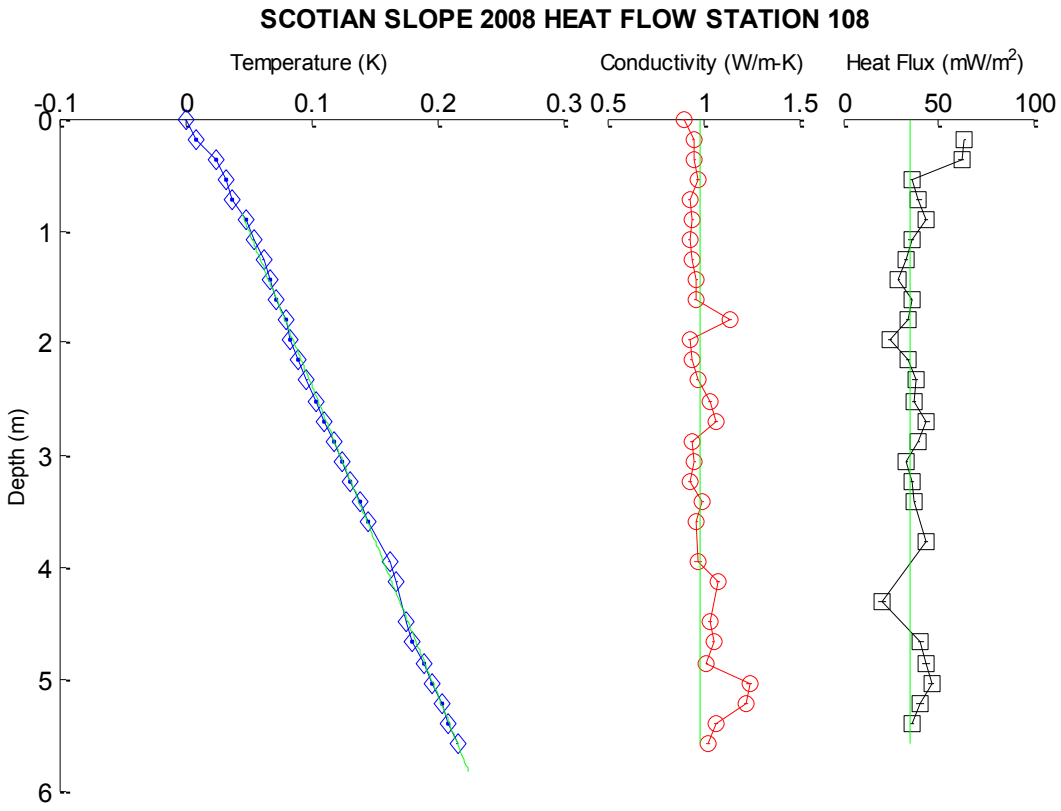

SCOTIAN SLOPE 2008 HEAT FLOW STATION 107
Tilt (deg)= 1.0

Therm #:	1	2	3	4	5	6	7	8
Depth (m):	5.579	5.399	5.219	5.039	4.859	4.679	4.499	4.319
Temp (mK):	167.0	160.8	150.6	141.5	136.8	130.7	121.8	----
Cond (W/m-K):	1.039	1.068	1.023	1.087	1.006	1.059	1.138	----

Therm #:	9	10	11	12	13	14	15	16
Depth (m):	4.139	3.959	3.779	3.599	3.419	3.240	3.060	2.880
Temp (mK):	106.0	102.9	----	94.6	79.4	71.9	64.8	56.1
Cond (W/m-K):	0.980	0.944	----	1.173	0.965	0.992	0.972	0.917

Therm #:	17	18	19	20	21	22	23	24
Depth (m):	2.700	2.520	2.340	2.160	1.980	1.800	1.620	1.440
Temp (mK):	49.3	41.3	35.5	27.7	19.6	12.9	6.1	-0.3
Cond (W/m-K):	0.951	0.903	0.961	0.964	0.965	1.140	0.991	0.908

Therm #:	25	26	27	28	29	30	31	32
Depth (m):	1.260	1.080	0.900	0.720	0.540	0.360	0.180	0.000
Temp (mK):	-8.6	----	----	----	----	----	----	----
Cond (W/m-K):	0.926	----	----	----	----	----	----	----

Gradient (mK/m)= 40.72 ± 0.25
Conductivity (W/m-K)= 0.959 ± 0.087
Heat Flow (mW/m^2)= 39.04 ± 3.77

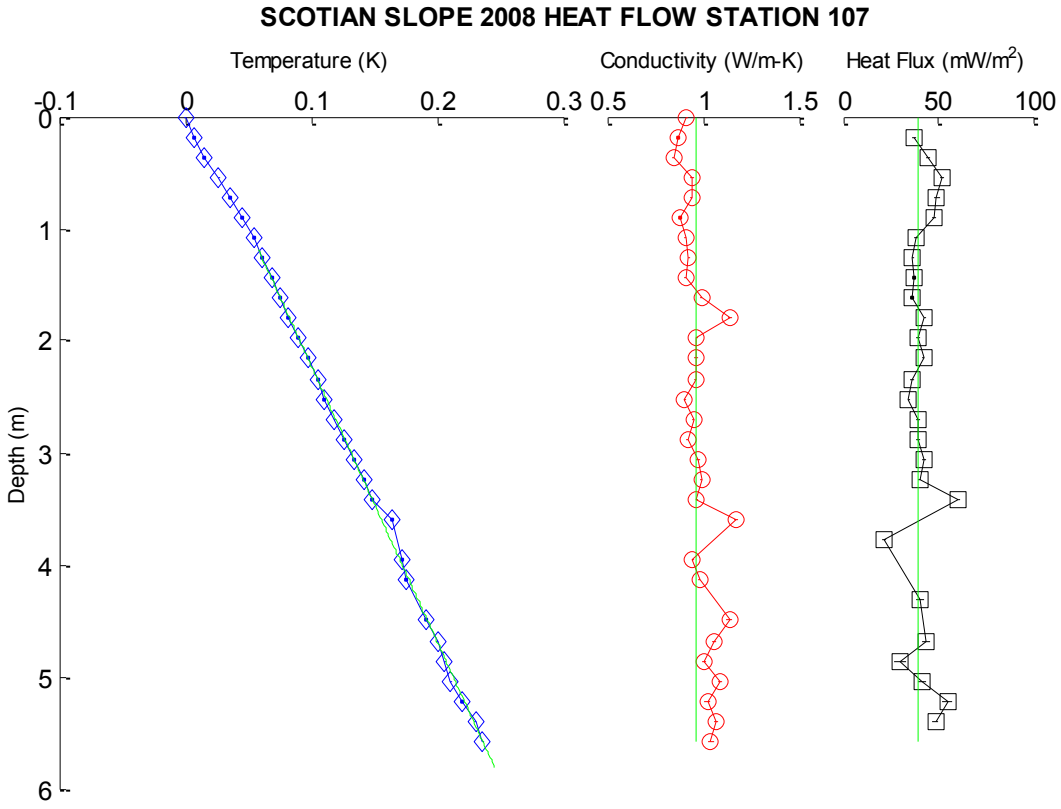

SCOTIAN SLOPE 2008 HEAT FLOW STATION 106
Tilt (deg)= 0.0

Therm #	1	2	3	4	5	6	7	8
Depth (m)	5.580	5.400	5.220	5.040	4.860	4.680	4.500	4.320
Temp (mK)	149.1	143.4	135.6	122.9	120.8	109.4	101.5	----
Cond (W/m-K)	1.020	1.087	1.080	1.044	1.058	1.050	1.132	----

Therm #	9	10	11	12	13	14	15	16
Depth (m)	4.140	3.960	3.780	3.600	3.420	3.240	3.060	2.880
Temp (mK)	85.8	80.6	----	82.9	63.3	53.3	47.2	41.9
Cond (W/m-K)	1.020	1.011	----	1.101	1.019	1.003	0.968	0.947

Therm #	17	18	19	20	21	22	23	24
Depth (m)	2.700	2.520	2.340	2.160	1.980	1.800	1.620	1.440
Temp (mK)	32.6	26.4	16.6	13.7	3.1	----	-9.0	-11.3
Cond (W/m-K)	0.979	0.917	0.962	0.923	0.960	----	0.995	0.938

Therm #	25	26	27	28	29	30	31	32
Depth (m)	1.260	1.080	0.900	0.720	0.540	0.360	0.180	0.000
Temp (mK)	-23.4	----	-38.5	-45.4	----	----	----	----
Cond (W/m-K)	0.868	----	0.857	0.950	----	----	----	----

Gradient (mK/m)= 39.74 ± 0.43
Conductivity (W/m-K)= 0.941 ± 0.088
Heat Flow (mW/m^2)= 37.40 ± 3.90

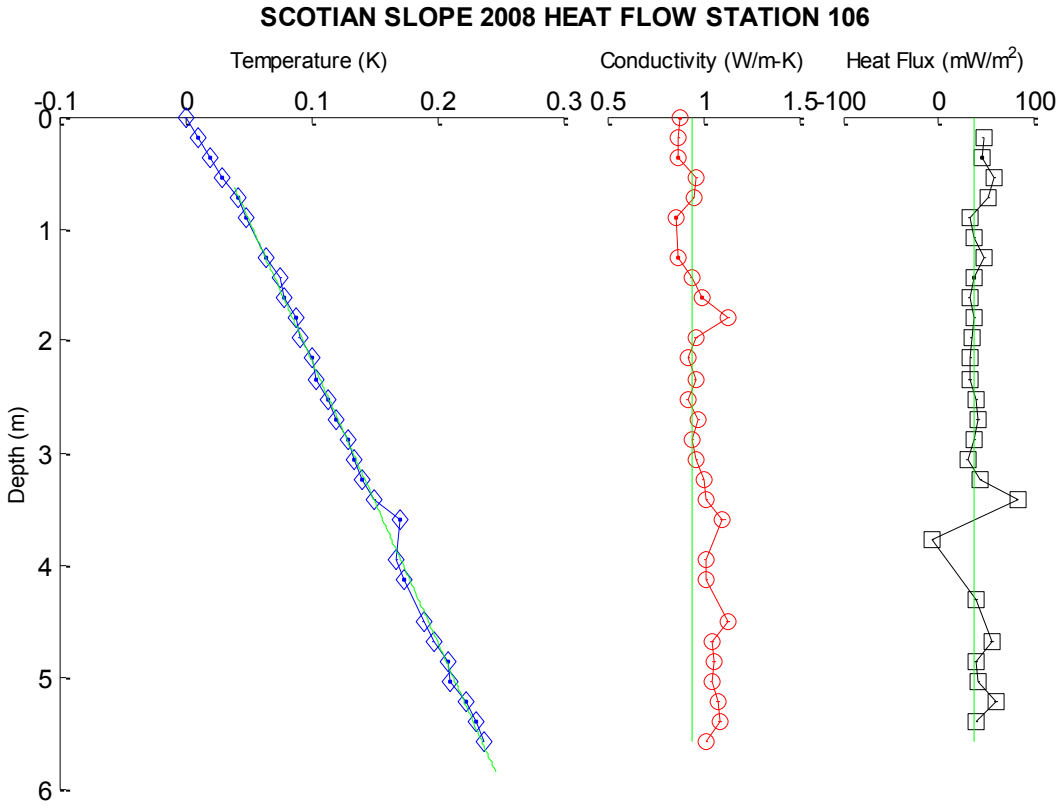

SCOTIAN SLOPE 2008 HEAT FLOW STATION 105
Tilt (deg)= 2.5

Therm #:	1	2	3	4	5	6	7	8
Depth (m):	5.575	5.395	5.215	5.035	4.855	4.676	4.496	4.316
Temp (mK):	205.8	197.5	189.9	180.9	171.5	163.3	154.1	----
Cond (W/m-K):	1.008	1.055	1.086	1.082	1.030	1.098	1.032	----

Therm #:	9	10	11	12	13	14	15	16
Depth (m):	4.136	3.956	3.776	3.597	3.417	3.237	3.057	2.877
Temp (mK):	135.5	128.7	----	112.2	104.5	97.2	88.8	80.6
Cond (W/m-K):	1.020	1.038	----	1.049	1.092	1.110	1.215	1.010

Therm #:	17	18	19	20	21	22	23	24
Depth (m):	2.697	2.518	2.338	2.158	1.978	1.798	1.618	1.439
Temp (mK):	73.2	64.0	57.8	49.6	43.5	36.0	26.1	----
Cond (W/m-K):	1.020	0.996	0.994	0.950	0.967	1.194	0.986	----

Therm #:	25	26	27	28	29	30	31	32
Depth (m):	1.259	1.079	0.899	0.719	0.539	0.360	0.180	0.000
Temp (mK):	9.1	----	-9.8	----	----	----	----	----
Cond (W/m-K):	0.925	----	0.886	----	----	----	----	----

Gradient (mK/m)= 45.36 ± 0.24
Conductivity (W/m-K)= 0.999 ± 0.084
Heat Flow (mW/m^2)= 45.33 ± 4.04

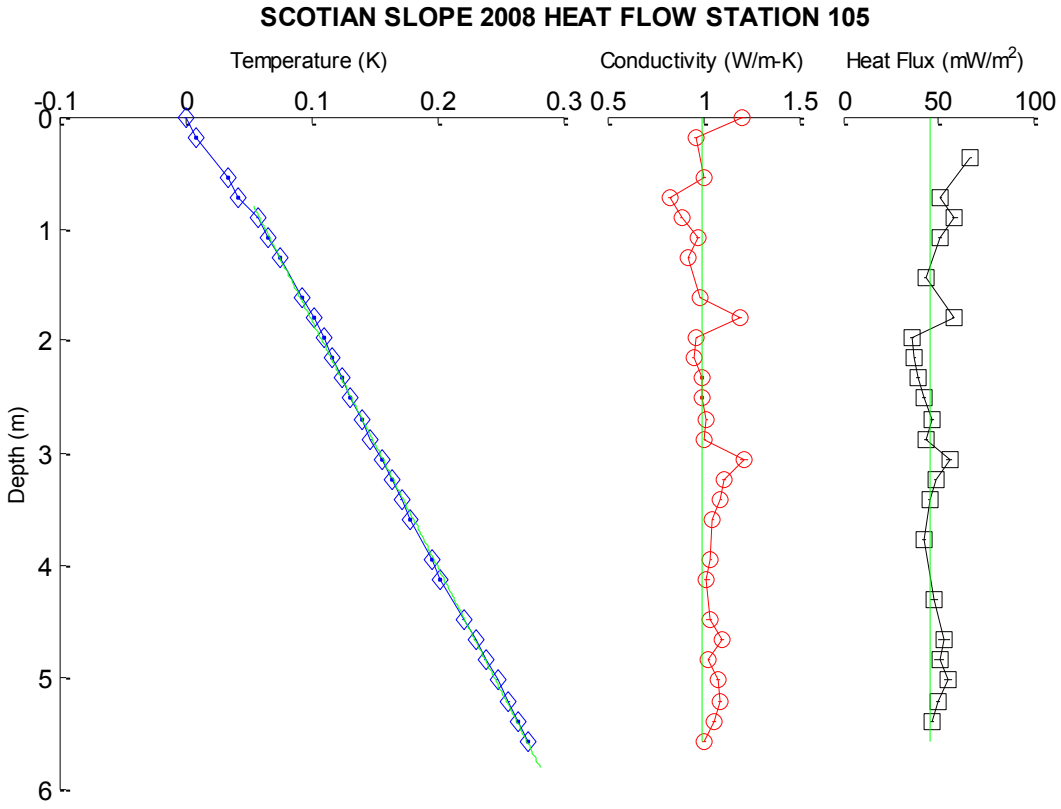

SCOTIAN SLOPE 2008 HEAT FLOW STATION 104
Tilt (deg)= 1.0

Therm #:	1	2	3	4	5	6	7	8
Depth (m):	5.579	5.399	5.219	5.039	4.859	4.679	4.499	4.319
Temp (mK):	180.0	171.8	165.3	150.9	152.2	141.9	135.1	----
Cond (W/m-K):	1.045	1.050	1.084	0.991	1.063	1.067	1.054	----

Therm #:	9	10	11	12	13	14	15	16
Depth (m):	4.139	3.959	3.779	3.599	3.419	3.240	3.060	2.880
Temp (mK):	118.1	112.3	----	100.0	92.5	87.0	78.0	72.6
Cond (W/m-K):	1.055	1.026	----	1.068	1.098	1.044	1.023	1.078

Therm #:	17	18	19	20	21	22	23	24
Depth (m):	2.700	2.520	2.340	2.160	1.980	1.800	1.620	1.440
Temp (mK):	65.5	62.0	53.8	48.2	41.0	----	27.3	20.5
Cond (W/m-K):	1.123	1.109	0.952	0.998	0.941	----	1.003	1.112

Therm #:	25	26	27	28	29	30	31	32
Depth (m):	1.260	1.080	0.900	0.720	0.540	0.360	0.180	0.000
Temp (mK):	11.7	----	-4.5	----	----	----	----	----
Cond (W/m-K):	0.964	----	0.960	----	----	----	----	----

Gradient (mK/m)= 37.76 ± 0.32
Conductivity (W/m-K)= 1.031 ± 0.053
Heat Flow (mW/m^2)= 38.94 ± 2.32

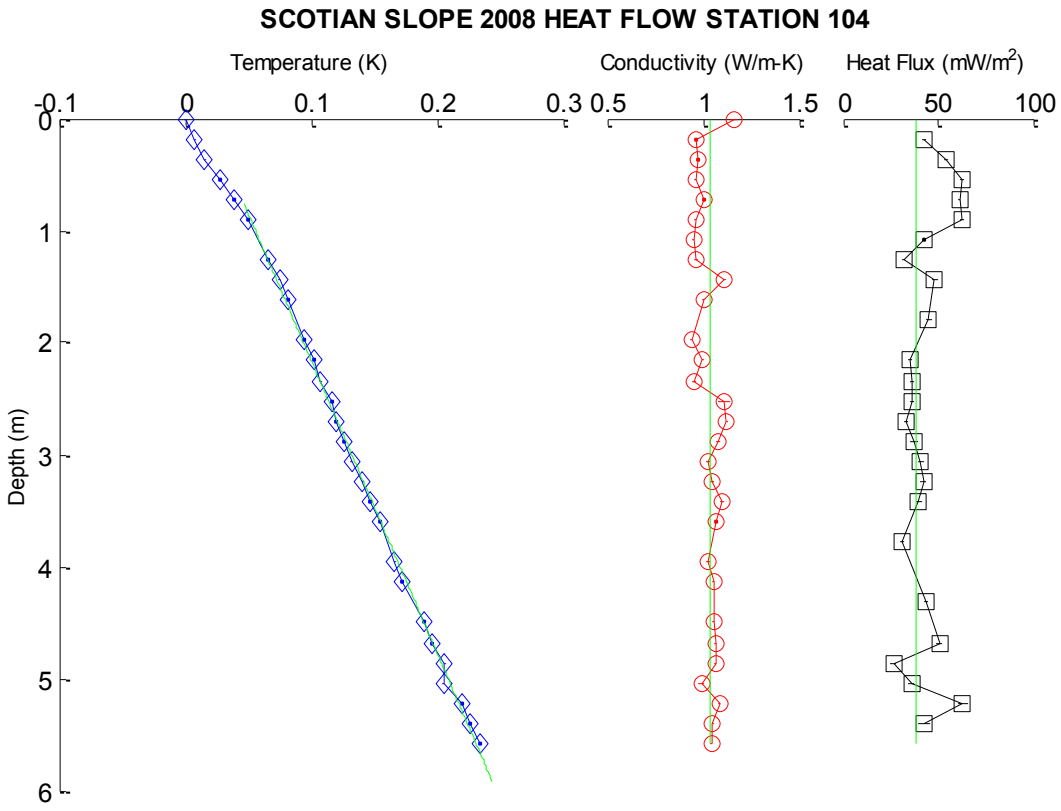

SCOTIAN SLOPE 2008 HEAT FLOW STATION 103
Tilt (deg)= 1.0

Therm #	1	2	3	4	5	6	7	8
Depth (m)	5.579	5.399	5.219	5.039	4.859	4.679	4.499	4.319
Temp (mK)	196.2	189.2	182.6	172.5	171.6	164.4	155.8	----
Cond (W/m-K)	1.006	1.038	1.148	1.119	1.319	1.075	1.009	----

Therm #	9	10	11	12	13	14	15	16
Depth (m)	4.139	3.959	3.779	3.599	3.419	3.240	3.060	2.880
Temp (mK)	143.9	136.4	----	125.1	112.0	107.8	99.9	97.3
Cond (W/m-K)	0.906	0.900	----	1.001	1.001	0.998	1.008	1.019

Therm #	17	18	19	20	21	22	23	24
Depth (m)	2.700	2.520	2.340	2.160	1.980	1.800	1.620	1.440
Temp (mK)	88.6	82.7	74.9	71.7	62.9	55.5	48.0	37.5
Cond (W/m-K)	1.091	0.975	1.012	1.063	1.109	1.280	0.959	1.039

Therm #	25	26	27	28	29	30	31	32
Depth (m)	1.260	1.080	0.900	0.720	0.540	0.360	0.180	0.000
Temp (mK)	27.3	----	----	----	----	----	----	----
Cond (W/m-K)	0.946	----	----	----	----	----	----	----

Gradient (mK/m)= 37.63 ± 0.30
Conductivity (W/m-K)= 1.013 ± 0.104
Heat Flow (mW/m^2)= 38.12 ± 4.23

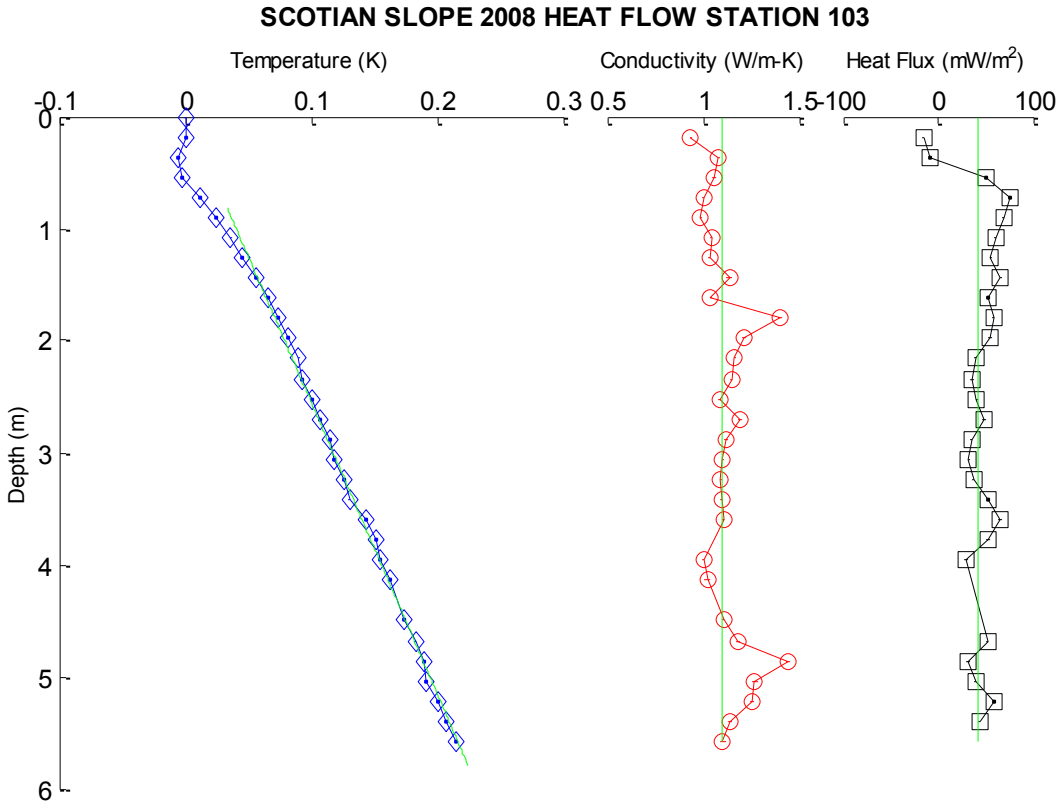

SCOTIAN SLOPE 2008 HEAT FLOW STATION 102
Tilt (deg)= 1.5

Therm #:	1	2	3	4	5	6	7	8
Depth (m):	5.578	5.398	5.218	5.038	4.858	4.678	4.498	4.319
Temp (mK):	220.5	200.4	196.9	198.6	186.9	186.0	172.5	----
Cond (W/m-K):	1.046	1.203	1.295	1.241	1.176	1.094	1.244	----

Therm #:	9	10	11	12	13	14	15	16
Depth (m):	4.139	3.959	3.779	3.599	3.419	3.239	3.059	2.879
Temp (mK):	153.3	151.4	----	139.6	140.7	130.9	131.0	122.6
Cond (W/m-K):	1.035	1.077	----	1.050	1.084	1.111	0.968	1.046

Therm #:	17	18	19	20	21	22	23	24
Depth (m):	2.699	2.519	2.339	2.159	1.979	1.799	1.619	1.440
Temp (mK):	112.9	119.5	101.7	95.6	87.4	83.5	81.6	72.0
Cond (W/m-K):	1.115	1.107	1.151	1.178	1.067	1.298	1.144	1.184

Therm #:	25	26	27	28	29	30	31	32
Depth (m):	1.260	1.080	0.900	0.720	0.540	0.360	0.180	0.000
Temp (mK):	68.8	----	54.4	47.9	----	----	----	----
Cond (W/m-K):	1.064	----	1.270	0.965	----	----	----	----

Gradient (mK/m)= 34.20 ± 0.55
Conductivity (W/m-K)= 1.065 ± 0.112
Heat Flow (mW/m^2)= 36.43 ± 4.41

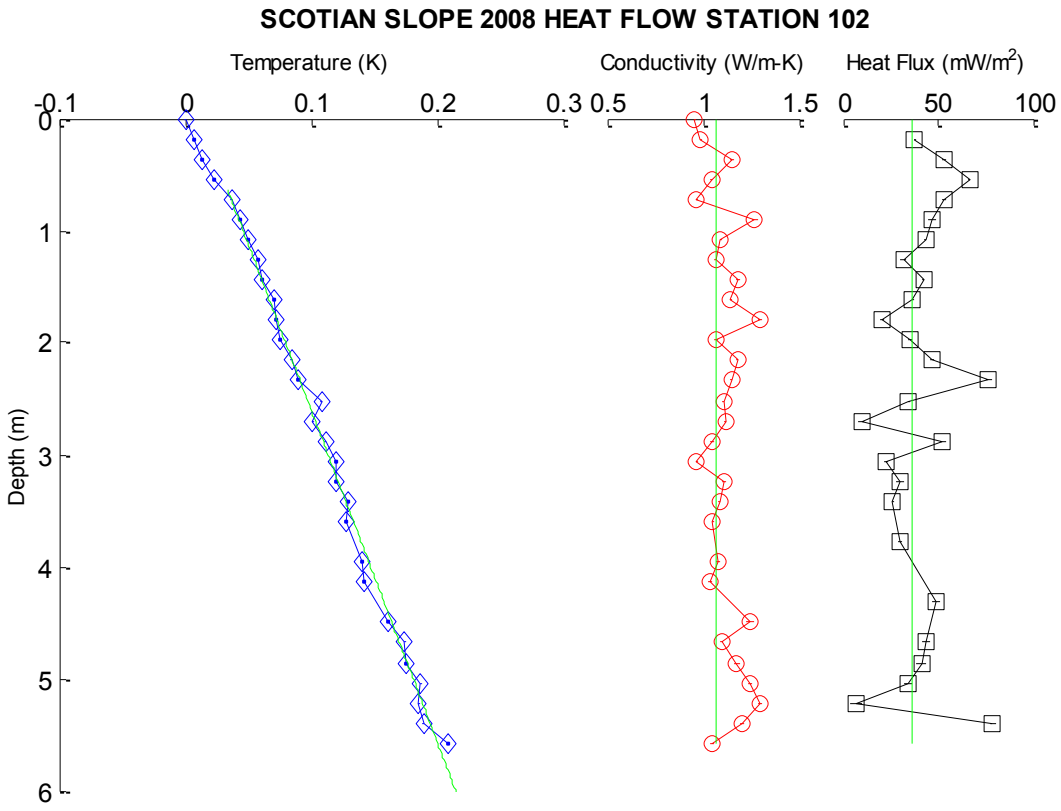

SCOTIAN SLOPE 2008 HEAT FLOW STATION 101
Tilt (deg)= 1.5

Therm #:	1	2	3	4	5	6	7	8
Depth (m):	5.578	5.398	5.218	5.038	4.858	4.678	4.498	4.319
Temp (mK):	124.6	115.5	111.6	114.4	101.4	96.8	94.4	----
Cond (W/m-K):	1.077	1.141	1.231	1.506	1.368	1.374	1.389	----

Therm #:	9	10	11	12	13	14	15	16
Depth (m):	4.139	3.959	3.779	3.599	3.419	3.239	3.059	2.879
Temp (mK):	74.9	76.2	----	72.6	73.4	70.5	66.8	59.6
Cond (W/m-K):	1.092	0.938	----	1.313	1.317	1.307	1.283	1.274

Therm #:	17	18	19	20	21	22	23	24
Depth (m):	2.699	2.519	2.339	2.159	1.979	1.799	1.619	1.440
Temp (mK):	56.1	54.6	51.3	47.5	42.7	44.5	----	----
Cond (W/m-K):	1.168	1.025	0.955	1.002	0.983	1.263	----	----

Therm #:	25	26	27	28	29	30	31	32
Depth (m):	1.260	1.080	0.900	0.720	0.540	0.360	0.180	0.000
Temp (mK):	----	----	----	----	----	----	----	----
Cond (W/m-K):	----	----	----	----	----	----	----	----

Gradient (mK/m)= 20.29 ± 0.86
Conductivity (W/m-K)= 1.191 ± 0.161
Heat Flow (mW/m^2)= 24.18 ± 4.30

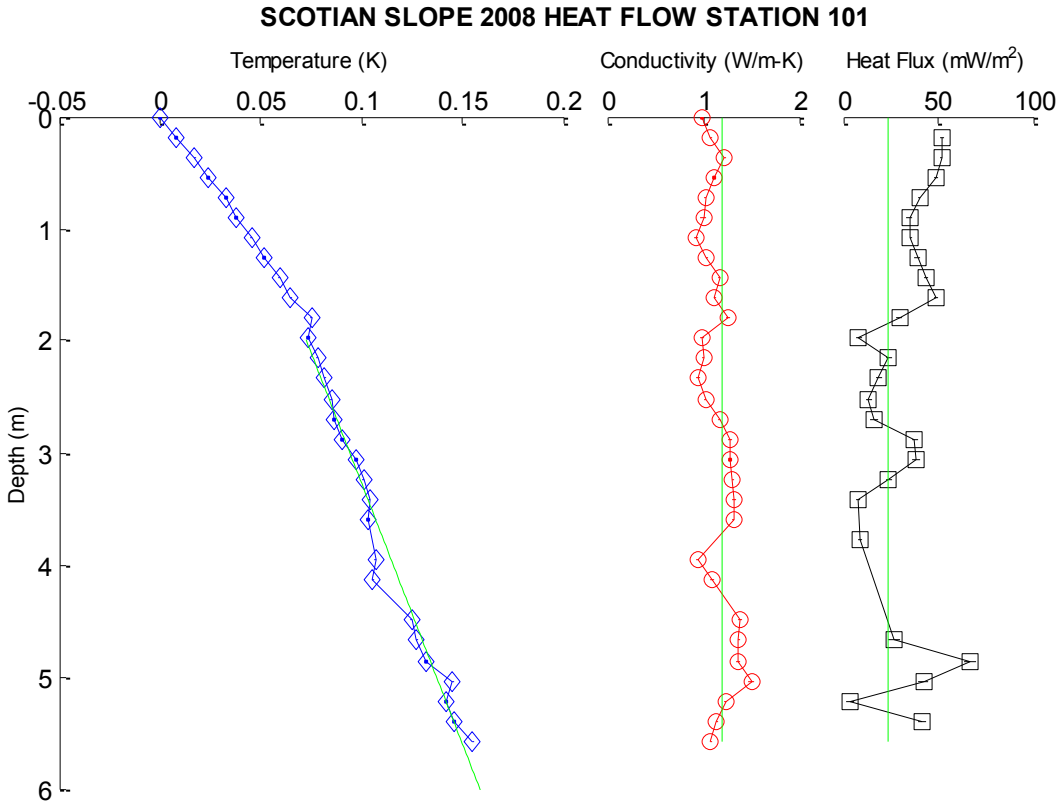

C-3: Line 2 Heat Flow Stations

SCOTIAN SLOPE 2008 HEAT FLOW STATION 201
Tilt (deg)= 2.0

Therm #	1	2	3	4	5	6	7	8
Depth (m)	5.577	5.397	5.217	5.037	4.857	4.677	4.497	4.317
Temp (mK)	----	180.0	175.1	175.5	185.0	----	160.8	----
Cond (W/m-K)	----	1.533	1.436	1.296	1.339	----	1.513	----

Therm #	9	10	11	12	13	14	15	16
Depth (m)	4.137	3.958	3.778	3.598	3.418	3.238	3.058	2.878
Temp (mK)	148.8	151.7	----	152.4	138.6	132.2	142.6	126.0
Cond (W/m-K)	1.559	1.226	----	1.217	1.143	1.149	1.136	1.258

Therm #	17	18	19	20	21	22	23	24
Depth (m)	2.698	2.518	2.339	2.159	1.979	1.799	1.619	1.439
Temp (mK)	----	----	135.0	130.5	105.1	107.3	92.1	88.7
Cond (W/m-K)	----	----	1.363	1.330	1.225	1.426	1.272	1.234

Therm #	25	26	27	28	29	30	31	32
Depth (m)	1.259	1.079	0.899	0.720	0.540	0.360	0.180	0.000
Temp (mK)	88.2	----	----	----	----	----	----	----
Cond (W/m-K)	1.300	----	----	----	----	----	----	----

Gradient (mK/m)= 22.55 ± 1.56
Conductivity (W/m-K)= 1.243 ± 0.145
Heat Flow (mW/m^2)= 28.02 ± 5.20

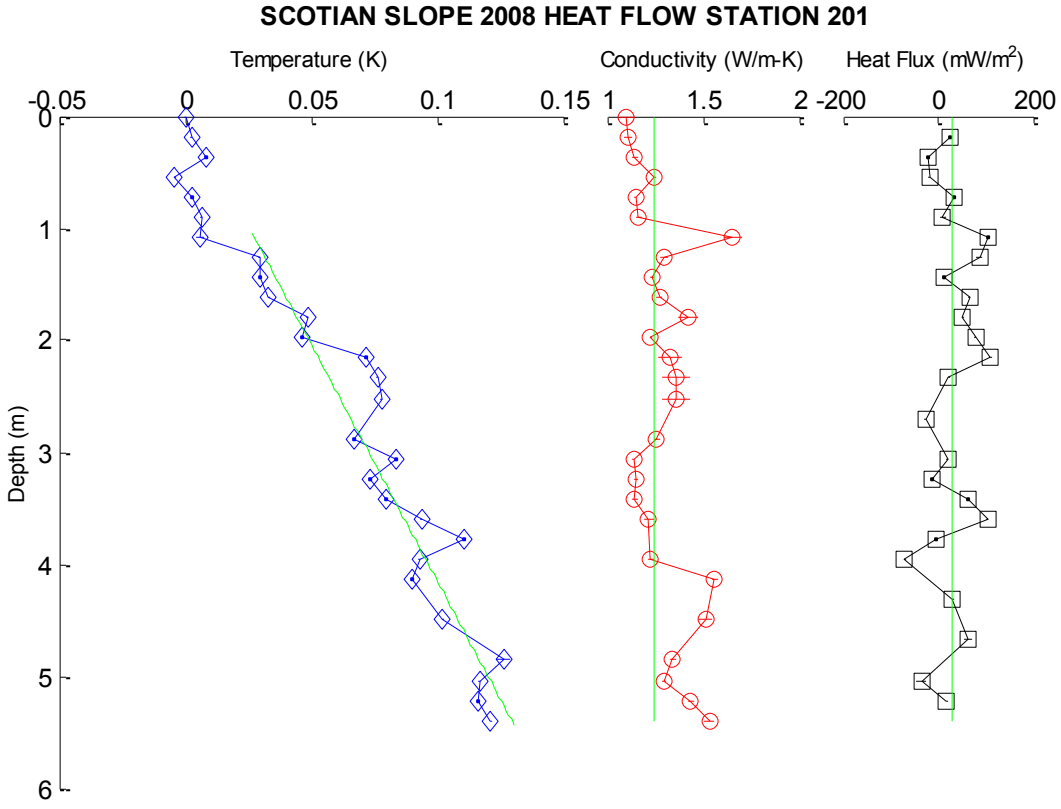

SCOTIAN SLOPE 2008 HEAT FLOW STATION 202ar2
Tilt (deg)= 2.0

Therm #	1	2	3	4	5	6	7	8
Depth (m)	5.577	5.397	5.217	5.037	4.857	4.677	4.497	4.317
Temp (mK)	----	240.8	234.4	238.7	219.3	----	203.8	----
Cond (W/m-K)	----	1.411	1.391	1.211	1.386	----	1.225	----

Therm #	9	10	11	12	13	14	15	16
Depth (m)	4.137	3.958	3.778	3.598	3.418	3.238	3.058	2.878
Temp (mK)	191.8	----	----	193.1	178.3	178.8	185.0	----
Cond (W/m-K)	1.238	----	0.921	1.248	1.167	1.223	1.103	----

Therm #	17	18	19	20	21	22	23	24
Depth (m)	2.698	2.518	2.339	2.159	1.979	1.799	1.619	1.439
Temp (mK)	138.0	----	148.5	----	129.7	142.9	127.7	124.9
Cond (W/m-K)	1.024	----	1.117	----	0.997	1.267	1.151	1.213

Therm #	25	26	27	28	29	30	31	32
Depth (m)	1.259	1.079	0.899	0.720	0.540	0.360	0.180	0.000
Temp (mK)	----	----	----	----	----	----	----	----
Cond (W/m-K)	----	----	----	----	----	----	----	----

Gradient (mK/m)= 30.49 ± 1.88
Conductivity (W/m-K)= 1.187 ± 0.132
Heat Flow (mW/m^2)= 36.20 ± 6.25

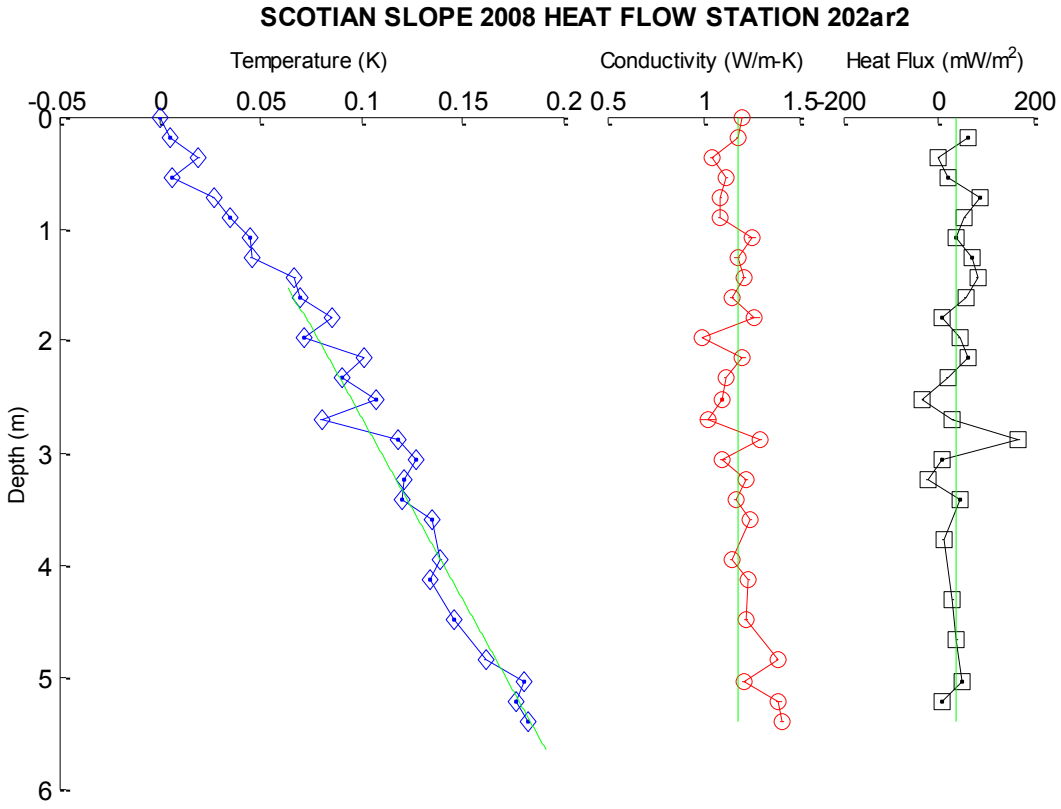

SCOTIAN SLOPE 2008 HEAT FLOW STATION 203r
Tilt (deg)= 1.0

Therm #:	1	2	3	4	5	6	7	8
Depth (m):	5.579	5.399	5.219	5.039	4.859	4.679	4.499	4.319
Temp (mK):	----	279.4	257.8	260.3	243.5	----	237.7	----
Cond (W/m-K):	----	1.141	1.215	1.220	1.239	----	1.244	----

Therm #:	9	10	11	12	13	14	15	16
Depth (m):	4.139	3.959	3.779	3.599	3.419	3.240	3.060	2.880
Temp (mK):	227.2	208.6	----	182.0	199.2	191.1	184.6	178.9
Cond (W/m-K):	1.139	1.234	----	1.287	1.059	1.078	1.043	1.035

Therm #:	17	18	19	20	21	22	23	24
Depth (m):	2.700	2.520	2.340	2.160	1.980	1.800	1.620	1.440
Temp (mK):	158.8	----	149.7	148.6	138.8	----	120.0	109.6
Cond (W/m-K):	0.905	----	1.118	1.109	1.056	----	0.928	1.027

Therm #:	25	26	27	28	29	30	31	32
Depth (m):	1.260	1.080	0.900	0.720	0.540	0.360	0.180	0.000
Temp (mK):	105.2	----	79.6	----	----	----	----	----
Cond (W/m-K):	0.967	----	0.968	----	----	----	----	----

Gradient (mK/m)= 41.48 ± 1.20
Conductivity (W/m-K)= 1.027 ± 0.132
Heat Flow (mW/m^2)= 42.61 ± 6.72

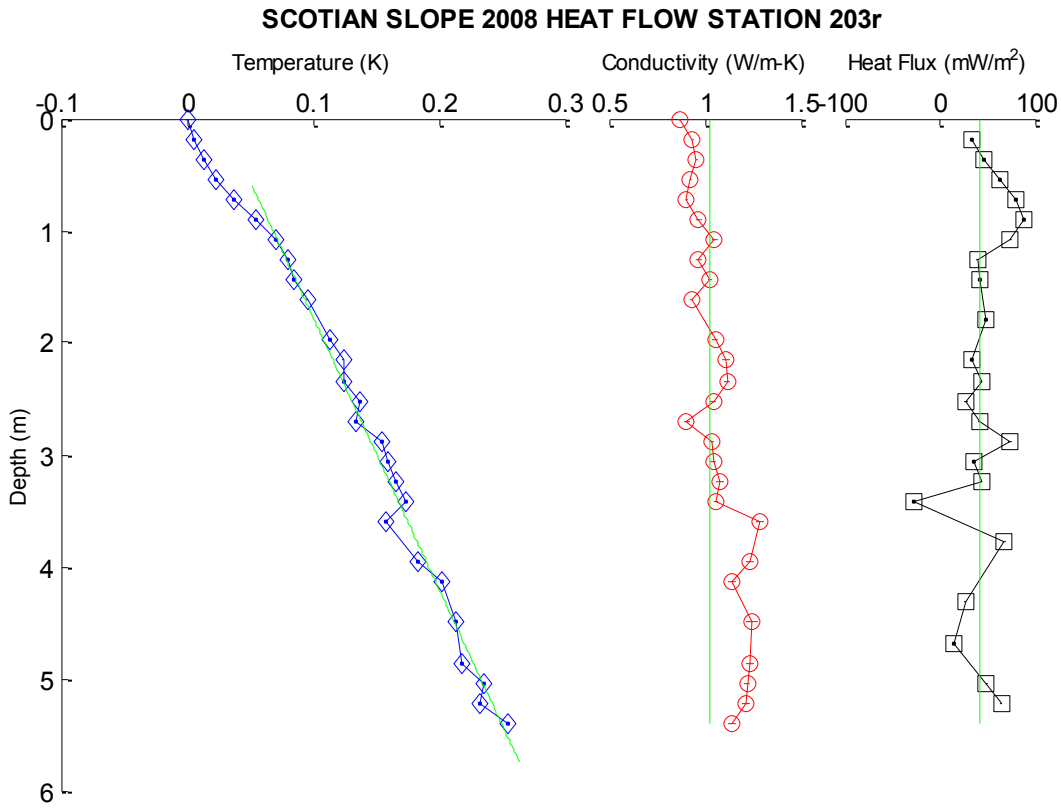

SCOTIAN SLOPE 2008 HEAT FLOW STATION 204
Tilt (deg)= 0.5

Therm #:	1	2	3	4	5	6	7	8
Depth (m):	5.580	5.400	5.220	5.040	4.860	4.680	4.500	4.320
Temp (mK):	----	----	209.8	195.9	----	----	----	----
Cond (W/m-K):	----	----	1.388	1.439	----	----	----	----

Therm #:	9	10	11	12	13	14	15	16
Depth (m):	4.140	3.960	3.780	3.600	3.420	3.240	3.060	2.880
Temp (mK):	174.7	162.5	----	148.6	139.7	132.0	----	----
Cond (W/m-K):	1.516	1.065	----	1.130	1.161	1.113	----	----

Therm #:	17	18	19	20	21	22	23	24
Depth (m):	2.700	2.520	2.340	2.160	1.980	1.800	1.620	1.440
Temp (mK):	----	89.6	79.9	59.0	53.3	50.5	----	----
Cond (W/m-K):	----	1.135	1.059	0.945	0.939	1.157	----	----

Therm #:	25	26	27	28	29	30	31	32
Depth (m):	1.260	1.080	0.900	0.720	0.540	0.360	0.180	0.000
Temp (mK):	17.5	----	----	----	----	----	----	----
Cond (W/m-K):	1.084	----	----	----	----	----	----	----

Gradient (mK/m)= 53.77 ± 2.28
Conductivity (W/m-K)= 0.991 ± 0.243
Heat Flow (mW/m^2)= 53.27 ± 15.34

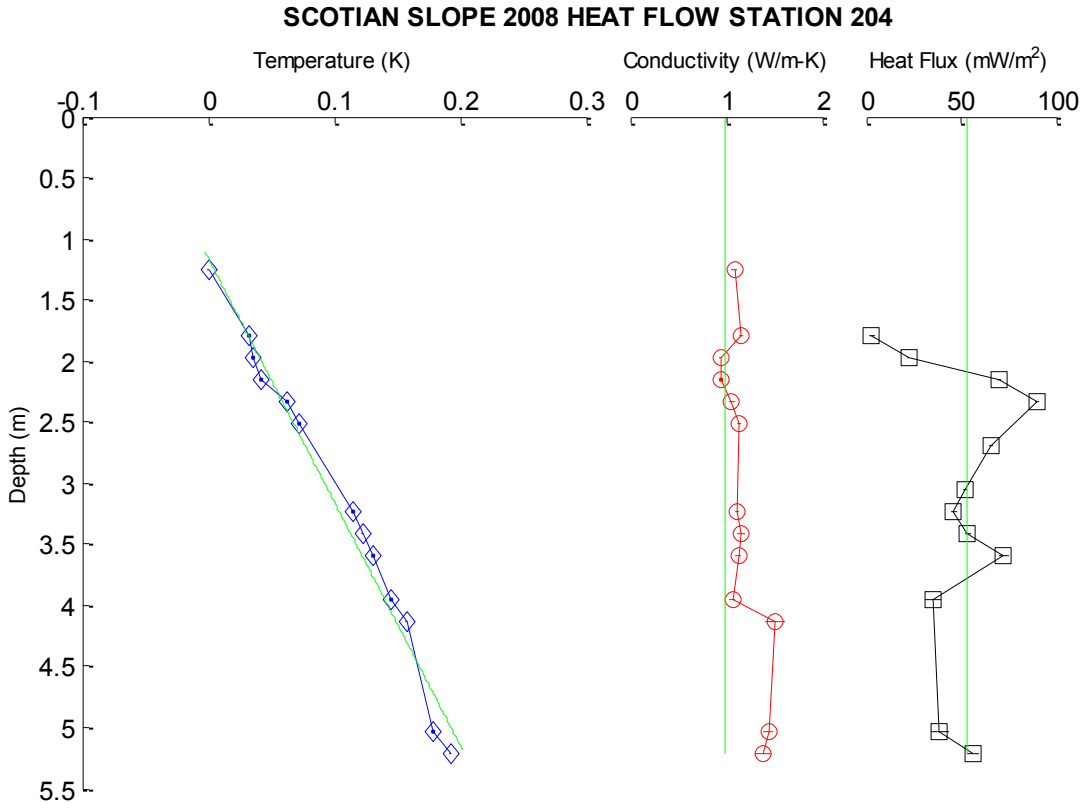

SCOTIAN SLOPE 2008 HEAT FLOW STATION 205
Tilt (deg)= 1.0

Therm #:	1	2	3	4	5	6	7	8
Depth (m):	5.579	5.399	5.219	5.039	4.859	4.679	4.499	4.319
Temp (mK):	----	340.6	327.6	309.3	309.2	297.7	----	----
Cond (W/m-K):	0.921	1.105	1.084	1.087	1.120	1.135	----	----

Therm #:	9	10	11	12	13	14	15	16
Depth (m):	4.139	3.959	3.779	3.599	3.419	3.240	3.060	2.880
Temp (mK):	260.6	254.5	----	233.9	231.7	216.8	200.3	197.8
Cond (W/m-K):	1.086	1.118	----	1.141	1.377	1.318	1.154	1.203

Therm #:	17	18	19	20	21	22	23	24
Depth (m):	2.700	2.520	2.340	2.160	1.980	1.800	1.620	1.440
Temp (mK):	185.8	173.4	164.0	155.2	140.3	130.6	120.0	110.5
Cond (W/m-K):	1.197	1.091	1.070	1.283	1.054	1.171	1.089	1.109

Therm #:	25	26	27	28	29	30	31	32
Depth (m):	1.260	1.080	0.900	0.720	0.540	0.360	0.180	0.000
Temp (mK):	95.3	----	----	----	----	----	----	----
Cond (W/m-K):	1.111	----	----	----	----	----	----	----

Gradient (mK/m)= 56.20 ± 0.61
Conductivity (W/m-K)= 1.114 ± 0.097
Heat Flow (mW/m^2)= 62.59 ± 6.13

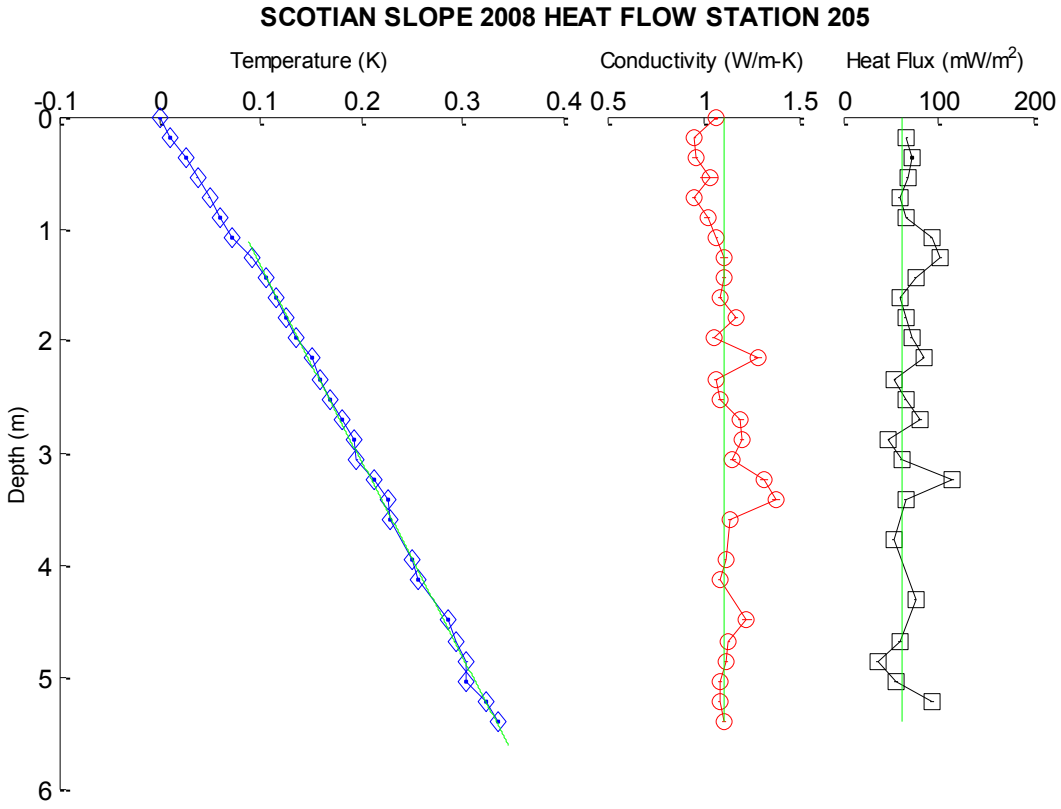

SCOTIAN SLOPE 2008 HEAT FLOW STATION 206
Tilt (deg)= 0.0

Therm #	1	2	3	4	5	6	7	8
Depth (m)	5.580	5.400	5.220	5.040	4.860	4.680	4.500	4.320
Temp (mK)	----	307.5	295.8	277.8	278.3	266.0	----	----
Cond (W/m-K)	----	1.133	1.152	1.181	1.211	1.183	----	----

Therm #	9	10	11	12	13	14	15	16
Depth (m)	4.140	3.960	3.780	3.600	3.420	3.240	3.060	2.880
Temp (mK)	237.9	233.3	----	221.2	202.3	192.6	179.1	173.5
Cond (W/m-K)	1.078	1.084	----	1.155	1.083	1.143	1.127	1.079

Therm #	17	18	19	20	21	22	23	24
Depth (m)	2.700	2.520	2.340	2.160	1.980	1.800	1.620	1.440
Temp (mK)	163.0	152.4	143.1	131.3	116.8	107.4	93.9	85.4
Cond (W/m-K)	1.064	1.012	0.988	1.027	0.874	1.043	1.019	1.007

Therm #	25	26	27	28	29	30	31	32
Depth (m)	1.260	1.080	0.900	0.720	0.540	0.360	0.180	0.000
Temp (mK)	70.5	----	44.1	----	----	----	----	----
Cond (W/m-K)	1.024	----	0.891	----	----	----	----	----

Gradient (mK/m)= 59.76 ± 1.08
Conductivity (W/m-K)= 0.997 ± 0.113
Heat Flow (mW/m^2)= 59.61 ± 7.85

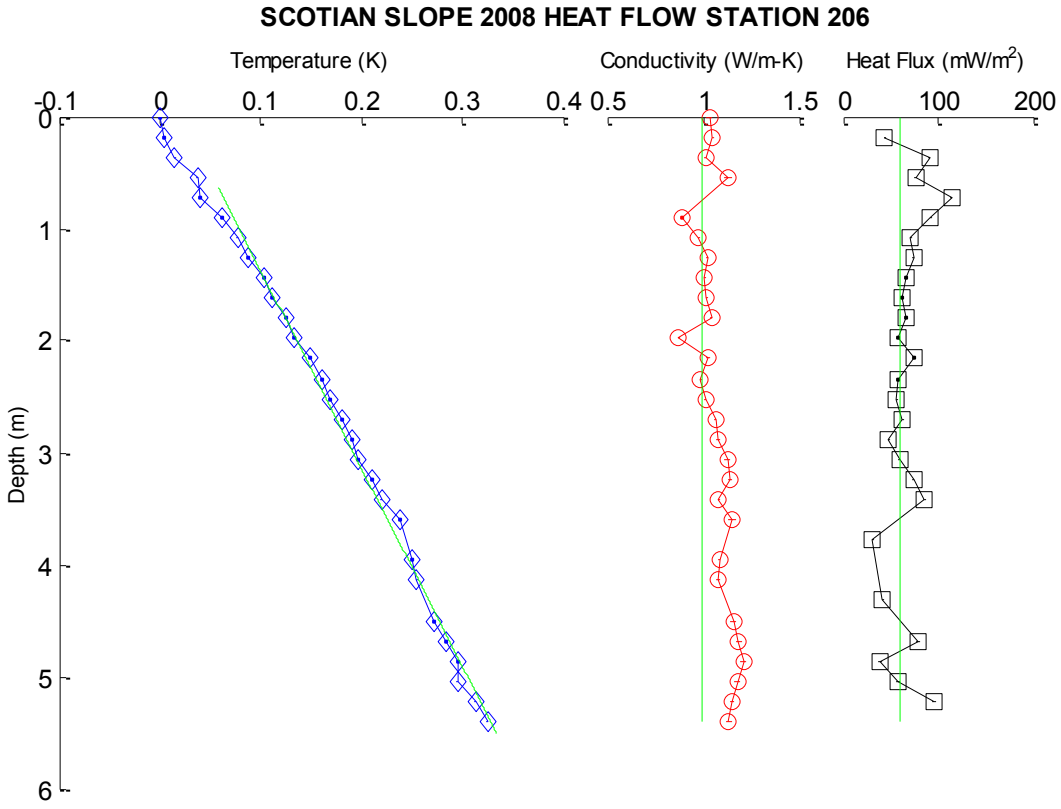

SCOTIAN SLOPE 2008 HEAT FLOW STATION 207r3
Tilt (deg)= 1.0

Therm #:	1	2	3	4	5	6	7	8
Depth (m):	5.579	5.399	5.219	5.039	4.859	4.679	4.499	4.319
Temp (mK):	----	284.9	273.3	257.2	252.1	234.8	224.6	----
Cond (W/m-K):	----	1.137	1.112	1.165	1.083	1.106	1.130	----

Therm #:	9	10	11	12	13	14	15	16
Depth (m):	4.139	3.959	3.779	3.599	3.419	3.240	3.060	2.880
Temp (mK):	195.9	187.3	----	161.0	149.2	135.8	123.8	116.0
Cond (W/m-K):	1.090	1.115	----	1.085	1.076	1.101	1.168	1.116

Therm #:	17	18	19	20	21	22	23	24
Depth (m):	2.700	2.520	2.340	2.160	1.980	1.800	1.620	1.440
Temp (mK):	102.9	91.8	80.1	64.8	50.0	40.5	27.6	17.0
Cond (W/m-K):	1.186	1.196	1.008	0.933	0.999	1.083	1.019	0.995

Therm #:	25	26	27	28	29	30	31	32
Depth (m):	1.260	1.080	0.900	0.720	0.540	0.360	0.180	0.000
Temp (mK):	3.6	----	----	----	----	----	----	----
Cond (W/m-K):	1.077	----	----	----	----	----	----	----

Gradient (mK/m)= 67.76 ± 0.38
Conductivity (W/m-K)= 1.055 ± 0.074
Heat Flow (mW/m^2)= 71.49 ± 5.38

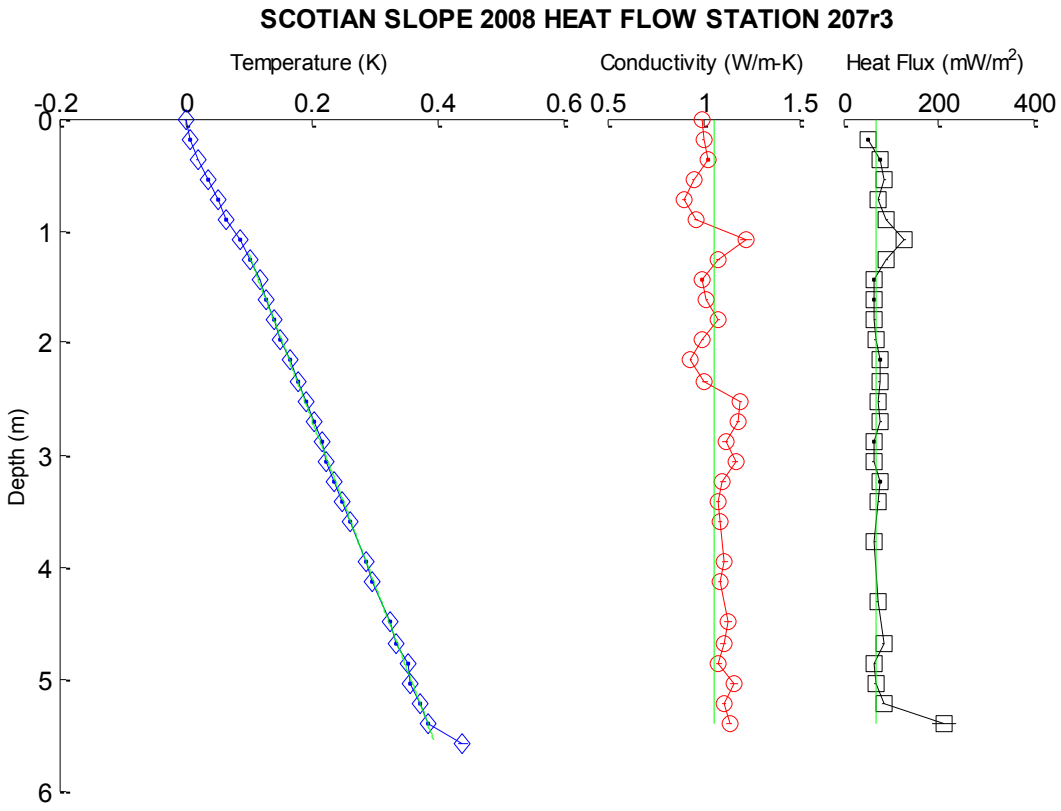

SCOTIAN SLOPE 2008 HEAT FLOW STATION 208
Tilt (deg)= 0.5

Therm #	1	2	3	4	5	6	7	8
Depth (m)	5.580	5.400	5.220	5.040	4.860	4.680	4.500	4.320
Temp (mK)	----	273.4	267.2	249.5	267.6	230.7	----	----
Cond (W/m-K)	----	1.246	1.325	1.302	1.255	1.118	----	----

Therm #	9	10	11	12	13	14	15	16
Depth (m)	4.140	3.960	3.780	3.600	3.420	3.240	3.060	2.880
Temp (mK)	204.1	186.7	----	165.4	158.2	143.8	129.3	121.2
Cond (W/m-K)	1.335	1.255	----	1.140	1.152	1.114	1.119	0.967

Therm #	17	18	19	20	21	22	23	24
Depth (m)	2.700	2.520	2.340	2.160	1.980	1.800	1.620	1.440
Temp (mK)	119.3	111.9	101.2	92.2	76.2	66.1	52.2	46.0
Cond (W/m-K)	1.065	0.996	1.136	0.938	1.021	1.104	1.048	1.042

Therm #	25	26	27	28	29	30	31	32
Depth (m)	1.260	1.080	0.900	0.720	0.540	0.360	0.180	0.000
Temp (mK)	37.8	----	----	----	----	----	----	----
Cond (W/m-K)	1.029	----	----	----	----	----	----	----

Gradient (mK/m)= 57.08 ± 1.11
Conductivity (W/m-K)= 1.041 ± 0.145
Heat Flow (mW/m^2)= 59.41 ± 9.44

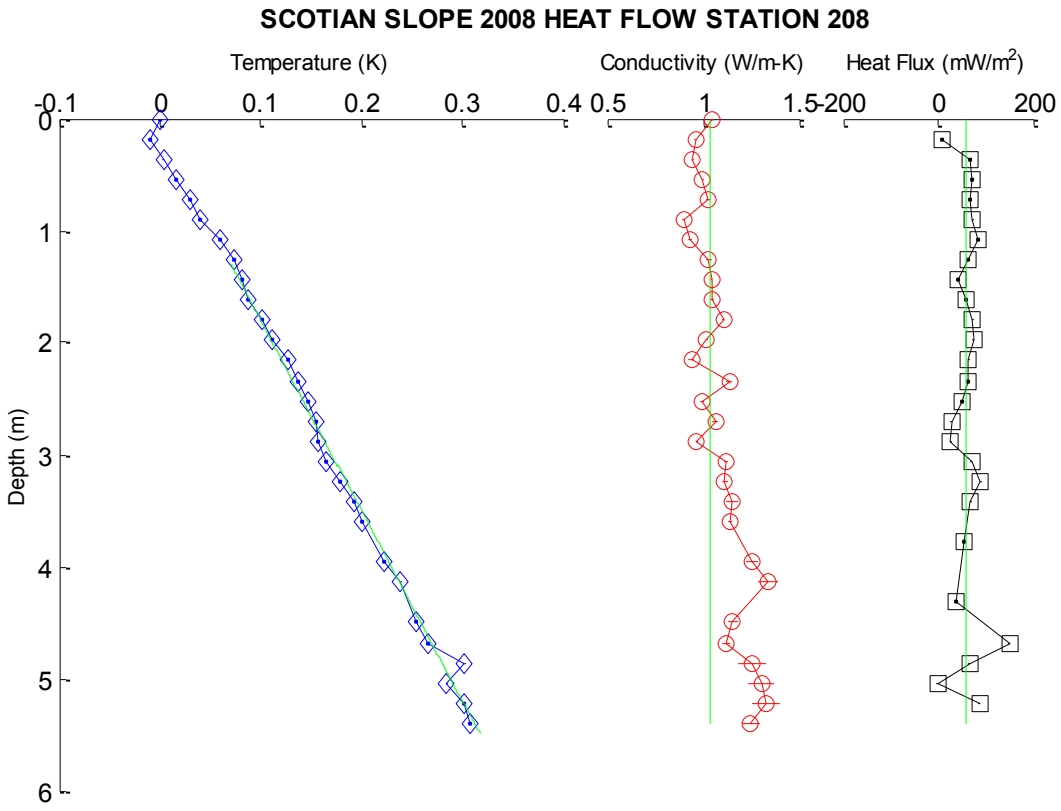

SCOTIAN SLOPE 2008 HEAT FLOW STATION 209_noHP
Tilt (deg)= 1.0

Therm #:	1	2	3	4	5	6	7	8
Depth (m):	5.579	5.399	5.219	5.039	4.859	4.679	4.499	4.319
Temp (mK):	----	151.6	143.0	----	128.5	116.3	105.8	----
Cond (W/m-K):	----	0.980	0.980	----	0.980	0.980	0.980	----

Therm #:	9	10	11	12	13	14	15	16
Depth (m):	4.139	3.959	3.779	3.599	3.419	3.240	3.060	2.880
Temp (mK):	90.6	83.6	95.9	76.8	----	46.3	40.7	----
Cond (W/m-K):	0.980	0.980	0.980	0.980	----	0.980	0.980	----

Therm #:	17	18	19	20	21	22	23	24
Depth (m):	2.700	2.520	2.340	2.160	1.980	1.800	1.620	1.440
Temp (mK):	32.4	22.8	13.5	1.2	-6.4	-12.5	-23.0	-29.7
Cond (W/m-K):	0.980	0.980	0.980	0.980	0.980	0.980	0.980	0.980

Therm #:	25	26	27	28	29	30	31	32
Depth (m):	1.260	1.080	0.900	0.720	0.540	0.360	0.180	0.000
Temp (mK):	-38.8	----	-56.0	-61.4	----	----	----	----
Cond (W/m-K):	0.980	----	0.980	0.980	----	----	----	----

Gradient (mK/m)= 45.78 ± 0.64
Conductivity (W/m-K)= 0.980 ± 0.000
Heat Flow (mW/m^2)= 44.87 ± 0.63

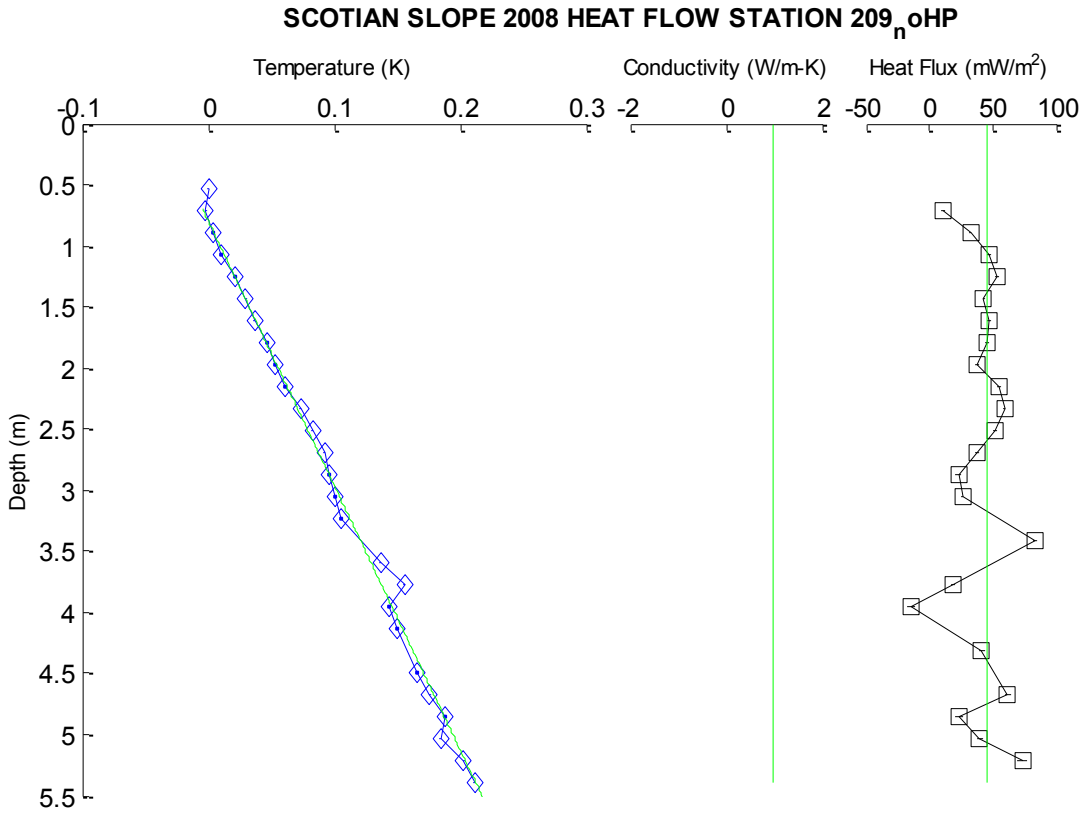

SCOTIAN SLOPE 2008 HEAT FLOW STATION 210ar3
Tilt (deg)= 4.0

Therm #:	1	2	3	4	5	6	7	8
Depth (m):	5.566	5.387	5.207	5.028	4.848	4.669	4.489	4.309
Temp (mK):	----	----	143.7	130.0	124.3	112.4	----	----
Cond (W/m-K):	----	----	1.149	1.195	1.115	1.053	----	----

Therm #:	9	10	11	12	13	14	15	16
Depth (m):	4.130	3.950	3.771	3.591	3.412	3.232	3.053	2.873
Temp (mK):	91.6	78.9	----	59.2	50.4	33.3	----	----
Cond (W/m-K):	1.073	1.085	----	1.126	0.944	0.832	----	----

Therm #:	17	18	19	20	21	22	23	24
Depth (m):	2.693	2.514	2.334	2.155	1.975	1.796	1.616	1.436
Temp (mK):	17.2	8.7	6.0	-2.5	-13.5	-18.6	-19.3	----
Cond (W/m-K):	1.241	0.940	0.909	0.868	0.834	1.013	0.938	----

Therm #:	25	26	27	28	29	30	31	32
Depth (m):	1.257	1.077	0.898	0.718	0.539	0.359	0.180	0.000
Temp (mK):	----	----	----	----	----	----	----	----
Cond (W/m-K):	----	----	----	----	----	----	----	----

Gradient (mK/m)= 45.14 ± 0.80
Conductivity (W/m-K)= 0.922 ± 0.158
Heat Flow (mW/m^2)= 41.62 ± 7.89

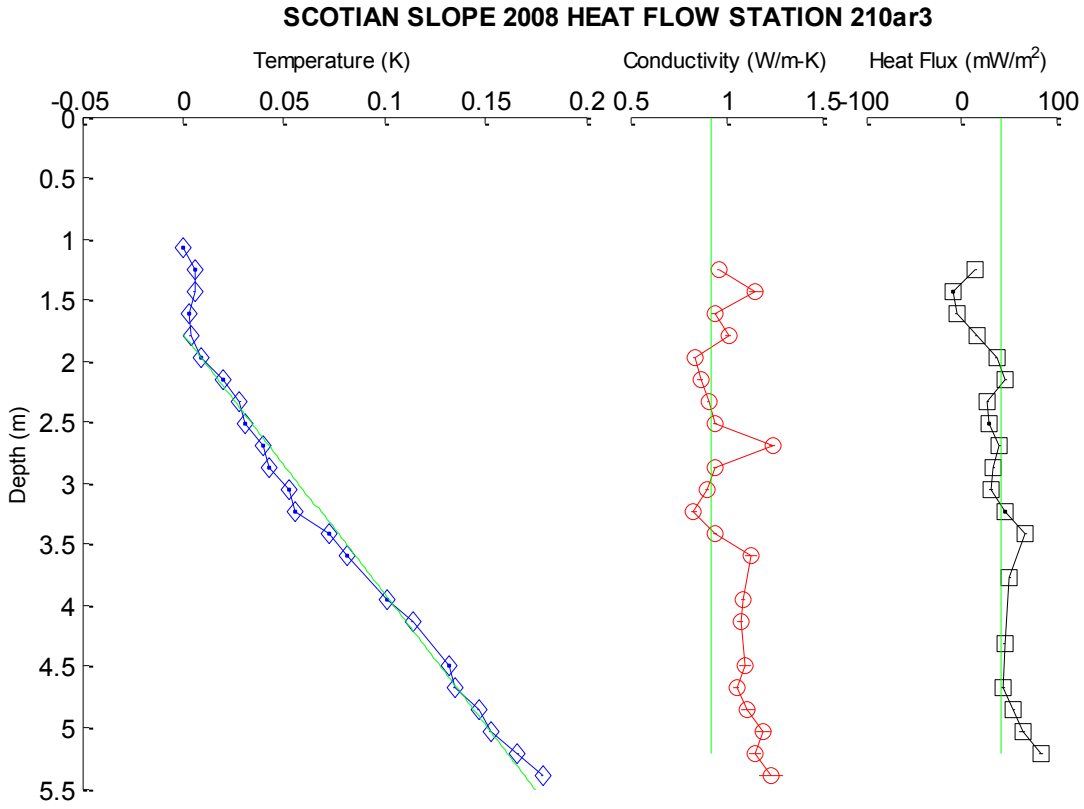

SCOTIAN SLOPE 2008 HEAT FLOW STATION 219ar
Tilt (deg)= 2.5

Therm #:	1	2	3	4	5	6	7	8
Depth (m):	5.575	5.395	5.215	5.035	4.855	4.676	4.496	4.316
Temp (mK):	----	233.7	227.9	221.8	211.4	182.0	----	----
Cond (W/m-K):	----	1.111	1.075	1.192	1.045	0.861	----	----

Therm #:	9	10	11	12	13	14	15	16
Depth (m):	4.136	3.956	3.776	3.597	3.417	3.237	3.057	2.877
Temp (mK):	182.1	177.1	----	164.0	157.3	150.7	143.7	135.7
Cond (W/m-K):	1.105	1.181	----	1.201	1.268	1.019	1.033	1.135

Therm #:	17	18	19	20	21	22	23	24
Depth (m):	2.697	2.518	2.338	2.158	1.978	1.798	1.618	1.439
Temp (mK):	127.5	121.1	110.9	103.3	95.4	90.9	80.0	76.7
Cond (W/m-K):	1.095	1.089	0.968	0.978	1.036	1.210	1.042	1.025

Therm #:	25	26	27	28	29	30	31	32
Depth (m):	1.259	1.079	0.899	0.719	0.539	0.360	0.180	0.000
Temp (mK):	65.2	----	47.9	38.0	----	----	----	----
Cond (W/m-K):	1.038	----	0.994	0.964	----	----	----	----

Gradient (mK/m)= 41.19 ± 0.39
Conductivity (W/m-K)= 1.072 ± 0.093
Heat Flow (mW/m^2)= 44.15 ± 4.27

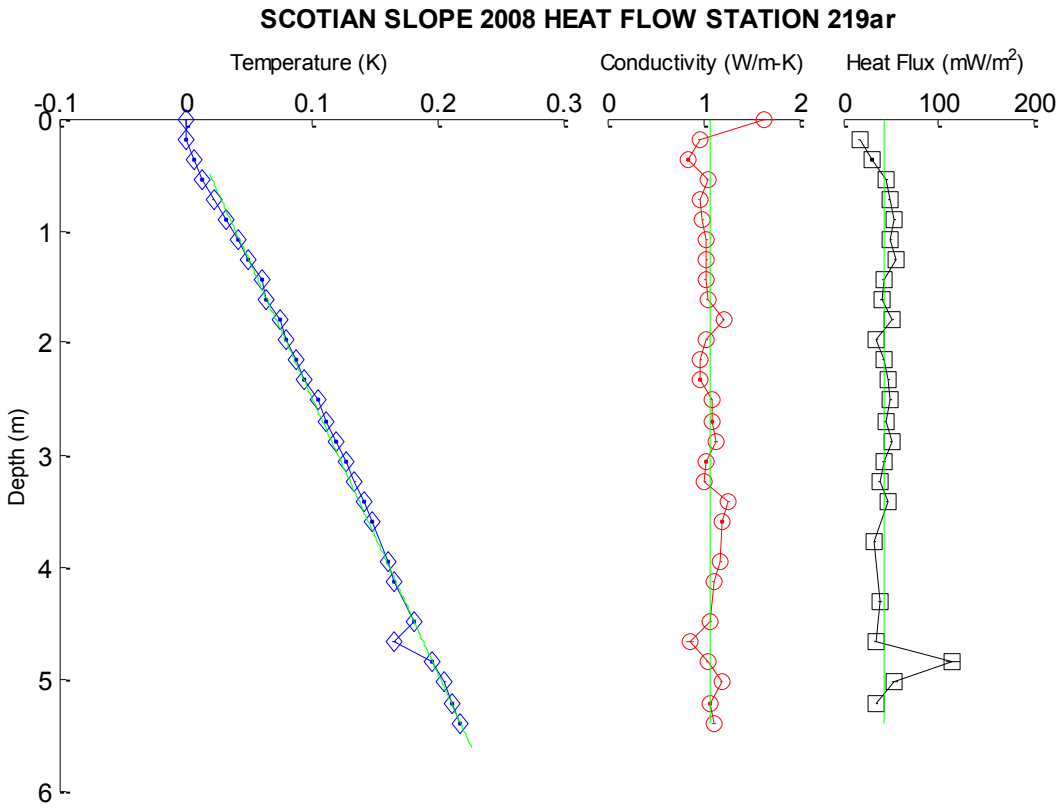

SCOTIAN SLOPE 2008 HEAT FLOW STATION 220r2
Tilt (deg)= 0.5

Therm #:	1	2	3	4	5	6	7	8
Depth (m):	5.580	5.400	5.220	5.040	4.860	4.680	4.500	4.320
Temp (mK):	255.6	244.2	238.4	234.5	221.9	217.3	206.1	----
Cond (W/m-K):	1.144	1.042	1.056	1.103	1.086	1.068	1.050	----

Therm #:	9	10	11	12	13	14	15	16
Depth (m):	4.140	3.960	3.780	3.600	3.420	3.240	3.060	2.880
Temp (mK):	187.6	185.3	----	170.8	162.2	155.5	147.4	139.7
Cond (W/m-K):	0.956	0.972	----	1.035	1.049	1.070	1.039	1.048

Therm #:	17	18	19	20	21	22	23	24
Depth (m):	2.700	2.520	2.340	2.160	1.980	1.800	1.620	1.440
Temp (mK):	130.9	121.4	111.3	105.8	95.8	94.7	83.9	77.3
Cond (W/m-K):	1.084	1.046	0.992	0.992	0.995	1.195	1.065	1.030

Therm #:	25	26	27	28	29	30	31	32
Depth (m):	1.260	1.080	0.900	0.720	0.540	0.360	0.180	0.000
Temp (mK):	----	----	----	----	----	----	----	----
Cond (W/m-K):	----	----	----	----	----	----	----	----

Gradient (mK/m)= 43.29 ± 0.42
Conductivity (W/m-K)= 1.039 ± 0.054
Heat Flow (mW/m^2)= 44.98 ± 2.78

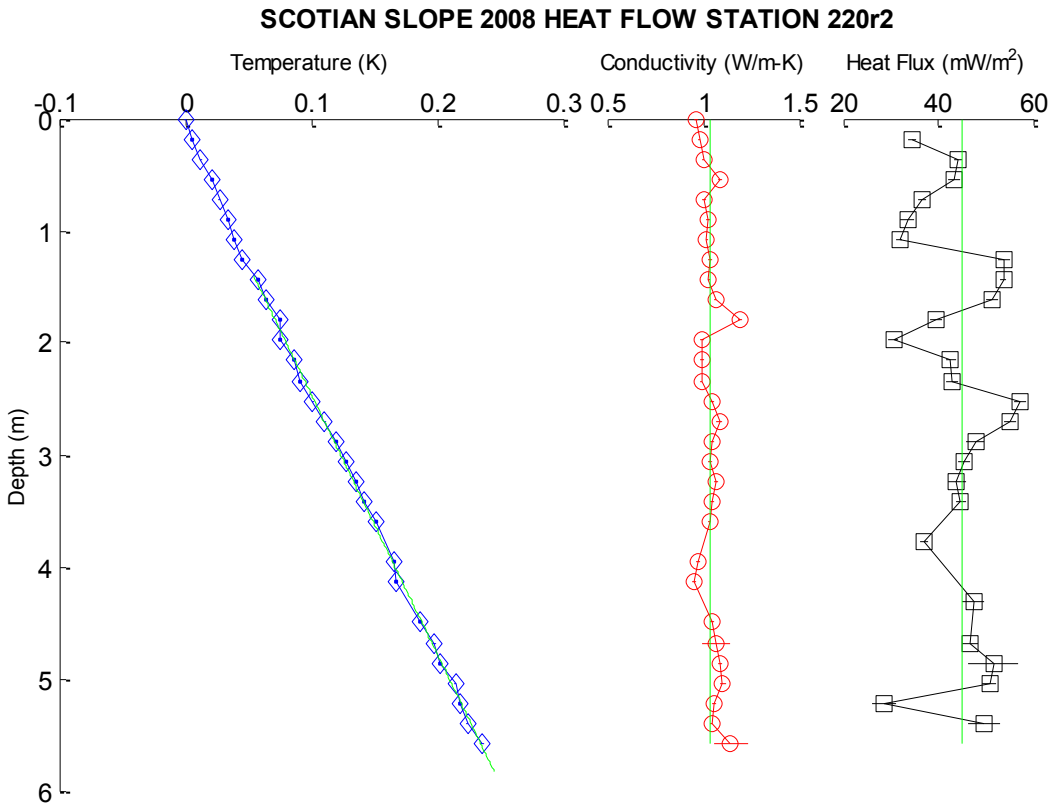

SCOTIAN SLOPE 2008 HEAT FLOW STATION 221
Tilt (deg)= 2.0

Therm #:	1	2	3	4	5	6	7	8
Depth (m):	5.577	5.397	5.217	5.037	4.857	4.677	4.497	4.317
Temp (mK):	229.6	215.1	207.3	----	199.7	----	180.0	----
Cond (W/m-K):	1.404	1.183	1.253	----	1.316	----	0.985	----

Therm #:	9	10	11	12	13	14	15	16
Depth (m):	4.137	3.958	3.778	3.598	3.418	3.238	3.058	2.878
Temp (mK):	171.7	169.4	----	151.5	143.8	135.0	128.1	119.9
Cond (W/m-K):	1.060	1.155	----	0.958	0.943	0.942	0.947	0.947

Therm #:	17	18	19	20	21	22	23	24
Depth (m):	2.698	2.518	2.339	2.159	1.979	1.799	1.619	1.439
Temp (mK):	112.4	102.2	95.7	87.9	----	73.7	63.2	59.3
Cond (W/m-K):	0.988	0.905	0.939	1.058	----	1.142	0.957	0.964

Therm #:	25	26	27	28	29	30	31	32
Depth (m):	1.259	1.079	0.899	0.720	0.540	0.360	0.180	0.000
Temp (mK):	----	----	31.2	----	----	----	----	----
Cond (W/m-K):	----	----	0.997	----	----	----	----	----

Gradient (mK/m)= 40.81 ± 0.76
Conductivity (W/m-K)= 0.986 ± 0.154
Heat Flow (mW/m^2)= 40.25 ± 7.03

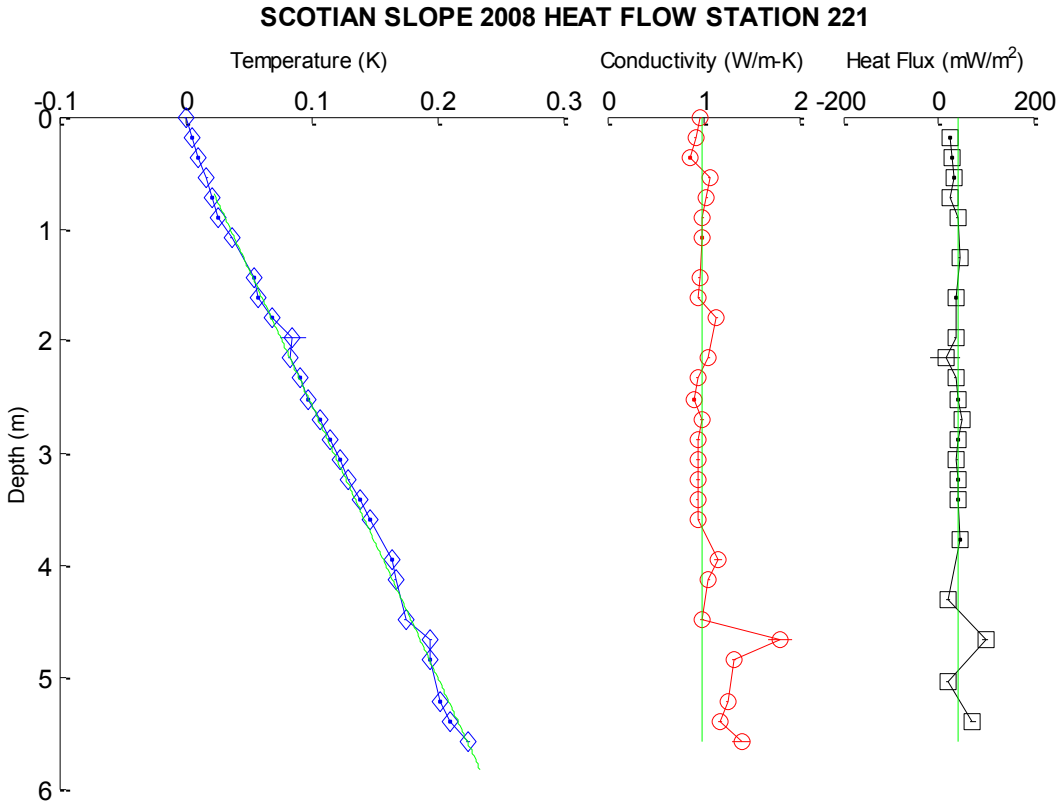

C-4: Line 3 Heat Flow Stations

SCOTIAN SLOPE 2008 HEAT FLOW STATION 317
Tilt (deg)= 0.5

Therm #:	1	2	3	4	5	6	7	8
Depth (m):	5.580	5.400	5.220	5.040	4.860	4.680	4.500	4.320
Temp (mK):	----	271.3	265.5	247.6	250.7	237.8	----	----
Cond (W/m-K):	----	1.032	1.007	1.019	0.973	0.797	----	----

Therm #:	9	10	11	12	13	14	15	16
Depth (m):	4.140	3.960	3.780	3.600	3.420	3.240	3.060	2.880
Temp (mK):	217.1	213.7	----	196.5	188.9	178.2	170.1	166.4
Cond (W/m-K):	1.005	0.942	----	0.988	1.036	0.997	1.021	1.055

Therm #:	17	18	19	20	21	22	23	24
Depth (m):	2.700	2.520	2.340	2.160	1.980	1.800	1.620	1.440
Temp (mK):	157.9	153.4	148.7	138.8	134.6	119.9	111.9	106.7
Cond (W/m-K):	1.088	1.074	1.028	1.173	1.025	1.112	1.004	0.936

Therm #:	25	26	27	28	29	30	31	32
Depth (m):	1.260	1.080	0.900	0.720	0.540	0.360	0.180	0.000
Temp (mK):	92.5	----	----	----	----	----	----	----
Cond (W/m-K):	1.033	----	----	----	----	----	----	----

Gradient (mK/m)= 41.18 ± 0.61
Conductivity (W/m-K)= 1.010 ± 0.072
Heat Flow (mW/m^2)= 41.57 ± 3.59

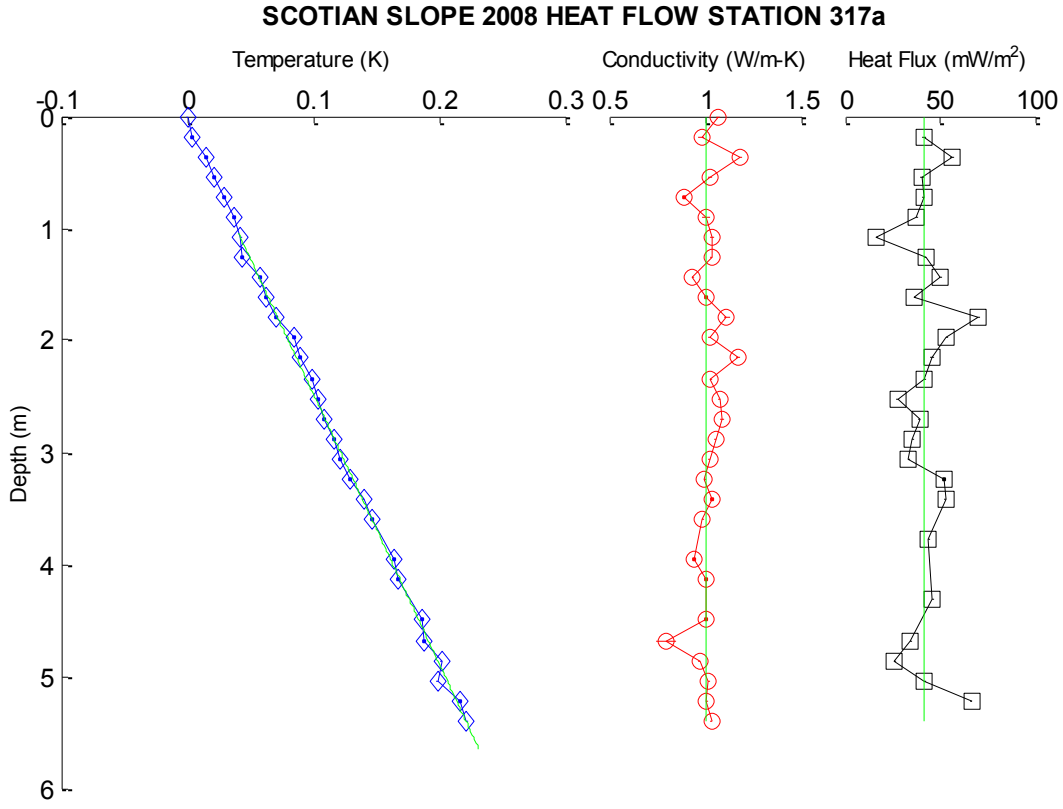

SCOTIAN SLOPE 2008 HEAT FLOW STATION 316
Tilt (deg)= 0.0

Therm #	1	2	3	4	5	6	7	8
Depth (m)	5.580	5.400	5.220	5.040	4.860	4.680	4.500	4.320
Temp (mK)	----	217.1	208.9	194.3	----	----	----	----
Cond (W/m-K)	0.921	1.112	1.103	1.127	----	----	----	----

Therm #	9	10	11	12	13	14	15	16
Depth (m)	4.140	3.960	3.780	3.600	3.420	3.240	3.060	2.880
Temp (mK)	161.0	157.3	----	142.2	132.7	125.5	116.6	111.3
Cond (W/m-K)	1.086	1.025	----	1.026	1.017	1.045	1.116	1.076

Therm #	17	18	19	20	21	22	23	24
Depth (m)	2.700	2.520	2.340	2.160	1.980	1.800	1.620	1.440
Temp (mK)	----	----	88.9	82.7	74.5	67.5	59.0	53.8
Cond (W/m-K)	----	----	1.125	1.072	1.076	1.138	1.136	1.061

Therm #	25	26	27	28	29	30	31	32
Depth (m)	1.260	1.080	0.900	0.720	0.540	0.360	0.180	0.000
Temp (mK)	44.0	----	31.8	25.1	----	----	----	----
Cond (W/m-K)	1.123	----	1.031	1.011	----	----	----	----

Gradient (mK/m)= 40.66 ± 0.30
Conductivity (W/m-K)= 1.064 ± 0.054
Heat Flow (mW/m^2)= 43.26 ± 2.53

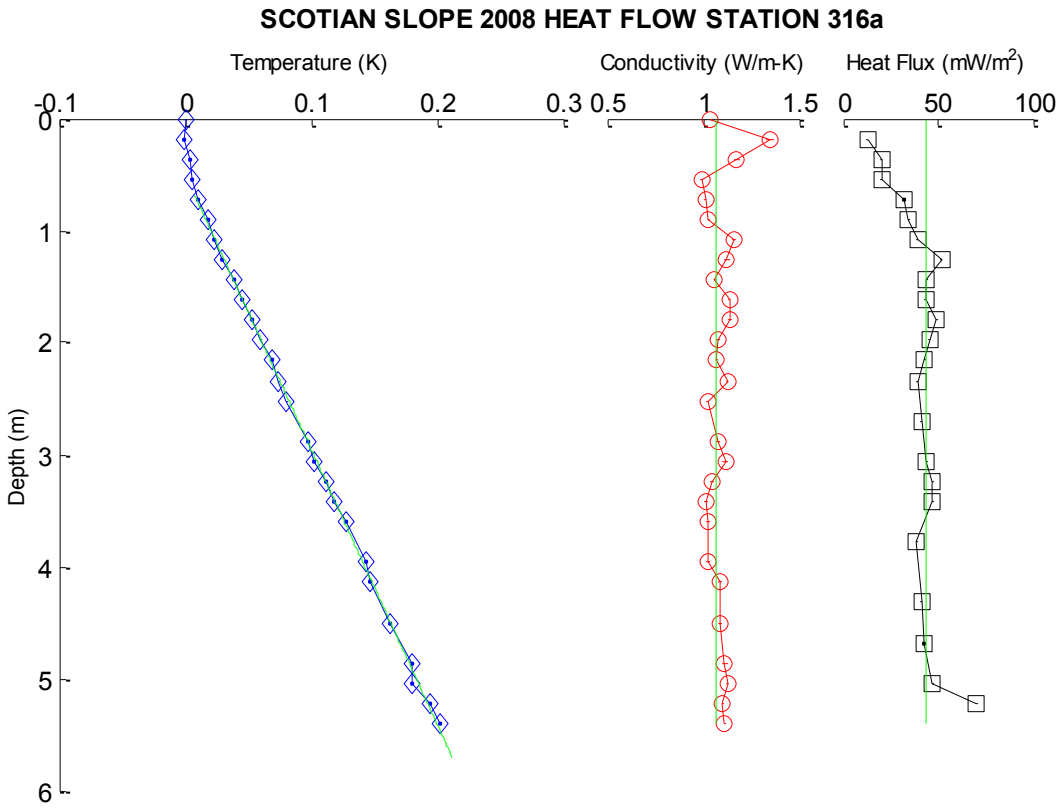

SCOTIAN SLOPE 2008 HEAT FLOW STATION 315
Tilt (deg)= 0.0

Therm #	1	2	3	4	5	6	7	8
Depth (m)	5.580	5.400	5.220	5.040	4.860	4.680	4.500	4.320
Temp (mK)	----	----	241.6	228.0	228.2	----	----	----
Cond (W/m-K)	----	----	1.103	1.127	1.064	----	----	----

Therm #	9	10	11	12	13	14	15	16
Depth (m)	4.140	3.960	3.780	3.600	3.420	3.240	3.060	2.880
Temp (mK)	200.3	205.2	----	----	171.8	----	151.4	148.3
Cond (W/m-K)	1.086	1.025	----	----	1.017	----	1.116	1.076

Therm #	17	18	19	20	21	22	23	24
Depth (m)	2.700	2.520	2.340	2.160	1.980	1.800	1.620	1.440
Temp (mK)	----	----	126.7	121.2	----	103.8	----	89.7
Cond (W/m-K)	----	----	1.125	1.072	----	1.138	----	1.061

Therm #	25	26	27	28	29	30	31	32
Depth (m)	1.260	1.080	0.900	0.720	0.540	0.360	0.180	0.000
Temp (mK)	84.6	----	----	----	----	----	----	----
Cond (W/m-K)	1.123	----	----	----	----	----	----	----

Gradient (mK/m)= 39.70 ± 0.63
Conductivity (W/m-K)= 1.086 ± 0.038
Heat Flow (mW/m^2)= 43.11 ± 2.18

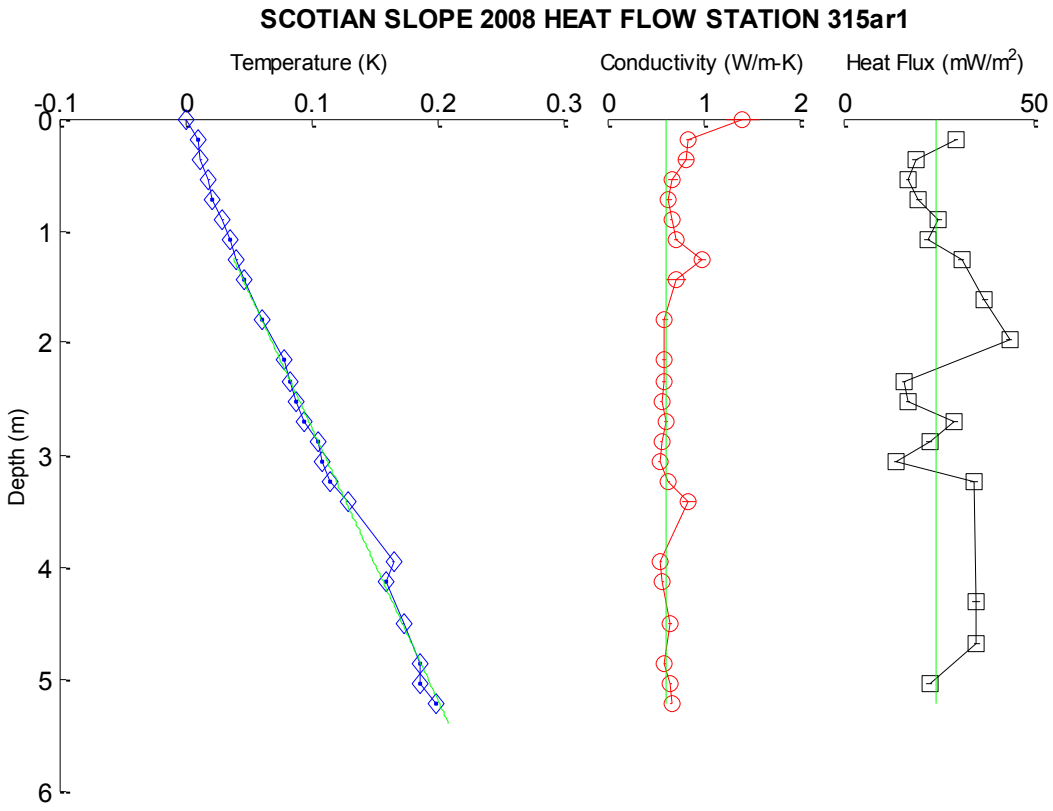

SCOTIAN SLOPE 2008 HEAT FLOW STATION 314_noHP
Tilt (deg)= 1.0

Therm #:	1	2	3	4	5	6	7	8
Depth (m):	5.579	5.399	5.219	5.039	4.859	4.679	4.499	4.319
Temp (mK):	----	----	----	278.9	276.2	265.5	----	----
Cond (W/m-K):	----	----	----	1.040	1.040	1.040	----	----

Therm #:	9	10	11	12	13	14	15	16
Depth (m):	4.139	3.959	3.779	3.599	3.419	3.240	3.060	2.880
Temp (mK):	----	240.1	----	221.7	213.5	200.4	185.7	193.2
Cond (W/m-K):	----	1.040	1.040	1.040	1.040	1.040	1.040	1.040

Therm #:	17	18	19	20	21	22	23	24
Depth (m):	2.700	2.520	2.340	2.160	1.980	1.800	1.620	1.440
Temp (mK):	----	172.9	166.1	163.3	157.1	142.0	135.6	129.7
Cond (W/m-K):	----	1.040	1.040	1.040	1.040	1.040	1.040	1.040

Therm #:	25	26	27	28	29	30	31	32
Depth (m):	1.260	1.080	0.900	0.720	0.540	0.360	0.180	0.000
Temp (mK):	121.0	----	----	----	----	----	----	----
Cond (W/m-K):	1.040	----	----	----	----	----	----	----

Gradient (mK/m)= 42.86 ± 0.66
Conductivity (W/m-K)= 1.040 ± 0.000
Heat Flow (mW/m^2)= 44.57 ± 0.69

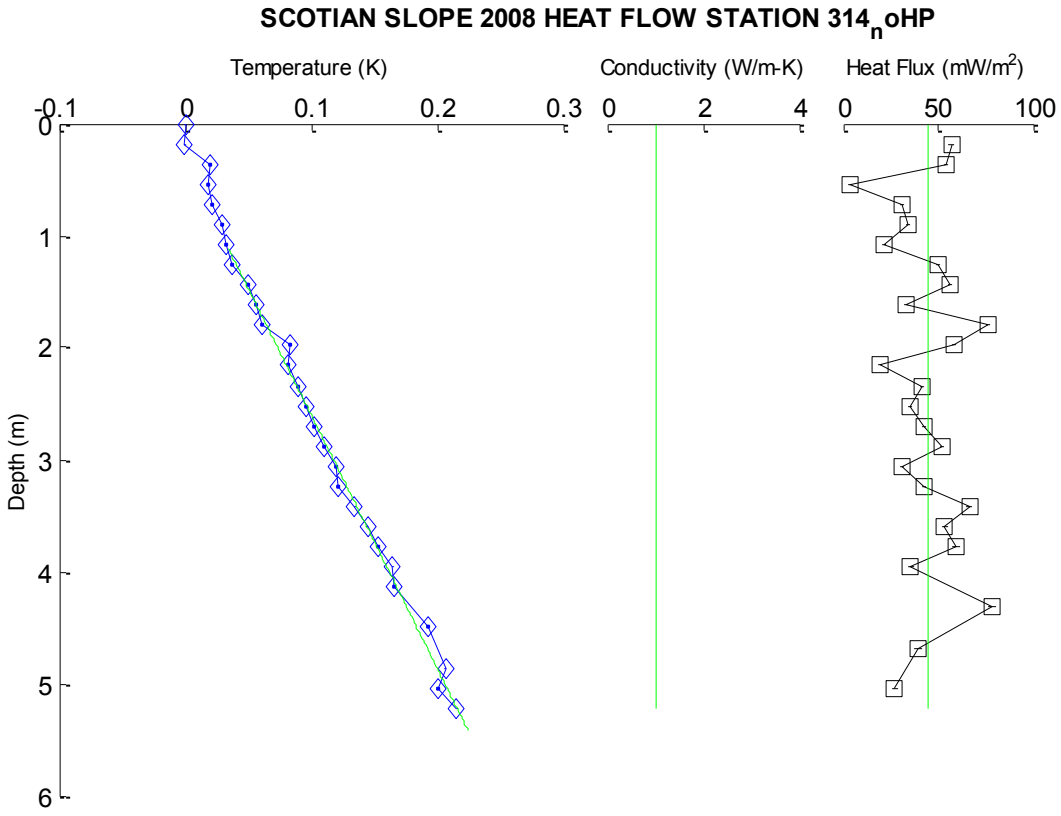

SCOTIAN SLOPE 2008 HEAT FLOW STATION 313
Tilt (deg)= 0.0

Therm #	1	2	3	4	5	6	7	8
Depth (m)	5.580	5.400	5.220	5.040	4.860	4.680	4.500	4.320
Temp (mK)	----	251.9	244.4	228.9	230.4	----	----	----
Cond (W/m-K)	----	1.054	0.953	1.071	1.020	----	----	----

Therm #	9	10	11	12	13	14	15	16
Depth (m)	4.140	3.960	3.780	3.600	3.420	3.240	3.060	2.880
Temp (mK)	202.3	199.7	----	188.7	180.5	172.9	163.7	161.6
Cond (W/m-K)	1.030	----	0.921	1.037	0.982	0.999	0.991	1.020

Therm #	17	18	19	20	21	22	23	24
Depth (m)	2.700	2.520	2.340	2.160	1.980	1.800	1.620	1.440
Temp (mK)	154.4	----	144.4	137.7	131.8	127.0	118.9	118.6
Cond (W/m-K)	1.043	----	1.019	1.045	1.014	1.070	1.050	1.068

Therm #	25	26	27	28	29	30	31	32
Depth (m)	1.260	1.080	0.900	0.720	0.540	0.360	0.180	0.000
Temp (mK)	105.7	----	----	----	----	----	----	----
Cond (W/m-K)	1.046	----	----	----	----	----	----	----

Gradient (mK/m)= 33.82 ± 0.54
Conductivity (W/m-K)= 1.018 ± 0.039
Heat Flow (mW/m^2)= 34.44 ± 1.87

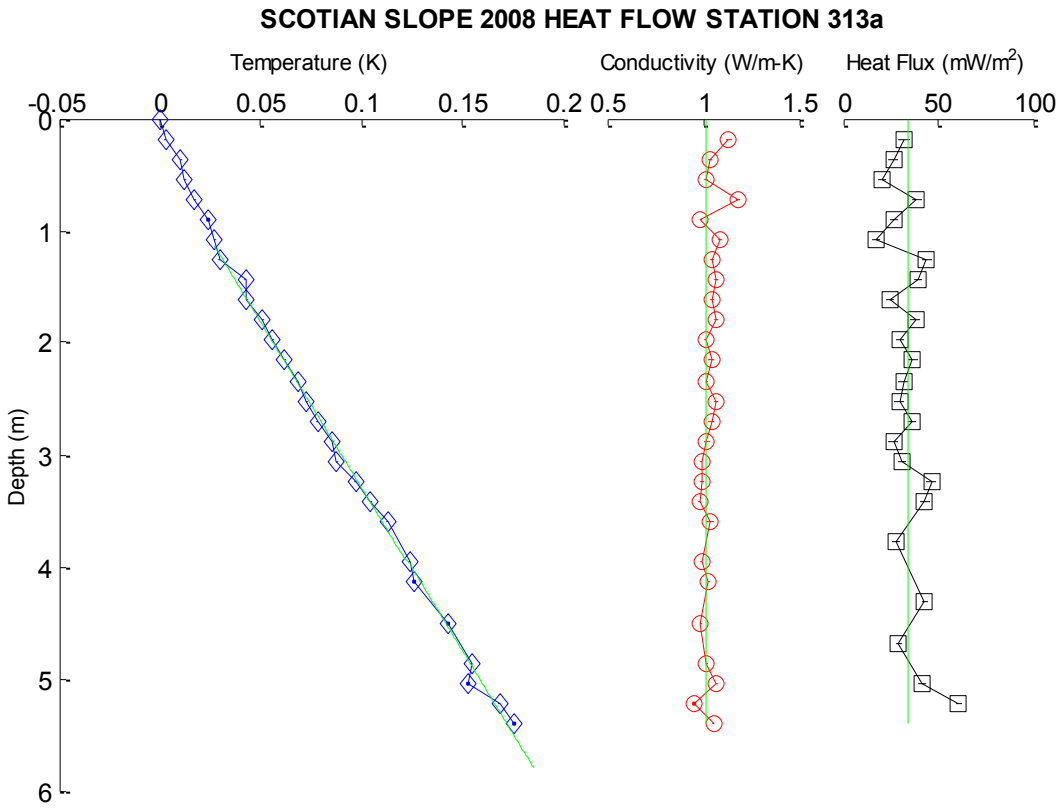

SCOTIAN SLOPE 2008 HEAT FLOW STATION 312
Tilt (deg)= 0.0

Therm #:	1	2	3	4	5	6	7	8
Depth (m):	5.580	5.400	5.220	5.040	4.860	4.680	4.500	4.320
Temp (mK):	----	314.8	----	289.8	293.9	----	278.7	----
Cond (W/m-K):	----	1.106	----	1.129	1.102	----	1.107	----

Therm #:	9	10	11	12	13	14	15	16
Depth (m):	4.140	3.960	3.780	3.600	3.420	3.240	3.060	2.880
Temp (mK):	----	----	----	243.2	235.8	225.8	215.8	213.6
Cond (W/m-K):	----	----	----	1.074	1.093	1.034	1.127	1.065

Therm #:	17	18	19	20	21	22	23	24
Depth (m):	2.700	2.520	2.340	2.160	1.980	1.800	1.620	1.440
Temp (mK):	207.4	----	----	----	180.2	169.6	161.6	158.0
Cond (W/m-K):	1.098	----	----	0.921	1.001	1.059	1.027	1.022

Therm #:	25	26	27	28	29	30	31	32
Depth (m):	1.260	1.080	0.900	0.720	0.540	0.360	0.180	0.000
Temp (mK):	146.9	----	----	----	----	----	----	----
Cond (W/m-K):	1.078	----	----	----	----	----	----	----

Gradient (mK/m)= 39.04 ± 0.64
Conductivity (W/m-K)= 1.075 ± 0.053
Heat Flow (mW/m^2)= 41.96 ± 2.77

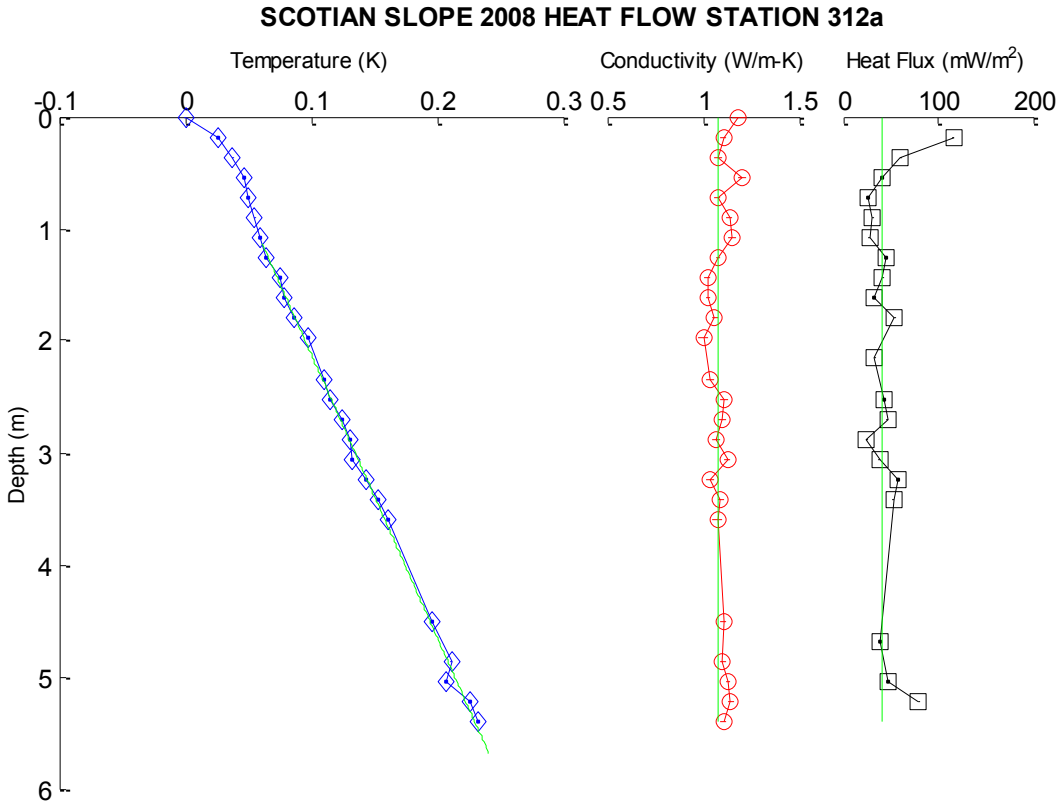

SCOTIAN SLOPE 2008 HEAT FLOW STATION 311
Tilt (deg)= 2.0

Therm #	1	2	3	4	5	6	7	8
Depth (m):	5.577	5.397	5.217	5.037	4.857	4.677	4.497	4.317
Temp (mK):	----	409.6	401.2	379.4	384.1	----	----	----
Cond (W/m-K):	----	1.104	1.073	1.096	1.050	----	----	----

Therm #	9	10	11	12	13	14	15	16
Depth (m):	4.137	3.958	3.778	3.598	3.418	3.238	3.058	2.878
Temp (mK):	343.4	341.3	----	320.9	311.1	299.9	287.5	284.6
Cond (W/m-K):	1.112	1.104	----	1.019	1.041	1.026	1.029	1.039

Therm #	17	18	19	20	21	22	23	24
Depth (m):	2.698	2.518	2.339	2.159	1.979	1.799	1.619	1.439
Temp (mK):	275.1	----	260.7	250.5	242.1	228.8	219.6	216.3
Cond (W/m-K):	1.116	----	1.043	1.023	0.985	1.126	1.098	1.113

Therm #	25	26	27	28	29	30	31	32
Depth (m):	1.259	1.079	0.899	0.720	0.540	0.360	0.180	0.000
Temp (mK):	202.0	----	----	----	----	----	----	----
Cond (W/m-K):	1.061	----	----	----	----	----	----	----

Gradient (mK/m)= 48.82 ± 0.71
Conductivity (W/m-K)= 1.058 ± 0.041
Heat Flow (mW/m^2)= 51.66 ± 2.77

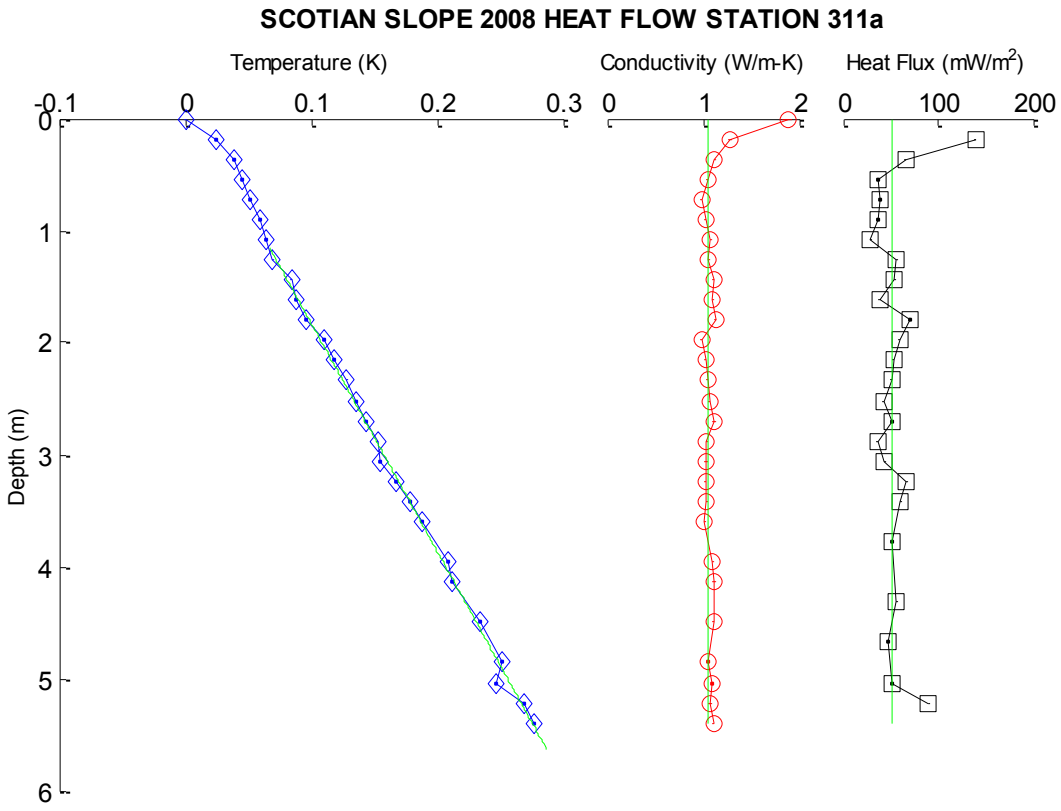

SCOTIAN SLOPE 2008 HEAT FLOW STATION 310
Tilt (deg)= 0.5

Therm #	1	2	3	4	5	6	7	8
Depth (m)	5.580	5.400	5.220	5.040	4.860	4.680	4.500	4.320
Temp (mK)	----	316.2	309.1	293.1	291.4	----	----	----
Cond (W/m-K)	----	1.099	1.147	1.126	1.100	----	----	----

Therm #	9	10	11	12	13	14	15	16
Depth (m)	4.140	3.960	3.780	3.600	3.420	3.240	3.060	2.880
Temp (mK)	254.0	251.9	----	236.4	225.7	219.3	206.7	202.6
Cond (W/m-K)	1.124	1.060	----	1.093	1.123	1.047	1.061	1.046

Therm #	17	18	19	20	21	22	23	24
Depth (m)	2.700	2.520	2.340	2.160	1.980	1.800	1.620	1.440
Temp (mK)	189.7	----	174.3	169.4	157.3	149.2	141.3	137.6
Cond (W/m-K)	1.041	----	1.051	1.031	1.052	1.065	0.994	1.099

Therm #	25	26	27	28	29	30	31	32
Depth (m)	1.260	1.080	0.900	0.720	0.540	0.360	0.180	0.000
Temp (mK)	130.0	----	----	----	----	----	----	----
Cond (W/m-K)	1.135	----	----	----	----	----	----	----

Gradient (mK/m)= 45.38 ± 0.72
Conductivity (W/m-K)= 1.063 ± 0.043
Heat Flow (mW/m^2)= 48.22 ± 2.73

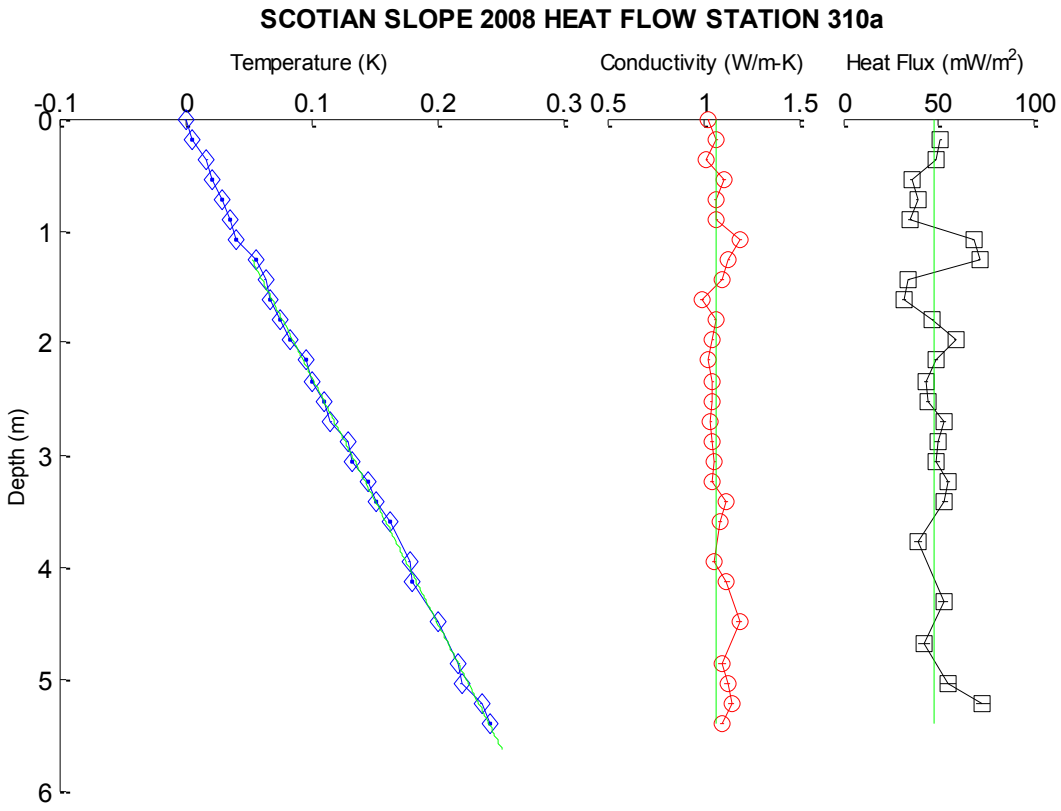

SCOTIAN SLOPE 2008 HEAT FLOW STATION 309
Tilt (deg)= 2.0

Therm #:	1	2	3	4	5	6	7	8
Depth (m):	5.577	5.397	5.217	5.037	4.857	4.677	4.497	4.317
Temp (mK):	----	282.9	277.1	260.3	256.6	----	----	----
Cond (W/m-K):	----	1.067	1.152	1.087	1.036	----	----	----

Therm #:	9	10	11	12	13	14	15	16
Depth (m):	4.137	3.958	3.778	3.598	3.418	3.238	3.058	2.878
Temp (mK):	223.9	221.4	----	204.7	194.2	187.5	176.8	171.5
Cond (W/m-K):	1.135	1.079	----	1.067	1.070	1.076	1.100	1.051

Therm #:	17	18	19	20	21	22	23	24
Depth (m):	2.698	2.518	2.339	2.159	1.979	1.799	1.619	1.439
Temp (mK):	163.1	----	146.1	140.8	130.0	124.0	110.4	106.9
Cond (W/m-K):	1.099	----	1.018	1.061	1.032	1.140	1.218	1.023

Therm #:	25	26	27	28	29	30	31	32
Depth (m):	1.259	1.079	0.899	0.720	0.540	0.360	0.180	0.000
Temp (mK):	92.8	----	72.6	62.1	----	----	----	----
Cond (W/m-K):	1.007	----	0.970	0.989	----	----	----	----

Gradient (mK/m)= 45.80 ± 0.59
Conductivity (W/m-K)= 1.043 ± 0.063
Heat Flow (mW/m^2)= 47.76 ± 3.52

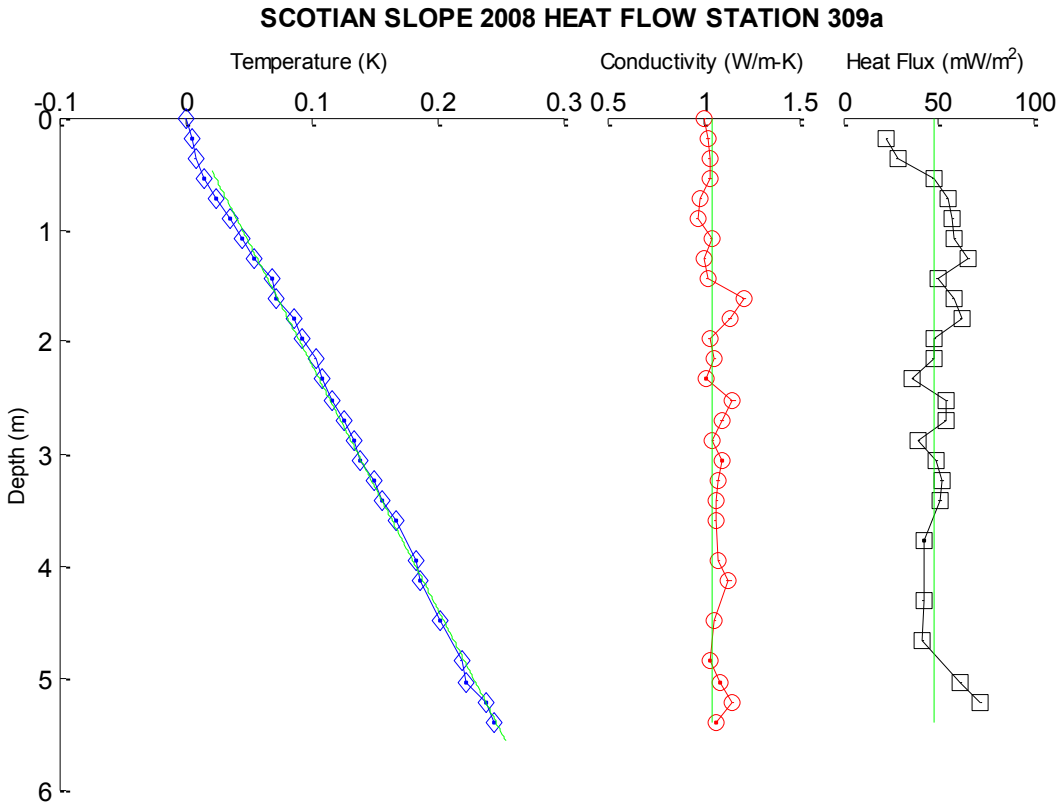

Appendix D: CTD Temperature Plots

Plots showing the temperature gradient through the bottom ~600 m of the water column for all heat flow stations with CTD data are included below.

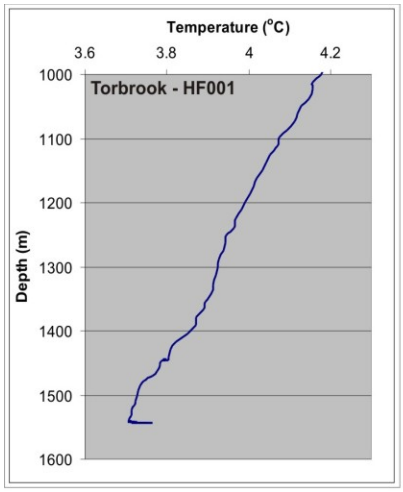

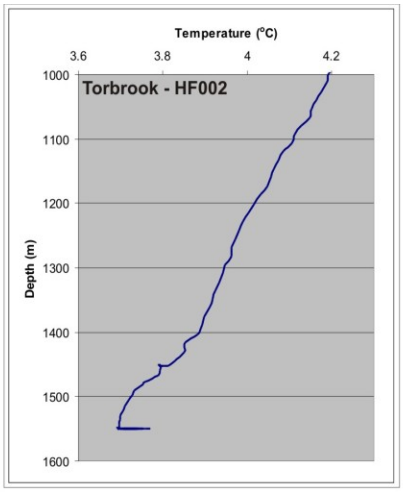

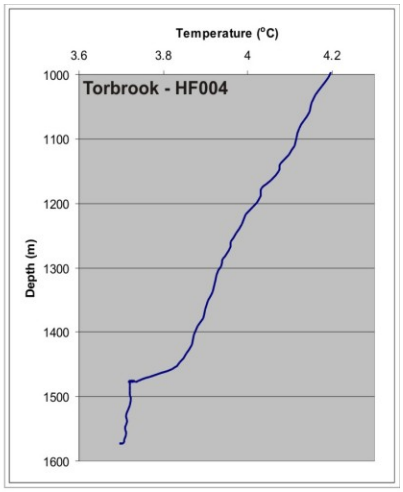

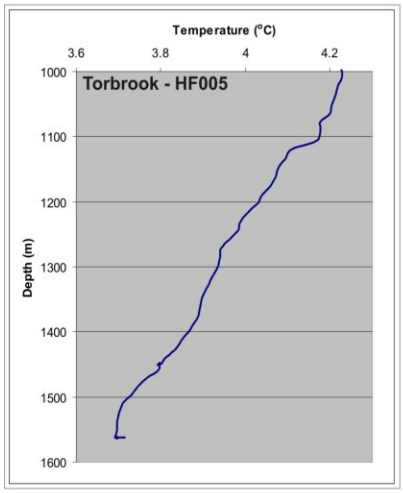

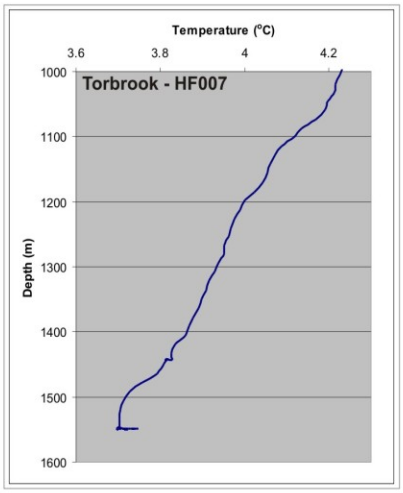

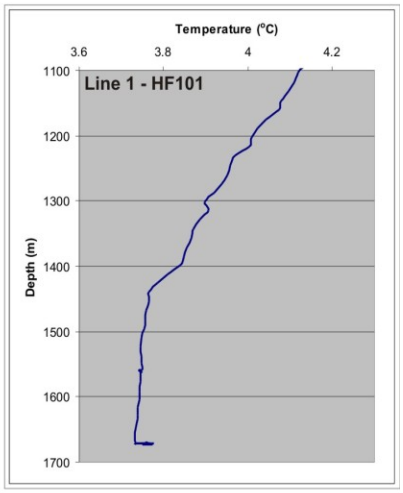

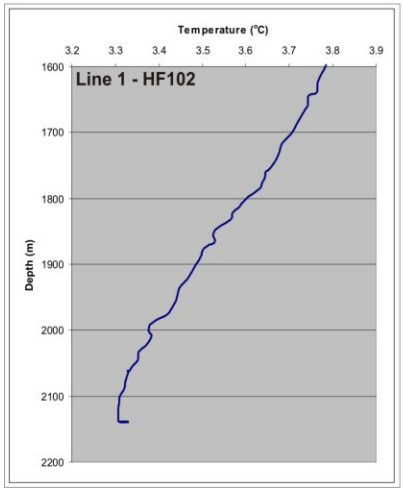

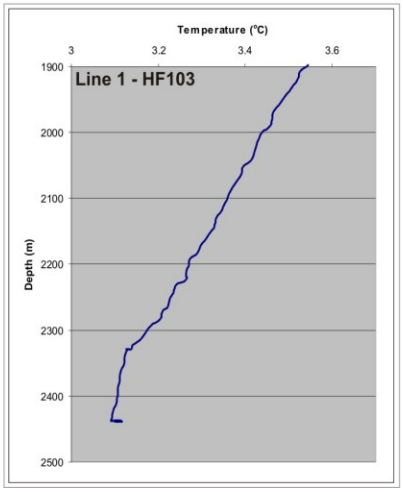

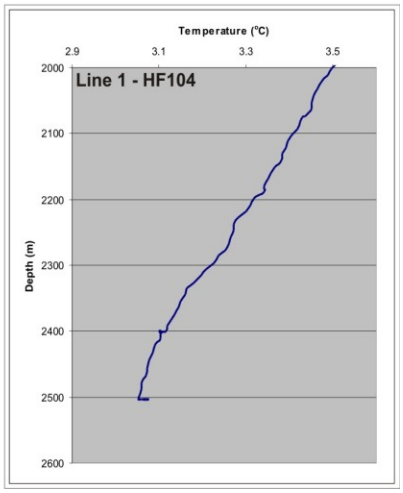

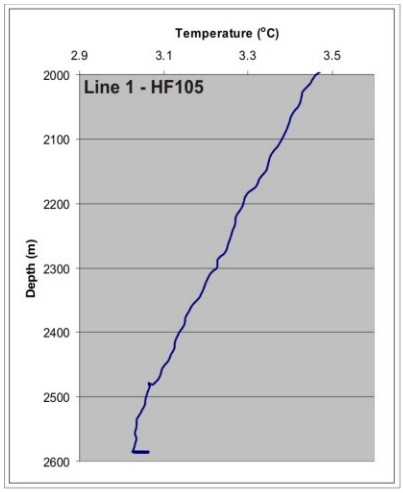
Temperature (°C)
2.9
3.1
3.3
3.5
Line 1 - HF105
Depth (m)
2000
2100
2200
2300
2400
2500
2600

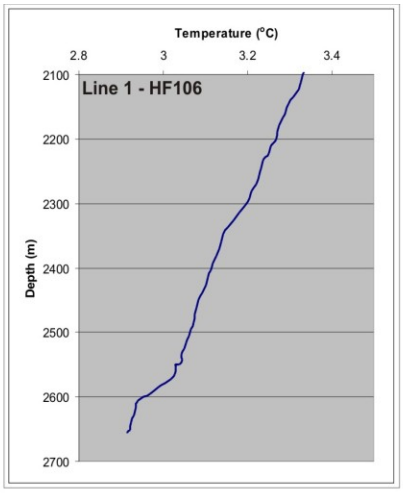
Temperature (°C)
2.8
3
3.2
3.4
Line 1 - HF106
Depth (m)
2100
2200
2300
2400
2500
2600
2700

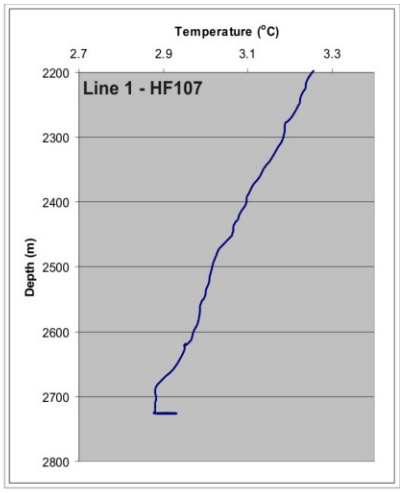
Temperature (°C)
2.7
2.9
3.1
3.3
Line 1 - HF107
Depth (m)
2200
2300
2400
2500
2600
2700
2800

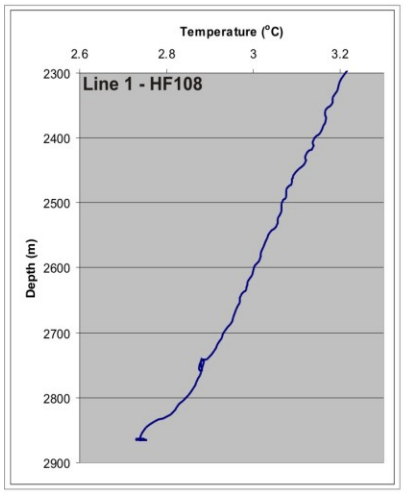
Temperature (°C)
2.6
2.8
3
3.2
Line 1 - HF108
Depth (m)
2300
2400
2500
2600
2700
2800
2900

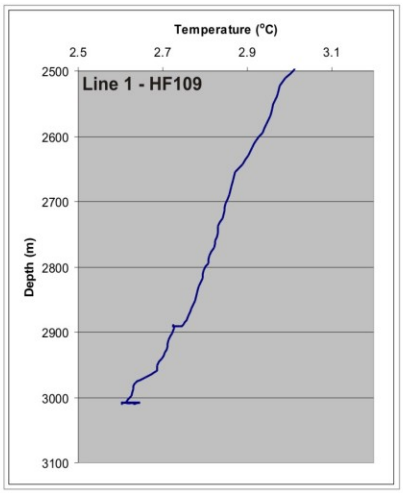
Temperature (°C)
2.5
2.7
2.9
3.1
Line 1 - HF109
Depth (m)
2500
2600
2700
2800
2900
3000
3100

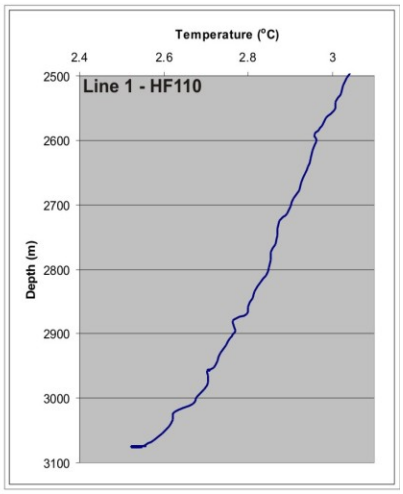
Temperature (°C)
2.4
2.6
2.8
3
Line 1 - HF110
Depth (m)
2500
2600
2700
2800
2900
3000
3100

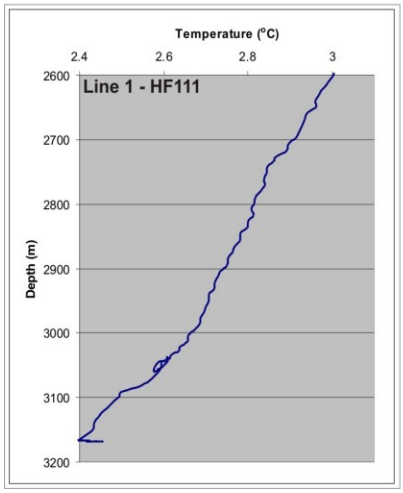
Temperature (°C)
2.4
2.6
2.8
3
Line 1 - HF111
Depth (m)
2600
2700
2800
2900
3000
3100
3200

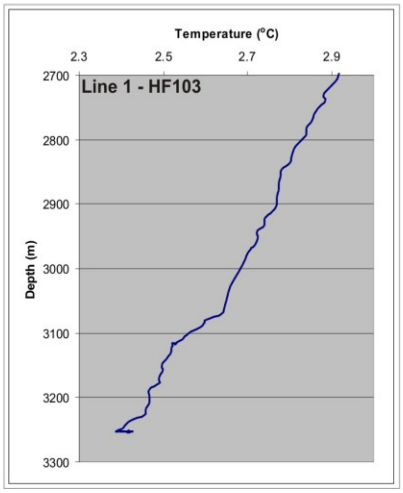
Temperature (°C)
2.3
2.5
2.7
2.9
Line 1 - HF103
Depth (m)
2700
2800
2900
3000
3100
3200
3300

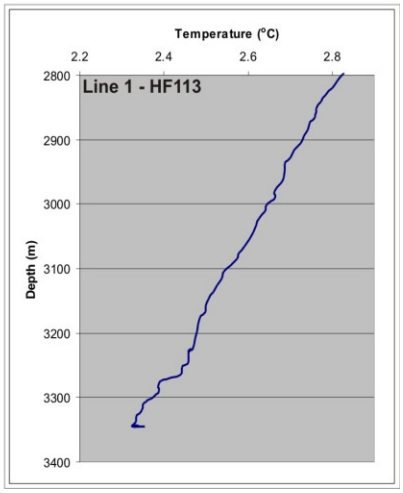
Temperature (°C)
2.2
2.4
2.6
2.8
Line 1 - HF113
Depth (m)
2800
2900
3000
3100
3200
3300
3400

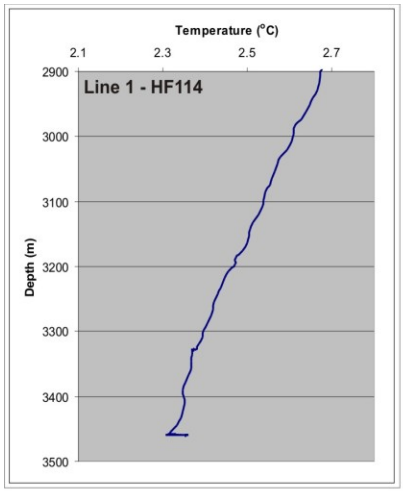
Temperature (°C)
2.1
2.3
2.5
2.7
Line 1 - HF114
Depth (m)
2900
3000
3100
3200
3300
3400
3500

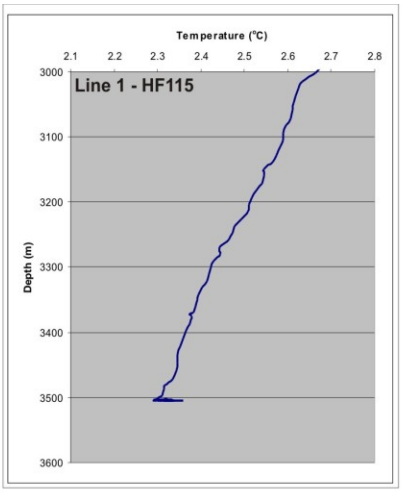
Temperature (°C)
2.1
2.2
2.3
2.4
2.5
2.6
2.7
2.8
Line 1 - HF115
Depth (m)
3000
3100
3200
3300
3400
3500
3600

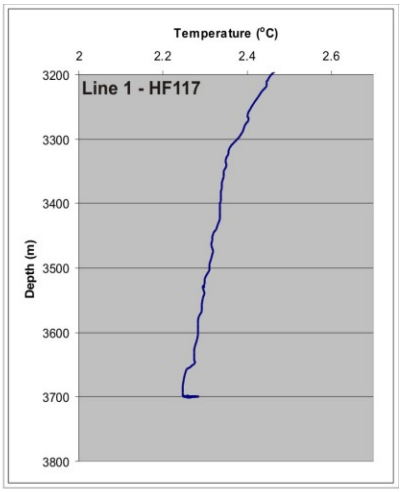
Temperature (°C)
2
2.2
2.4
2.6
Line 1 - HF117
Depth (m)
3200
3300
3400
3500
3600
3700
3800

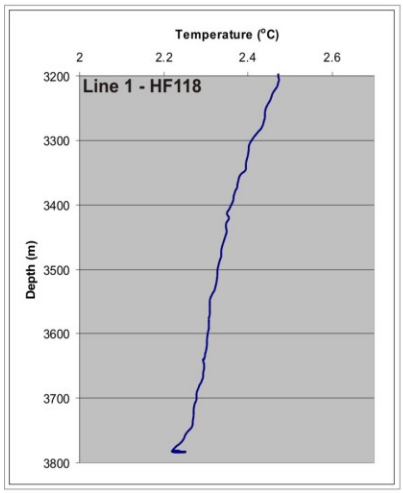
Temperature (°C)
2
2.2
2.4
2.6
Line 1 - HF118
Depth (m)
3200
3300
3400
3500
3600
3700
3800

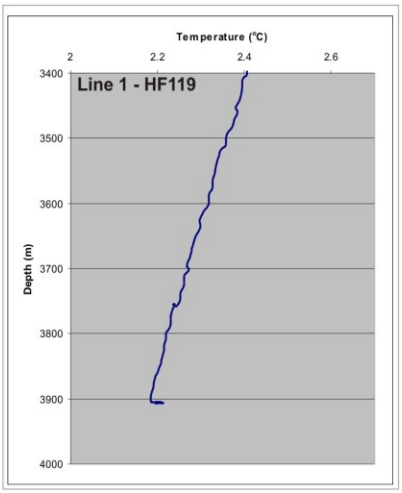
Temperature (°C)
2
2.2
2.4
2.6
Line 1 - HF119
Depth (m)
3400
3500
3600
3700
3800
3900
4000

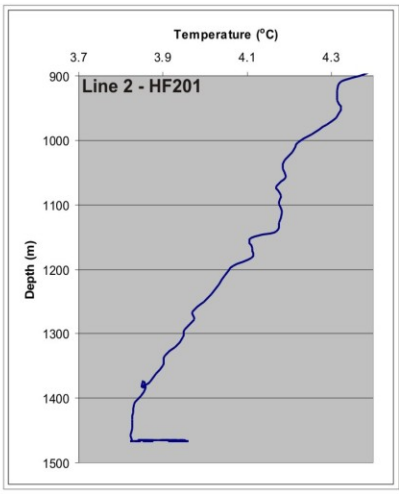
Temperature (°C)
3.7
3.9
4.1
4.3
Line 2 - HF201
Depth (m)
900
1000
1100
1200
1300
1400
1500

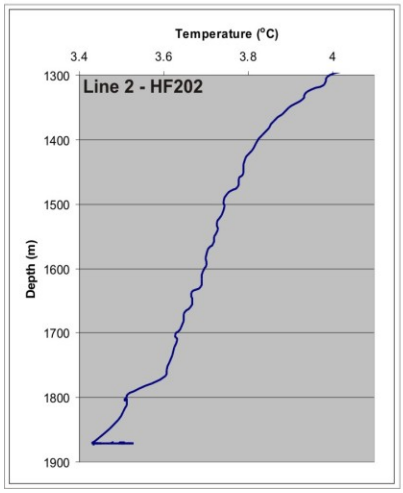
Temperature (°C)
3.4
3.6
3.8
4
Line 2 - HF202
Depth (m)
1300
1400
1500
1600
1700
1800
1900

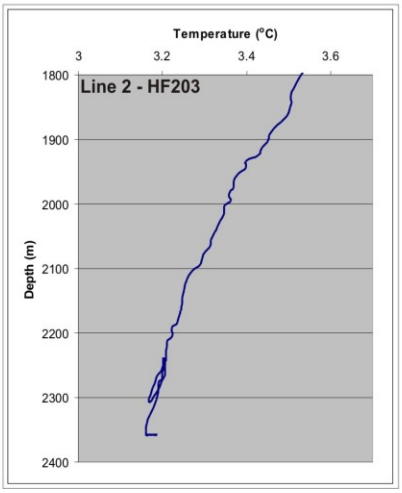
Temperature (°C)
3
3.2
3.4
3.6
Line 2 - HF203
Depth (m)
1800
1900
2000
2100
2200
2300
2400

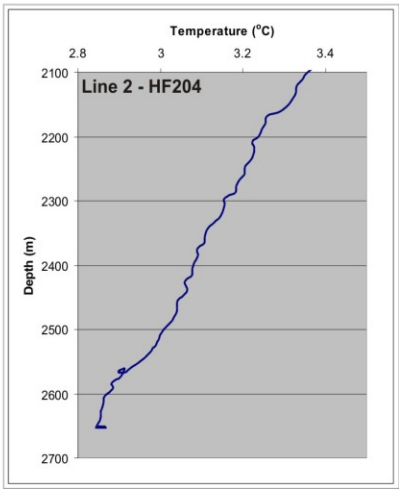
Temperature (°C)
2.8
3
3.2
3.4
Line 2 - HF204
Depth (m)
2100
2200
2300
2400
2500
2600
2700

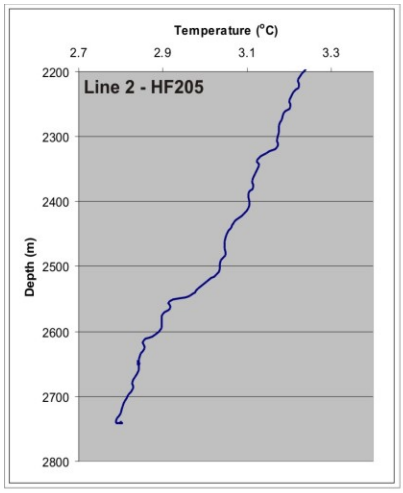
Temperature (°C)
2.7
2.9
3.1
3.3
Line 2 - HF205
Depth (m)
2200
2300
2400
2500
2600
2700
2800

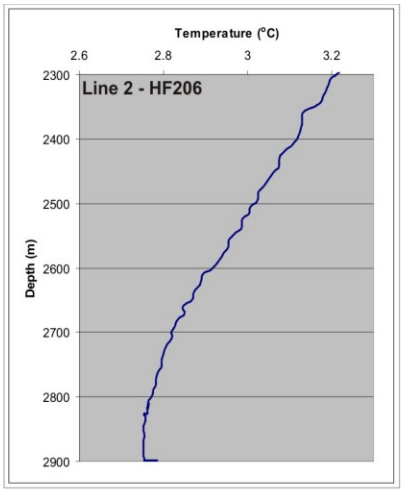
Temperature (°C)
2.6
2.8
3
3.2
Line 2 - HF206
Depth (m)
2300
2400
2500
2600
2700
2800
2900

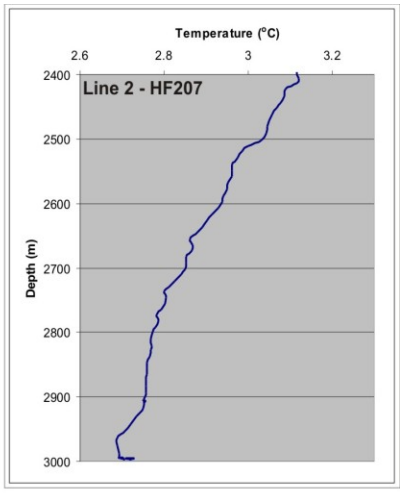
Temperature (°C)
2.6
2.8
3
3.2
Line 2 - HF207
Depth (m)
2400
2500
2600
2700
2800
2900
3000

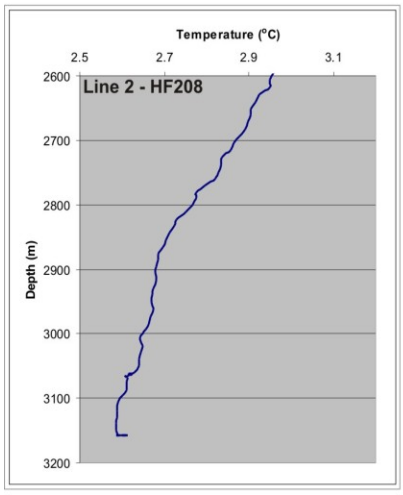
Temperature (°C)
2.5
2.7
2.9
3.1
Line 2 - HF208
Depth (m)
2600
2700
2800
2900
3000
3100
3200

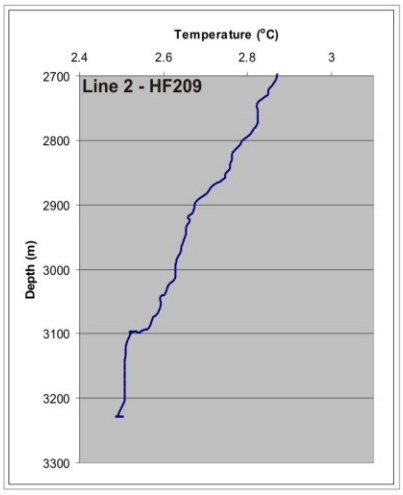
Temperature (°C)
2.4
2.6
2.8
3
Line 2 - HF209
Depth (m)
2700
2800
2900
3000
3100
3200
3300

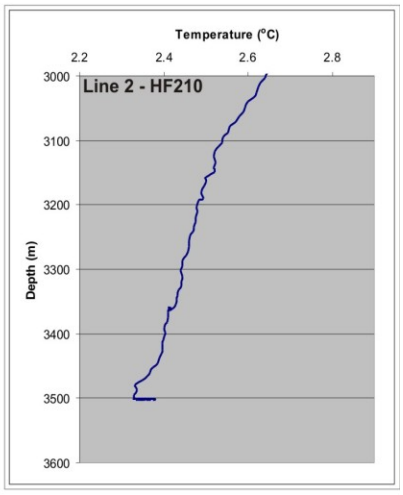
Temperature (°C)
2.2
2.4
2.6
2.8
Line 2 - HF210
Depth (m)
3000
3100
3200
3300
3400
3500
3600

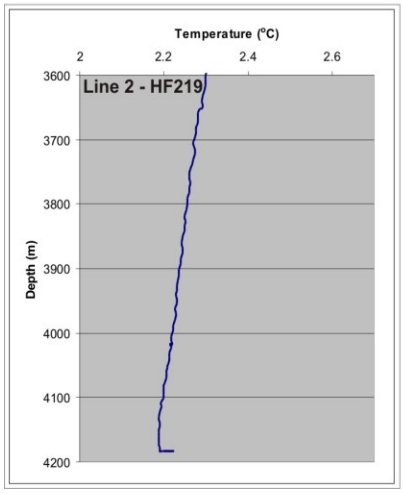
Temperature (°C)
2
2.2
2.4
2.6
Line 2 - HF219
Depth (m)
3600
3700
3800
3900
4000
4100
4200

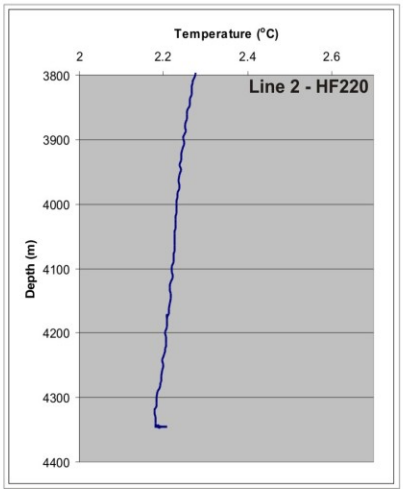
Temperature (°C)
2
2.2
2.4
2.6
Line 2 - HF220
Depth (m)
3800
3900
4000
4100
4200
4300
4400

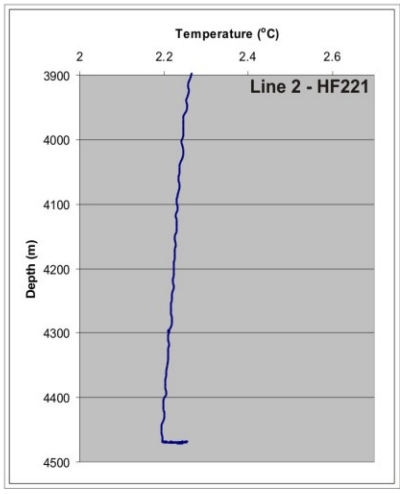
Temperature (°C)
2
2.2
2.4
2.6
Line 2 - HF221
Depth (m)
3900
4000
4100
4200
4300
4400
4500

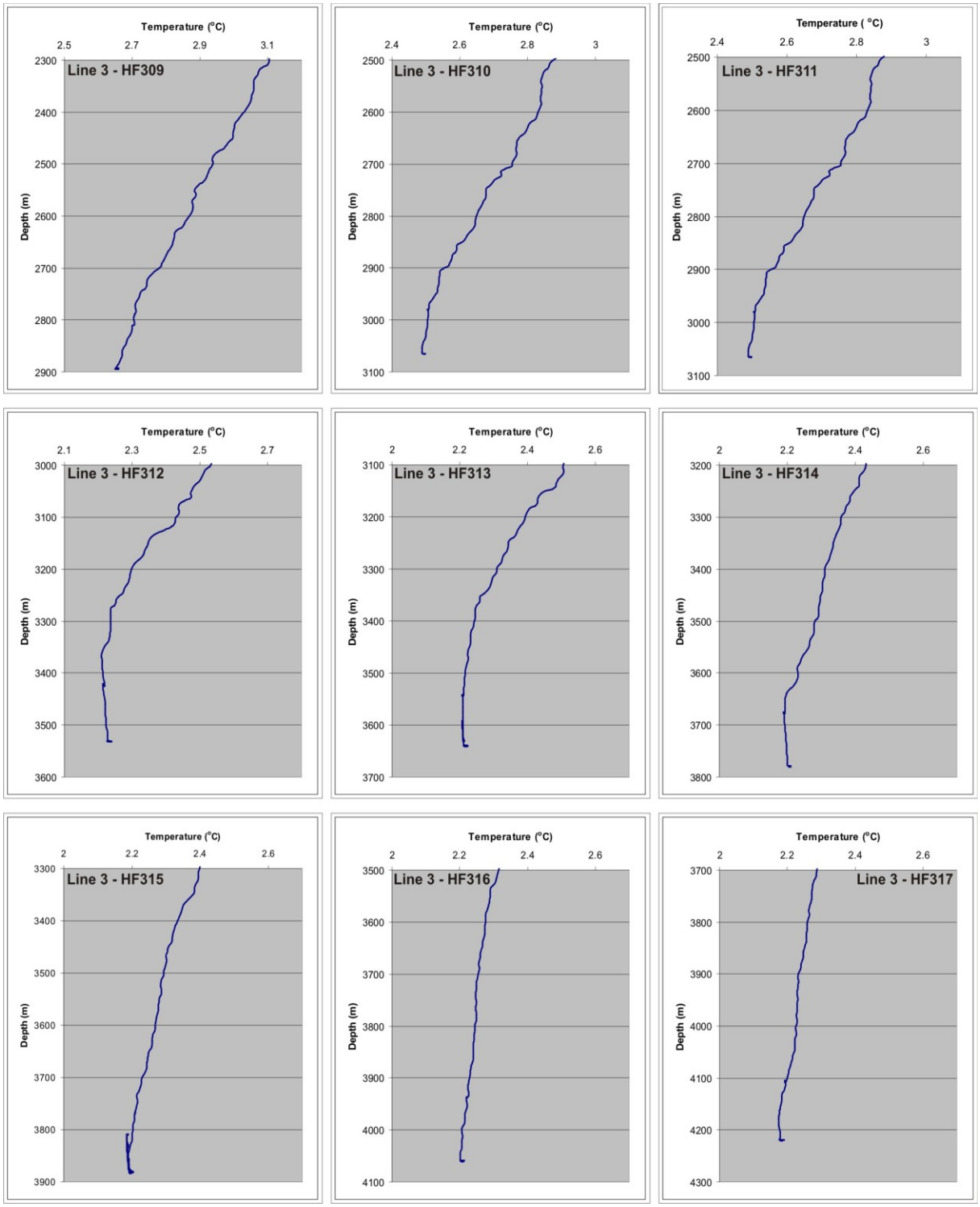

Figure D 1: Temperature vs. Depth plots for the bottom ~600 m of the water column for all heat flow stations with CTD data from the Hudson 2008 heat flow cruise.

Appendix E: 2D static conductivity based salt models

This appendix contains plots showing the effects of different basement heat fluxes and salt distributions on seafloor heat flow using simple static 2D conductivity based numerical models (Fig. E1-E8). Models are run with diapir morphologies after D1-D5 on seismic lines 1400 and 88-1A (Fig. 3.5 and 3.6). Conductivity values are the same in all models. Salt is given a conductivity of 5.9 $Wm^{-1}K^{-1}$, and sediments are assigned conductivities increasing with depth from 2.2 $Wm^{-1}K^{-1}$ at the seafloor to 3.1 $Wm^{-1}K^{-1}$ above the basal salt layer, to account for variations in conductivity associated with sediment compaction. Multiple models with slight variations to diapir D5 were run. Basal heat fluxes of 50 mWm^{-2} and 70 mWm^{-2} were tested to see how varying the input heat flux would effect the seafloor heat flow values in the presence of salt. To determine how significantly height and proximity to the seafloor would effect seafloor heat flow values the height of the diapir was increased by 20% for Salt Model 3. Finally, a model was run assuming a cylindrical salt body to determine how this would effect the model output in place a of a strictly 2D model.

Salt Model 2 (Fig. E2) showed the best match to our measured seafloor heat flow data in regions unaffected by salt as both measured and modelled heat flow yielded values of ~43 mWm^{-2}. However, modelled seafloor heat flow above the salt diapir was significantly lower than measured values for this model yielding a maximum value of 55.95 mWm^{-2} compared to the maximum measured value of 72.8 mWm^{-2}. Increasing the basal heat flux in Salt Model 3 to 70 mWm^{-2} resulted in a better, although slightly higher, fit to the measured data above the diapir yielding maximum seafloor heat flow values of ~78 mWm^{-2} (Fig. E3). However, regions unaffected by salt also showed elevated seafloor

heat flow predicting values of ~60 mWm^{-2}. Salt Model 5 with the assumed cylindrical diapir configuration (Fig. E5) yielded results almost identical to the simple 2D Salt Model 2.

Models of all diapirs on seismic line 1400 (D1-D4) were run with the same input parameters as Model 2 of D5 as we determined this model best matched our measured data. Models 6-8 represent the four diapirs present in line 1400.

Salt Model 1: Initial Model Configuration

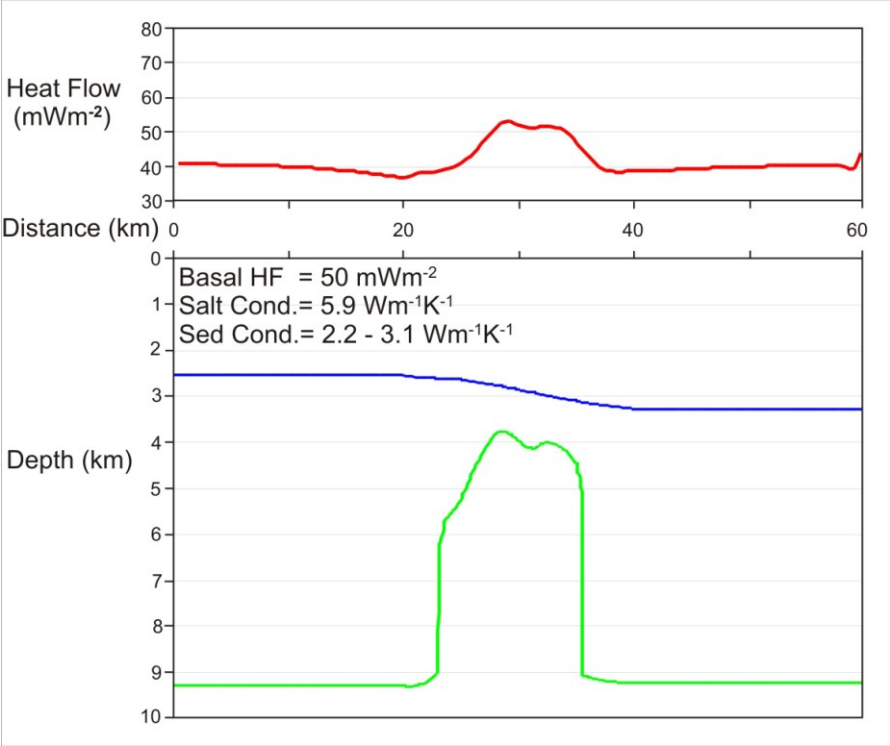

Figure E 1: Simple 2D model of D5 showing modelled seafloor heat flow data.

Salt Model 2: Copy of Salt Model 1 extended laterally.

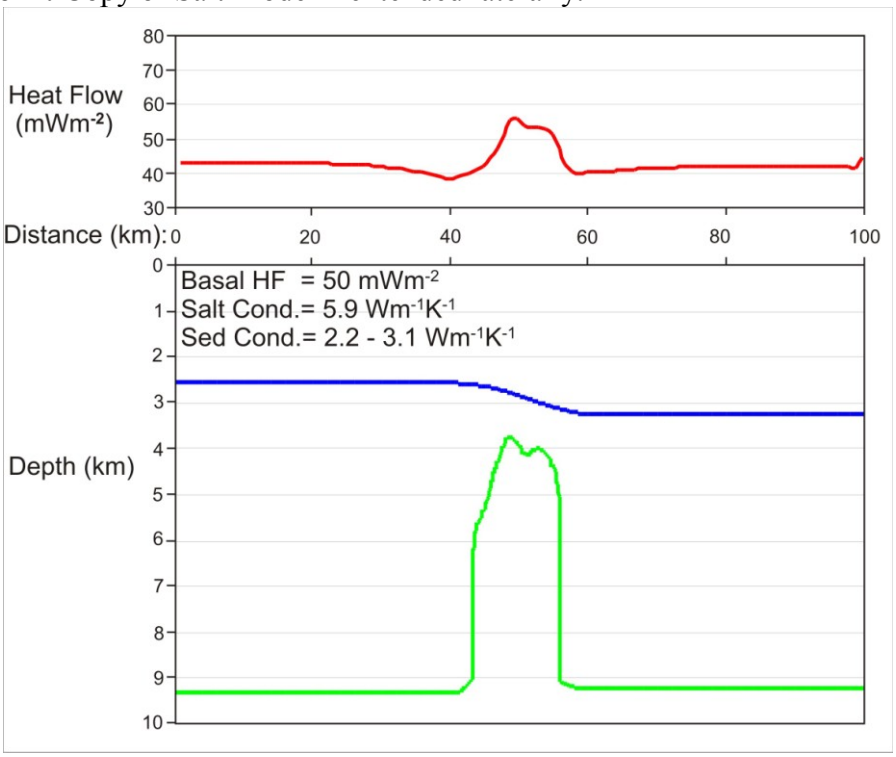

Figure E 2: Replica of Salt Model 1 extended laterally by 40 km to escape edge effects.

Salt Model 3: Copy of Salt Model 2 with higher basal heat flux (70 mWm^{-2}).

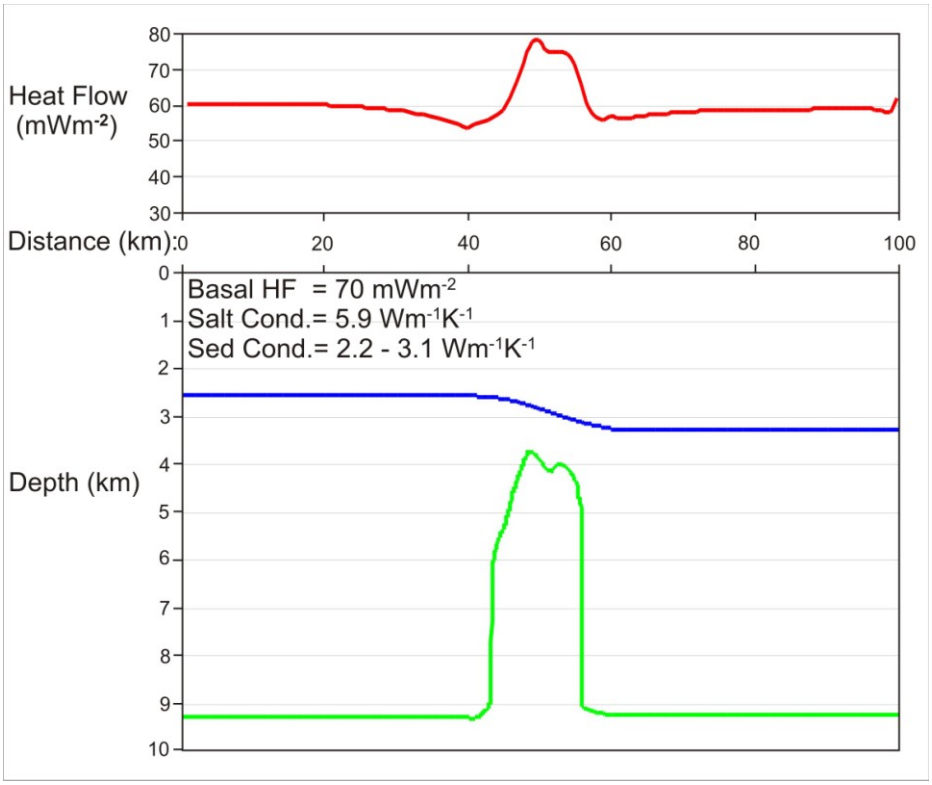

Figure E 3: Replica of Salt Model 2 with increased basal heat flux.

Model 4: Copy of Salt Model 2 with a taller diapir (20% taller)

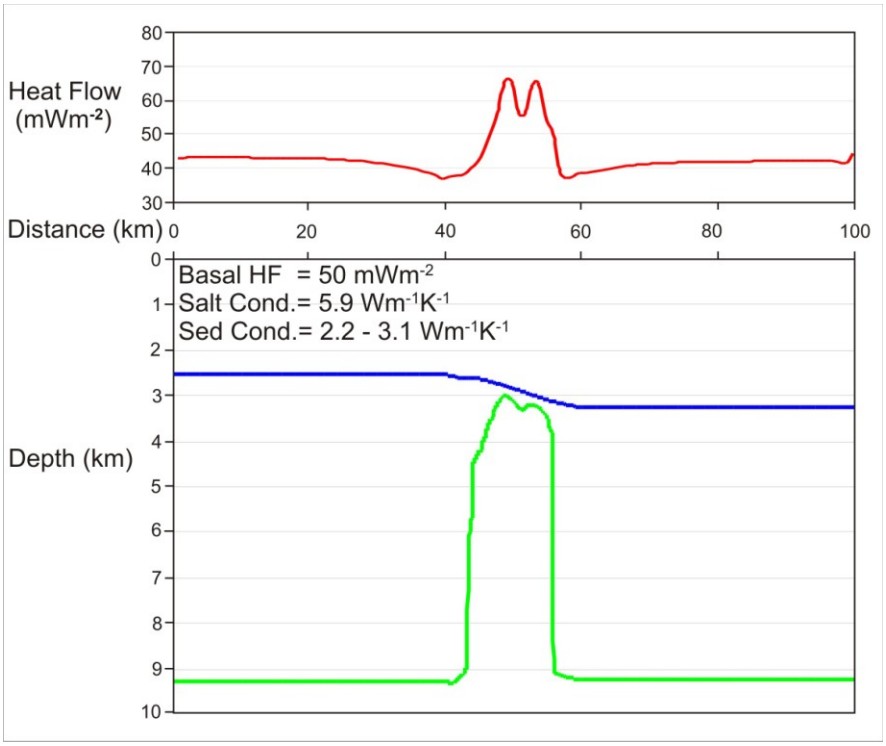

Figure E 4: Replica of Salt Model 2 with taller salt diapir.

Salt Model 5: A copy of Model 2 using the cylindrical diapir calculation.

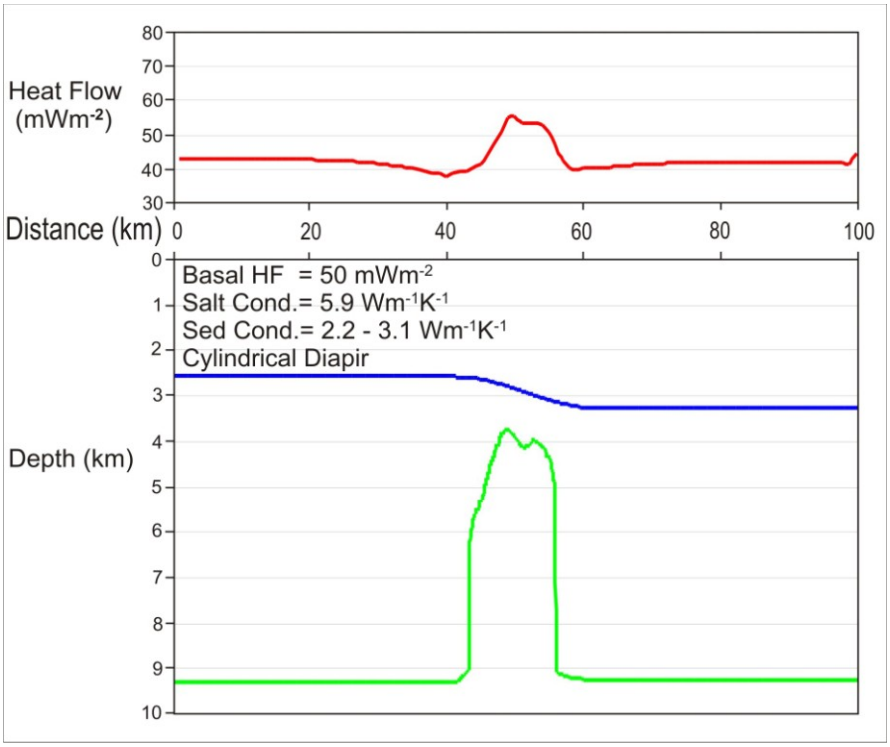

Figure E 5: Replica of Salt Model 2 assuming cylindrical diapir.

Salt Model 6: Modelled after D1 in line 1400

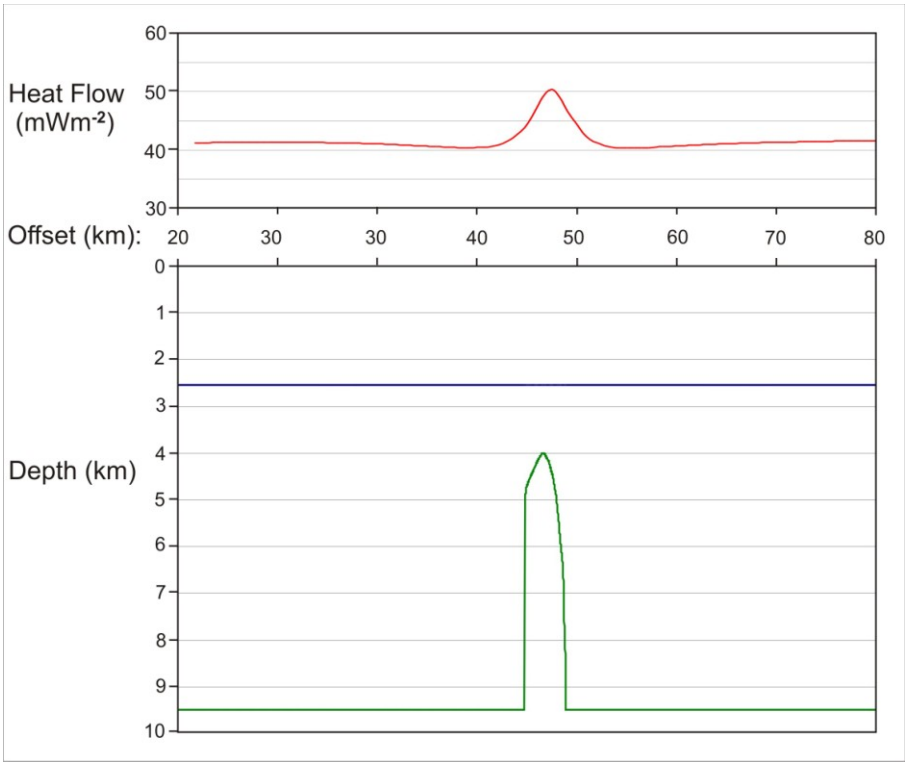

Figure E 6: Model of salt diapir D1 in line 1400.

Salt Model 7: Modelled after D1 in line 1400

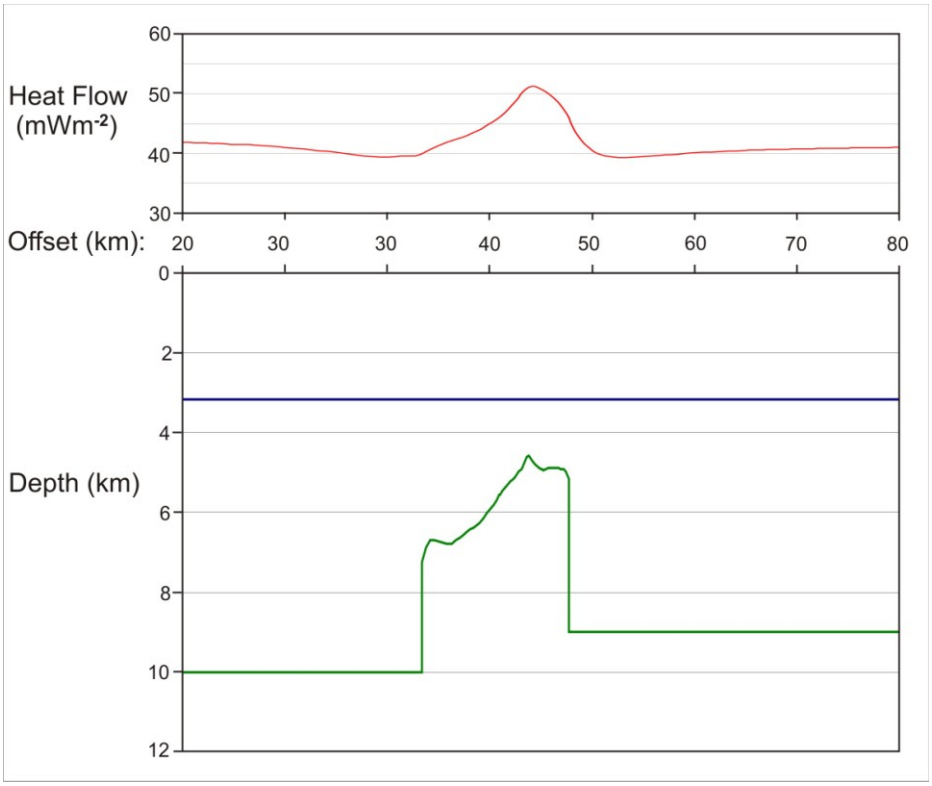

Figure E 7: Model of salt diapir D2 in line 1400**.**

Salt Model 8: Modelled after D3-4 in line 1400

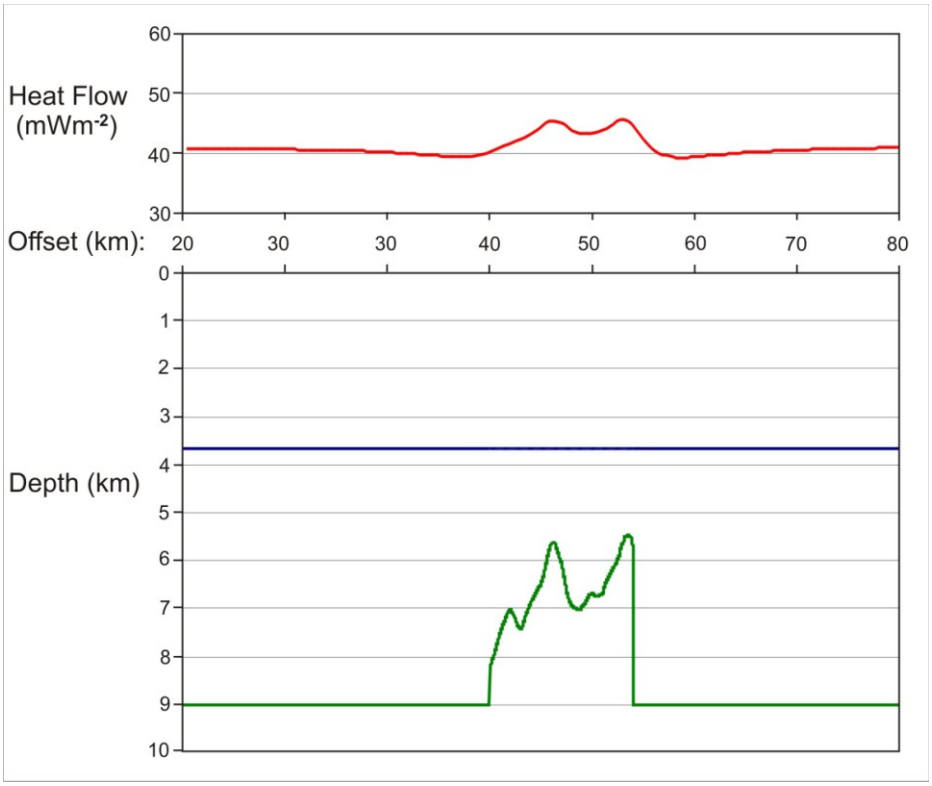

Figure E 8: Model of salt diapirs D3-4 in line 1400.

Appendix F: Introduction to Simple Crustal Rift Models

Many simple numerical models have been proposed in an attempt to better understand the rifting process associated with continental extension and breakup. These models, in addition to explaining the general process of rifting from initiation of crustal extension to the continental drift phase, are focused on predicting and describing changes in crustal subsidence, temperature, and heat flow through time following the onset of rifting. Multiple phases of 2D thermal models including the boundary layer model (half space model) (Davis and Lister 1974), the pure shear model/uniform stretching model (McKenzie 1978), the dual stretching model (Royden and Keen 1980), and the simple shear model (Wernicke 1985) have been proposed. In addition to the more simplistic thermal models of rift evolution, many phases of dynamic thermo-mechanical models have also been proposed to help better understand the evolution of rifted continental margins (e.g. Keen and Beaumont 1990). As our goal is simply to match measured seafloor heat flow data with crustal heat flux predictions we have employed only the simple and dual stretching models of McKenzie (1978) and Royden and Keen (1980).

The pure shear model assumes a uniform plate of known thickness (L) is stretched by a factor β at the onset of rifting with a lower boundary set as a constant isotherm (McKenzie 1978) (Fig. 3.12). There are two factors contributing to the total tectonic subsidence following thinning: the initial subsidence associated with isostatic balancing of the cooler, less dense lithosphere with the hotter and denser upwelling asthenosphere, and the thermal subsidence associated with the thermal contraction of the cooling asthenosphere with time following rifting. Upon initiation of thinning comes an increase in surface heat flux as heat from the hot asthenosphere is conducted vertically through the

thinned lithosphere to the surface. Larger stretching factors result in higher seafloor heat flux values following rifting which eventually return to the original unstretched values as time approaches infinity (Fig. F1). The dual stretching model is similar, however, it allows for non-uniform stretching of the upper and lower lithosphere by factors of β and δ respectively (Royden and Keen 1980). Different stretching factors of the upper and lower lithosphere will result in drastically different heat flow histories.

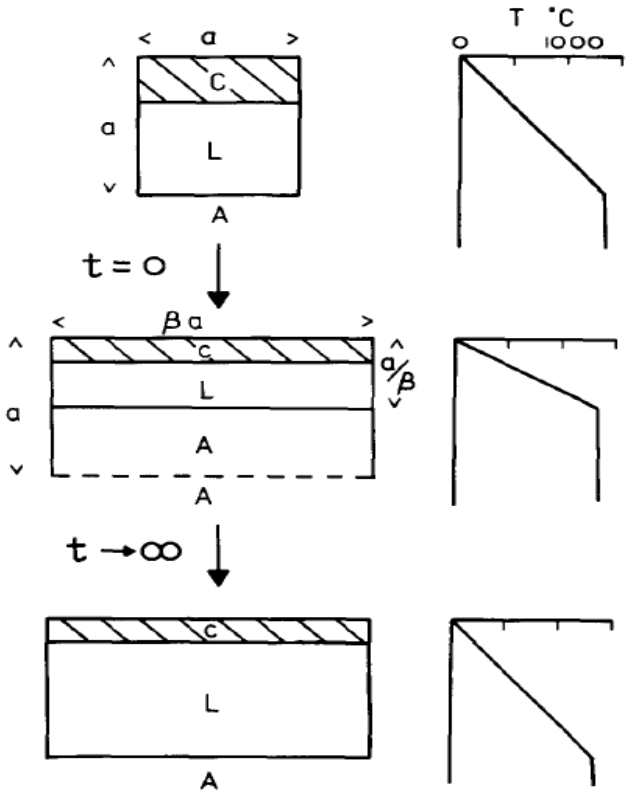

Figure F 1: Cross sections show extension of the lithosphere of original thickness α by a factor of β, thus thinning by α /β. Thinning results in upwelling of the hot asthenosphere. As cooling occurs, there is a resulting thermal subsidence of the crust. Changes in the temperature profile associated with the upwelling asthenosphere are shown to the right (From McKenzie 1978).

As an alternative to the McKenzie pure shear model Wernicke (1981) proposed a simple shear model in which extension in the crust and mantle lithosphere are not uniform in a vertical plane. The model proposes that a low angle normal fault forms a detachment which penetrates deep into the crust and possibly through the entire

lithosphere (Fig. F2), allowing for the structural asymmetry observed across many rifted continental margins (Wernicke, 1985). It is along this detachment that extension occurs, and along which fault blocks of the upper crust are created and transported to accommodate the extension. The margin is divided into upper and lower plates as separated by the detachment fault. The depth of this detachment varies laterally, thus there will be a lateral transition from brittle shear to ductile shear along the detachment as it reaches the transition from the solid crust to the ductile upper mantle. This results in the formation of numerous smaller fault blocks in the regions overlying the brittle detachment, to fewer larger fault blocks in the region overlying the ductile detachment (Wernicke, 1981).

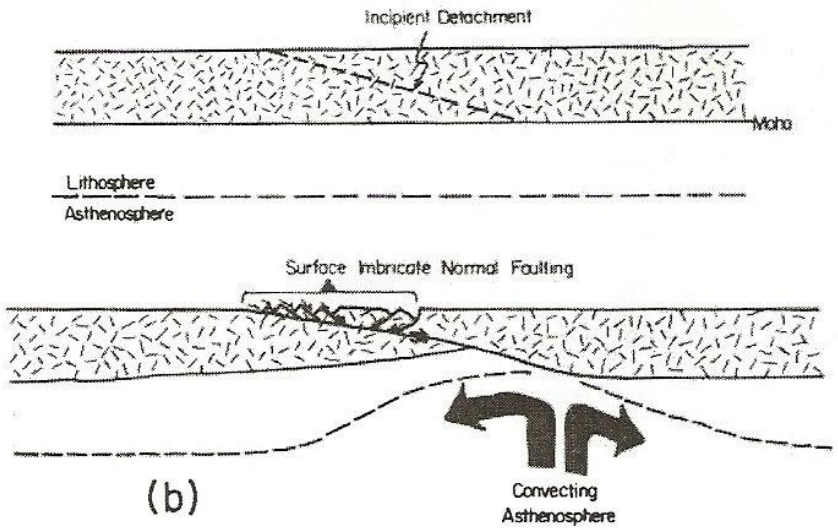

Figure F 2: Simple shear model depicting a low angle detachment penetrating the lithosphere to accommodate extension (From Wernicke, 1985).

We have written MatLab scripts for the calculating crustal heat flux following rifting after Equation 7 of McKenzie (1978) (Script 1) and Equation A-2 after Royden and Keen (1980) (Script 2). Crustal stretching factors (β) were constrained after Wu (2007) for the central Scotian Slope at the locations of our seafloor heat flow stations as

described in Section 3.6. Two original lithospheric thickness' (A), 100 km and 125 km, were tested in the models and the asthenospheric temperature was held constant at 1350 °C for all models run.

Pure Shear (Uniform stretching) Heat Flow Script

```
% calculates heat flow from Eq. 7 McKenzie, 1978
% here calculate HF for t=0 to 250 Ma
% here we also plot different B values how different constant B values vary with t

clear
T1=1350  %T at base of lithosphere
A=125000  %thickness of lithosphere (m)
pi=3.1415926
K=3150  %thermal conductivity of lithosphere (mW/m*deg)
B=[1 1.125 1.5 2 4];
t=[0:200];
tau=62.8;
x=0
for i=[1:201]
   for j=[1:5]
      for n=1:100
   x1=[(B(j)/(n.*pi))*sin(n.*pi/B(j))]*exp(-(n.*n.*t(i)/tau));
x=x+x1;
end
HF(i,j)=(K*T1/A)*[1+2*(x)];
x=0;
end
end
plot(t,HF)                    Fig. F3
ylabel('HF (mW/m^2)'), xlabel('time (Ma)')
legend('B=1','B=1.125','B=1.5','B=2.0','B=4.0')
```

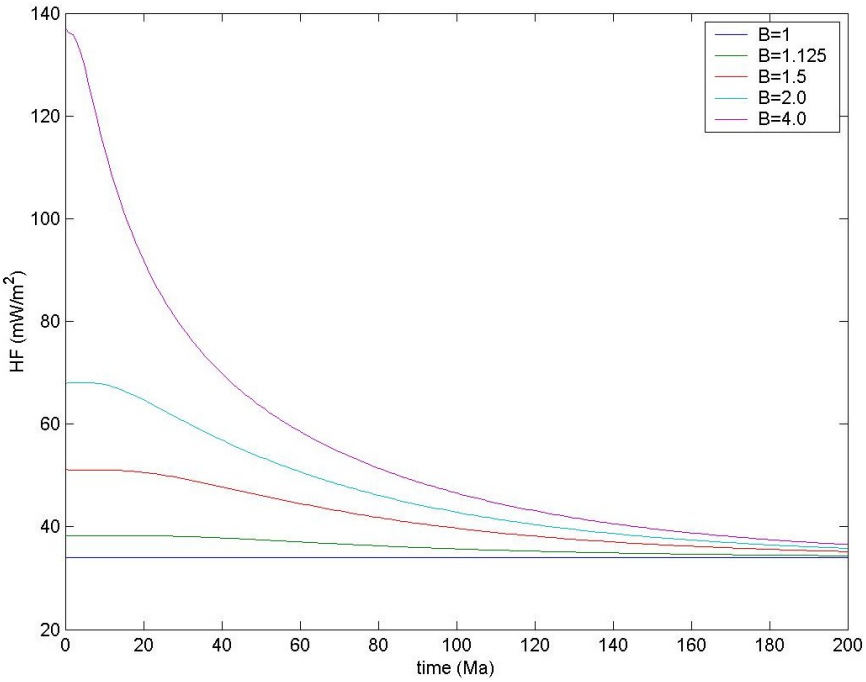

Figure F 3: Heat flow vs. time plot for the pure shear model showing effects of varying crustal stretching factors (B) on heat flow. Time represents time since onset of rifting in Ma.

Dual Stretching Heat Flow Script

```
% Eq. A-2 Royden and Keen, 1980
% Calculate crustal Heat Flux as a function of time, Beta and Delta

clear
% Note: I have switched B and D from in the paper so B=crustal thinning.
T1=1350;  %T at base of lithosphere
A=125;  %thickness of lithosphere (km)
pi=3.1415926;
Q=ones(5,5,201);
K=3.15;  %thermal conductivity of ??lithosphere (in W/m/degC)
k=7.5e-7;  %thermal diffusivity of the lithosphere (m^2/s)
B=[1 1.125 1.5 2 4 8];     %crustal stretching factor stretching factor, B=j
D=[1 1.125 1.5 2 4 8];   % lithospheric (upper mantle) stretching factor, D=i
Y=0;  % fraction of the lithosphere replaced with dykes
t=[0:200]; %time after rifting (in Ma)
tau=62.8; %thermal time constant
y=30;  %thickness of the crust (point of separation of B and D) (in km)
pm=3.3;  %density mantle
pc=2.8;  %density crust
pw=1.0;  %density seawater
n=[1:500];
a=3.3e-5;    %thermal expansion coefficient
% now I start to group together constants and reoccurring terms
% C1=K*T1/A; %(in W/m^2)
C1=0.033472*1000 ;
x=0 ;
for j=[1:6]
   H=1-(y/(A.*B(j)));
   for i=[1:6]
      G=1-(y/(A.*B(j)))-((1-y/A)/D(i));
      for h=[1:201]
         for n=1:500
        x1=(B(j)-D(i))*sin(n.*pi.*H);
        x2=[D(i)*sin(n.*pi.*G)];
        x3=[(-1)^(n+1)]/(n.*pi);
 xn=(x1+x2).*x3;
 xf=2.*xn.*exp(-(n.*n.*pi.*pi.*(k.*t(h).*1000000.*31556926/(A.*A.*1000000)))); % as t
increases, xf decreases
   x=x+xf;
         end
Q(j,i,h)=C1.*(1+x);

x=0;
      end
   end
end

plot(t,squeeze(Q(1,1,:)),t,squeeze(Q(3,3,:)),t,squeeze(Q(2,2,:)),t,squeeze(Q(4,4,:)),t,squeeze(Q(5,5,
:)));                                Fig. F4
ylabel('HF (mW/m^2)'), xlabel('time (Ma)')
legend('B=1 D=1','B=1.125 D=1.125','B=1.5 D=1.5','B=2.0 D=2','B=4.0 D=4')
```

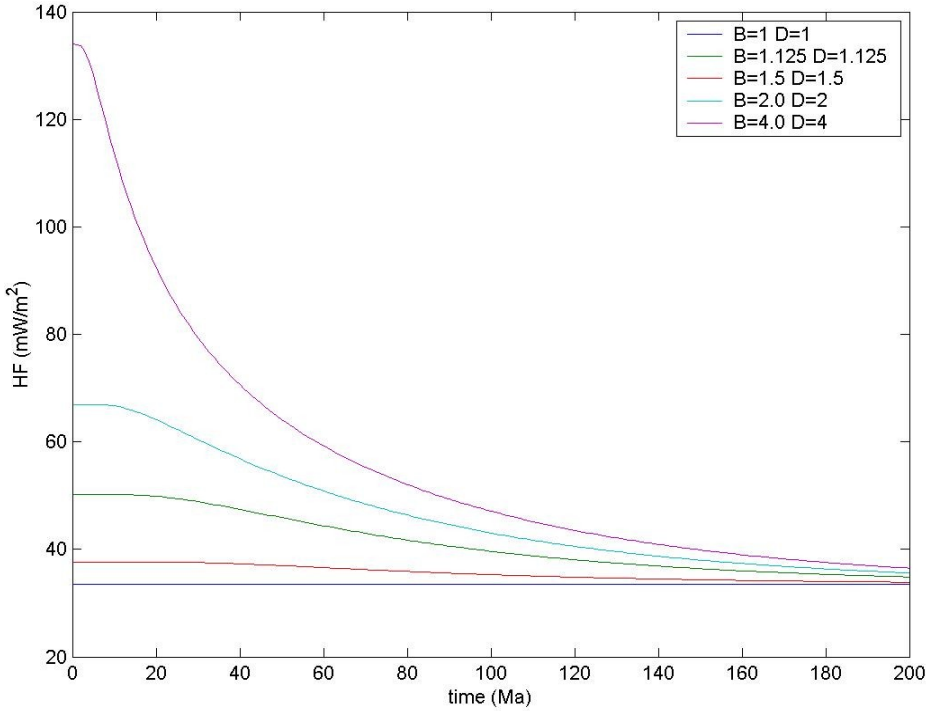

Figure F 4: Heat Flow vs. Time plot for dual stretching model with equal components of upper (B) and lower (D) lithospheric thinning.

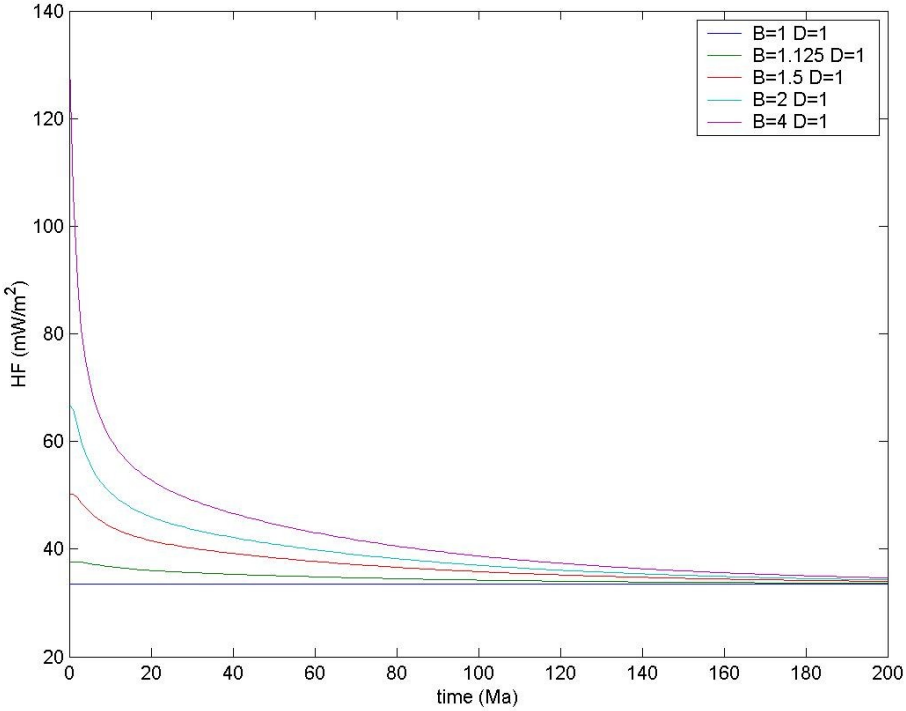

Figure F 5: Heat flow vs. time plot for dual stretching model with unstretched lower lithosphere (D), and varying upper lithospheric stretching (B).

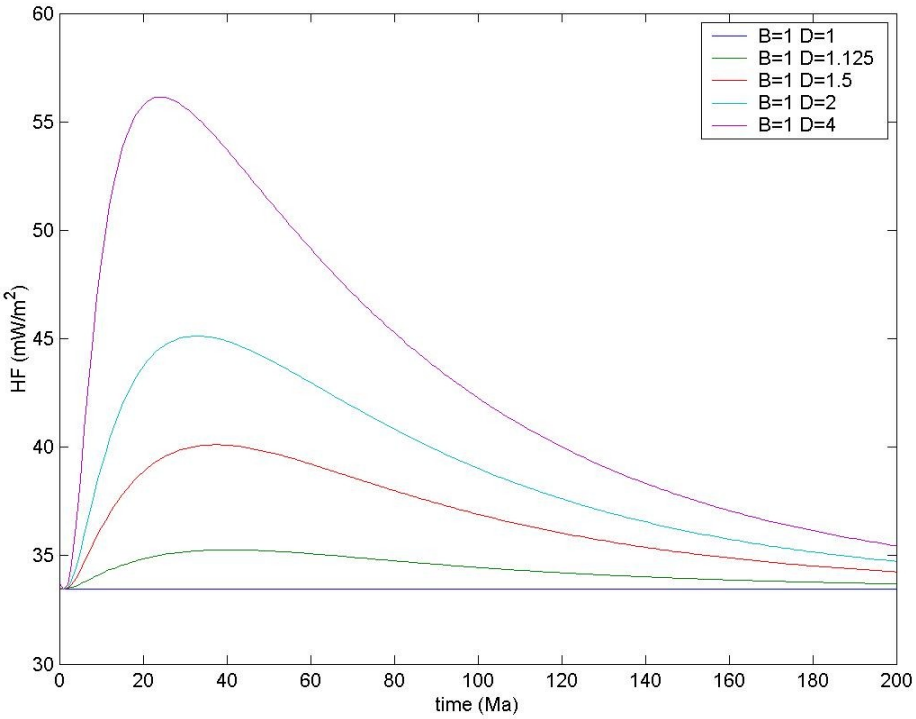

Figure F 6: Heat flow vs. time plot for dual stretching model with unstretched upper lithosphere (B), and varying lower lithospheric stretching (D).

Appendix G: Conversion of Analogue Data to SEG Y Format

The TGS-Nopec 2D seismic reflection survey is only publicly available as paper copy time sections. As a requirement for geological interpretation and consistency with other data in our seismic database this analogue data must be converted to digital depth sections. The standard data format required for input into seismic interpretation packages such as Kingdom Suite is the segy file. All TGS-Nopec lines in our seismic database have been converted to segy files and later depth converted. The process of converting the data involves four main steps: 1) Scanning and reformatting the original paper copy analogue data into tif images that meet the requirements of the "tif2segy" program which converts analogue data to segy files, 2) Running the "tif2segy" program to produce the original segy files, 3) Creating digital navigation files for each of the scanned lines, and 4) producing velocity models for each seismic line and depth converting the sections to maintain consistency with our other depth converted seismic profiles. The method of data conversion is outlined below.

As of May 2009 both paper and mylar copies of the seismic profiles acquired during the first phase of the TGS-Nopec NS-100 survey shot in 1998 have been publicly available through the CNSOPB as file NS24-G26-1P. To better constrain the 3D distribution and structure of salt bodies within the vicinity of Lithoprobe seismic line 88-1a we have selected 12 seismic lines from the NS 100 survey for interpretation in addition to line 88-1a and NovaSPAN lines 5100 and 5300 of our initial seismic database. The additional TGS-Nopec lines include strike lines 157-100, 173-100, 181-100,189-100, 197-100, 205-100, 213-100 and 229-100, and dip lines 552-100, 560-100, 568-100 and 576-100 (Fig. 4.1).

Once the lines have been selected the first step involves scanning the seismic images and preparing them for conversion to segy format. Images are converted to segy using the “tif2segy” program written by Andrew MacCrae of St. Mary’s University (MacCrae 2001). In preparing the scanned image for conversion there are numerous requirements that must be met in order for the conversion to be successful. The image must first be rotated so that all seismic traces are vertical (or as close to vertical as possible), then cropped so that all headers and borders are removed, and that the only data present in the images is the vertical wiggle traces from 0 s twt down to the end of the trace, in this case 12 s twt. The image must then be resampled so that each seismic trace in the x-axis corresponds to one pixel, and each sample in the y-axis corresponds to one pixel. For example, an image with 2000 traces, showing 12 s of data recorded at a sample rate of 2 ms would be resampled to produce a 2000 x 6000 pixel image. Finally, the image must be saved as an 8-bit grey scale tiff file before it is ready to be converted to a segy file.

The tiff to segy conversion is done quite easily using Andrew MacCrae's "tif2segy" script. The script involves a series of commands which convert an input tiff file to an output segy file, creating the seismic traces, setting the sample interval and building a simple header in the process. The number of traces in the output segy file corresponds with the number of pixels in the x-axis of the input image, and the output sample size and rate are related to the number of pixels in the y-axis of the image and the sample rate defined by the user. The script uses both NetPBM and Seismic Unix during the conversion, and it is required that both these programs are installed on the machine running the script. NetPBM is used for the manipulation of graphic images, in this case,

the conversion of the of the input tiff to a pnm format required for use in Seismic Unix. Seismic Unix is a geophysical processing package and is used to create the seismograms and to add a define the information in the trace. Finally the segy file is written using the recently created headers and the Seismic Unix file.

As digital navigation data was not available for any of the TGS-Nopec lines navigation files must be built for each seismic profile from data digitized from the available shot point map. A paper copy shot point map was included with the NS24-G26-1P file by the CNSOPB which contains both X/Y and Lat/Long coordinates, as well as the location of the seismic lines in the survey showing every hundredth shot point. The map was scanned for digitization using "DigitizeIt" software.

The first step is to geo-reference the map by digitizing four known points on the scanned image and defining the associated X/Y coordinates in the DigitizeIt program. The four corners of the map were selected, from which DigitizeIt defines an X/Y grid for the rest of the map. The intersections of latitude and longitudes on the map are plotted as large cross hairs which we used to test the accuracy of the X/Y grid calculated for the map based on the four points we defined. This was done by digitizing points on the lat/long intersections and recording both the given lat/long values from the shot point map, and the inferred X/Y values as given from the digitize it program. The calculated X/Y values were then converted back to lat long coordinates using the mapproject function of GMT (generic mapping tool), which were compared to the original Lat/Long values digitized from the shot point map. This was done for the 14 Lat/Long intersections. It was found that in digitizing longitude values were shifted an average of -0.00231, and latitudes were shifted an average -0.00196, and when corrected for this

shift, points were within 250 m of the original digitized location on the S.P. map. This processes of digitizing the Lat/Long cross hairs was included simply as a test of the accuracy of the digitization process and in order to determine the shift required to minimize the offset in digitized locations from true locations.

Finally, the individual S.P.s must be digitized for each seismic line of the survey in order to attach navigations to the recently created segy files. Every hundredth S.P. is shown as small blue tick on the S.P. map, and for each line, all plotted S.P.s are digitized with the corresponding shot number recorded. The digitized S.P.s are corrected for the shift associated with digitizing using the average value calculated from the lat/long cross hairs truthing described above. Once complete, with the scanned images converted to segys, and the accompanying navigation data derived from the S.P. map, the seismic profiles can be loaded into Kingdom Suite® as time sections, however the data must still be depth converted to maintain consistency with the Lithoprobe and NovaSPAN data.

Depth Conversion

In order to convert the TGS Nopec data from twt to depth sections, a simple velocity model modified after Wu (2007) was employed. The velocity model includes only four layers corresponding to seawater, general Scotian Slope sediment, salt, and basement. The top layer has a velocity increasing from 1.47 km/s at its surface to 1.49 km/s at its base and corresponds to seawater velocities. The second layer corresponds to main sediment succession of the Scotian Slope and has velocities increasing from 1.7 km/s at the seafloor to 4.5 km/s at the basement boundary due increasing velocities associated with the compaction of sediment. The third layer corresponds to the salt layer, and maintains a constant velocity of 4.5 km/s. As we are not so much concerned with

structures within the basement surface the entire basement layer was designated an increasing velocity from 4.6 km/s to 6.0 km/s.

For each line the velocities in the velocity model remain the same, however the structure of the model must be tweaked to match water and basement depths and salt distribution. Velocity modelling was done using Seiswide software. The velocity model used to depth convert TGS Nopec seismic line 552-100 is shown below as an example (Fig. G1).

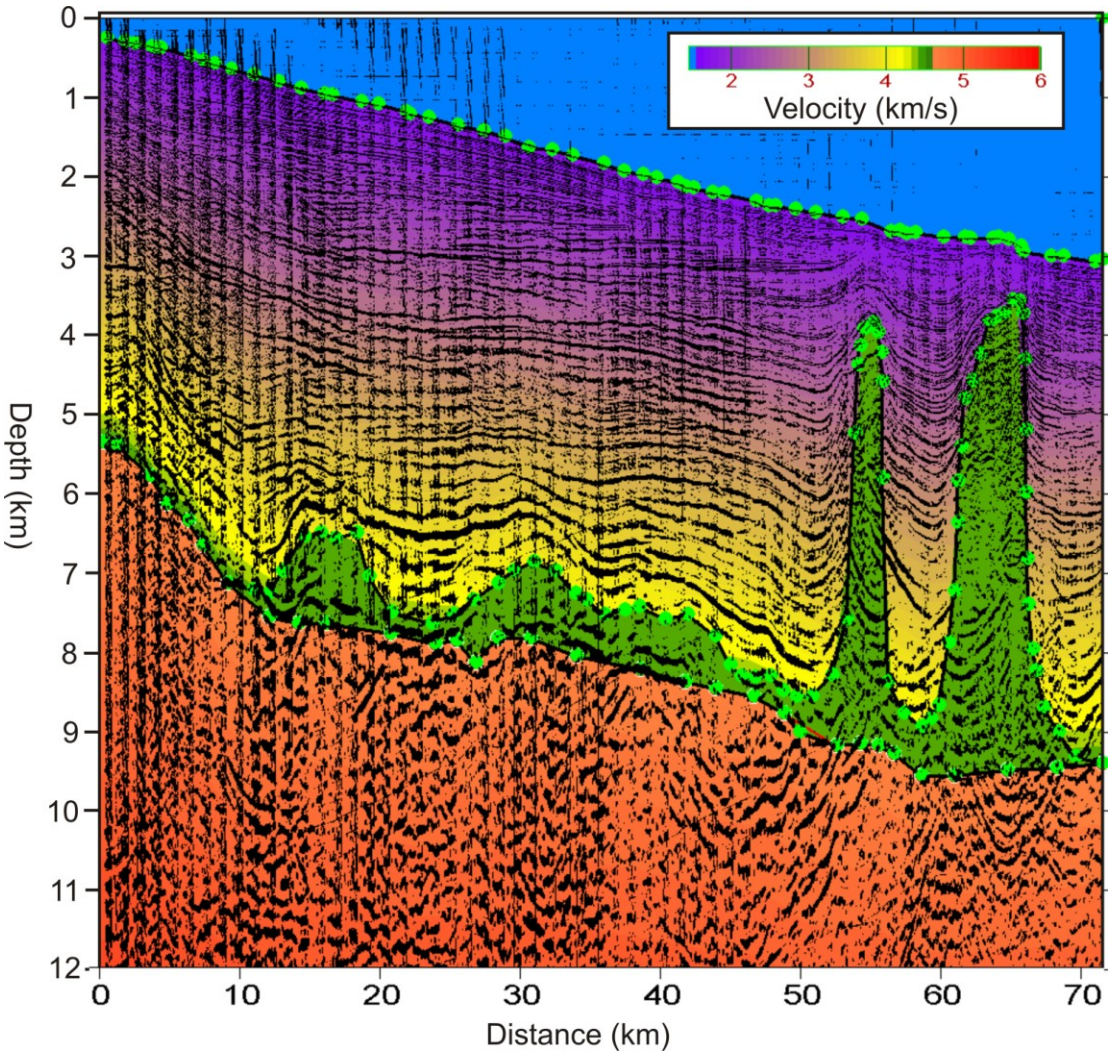

Figure G 1: Depth converted section of TGS Nopec 2D seismic line 552-100 with the velocity model used for depth conversion as a transparent color overlay.